UNIVERSITÀ DEGLI STUDI DI UDINE

DIPARTIMENTO POLITECNICO DI INGEGNERIA E ARCHITETTURA

PHD IN INDUSTRIAL AND INFORMATION ENGINEERING

XXX CYCLE

SHUNTED ELECTRO - MAGNETIC TRANSDUCERS FOR BROADBAND NOISE AND VIBRATION CONTROL OF CYLINDRICAL SHELLS

BY

Emanuele Turco

SUPERVISOR: Prof. Paolo Gardonio

CO-SUPERVISOR: Prof. Roberto Petrella

ACADEMIC YEAR 2016-2017

ABSTRACT

This thesis is focused on theoretical and experimental studies regarding semi-active control of the noise and vibration response of a thin cylindrical shell using electromagnetic transducers. The motivation of this research is the increasing interest in low cost, low energy consumption and low weight practical solution to the noise and vibration problems encountered in transportation vehicles such as cruise ships, trains, aircraft and cars.

Initially, a fully coupled structural-acoustic model of a cylindrical shell and acoustic enclosure, based on the Modal-Interaction-Model, is presented, which derives flexural displacement from a modal expansions of the *in vacuo* flexural modes of a simply supported cylinder and the interior acoustic pressure field from a modal expansion of acoustic natural modes for the *rigidly-walled* cylindrical cavity. An energy formulation is adopted to describe the flexural and acoustic response of the system subject to a rain-on-the-roof stochastic excitation. A systematic convergence analysis aimed at finding the natural modes that should be included in the modal expansion for the sound pressure response of the cylindrical enclosure and for the flexural response of the cylindrical wall is presented.

Then, the effects of classical mechanical fixed Tuned Vibration Absorbers (TVA) are assessed with a low-frequency simulation study. The tuning criteria of the classical fixed TVA are first recalled and a reduced structural-TVA model that considers only one natural structural mode was used to derive general guidelines regarding the positions of vibration absorbers on cylindrical structures.

The last part of the thesis is devoted to the time-varying shunted electromagnetic absorbers. An electro-mechanical analogy study, which lead to the design of the RL shunt circuit, is presented. The shunted electromagnetic absorber is operated in the sweeping mode, in which the values of shunt elements are continuously varied as to harmonically vary the stiffness and damping properties of the absorber so that its mechanical fundamental natural frequency is continuously swept in a broad frequency range which correspond to the frequency range of interest whereas its mechanical damping is continuously adapted to maximise the vibration absorption from the hosting structure. In this operation mode the time-varying shunted electromagnetic absorber produces a broad-

band control of the cylinder flexural response and of the interior noise without need of tuning and system identification of the structure.

CONTENTS

LIST OF FIGURES

LIST OF TABLES

NOMENCLATURE

LIST OF ACRONYMS

ADC	Analogue-to-digital converters
ANC	Active Noise Control
ASAC	Active structural acoustical control
AVC	Active vibration control
CPU	Central processing unit
DAC	Digital-to-analogue converters
DVA	Dynamic Vibration Absorber
EM	Electro-magnetic
FRF	Frequency response function
HR	Helmholtz Resonator
IEPE	Integrated electronic piezoelectric
LC	Inductive-capacitive
MIA	Modal Interaction Analysis
MIM	Modal Interaction Model
PSD	Power Spectral Density
RL	Resistive-inductive
RLC	Resistive-inductive-capacitive
sdof	Single-degree-of-freedom
TMD	Tuned Mass Damper
TVA	Tuned Vibration Absorber

LIST OF SYMBOLS

Parameter	Description	Unit
L	Length of the cylindrical shell	[m]
R	Radius of the cylindrical shell	[m]
h	Thickness of the cylindrical shell	[m]

Parameter	Description	Unit
E	Young's modulus	[N/m^2]
ν	Poissons's ratio	—
U, V and W	Displacements along the axial, circumferential and transverse (radial) directions respectively, at an arbitrary point of the cylindrical shell	[m]
u, v and w	Displacements along the axial, circumferential and transverse (radial) directions respectively, at an arbitrary point at the middle surface of the cylindrical shell	[m]
K	Membrane stiffness	[N/m]
D	Bending stiffness	[Nm^2]
$\omega_{s,m}$	m-th structural natural angular frequency	[rad/s]
φ_m	m-th structural mode shape	—
ζ_s	structural modal damping	–
S_K	PSD of the total kinetic energy of the cylindrical shell	[J/(NHz)]
t	Time	[sec]
ρ_0	Density of the fluid	[kg/m^3]
c_0	Speed of sound in the fluid	[m/s]
ζ_0	acoustical modal damping	–
$\omega_{a,n}$	n-th acoustical natural angular frequency	[rad/s]
ψ_n	n-th acoustical mode shape	—
S_P	PSD of the total acoustic potential energy of the cylindrical enclosure	[J/(NHz)]
R	acoustic-structural coupling matrix	—
S	structural-acoustic coupling matrix	—
m_s	Seismic mass of the TVA	[kg]
m_b	Base mass of the TVA	[kg]
k	Stiffness coefficient	[N/m]
c	Damping coefficient	[Ns/m]
μ	Mass ratio	—
ψ	Electro-mechanical coupling coefficient	[N/A]

Parameter	Description	Unit
ω	Angular frequency	[rad/s]
f	Frequency	[Hz]
j	Imaginary unit defined as $j = \sqrt{-1}$	—

1

INTRODUCTION

Flexural vibration of distributed structures is an important practical problem, especially when it is associated to noise radiation into enclosures such as for example the passenger cabins in cruise ships, trains, aircraft and cars [1–3]. Indeed the undesired and potentially dangerous effects of noise and vibration on humans could cause, in the harmless case, discomfort and annoyance, leading to speech interference or activity disturbance, interfering with wanted activities such as, for example, rest, relaxation and hand or foot movements. Also, the effects of vibrations or acoustical disturbances could lead to hearing damage risks, sleep disturbances, vision difficulties, headaches, nausea, effects on cognitive performances and a wide variety of health diseases [4–6].

Excessively high levels of noise and vibration could also be harmful for the structures involved, they can lead to large displacements and stresses which may cause fatigue, breakage, wear or improper operation [7, 8].

The address of the noise and vibration issues are driven by two main motivating factors. The first comes from the legal regulations that many countries have set on these topic; in the European Union some of them are for example the Noise at Work Directive 2003/10/EC [9], the Directive 2006/42/EC on machinery [10], the Human Vibration Directive 2002/44/EC [11] and the Directive 2000/14/EC on the approximation of laws of the member states relating to the noise emission in the environment by equipment for use outdoors [12].The second aspect is related to customer demand. Customer requirements and expectation represent an incentive to the noise and vibration control problem, since the user discomfort leads to competitive disadvantage and a loss of the market share.

Over the years several materials, designs, mechanical treatments and control devices have been developed to mitigate vibrations in thin walled structures [7, 13–21]. Mass, stiffness and damping treatments, double wall constructions with sound absorbing materials, Tuned Vibration Absorbers (TVA), Helmholtz

Resonators (HR) and composite materials are typical examples of noise and vibration treatments.

The amplitude of mechanical vibrations can span from metres to nanometres and the associated frequency can varies from a fraction of Hertz to several kHz. Thus, the selection and the design of the most appropriate treatment for a system is a complex process and the solution is often a trade-off between the design constrains (weight and dimension limits, fabrication and maintenance costs, structural requirements, etc.) and the effectiveness of the remedy.

Usually, the control techniques are categorised, depending on the use of external power sources, in passive and active systems [17, 22–27]. Recently, a big effort has been dedicated to the study and development of a new category of control techniques, the semi-active. These systems enhance the control effects obtained with classical passive treatments but require less energy and are more robust to sensor failure than active devices.

1.1 PASSIVE VIBRATION CONTROL

The aim of the passive treatments is to modify the response of the system in order to make it less sensitive to the excitation. No external energy is given to the system to obtain the change of the response.

The modification of the response can be obtained changing the structural properties of the systems by means of mass, stiffness and damping treatments. The classical classification [17] divides the passive vibration approaches into four main categories. The first approach of passive vibration control is by structural design. This method relies on a full knowledge of the excitation source and requires an accurate model to estimate the level of structural vibration. The design process should therefore be focused on the optimisation of the structural quantities in order to reduce the vibration level, e.g. by shifting the system resonances away from the frequencies of the excitation field [28].

A second approach, particularly suitable when the vibration of structure is characterised by many resonance, involves the increasing of the structure damping [21]. This approach, in the past misapplied and thus undervalued, emerged in the last years due also to the development of new and advanced materials. The basic principle of this approach is to convert the vibration energy into heat; this can be done applying highly damped materials, such as especially manufactured polymers, on strategic positions in the structure.

The third approach, referred as isolation [29], is applied when the vibration is transmitted through different components of the system. For example, the en-

gine of a car generates unbalanced oscillatory forces which can propagate to the supporting structure. A second case of application of this technique is encountered when a sensitive equipment is connected to a support characterised by a high vibration level, as for example in the case of the cutting tool connected to the lathe. The transmission of the vibration may be efficiently reduced by making the connections sufficiently soft or resilient so to isolate the sensitive system from the source of vibration.

The fourth approach is related to the addition of localised elements, which may be simple elements as a lumped mass [30], or combination of mass, stiffness and damping elements which can be either tuned to a resonance of the structure (Vibration Absorber) or to the disturbance frequency (Vibration Neutralized) [31–34]. These system can effectively reduce the vibration level of the hosting structure only over a narrow frequency range to which they are tuned. These devices thus require an *a priori* knowledge of the structural response or the frequency characteristics of the excitation field.

1.2 ACTIVE VIBRATION CONTROL

The active control system strongly rely on an external source of power. These system uses sensors applied on the structure to detect the vibration level, the signal is then precessed by electronic systems to drive active actuators (which may be electromechanical, electrohydraulic or electropneumatic) which reduce the vibrations. The effects of the actuators on the structure is to generate a vibration that counteracts that produced by the excitation field. The requirement of an external power supply makes them more costly but generally the active system achieve performances that no passive system can achieve [22, 29]. The need of a proper maintenance and the possibility of failure, which require a passive system as a back-up, are others drawbacks of the active systems. The way a disturbance is rejected leads the classification of active control systems into two main approaches [22, 29]:

FEEDFORWARD: generally used when the excitation is tonal or deterministic and the reference signal is correlated to the disturbance. The idea, originally developed for noise control [23], is to produce a secondary disturbance such that it destructively interfere with the primary disturbance at the location of the sensors [35]. This does not guarantee global control, unless the system is characterised by a small number of modes. Using the reference signal allows the control system to adapt to different working conditions. Thus, to obtain good performances of the controller it is

of paramount importance to exploit efficient algorithms to tune the controller in real time.

FEEDBACK: generally adopted when a reference signal is not available, e.g. when the structure is subject to a broadband random disturbance from many sources. This kind of control system is widely used for controlling the vibration of lightly damped structures, characterised by well separated resonance peaks in the low frequency region. Control of such structures is achieved with direct velocity feedback, which increases the effective damping in the system, as in the sky-hook damper [36].

1.3 SEMI-ACTIVE VIBRATION CONTROL

Semi-active control devices are passive systems that can adjust their parameters to adapt to changes in the working conditions, as for example temperature, pressurisation or tensioning effects that alter the dynamic response of the hosting structure, but they do not put energy directly in the hosting system.

Their development was driven by the will to overcome the drawbacks of the passive and active techniques. A passive resonant device gradually loses its control performances if there is a change of the operating conditions. Active systems are power-consuming devices, which makes them costly and extremely vulnerable to power failure. They effectiveness is also affected by sensor failure, which can compromise the stability of the control system, yielding to an enhancement of the vibration level of the system under control.

Many efforts were made to develop techniques that can change the properties of semi-active devices. Magneto-rheological fluids are used in magneto-rheological dampers to obtain devices which can vary their damping effect. The viscosity of these fluids can be modified when they are exposed to a magnetic field, which is usually produced with an electromagnet. Varying the current across the coil that generates the magnetic field it is thus possible to change the viscous damping of the device [29].

The stiffness of the device could be varied in order to track the frequency changes of the excitation field. This can be achieved, for example, changing the pressure of the air in pneumatic springs [37]. Shape memory alloys, which changes the Young's modulus with temperature, could also be used to control the stiffness of the device [38]. Another example of tuning the stiffness of the semi-active element is to change the geometric shape of the stiffness element, for example using piezoelectric materials [39].

The field of metamaterials gained a lot of popularity in the last years. These are engineered materials whose vibro-acoustic properties derive from the periodic repeating patterns in which, for example, piezoelectric patches are arranged. A vibration stop band effect could also be obtained using shunted piezoelectric patch vibration absorbers, both via the spatial distribution of the patches and via the resonating shunts connected to the piezoelectric patches [40–43].

Semi-active systems could also be obtained by properly shunting an electromechanical transducer. This approach has been used for both electromagnetic and piezoelectric transducers [44–48]. The electric elements of the shunt circuit are varied to obtain a mechanical effect which correspond to the desired control effect; the electrical elements could also be implemented digitally because their value could lay outside from the commercial ranges or because their size and weight could represent a problem for the particular application.

1.4 TIME-VARYING TUNEABLE VIBRATION ABSORBER

At the end of the previous century and during the first years of the current one, the switching techniques were developed. They basically consist in cyclically open and close the shunt circuit connected to the transducer according to a time-dependent law related to the motion of the structure [49–51].

Switching Tuneable Vibration Absorbers, whose stiffness and damping properties varies between discrete values, has been firstly investigated [52–56]. In the switching operation mode, the control algorithm switches the stiffness and damping parameters of the absorbers such that the device is sequentially tuned to control the response of several resonant modes of the hosting structure. The effectiveness in the control performances of this operation mode strongly rely on the knowledge of the dynamic response of the hosting structure.

Recent studies have shown the possibility of blindly control the flexural response of thin structures over a broad frequency band using sweeping absorbers [57–63]. In the sweeping operation mode, the stiffness and damping properties of the device are continuously varied such that its natural frequency is uniformly varied within a given band and the damping ratio is maintained constant. In this way the absorber periodically control the vibration response due to the several modes that resonate within the frequency band.

As highlighted in reference [56], for semi-active or adaptive absorbers, the prefix *tuneable* is more advisable in place of tuned.

1.5   OBJECTIVE OF THE THESIS

The main objective of this thesis is to study and develop semi-active vibration absorbers using shunted electromagnetic transducers for the broadband control of the flexural and acoustic response of a cylindrical shell and enclosure. The electrical parameters of the shunt circuit can be adjusted to adapt the mechanical properties of the device.

1.6   CONTRIBUTIONS OF THE THESIS

The main contributions of this thesis are:

- development of a structural-acoustic fully coupled model for the noise and vibration analysis of cylindrical systems (chapter 3);

- analysis of the traditional mechanical fixed tuned vibration absorber effect on the noise and vibration response of cylindrical structures (chapter 4);

- development of general guidelines regarding the positions for vibration absorbers on cylindrical structures (chapter 4);

- development of an electrical-mechanical equivalence criteria for the electromagnetic transducer (chapter 5);

- development of a RL shunt circuit for the tuning of electromagnetic transducer used as vibration absorber (chapter 5);

- development of sweeping vibration absorbers, which use electromagnetic transducers connected to time-varying RL shunts for the broadband control of the flexural and acoustic response of a thin circular cylinder (chapter 5).

- realisation and testing an electro-magnetic shunted vibration absorbers (chapter 6);

- testing the vibration control performances of an digitally implemented shunted electro-magnetic vibration absorbers on a thin cylindrical structure (chapter 6).

1.7 STRUCTURE OF THE THESIS

CHAPTER TWO presents the model of the problem at hand, summarising the geometrical and physical parameters of the cylindrical shell and acoustic enclosure. The objective of the thesis is briefly reported in this section.

CHAPTER THREE introduces the fully coupled structural-acoustic model to analyse the coupled structural and acoustic cylindrical system. First the derivation of the *in vacuo* response of the cylindrical shell and the *rigidly walled* response of the acoustic enclosure are presented. These formulations represent the basis for the Modal Interaction Model used to describe the coupled response, in which the flexural displacement and the acoustic response are described in terms of simply supported *in vacuo* structural flexural and of *rigidly walled* acoustic mode shapes. An energy formulation is used to describe the structural and acoustic responses, which are expressed by means of the Power Spectral Density of the total kinetic energy and of the Power Spectral Density of the total acoustic potential energy.

CHAPTER FOUR presents the classical mechanical Tuned Vibration Absorber. First the characterisation of the mechanical behaviour is expressed in terms of base impedance. Several tuning criteria are presented and the optimum values of the damping and stiffness elements to maximise the vibration absorption effect are adopted. The vibration control effect of the mechanical absorbers are initially assessed considering first the *in vacuo* cylindrical shell. From this study the guidelines for the positioning of the vibration absorbers on cylinders are derived. The effects of the fixed tuned vibration absorbers on the coupled noise and vibration response are then assessed through simulation results.

CHAPTER FIVE starts with the description of the electro-magnetic coupling phenomenon and its application to the electromagnetic transducer. The constitutive equations and the parameters that characterise electromagnetic transducers are presented. An electro-mechanical equivalence study is presented, which constitute the basis to the development of the shunt circuit for the electromagnetic transducers. The electrical elements can indeed be used to modify the mechanical response of the transducer. These can therefore be selected in order to make the electromagnetic transducer suitable for flexural control of thin structures. Then the time-varying electromagnetic absorber is presented. In the so called sweeping operation

mode an harmonic function is used to continuously vary the shunt inductance and resistance between a lower and upper value, corresponding with the lower and upper values of the frequency range of interest. The results obtained with the time-varying sweeping electromagnetic absorbers are compared to the results obtained using the classical mechanical fixed tuned absorbers.

CHAPTER SIX presents the experimental results of the digitally implemented shunted electro-magnetic TVA. In the first part of the chapter the mechanical and electrical experimental characterisation of an actual transducer is presented. The digital implementation of the shunt circuit is then reported, focusing on both the front-end circuit and the digital algorithm for the realisation of the shunt circuit. The measured effects of several resistive and resistive-inductive shunt circuits on the base impedance of the transducer are presented, providing general guidelines to the tuning of the actual transducer. The vibration control performances of the digitally implemented shunted electro-magnetic TVA are then assessed considering both the fixed and the sweeping operation modes. Experimental tests of the TVA mounted on a cylindrical shell are presented.

CHAPTER SEVEN summarises the presented studies and suggested ideas for future work.

MODEL PROBLEM CONSIDERED IN THIS THESIS

The model used in this thesis is composed by a thin walled aluminium cylinder of length L simply-supported at the two ends, which is connected to rigid cylindrical extensions, which form rigid baffles for the exterior unbounded air fluid. The interior cylindrical cavity is also filled with air and is bounded by rigid walls placed in correspondence to the circular edges of the flexible cylindrical wall [28, 64, 65], as depicted in figure 2.1 (a). The geometrical and physical properties of the thin cylinder and of the interior cavity, summarised in table 2.1, are adapted from references [66–69] to resemble the fuselage section of small aircraft. Figure 2.1 (a) also shows the generic Cartesian reference system (x, y', z') and the cylindrical reference system (x, r, ϑ), which will be adopted for the description of the acoustical cylindrical domain. The superscripts on the y and z Cartesian axes are adopted to distinguish them from the ones used in Chapter 3 in the derivation of the structural equations on motion.
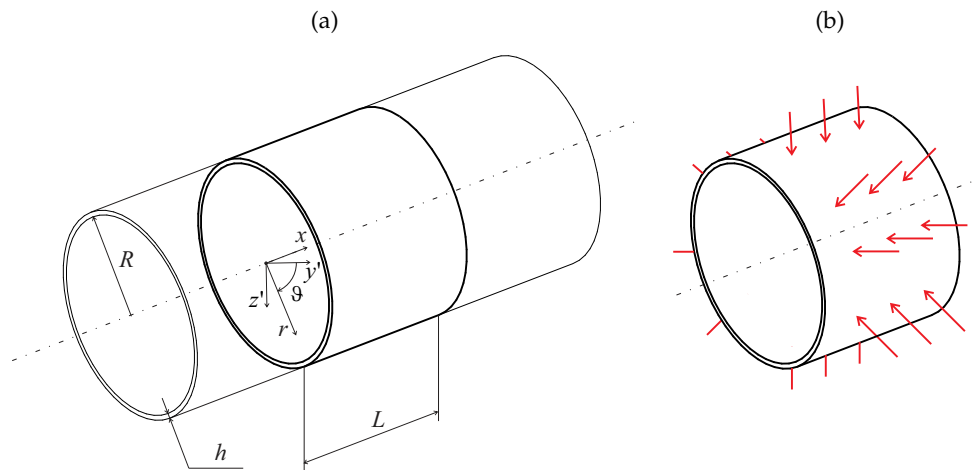
Figure 2.1: Thin walled cylindrical shell; dimensions with coordinate system (a) and distribution of the 24 uncorrelated white noise point forces (b).

Table 2.1: Geometrical and physical properties of the thin walled cylinder and acoustic cavity.

	Parameter	Symbol	Value	
Cylindrical shell	Length	L	2	[m]
	Radius	R	1.3	[m]
	Thickness	h	1.2	[mm]
	Density	ρ	2700	[kg/m^3]
	Young's modulus	E	71	[GPa]
	Poisson ratio	ν	0.3	[$-$]
	Modal damping ratio	ζ_s	1%	[$-$]
Acoustic cavity	Density	ρ_0	1.21	[kg/m^3]
	Speed of sound	c_0	343	[m/s]
	Modal damping ratio	ζ_0	5%	[$-$]

The aircraft considered is the Hawker Siddeley HS 748, whose drawings and picture are shown in figure 2.2, which is a medium-sized two-engines turbo-prop airliner.

The model used in this thesis has the purpose of provide an estimation of the effect of the control devices, so it is not necessary to provide a point to point representation of the structural response of the cylindrical shell nor the internal acoustic field. The aircraft fuselage is generally composed of a huge amount of structural elements (frames, stringers, floor, trim, shell, etc.) but in this study it is modelled by a finite, isotropic and homogeneous cylinder. In this model the increased stiffness and mass effects due to the presence of the rings and stringers is considered by adjusting the thickness and the structural damping, such as smearing the effects of the structural reinforcing elements over the entire surface of the cylinder [67, 68].

As shown in figure 2.1 (b), the cylinder is considered to be exposed to a white noise rain on the roof excitation [28, 47, 63, 72], which is approximated by a uniform grid of uncorrelated point forces oriented in the radial direction, equally spaced in 8 circumferential and 3 axial positions [64, 65]. The excitation field considered, as discussed in [28, 73], has the property to equally excite all the flexural mode. Thus, it can be conveniently used to asses the intrinsic control effects of the control devices considered. The vibrational field of the

---

[1]Images licensed under the Creative Commons Attribution 3.0 Unported license.

(a)

(b)
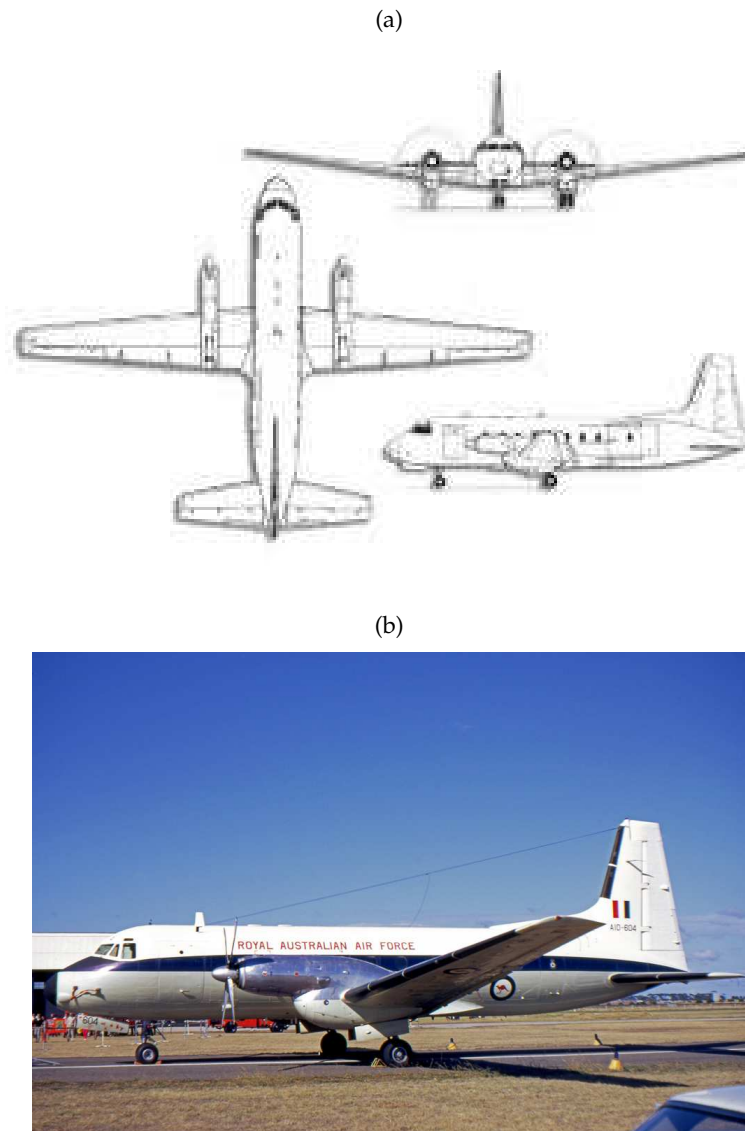
Figure 2.2: Three-view drawing (a) [70] and picture (b) [71] of the Hawker Siddeley HS 748[1].

shell and the acoustic field in the enclosure are studied in the 20 - 100 Hz frequency band.

Figure 2.3 schematically shows the cylindrical shell equipped with a classical mechanical fixed Tuned Vibration Absorber (TVA), plot (a), and with the device proposed in this study, which is a time-varying shunted electromagnetic TVA, plot (b).

The classical mechanical TVA, which will be described in chapter 4, is a well-known passive device composed essentially by a mass suspended by a spring [19, 31, 32, 74, 75]. This device can be used to reduce the harmonic response
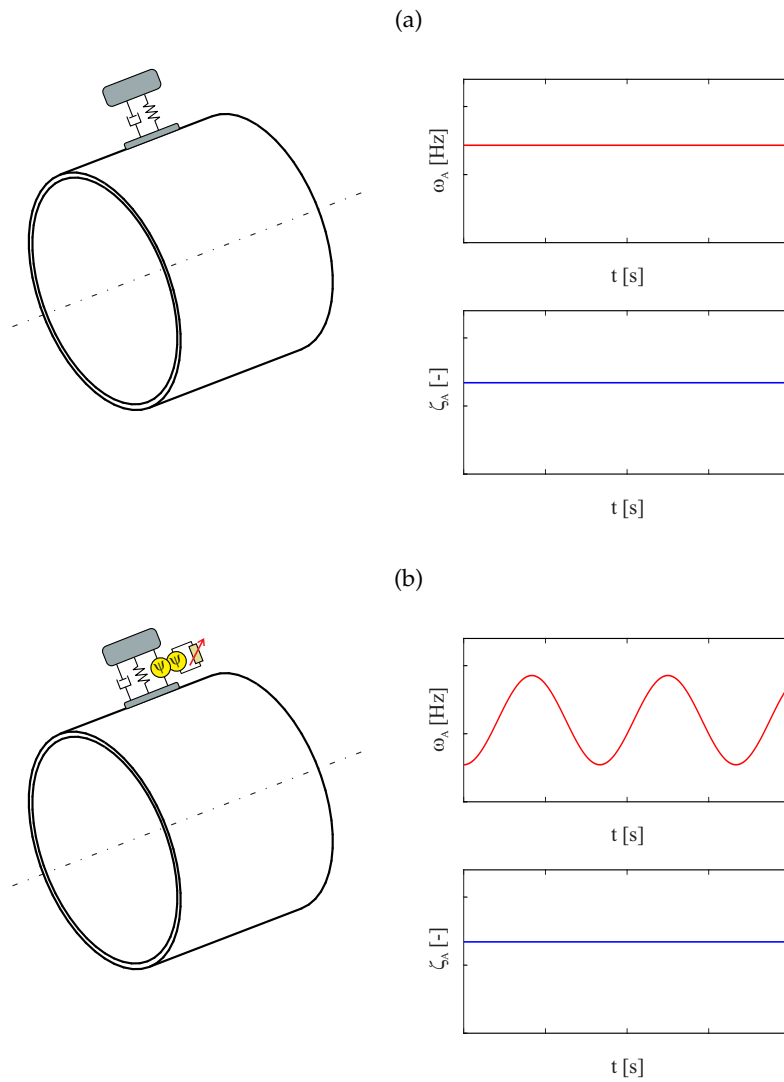
Figure 2.3: Thin walled equipped with a classical mechanical TVA (a) and with a time-varying shunted electromagnetic TVA (b). (The dimensions of the two TVAs are intentionally bigger than their actual values to highlight the differences between the two devices).

amplitude of the hosting system subject to tonal excitation or alternately it can be used to control the hosting structure resonant response subject to broad band disturbances.

Recent studies have shown the possibility to blindly control the response of hosting structures over a broad frequency band using time-varying vibration absorbers [47, 56, 57, 60, 63]. As will be discussed in chapter 5, the time-varying TVAs could be obtained considering a time-varying RL shunt which periodically varies the mechanical proprieties of an electromagnetic transducer [64, 65].

3

COUPLED STRUCTURAL-ACOUSTIC RESPONSE: MODEL AND SIMULATION RESULTS

This chapter presents the mathematical model for the structural-acoustic coupled response of a thin cylindrical structure. The structural vibrations of the shell and the acoustic pressure fluctuations of the cylindrical enclosure subject to structural and acoustic stochastic excitation are first presented as uncloupled. Particular attention is given to the structural and acoustic mode shapes, highlighting the positions of nodal and anti-nodal patterns. The orientation of both the flexural deflection and the acoustic pressure was assessed considering arrays of single and double point excitation sources.

The last part of the chapter is devoted to the derivation of the fully coupled structural-acoustic equation of motion, which is derived using the Modal Interaction Analysis.

Contents

3.1 INTRODUCTION

Large cylindrical structures are very common in every field of structural engineering, with examples of applications from the aerospace and aeronautical engineering [76–78] to naval engineering [79–81] and small scale piping system [82, 83]. The case analysed in this thesis, which is focused on the interaction between the flexural vibration of the cylindrical shell and the internal acoustic sound pressure, falls into the field of *acoustoelasticity* [84–87]. Representative examples of this kind of problems are the cabin noise in flight vehicles and the internal sound field in a transportation vehicle.

As shown in chapter 2, the parameters of the cylindrical shell are chosen such that it resembles the fuselage section of a small aircraft. This kind of structure is usually composed by a huge variety of structural elements, such as stingers, frames, rings, bulkheads and longerons. A lot of effort has been given to model these structural elements in conjunction with the cylindrical shell, which represents the so-called *skin* of the fuselage [88–92]. Nevertheless, a first order estimation of the fuselage vibration and of the internal acoustic fields could be obtained considering a simple model in which the fuselage is composed by a simply supported cylinder [30, 66–68, 93–97].

In the first part of the chapter the response of the *in vacuo* cylindrical shell is considered. The fundamental steps needed to obtain the structural equation of motion for the flexural displacements are presented, giving some details about the several shell theories proposed in literature. In particular, the equation of motion is derived considering the Donnell-Mushtari shell theory (also called the Donnell-Mushtari-Vlasov shell theory) [98], which represents the most commonly adopted approach to describe the flexural vibration of cylindrical shells. With the considered theory it is indeed possible to uncouple the equation of motion for the flexural (radial) displacement from the ones for the axial and circumferential deformations. The separation of variable approach is used to obtain the structural natural frequencies and the structural mode shapes for the simply supported cylindrical shell considered. Due to the cylindrical symmetry of the case considered, it is shown that two components for each mode shapes have to be considered in order to describe a general flexural deflection field. A description of the nodal patterns and their locations is also provided. The response of the simply supported cylindrical shell exposed to a white noise rain-on-the-roof excitation is derived considering an energetic approach, which describe the global flexural response in terms of the flexural kinetic energy PSD. Finally, a simplified model composed by a single structural mode subject

to different configurations of the excitation field, is used to obtain indications regarding the orientation of the flexural deflection in relation with the orientation of the excitation field.

The second part of the chapter is devoted to the analysis of the acoustic cylindrical cavity. The wave equation is first derived for the one-dimensional case and then applied to the three dimensional *rigidly walled* cylindrical case considered in this study. The homogeneous wave equation is then considered, which, together with the separation of variables procedure, lead to the definition of the acoustic natural frequencies and mode shapes. As well as for the structural case, due to the cylindrical symmetry of the acoustic enclosure, two components for each acoustic mode are needed to obtain a complete representation of the internal sound field. Considering a specific excitation field, composed by an array of white noise uncorrelated point monopole sources, the acoustic response of the enclosure is derived in terms of the total acoustic potential energy PSD. A simplified model, composed by a single acoustic mode, is used to gather the relationship between the circumferential orientation of the acoustic pressure inside the cylindrical domain and the orientation of the array of point monopole sources.

Finally, the last part of the chapter consider the coupled structural-acoustic system. The structural response and the transmitted noise are investigated by means of a Modal Interaction Analysis (MIA) [30, 99, 100]. As discussed in reference [3], the sound transmission through the aircraft fuselage could be described with three different models, depending on the frequency range considered. In the low frequency range considered in this thesis, the sound transmissions may be calculated using a shell model in which the structural properties are *smeared* in an equivalent isotropic cylindrical skin. The Modal Interaction Model [64, 99] developed expresses the shell response in terms of the *in vacuo* structural modes and the interior acoustic response in terms of the uncoupled interior cavity modes for the fluid in the enclosure with rigid boundaries. The use of rigid-walled cavity modes guarantee convergence to the acoustic pressure on the interior and on the wall surface of the cylindrical cavity but not to the normal acoustic particle velocity at the flexible walls of the cavity [99]. However only the former acoustic quantity is used in the energy formulation, while the latter is not actually taken into account. The MIA formulation leads to a fully coupled equation of motion which results in a non-symmetric equation due to the presence of the structural-acoustic and acoustic-structural coupling terms. A particular converge study is required to obtain the correct number of structural and acoustic modes which guarantee an accurate representation

of the structural and acoustic response. This systematic convergence analysis is described in appendix B. As well as for the uncoupled cases, for the fully coupled system the responses are obtained with an energetic approach which describe the structural response in terms of the flexural kinetic energy PSD and the internal sound response in terms of theacoustic potential energy PSD.

3.2   EQUATION OF MOTION FOR THE CYLINDRICAL SHELL

A cylindrical shell, as shown in figure 2.1 (a), is a thin sheet of elastic material formed into a cylinder. It could be considered as a generalization of a flat plate, while a flat plate could be considered as a special case of shell having no curvature [98]. In the first part of this chapter the fundamental equations of the thin shell theory are presented in their most simple form, considering the material as linearly elastic, isotropic and homogeneous; the thickness is assumed constant due to the assumption of the smeared structural properties and the displacements are assumed to be small compared to the geometrical dimensions. Furthermore the shear deformation and the rotary inertia are neglected.

A large number of different shell theory have been proposed in literature [98, 101, 102] and several studies have been proposed to highlight the differences between the various thin shell theories [103–105]. Compared to the thin plate theory, which yields to a single fourth order differential equation of motion universally accepted, the shell theory represent a slightly difficult, and thus interesting, problem. Several monographs are presented on the subject [98, 106–109].

Differences in the theories result from slightly different simplifications or in the point in which the simplifications are made. However, all the theories are based on common steps in the derivation of the equation of motion of a curved shell, which are as follow [98, 101, 106, 107, 110]:

1. Derivation of the strain - displacement relations;

2. Derivation of the stress - strain relations using Hooke's law;

3. Obtaining the force and moment resultants by integrating the stresses;

4. Using the resultants in the equilibrium equations to obtain the equations of motions in terms of the displacements.

In the classical theory of small displacements of thin shells, the following assumptions were made by Love [98, 111, 112]:

1. The thickness of the shell is small compared to other dimensions;

2. Strains and displacements are sufficiently small so that the quantities of second- and higher-order magnitude in the strain - displacements relations may be neglected in comparison with the first-order terms;

3. The transverse normal stresses are small compared with the other normal stress components and may be neglected;

4. Normals to the undeformed middle surface remain straight and normal to the deformed middle surface and suffer no extension.

These assumptions, which lead to the so called first approximation shell theory, are universally adopted in all the different shell theories. The first assumption leads to the definition of thin shell and permits to neglect the term h/R, being h the thickness and R the radius of the shell, at various places in the derivation of the equation of motion. The second assumption allows to refer the calculations to the undeformed shell and ensures that the differential equations will be linear. The third and fourth assumptions, known as Kirchhoff's hypotheses, are related to the constitutive equations and lead to consider a special type of orthotropy of the shell.

3.2.1 *Strain - displacement relations*

The strain - displacements relations of the three - dimensional theory of elasticity can be expressed in the cylindrical coordinate system of figure 3.1 (a) as [98, 106]:

$$\varepsilon_x = \frac{\partial U}{\partial x}, \tag{3.1a}$$

$$\varepsilon_\vartheta = \frac{\partial V}{R\partial\vartheta} + \frac{W}{R}, \tag{3.1b}$$

$$\varepsilon_z = \frac{\partial W}{\partial z}, \tag{3.1c}$$

$$\gamma_{x\vartheta} = \frac{\partial U}{R\partial\vartheta} + \frac{\partial V}{\partial x}, \tag{3.1d}$$

$$\gamma_{xz} = \frac{\partial U}{\partial z} + \frac{\partial W}{\partial x} \quad \text{and} \tag{3.1e}$$

$$\gamma_{\vartheta z} = \frac{\partial V}{\partial z} - \frac{V}{R} + \frac{\partial W}{R\partial\vartheta}, \tag{3.1f}$$

where ε_x, ε_ϑ and ε_z are the normal strains, $\gamma_{x\vartheta}$, γ_{xz} and $\gamma_{\vartheta z}$ are the shear strains and U, V and W are the displacements along the axial, circumferential and

transverse (radial) directions respectively, at an arbitrary point. Figure 3.1 (a) shows the generic Cartesian reference system (x, y, z) and the cylindrical reference system (x, z, ϑ). The radial z direction is supposed to assume zero value in correspondence to the neutral surface of the shell, which corresponds to a distance R from the axis of the cylinder. The three displacements are also shown in figure 3.1 (a). In order to satisfy the Kirchhoff's hypotheses, the displacements are restrict to a class which respects the following linear relationships:

$$U(x, \vartheta, z) = u(x, \vartheta) + z\beta_1(x, \vartheta), \tag{3.2a}$$

$$V(x, \vartheta, z) = v(x, \vartheta) + z\beta_2(x, \vartheta) \quad \text{and} \tag{3.2b}$$

$$W(x, \vartheta, z) = w(x, \vartheta), \tag{3.2c}$$

where u, v and w are the components of the displacement at the middle surface in the x, ϑ and z directions and β_1 and β_2 are the rotations of the normal to the middle surface during deformation about the ϑ and x axes respectively, given by:

$$\beta_1 = \frac{\partial U(x, \vartheta, z)}{\partial z} \quad \text{and} \tag{3.3a}$$

$$\beta_2 = \frac{\partial V(x, \vartheta, z)}{\partial z}. \tag{3.3b}$$

Substituting equations (3.3) into equations (3.2) and then substituting the resulting equations into equations (3.1), yields:

$$\varepsilon_x = \varepsilon_x^o + z\,\mathcal{K}_x, \tag{3.4a}$$

$$\varepsilon_\vartheta = \varepsilon_\vartheta^o + z\,\mathcal{K}_\vartheta, \tag{3.4b}$$

$$\gamma_{x\vartheta} = \gamma_{x\vartheta}^o + z\,\mathcal{K}_{x\vartheta}, \tag{3.4c}$$

$$\gamma_{xz} = 0, \tag{3.4d}$$

$$\gamma_{\vartheta z} = 0 \quad \text{and} \tag{3.4e}$$

$$\varepsilon_z = 0. \tag{3.4f}$$

(a)

(b)
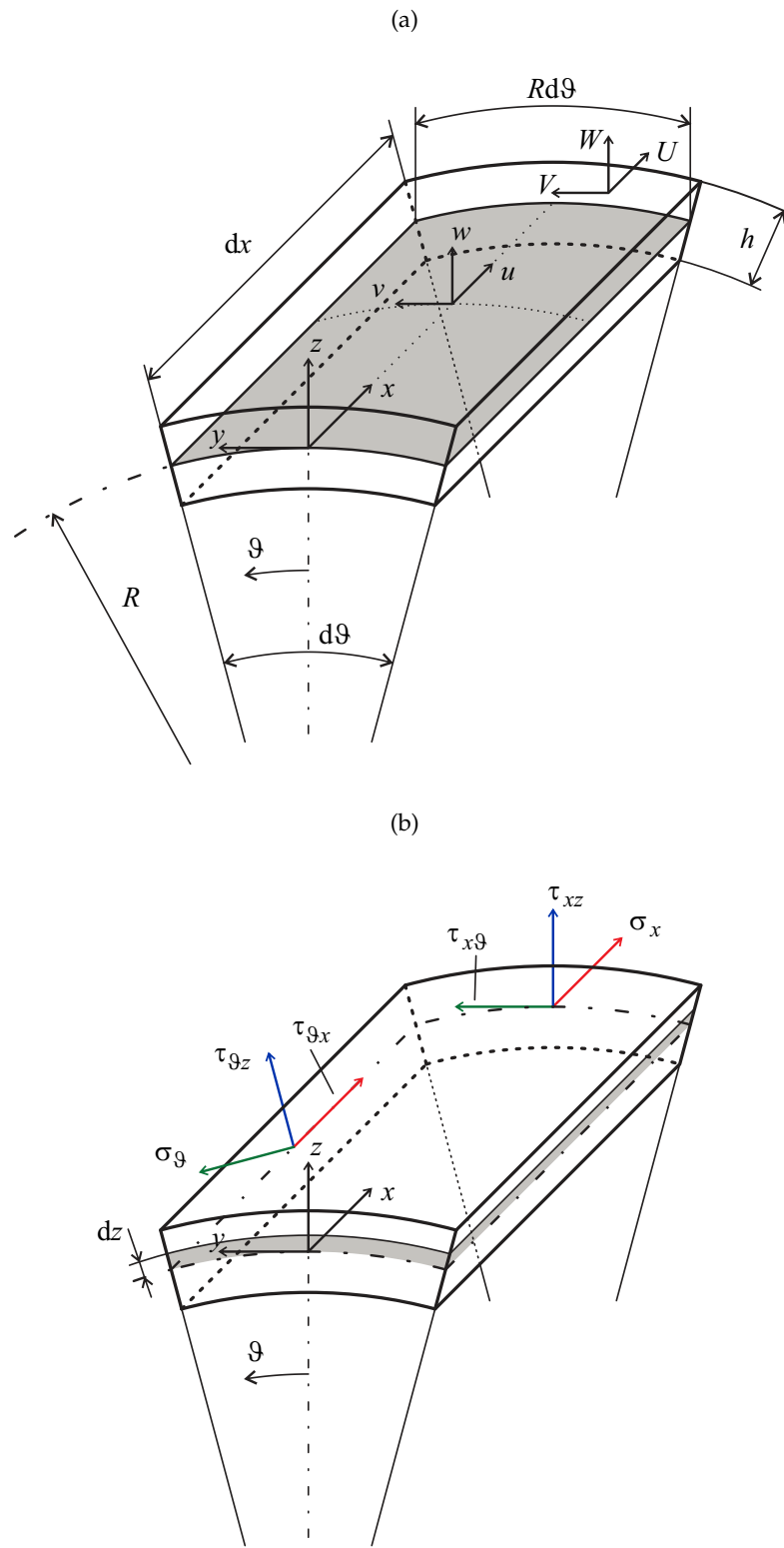
Figure 3.1: Notation and positive directions of displacements (plot (a)) and of stresses acting on a cylindrical shell element (plot (b)).

The transverse normal and shear strains, ε_z, γ_{xz} and $\gamma_{\vartheta z}$ are set to zero as a consequence to the assumption of the Kirchhoff's hypotheses. The normal and shear strains of the middle surface ($z = 0$) are given by:

$$\varepsilon_x^o = \frac{\partial u}{\partial x}, \tag{3.5a}$$

$$\varepsilon_\vartheta^o = \frac{\partial v}{R\partial\vartheta} + \frac{w}{R} \quad \text{and} \tag{3.5b}$$

$$\gamma_{x\vartheta}^o = \frac{\partial u}{R\partial\vartheta} + \frac{\partial v}{\partial x}. \tag{3.5c}$$

In this thesis the Donnell-Mushtari shell theory is considered. It applies to shells that are loaded normal to their surface and concentrates on transverse deflection behaviour. According to this theory, the contribution of the in-plane deflections can be neglected in the bending strains, therefore the changes in curvature and twist are given by [98, 101]:

$$\mathcal{K}_x = -\frac{\partial^2 w}{\partial x^2}, \tag{3.6a}$$

$$\mathcal{K}_\vartheta = -\frac{\partial^2 w}{R^2\partial\vartheta^2} \quad \text{and} \tag{3.6b}$$

$$\mathcal{K}_{x\vartheta} = -2\frac{\partial^2 w}{\partial x R\partial\vartheta}. \tag{3.6c}$$

3.2.2 *Stress - strain relationship*

Assuming the material is linearly elastic, isotropic and homogeneous, the three-dimensional Hooke's law can be written as [102, 113]:

$$\varepsilon_x = \frac{1}{E}\left[\sigma_x - \nu\left(\sigma_\vartheta + \sigma_z\right)\right], \tag{3.7a}$$

$$\varepsilon_\vartheta = \frac{1}{E}\left[\sigma_\vartheta - \nu\left(\sigma_x + \sigma_z\right)\right], \tag{3.7b}$$

$$\varepsilon_z = \frac{1}{E}\left[\sigma_z - \nu\left(\sigma_x + \sigma_\vartheta\right)\right], \tag{3.7c}$$

$$\gamma_{x\vartheta} = \frac{2\left(1+\nu\right)}{E}\tau_{x\vartheta} = \frac{1}{G}\tau_{x\vartheta}, \tag{3.7d}$$

$$\gamma_{xz} = \frac{2\left(1+\nu\right)}{E}\tau_{xz} = \frac{1}{G}\tau_{xz} \quad \text{and} \tag{3.7e}$$

$$\gamma_{\vartheta z} = \frac{2\left(1+\nu\right)}{E}\tau_{\vartheta z} = \frac{1}{G}\tau_{\vartheta z}, \tag{3.7f}$$

where σ_x, σ_ϑ and σ_z are the normal stresses, $\tau_{x\vartheta}$ is the shear stress in the tangential (x and ϑ) directions and τ_{xz} and $\tau_{\vartheta z}$ are the transverse (in the z direction) shear stresses, acting upon the transverse faces of a shell element as shown in figure 3.1 (b). Also, E is the Young modulus and G is the shear modulus. The assumptions of the Kirchhoff's hypothesis, expressed by equations (3.4d)-(3.4f), yields $\tau_{xz} = \tau_{\vartheta z} = 0$ and $\sigma_z = \nu\left(\sigma_x + \sigma_\vartheta\right)$.

Retaining the assumption that σ_z is negligible reduces the problem to a case of plane stress, so equations (3.7) reduce to

$$\varepsilon_x = \frac{1}{E}\left(\sigma_x - \nu\sigma_\vartheta\right), \tag{3.8a}$$

$$\varepsilon_\vartheta = \frac{1}{E}\left(\sigma_\vartheta - \nu\sigma_x\right) \quad \text{and} \tag{3.8b}$$

$$\gamma_{x\vartheta} = \frac{1}{G}\tau_{x\vartheta}, \tag{3.8c}$$

which can be inverted to obtain the stresses:

$$\sigma_x = \frac{E}{1-\nu^2}\left(\varepsilon_x - \nu\varepsilon_\vartheta\right), \tag{3.9a}$$

$$\sigma_\vartheta = \frac{E}{1-\nu^2}\left(\varepsilon_\vartheta - \nu\varepsilon_x\right) \quad \text{and} \tag{3.9b}$$

$$\tau_{x\vartheta} = G\gamma_{x\vartheta}. \tag{3.9c}$$

3.2.3 *Force and moments resultants*

The force resultants acting on the lateral faces of the shell element, shown in figure 3.2 (a), can be obtained integrating the stresses acting on each face over the element thickness dz. The force resultants, expressed in unit of force per unit length of middle surface can thus be expressed as [98]:

$$N_x = \int_{-h/2}^{h/2} \sigma_x\,\mathrm{d}z, \tag{3.10a}$$

$$N_\vartheta = \int_{-h/2}^{h/2} \sigma_\vartheta\,\mathrm{d}z \quad \text{and} \tag{3.10b}$$

$$N_{x\vartheta} = N_{\vartheta x} = \int_{-h/2}^{h/2} \tau_{x\vartheta}\,\mathrm{d}z, \tag{3.10c}$$

where the positive directions of the force resultants are shown in figure 3.2 (a).

(a)

(b)
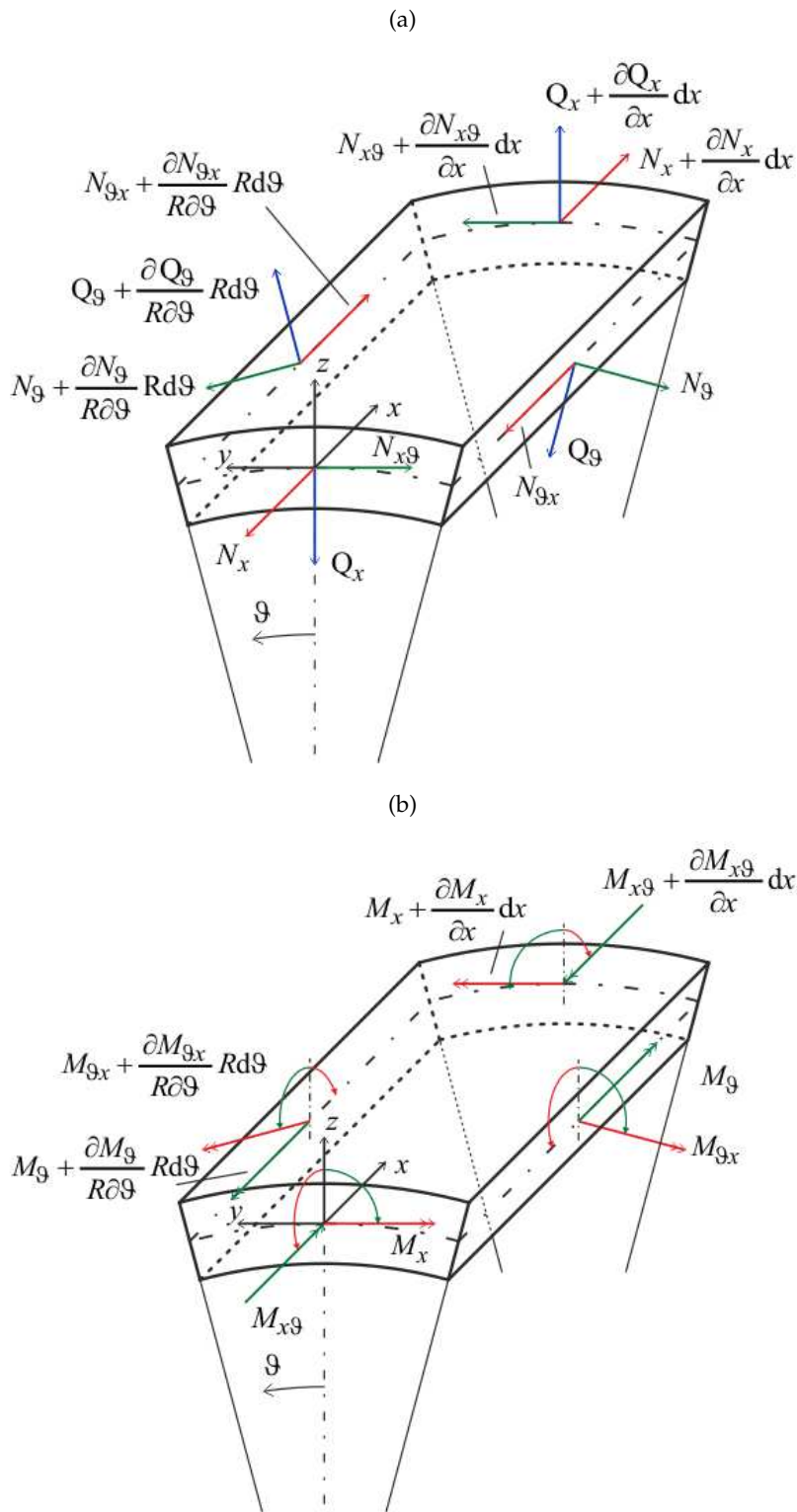
Figure 3.2: Notation and positive directions of force resultants (plot (a)) and of moment resultants (plot (b)) acting on a cylindrical shell element.

Similarly, the moment resultants shown in figure 3.2 (b) , having dimensions of moments per unit length of the middle surface, are given by:

$$M_x = \int_{-h/2}^{h/2} \sigma_x \, z \, dz, \tag{3.11a}$$

$$M_\vartheta = \int_{-h/2}^{h/2} \sigma_\vartheta \, z \, dz \quad \text{and} \tag{3.11b}$$

$$M_{x\vartheta} = M_{\vartheta x} = \int_{-h/2}^{h/2} \tau_{x\vartheta} \, z \, dz. \tag{3.11c}$$

Substitution of equations (3.9) into equations (3.10) and (3.11) and then the substitution of equations (3.5) and (3.6) into equation (3.4) and the resulting equation in the resulting equations (3.10) and (3.11) gives the expressions of the force and moment resultants in terms of the middle surface displacements:

$$N_x = K \left(\frac{\partial u}{\partial x} + v \frac{\partial v}{R \partial \vartheta} + v \frac{w}{R} \right), \tag{3.12a}$$

$$N_\vartheta = K \left(\frac{\partial v}{R \partial \vartheta} + \frac{w}{R} + v \frac{\partial u}{\partial x} \right), \tag{3.12b}$$

$$N_{x\vartheta} = N_{\vartheta x} = \frac{K(1-v)}{2} \left(\frac{\partial u}{R \partial \vartheta} + \frac{\partial v}{\partial x} \right), \tag{3.12c}$$

$$M_x = D \left(-\frac{\partial^2 w}{\partial x^2} - v \frac{\partial^2}{R^2 \partial \vartheta^2} \right), \tag{3.12d}$$

$$M_\vartheta = D \left(-\frac{\partial^2}{R^2 \partial \vartheta^2} - v \frac{\partial^2 w}{\partial x^2} \right) \quad \text{and} \tag{3.12e}$$

$$M_{x\vartheta} = M_{\vartheta x} = \frac{D(1-v)}{2} \left(-2 \frac{\partial^2 w}{\partial x R \partial \vartheta} \right), \tag{3.12f}$$

where

$$K = \frac{E \, h}{1 - v^2} \tag{3.13}$$

is the membrane stiffness and

$$D = \frac{E \, h^3}{12(1 - v^2)} \tag{3.14}$$

is the shell bending stiffness. The transverse force resultants Q_x and Q_ϑ have been omitted since their derivation is obtained from the equation of motion, by virtue of the moment equilibrium equations.

3.2.4 *Equation of motion*

Considering the shell element subject to the internal elastic force and moment resultants shown in figure 3.2, and under the influence of an external force $\mathbf{q}$, whose components q_x, q_ϑ and q_r act at the middle surface in the three directions respectively, the moment equilibrium equation leads to :

$$Q_x = \frac{\partial M_x}{\partial x} + \frac{\partial M_{\vartheta x}}{R \partial \vartheta} \quad \text{and} \tag{3.15a}$$

$$Q_\vartheta = \frac{\partial M_{x\vartheta}}{\partial x} + \frac{\partial M_\vartheta}{R \partial \vartheta}. \tag{3.15b}$$

In the Donnell-Mushtari shell theory, the transverse force resultants Q_x and Q_ϑ are neglected in the axial and circumferential components of the equation of motion but not in the radial component. Thus the force equilibrium equations can be written as:

$$\frac{\partial N_x}{\partial x} + \frac{\partial N_{\vartheta x}}{R \partial \vartheta} + q_x = 0, \tag{3.16a}$$

$$\frac{\partial N_{x\vartheta}}{\partial x} + \frac{\partial N_\vartheta}{R \partial \vartheta} + q_\vartheta = 0 \quad \text{and} \tag{3.16b}$$

$$-\frac{N_\vartheta}{R} + \frac{\partial Q_x}{\partial x} + \frac{\partial Q_\vartheta}{R \partial \vartheta} + q_r = 0. \tag{3.16c}$$

These force equilibrium equations become the dynamic equations of motion considering the forcing terms as the sum of the effective external forces (f_x, f_ϑ, f_r), which act in the axial, circumferential and radial direction respectively, and the translatory inertia forces:

$$q_x = f_x - \rho h \frac{\partial^2 u}{\partial t^2}, \tag{3.17a}$$

$$q_\vartheta = f_\vartheta - \rho h \frac{\partial^2 v}{\partial t^2} \quad \text{and} \tag{3.17b}$$

$$q_r = f_r - \rho h \frac{\partial^2 w}{\partial t^2}. \tag{3.17c}$$

Substituting equations (3.17) and (3.12) into equations (3.16) yield the expression of the equation of motion in terms of the displacements:

$$K \left[\frac{\partial^2 u}{\partial x^2} + \frac{1-\nu}{2} \frac{\partial^2 u}{R^2 \partial \vartheta^2} + \frac{1+\nu}{2} \frac{\partial^2 v}{\partial x R \partial \vartheta} + \frac{\nu}{R} \frac{\partial w}{\partial x} \right] - \rho h \frac{\partial^2 u}{\partial t^2} = -f_x, \qquad (3.18a)$$

$$K \left[\frac{1+\nu}{2} \frac{\partial^2 u}{\partial x R \partial \vartheta} + \frac{1-\nu}{2} \frac{\partial^2 v}{\partial x^2} + \frac{\partial^2 v}{R^2 \partial \vartheta^2} + \frac{\partial w}{R^2 \partial \vartheta} \right] - \rho h \frac{\partial^2 v}{\partial t^2} = -f_\vartheta \quad \text{and} \quad (3.18b)$$

$$K \left[-\frac{\nu}{R} \frac{\partial u}{\partial x} - \frac{\partial v}{R^2 \partial \vartheta} - \frac{w}{R^2} - \frac{h^2}{12} \nabla_s^4 w \right] - \rho h \frac{\partial^2 w}{\partial t^2} = -f_r, \qquad (3.18c)$$

where $\nabla_s^4 = \nabla_s^2 \nabla_s^2$ and

$$\nabla_s^2 = \frac{\partial^2 \cdot}{\partial x^2} + \frac{\partial^2 \cdot}{R^2 \partial \vartheta^2} \qquad (3.19)$$

is the two-dimensional Laplace operator in cylindrical coordinates.

The coupled equations of motions (3.18) can be written in a more compact fashion as:

$$\mathcal{L}_{\text{D-M}} \left[\mathbf{w}(\mathbf{x}_s, t) \right] - \rho h \, \mathcal{L}_t \left[\mathbf{w}(\mathbf{x}_s, t) \right] = -\mathbf{f}, \qquad (3.20)$$

where $\mathbf{w}(\mathbf{x}_s, t) = \begin{bmatrix} u & v & w \end{bmatrix}^T$ is the displacement vector at time t of the point $\mathbf{x}_s = (x, \vartheta)$ laying on the middle-surface, $\mathbf{f} = \begin{bmatrix} f_x & f_\vartheta & f_r \end{bmatrix}^T$ is the force vector, $\mathcal{L}_t \left[\cdot \right] = \begin{bmatrix} \frac{\partial^2 \cdot}{\partial t^2} & \frac{\partial^2 \cdot}{\partial t^2} & \frac{\partial^2 \cdot}{\partial t^2} \end{bmatrix}^T$ is the differential operator of time and $\mathcal{L}_{\text{D-M}} \left[\cdot \right]$ is the matrix differential operator of the Donnell - Mushtari's theory of thin cylindrical shells, expressed as:

$$\mathcal{L}_{\text{D-M}} \left[\cdot \right] = K \begin{bmatrix} \dfrac{\partial^2 \cdot}{\partial x^2} + \dfrac{1-\nu}{2} \dfrac{\partial^2 \cdot}{R^2 \partial \vartheta^2} & \dfrac{1+\nu}{2} \dfrac{\partial^2 \cdot}{\partial x R \partial \vartheta} & \dfrac{\nu}{R} \dfrac{\partial \cdot}{\partial x} \\[2ex] \dfrac{1+\nu}{2} \dfrac{\partial^2 \cdot}{\partial x R \partial \vartheta} & \dfrac{1-\nu}{2} \dfrac{\partial^2 \cdot}{\partial x^2} + \dfrac{\partial^2 \cdot}{R^2 \partial \vartheta^2} & \dfrac{\partial \cdot}{R^2 \partial \vartheta} \\[2ex] -\dfrac{\nu}{R} \dfrac{\partial \cdot}{\partial x} & -\dfrac{\partial \cdot}{R^2 \partial \vartheta} & -\dfrac{\cdot}{R^2} - \dfrac{h^2}{12} \nabla_s^4 w \end{bmatrix}. \qquad (3.21)$$

The form in which equation (3.20) is written makes it suitable to be used for shell theory other than the Donnell - Mushtari; indeed substituting the matrix differential operator with the general operator

$$\mathcal{L} \left[\cdot \right] = \mathcal{L}_{\text{D-M}} \left[\cdot \right] + \frac{h^2}{12R^2} \mathcal{L}_{\text{MOD}} \left[\cdot \right] \qquad (3.22)$$

yields to the equations of motion according to the shell theory selected with the modifying operator $\mathcal{L}_{\text{MOD}}$. As an example, the modifying operator in order to

obtain the equation of motion for the Love - Timoshenko shell theory is given by:

$$\mathcal{L}_{\text{L-T}}\left[\cdot\right] = \begin{bmatrix} 0 & 0 & 0 \\ 0 & (1-\nu)\dfrac{\partial^2 \cdot}{\partial x^2} + \dfrac{\partial^2 \cdot}{R^2 \partial \vartheta^2} & -\dfrac{\partial^3 \cdot}{\partial x^2 \partial \vartheta} - \dfrac{\partial^3 \cdot}{R^2 \partial \vartheta^3} \\ 0 & (2-\nu)\dfrac{\partial^3 \cdot}{\partial x^2 \partial \vartheta} + \dfrac{\partial^3 \cdot}{R^2 \partial \vartheta^3} & 0 \end{bmatrix}\cdot \qquad (3.23)$$

The circular cylindrical shell shown in figure 2.1 (a) is considered to be subject to the following boundary conditions:

$$v(0,\vartheta,t) = v(L,\vartheta,t) = 0, \qquad (3.24\text{a})$$

$$w(0,\vartheta,t) = w(L,\vartheta,t) = 0, \qquad (3.24\text{b})$$

$$N_x(0,\vartheta,t) = N_x(L,\vartheta,t) = 0 \quad \text{and} \qquad (3.24\text{c})$$

$$M_x(0,\vartheta,t) = M_x(L,\vartheta,t) = 0. \qquad (3.24\text{d})$$

The type boundary conditions described by means of equations (3.24) are usually called simply supported or shear diaphragms boundary conditions [98, 101, 106].

Solutions to the equations of motions (3.18), subject to the boundary conditions given in equations (3.24) can be assumed to have the form [98]:

$$u(x,\vartheta,t) = A\cos\left(\frac{m_1 \pi x}{L}\right)\cos\left(m_2 \vartheta\right)\cos\left(\omega t\right), \qquad (3.25\text{a})$$

$$v(x,\vartheta,t) = B\sin\left(\frac{m_1 \pi x}{L}\right)\sin\left(m_2 \vartheta\right)\cos\left(\omega t\right) \quad \text{and} \qquad (3.25\text{b})$$

$$w(x,\vartheta,t) = C\sin\left(\frac{m_1 \pi x}{L}\right)\cos\left(m_2 \vartheta\right)\cos\left(\omega t\right), \qquad (3.25\text{c})$$

where A, B and C are undetermined coefficients, $m_1 = 1, 2, 3, \ldots$, $m_2 = 0, 1, 2, \ldots$ and ω is the angular frequency of free vibration, in radians per seconds. Substitution of the set of solution given in equations (3.25) into the homogeneous equations of motion (3.20) and factorization the common terms, leads to a set of homogeneous equation which can be written in matrix form as:

$$\begin{bmatrix} \rho h\omega^2 - \mathcal{F}_{11} & \mathcal{F}_{12} & \mathcal{F}_{13} \\ \mathcal{F}_{21} & \rho h\omega^2 - \mathcal{F}_{22} & \mathcal{F}_{23} \\ \mathcal{F}_{31} & \mathcal{F}_{32} & \rho h\omega^2 - \mathcal{F}_{33} \end{bmatrix}\begin{bmatrix} A \\ B \\ C \end{bmatrix} = \begin{bmatrix} 0 \\ 0 \\ 0 \end{bmatrix}, \qquad (3.26)$$

where

$$\mathcal{F}_{11} = K\left[\left(\frac{m_1\pi}{L}\right)^2 + \frac{1-\nu}{2}\left(\frac{m_2}{R}\right)^2\right], \tag{3.27a}$$

$$\mathcal{F}_{12} = \mathcal{F}_{21} = K\frac{1+\nu}{2}\frac{m_1\pi}{L}\frac{m_2}{R}, \tag{3.27b}$$

$$\mathcal{F}_{13} = \mathcal{F}_{31} = \frac{\nu K}{R}\frac{m_1\pi}{L}, \tag{3.27c}$$

$$\mathcal{F}_{22} = K\left[\frac{1-\nu}{2}\left(\frac{m_1\pi}{L}\right)^2 + \left(\frac{m_2}{R}\right)^2\right], \tag{3.27d}$$

$$\mathcal{F}_{23} = \mathcal{F}_{32} = K\frac{m_2}{R^2} \quad \text{and} \tag{3.27e}$$

$$\mathcal{F}_{33} = \frac{K}{R^2} + D\left[\left(\frac{m_1\pi}{L}\right)^2 + \left(\frac{m_2}{R}\right)^2\right]^2. \tag{3.27f}$$

For a nontrivial solution, the determinant of the coefficient matrix of equation (3.26) has to be zero. The resulting characteristic equation can be written as

$$\omega^6 + a_1\omega^4 + a_2\omega^2 + a_3 = 0, \tag{3.28}$$

where

$$a_1 = -\frac{1}{\rho h}\left(\mathcal{F}_{11} + \mathcal{F}_{22} + \mathcal{F}_{33}\right), \tag{3.29a}$$

$$a_2 = \frac{1}{(\rho h)^2}\left(\mathcal{F}_{11}\mathcal{F}_{22} + \mathcal{F}_{11}\mathcal{F}_{33} + \mathcal{F}_{22}\mathcal{F}_{33} - \mathcal{F}_{12}^2 - \mathcal{F}_{13}^2 - \mathcal{F}_{23}^2\right) \quad \text{and} \tag{3.29b}$$

$$a_3 = \frac{1}{(\rho h)^3}\left(\mathcal{F}_{11}\mathcal{F}_{23}^2 + \mathcal{F}_{22}\mathcal{F}_{13^2} + \mathcal{F}_{33}\mathcal{F}_{12}^2 + 2\mathcal{F}_{12}\mathcal{F}_{13}\mathcal{F}_{23} - \mathcal{F}_{11}\mathcal{F}_{22}\mathcal{F}_{33}\right). \tag{3.29c}$$

The cubic frequency equation (3.28) has three positive, real roots for every given (m_1, m_2) combination. The cylindrical shell, defined by its geometrical parameters h, R and L, has three vibrational frequencies, each having an equal number of circumferential and longitudinal waves (related to the modal indices m_1 and m_2), which characterise a different vibrational mode. The modes associated with each frequency can be classified as primary radial (or flexural), longitudinal (or axial) or circumferential (or torsional).

Once m_1 and m_2 have been defined, three values of ω could be determined. Subsequently, for each ω, different values of A/C and B/C (*i.e.* the undetermined constants of equations (3.25)) are obtained. The lowest value of ω, out of the three possible ones, correspond to the case in which the amplitude ratios are $A/C < 1$ and $B/C < 1$. This indicates that the motion is primarily flexural (or radial), since the displacement w is dominant in comparison with u and v.

Another commonly adopted simplification in the Donnell - Mushtari shell theory is to neglect the in-plane (tangential) inertia terms in the equation of motion (3.18) [101]. These can thus be written as:

$$\frac{\partial N_x}{\partial x} + \frac{\partial N_{\vartheta x}}{R \partial \vartheta} = 0, \tag{3.30a}$$

$$\frac{\partial N_{x\vartheta}}{\partial x} + \frac{\partial N_\vartheta}{R \partial \vartheta} = 0 \quad \text{and} \tag{3.30b}$$

$$-\frac{N_\vartheta}{R} + \frac{\partial Q_x}{\partial x} + \frac{\partial Q_\vartheta}{R \partial \vartheta} - \rho h \frac{\partial^2 w}{\partial t^2} = -f_r. \tag{3.30c}$$

Introducing the Airy's stress function ϕ, defined as [101]:

$$N_x = \frac{\partial^2 \phi}{R^2 \partial \vartheta^2}, \tag{3.31a}$$

$$N_\vartheta = \frac{\partial^2 \phi}{\partial x^2} \quad \text{and} \tag{3.31b}$$

$$N_{x\vartheta} = -\frac{\partial^2 \phi}{\partial x R \partial \vartheta}, \tag{3.31c}$$

the first two equations (3.30) are satisfied, and the third becomes:

$$D\nabla_s^4 w + \frac{\partial^2 \phi}{R \partial x^2} + \rho h \frac{\partial^2 w}{\partial t^2} = f_r. \tag{3.32}$$

In order to eliminate the Airy's stress function from this equation, the strain - displacement relationship (3.4) are algebraic manipulated to eliminate from them the displacements. The resulting equation results:

$$\frac{Eh}{R} \frac{\partial^2 w}{\partial x^2} - \nabla_s^4 \phi = 0. \tag{3.33}$$

Operating on equation (3.32) with ∇_s^4 and on equation (3.33) with $\partial^2(\cdot)/R\partial x^2$, leads to the equation of motion for the flexural vibration of a cylindrical shell, uncoupled from the tangential displacements:

$$D\nabla_s^8 w + \frac{Eh}{R^2} \frac{\partial^4 w}{\partial x^4} + \rho h \nabla_s^4 \frac{\partial^2 w}{\partial t^2} = \nabla_s^4 f_r, \tag{3.34}$$

which can be written in a more compact form as:

$$\mathcal{L}_{\text{D-M},w}\left[w(\mathbf{x}_s, t)\right] + \rho h \, \mathcal{L}_{t,w}\left[\mathbf{w}(\mathbf{x}_s, t)\right] = \mathcal{L}_{\text{f,w}}\left[f_r(\mathbf{x}_s, t)\right], \tag{3.35}$$

where:

$$\mathcal{L}_{\text{D-M},w}\left[\cdot\right] = D\nabla_s^8(\cdot) + \frac{Eh}{R^2}\frac{\partial^4\cdot}{\partial x^4}, \tag{3.36a}$$

$$\mathcal{L}_{t,w}\left[\cdot\right] = \nabla_s^4\frac{\partial^2\cdot}{\partial t^2} \quad \text{and} \tag{3.36b}$$

$$\mathcal{L}_{\text{f,w}}\left[\cdot\right] = \nabla_s^4(\cdot). \tag{3.36c}$$

The in-plane (tangential) displacements can be obtained by means of the following relationships:

$$\nabla_s^4 u = \nu\frac{\partial^3 w}{R\partial x^3} - \frac{\partial^3 w}{\partial x R^3\partial\vartheta^2} \quad \text{and} \tag{3.37a}$$

$$\nabla_s^4 v = -(2+\nu)\frac{\partial^3 w}{\partial x^2 R^2\partial\vartheta} - \frac{\partial^3 w}{R\partial x^3}. \tag{3.37b}$$

3.3 STRUCTURAL NATURAL MODES AND FREQUENCIES

In the free vibration case, the forcing term is set equal to zero, $f_r = 0$, and the equation of motion (3.34) can be written as:

$$D\left[\frac{\partial^8 w}{\partial x^8} + 4\frac{\partial^8 w}{\partial x^6 R^2\partial\vartheta^2} + 6\frac{\partial^8 w}{\partial x^4 R^4\partial\vartheta^4} + 4\frac{\partial^8 w}{\partial x^2 R^6\partial\vartheta^6} + \frac{\partial^8 w}{R^8\partial\vartheta^8}\right] +$$
$$+ \frac{Eh}{R^2}\frac{\partial^4 w}{\partial x^4} + \rho h\left[\frac{\partial^4\ddot{w}}{\partial x^4} + 2\frac{\partial^4\ddot{w}}{\partial x^2 R^2\partial\vartheta^2} + \frac{\partial^4 w}{R^4\partial\vartheta^4}\right] = 0 \tag{3.38}$$

where the symbol $\ddot{w}$ indicates the double derivative with respect to time of the flexural displacement. The free vibration solution can be found using the method of separation of variables as [114]:

$$w(\mathbf{x}_s, t) = \varphi(\mathbf{x}_s)g(t) = \mathcal{X}(x)\Theta(\vartheta)g(t) \tag{3.39}$$

substituting equation (3.39) into equation (3.38), and dividing for $\mathcal{X}(x)\Theta(\vartheta)g(t)$ yields

$$D\left[\frac{1}{\mathcal{X}}\frac{\mathrm{d}^8\mathcal{X}}{\mathrm{d}x^8} + 4\left(\frac{1}{\mathcal{X}}\frac{\mathrm{d}^6\mathcal{X}}{\mathrm{d}x^6}\right)\left(\frac{1}{\Theta}\frac{\mathrm{d}^2\Theta}{\mathrm{d}R^2\vartheta^2}\right) + 6\left(\frac{1}{\mathcal{X}}\frac{\mathrm{d}^4\mathcal{X}}{\mathrm{d}x^4}\right)\left(\frac{1}{\Theta}\frac{\mathrm{d}^4\Theta}{\mathrm{d}R^4\vartheta^4}\right) +\right.$$
$$+ 4\left(\frac{1}{\mathcal{X}}\frac{\mathrm{d}^2\mathcal{X}}{\mathrm{d}x^2}\right)\left(\frac{1}{\Theta}\frac{\mathrm{d}^6\Theta}{\mathrm{d}R^6\vartheta^6}\right) + \frac{1}{\Theta}\frac{\mathrm{d}^8\Theta}{\mathrm{d}R^8\vartheta^8}\right] + \frac{Eh}{R^2}\left(\frac{1}{\mathcal{X}}\frac{\mathrm{d}^4\mathcal{X}}{\mathrm{d}x^4}\right) +$$
$$+ \rho h\left[\left(\frac{1}{\mathcal{X}}\frac{\mathrm{d}^4\mathcal{X}}{\mathrm{d}x^4}\right) + 2\left(\frac{1}{\mathcal{X}}\frac{\mathrm{d}^2\mathcal{X}}{\mathrm{d}x^2}\right)\left(\frac{1}{\Theta}\frac{\mathrm{d}^2\Theta}{\mathrm{d}R^2\vartheta^2}\right) + \left(\frac{1}{\Theta}\frac{\mathrm{d}^4\Theta}{\mathrm{d}R^4\vartheta^4}\right)\right]\left(\frac{1}{g}\frac{\mathrm{d}^2 g}{\mathrm{d}t^2}\right) = 0. \tag{3.40}$$

The functions $X(x)$ and $\Theta(\vartheta)$ are assumed to satisfy the conditions [101]:

$$\frac{\mathrm{d}^2 X}{\mathrm{d}x^2} = -k_x^2 X \qquad \text{and} \qquad \frac{\mathrm{d}^2 \Theta}{\mathrm{d}\vartheta^2} = -k_\vartheta^2 \Theta, \qquad (3.41)$$

thus, the higher order derivatives of $X(x)$ and $\Theta(\vartheta)$ are equal to

$$\frac{\mathrm{d}^4 X}{\mathrm{d}x^4} = k_x^4 X, \qquad\qquad \frac{\mathrm{d}^4 \Theta}{\mathrm{d}\vartheta^4} = k_\vartheta^4 \Theta, \qquad (3.42a)$$

$$\frac{\mathrm{d}^6 X}{\mathrm{d}x^6} = -k_x^6 X, \qquad\qquad \frac{\mathrm{d}^6 \Theta}{\mathrm{d}\vartheta^6} = -k_\vartheta^6 \Theta, \qquad (3.42b)$$

$$\frac{\mathrm{d}^8 X}{\mathrm{d}x^8} = k_x^8 X \quad \text{and} \qquad \frac{\mathrm{d}^8 \Theta}{\mathrm{d}\vartheta^8} = -k_\vartheta^8 . \Theta \qquad (3.42c)$$

Furthermore, the function $g(t)$ is assumed to satisfy the condition

$$\frac{\mathrm{d}^2 g}{\mathrm{d}t^2} = -\omega_s^2 g. \qquad (3.43)$$

Substitution of the assumptions given in equations (3.41), (3.42) and (3.43) into equation (3.40) gives

$$D \left[k_x^2 + \frac{k_\vartheta^2}{R^2} \right]^4 + \frac{Eh}{R^2} k_x^4 - \rho h \left[k_x^2 + \frac{k_\vartheta^2}{R^2} \right]^2 \omega^2 = 0. \qquad (3.44)$$

From equation (3.44) it is possible to obtain the angular frequency of the free vibration in terms of the axial and circumferential wavenumbers, k_x and k_ϑ, as

$$\omega_s^2 = \frac{E}{\rho R^2} \left\{ \frac{(Rk_x)^4}{\left[(Rk_x)^2 + k_\vartheta^2 \right]^2} + \frac{h^2/R^2}{12(1-\nu^2)} \left[(Rk_x)^2 + k_\vartheta^2 \right]^2 \right\}. \qquad (3.45)$$

The values of the axial and circumferential wavenumbers, k_x and k_ϑ, can be obtained by considering the general solution to equations (3.41), which are of the form:

$$X(x) = A_1 \cos(k_x x) + A_2 \sin(k_x x) \quad \text{and} \qquad (3.46a)$$

$$\Theta(\vartheta) = B_1 \cos(k_\vartheta \vartheta) + B_2 \sin(k_\vartheta \vartheta). \qquad (3.46b)$$

The boundary condition (3.24b) are satisfied if

$$A_1 = 0 \quad \text{and} \qquad (3.47a)$$

$$k_x L = m_1 \pi, \qquad (3.47b)$$

which yields to

$$k_x = \frac{m_1 \pi}{L},$$

(3.48)

with $m_1 = 1, 2, 3, \ldots$. No structural boundary condition applies to the function $\Theta(\vartheta)$ but a more physical boundary condition have to be satisfied, which requires that both the displacement and the slope of the displacement be continuous in the entire region $0 \leq \vartheta < 2\pi$. This condition can be be satisfied if only an integer number of wavelengths fits within the circumference $2\pi R$. Thus, the circumferential wavenumber has also to be an integer number:

$$k_\vartheta = m_2,$$

(3.49)

with $m_2 = 0, 1, 2, \ldots$. It is worth noting that this periodic boundary condition does not imply any limitation on the values of B_1 and B_2, thus both the cosine and sine function have to be taken into account.

Substitution of equations (3.48) and (3.49) into equation (3.45) gives the angular frequency in terms of the modal indices m_1 and m_2 [98, 101]:

$$\omega_{s,m}^2 = \frac{E}{\rho R^2} \left\{ \frac{\left(\frac{m_1 \pi R}{L}\right)^4}{\left[\left(\frac{m_1 \pi R}{L}\right)^2 + m_2^2\right]^2} + \frac{h^2 / R^2}{12(1 - \nu^2)} \left[\left(\frac{m_1 \pi R}{L}\right)^2 + m_2^2\right]^2 \right\},$$

(3.50)

at which correspond two distinct flexural natural modes, namely the symmetric and anti-symmetric flexural natural modes, given by

$$\varphi_m^s(\mathbf{x}_s) = \sin\left(\frac{m_1 \pi}{L} x\right) \cos(m_2 \vartheta) \quad \text{and}$$

(3.51a)

$$\varphi_m^a(\mathbf{x}_s) = \sin\left(\frac{m_1 \pi}{L} x\right) \sin(m_2 \vartheta),$$

(3.51b)

where the subscript m indicates the couple of indices (m_1, m_2).

A common representation of the natural structural frequencies for the cylindrical shell [98, 101] is reported in figure 3.3 (a), where the natural structural frequency obtained from equation (3.50) is plotted versus the circumferential index m_2 for several values of the axial index m_1. This plot highlights an important characteristic of the simply supported cylindrical shell, the minimum frequency occurs for combinations of the modal indices m_1 and m_2 which are not the minimum, as instead happen for the case on the flat rectangular plate [102, 113, 115–117]. Another common representation of the frequency trend is by means of the k-space [118–120], or wavenumber diagram [99, 121], shown in figure 3.3 (b). In

this rectangular domain the axial and circumferential wavenumbers k_x and k_ϑ are interpreted as Cartesian coordinates. Each of the values of k_x and k_ϑ given by equations (3.48) and (3.49) respectively, corresponds to a straight line perpendicular to the corresponding axis. The equations (3.48) and (3.49) represent two sets of equidistant and mutually orthogonal lines in the k-space and constitute the lattice represented with the light grey lines. The intersections of the lines correspond to a given natural frequency. The curves of constant frequency are represented with the solid black line. It can be clearly seen that these curve presents a twofold behaviour, depending on the frequency ratio

$$\Omega = \frac{\omega_{s,m}}{\omega_R}, \tag{3.52}$$

between the structural natural frequency and the ring frequency $\omega_R = \sqrt{E/(\rho R^2)}$, according to the definition given in references [122, 123]. For $\Omega < 1$, to a given value of k_x corresponds two possible values of k_ϑ, while for $\Omega > \sqrt{2}$ each value of k_x is associated with an unique value of k_ϑ. In the region comprised between this two values, only a limited number of value of k_x is associated with two values of k_ϑ.
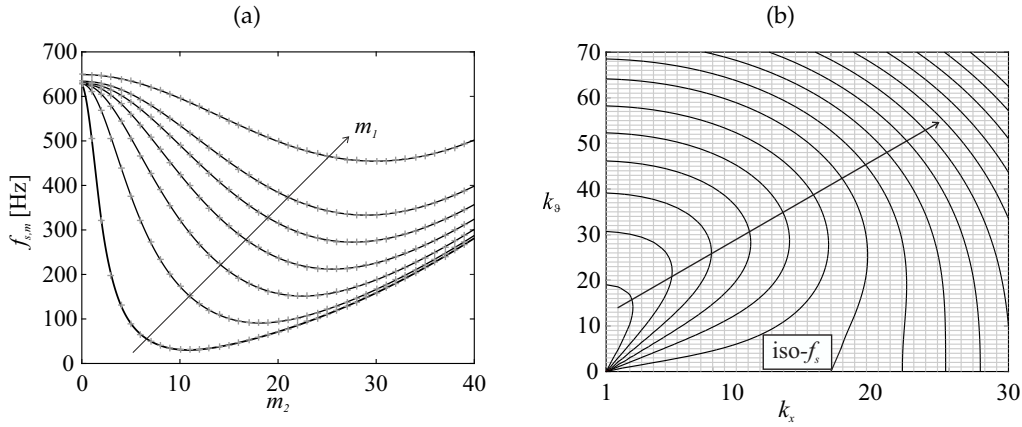
Figure 3.3: Variation of the structural natural frequency $f_{s,m}$ with the circumferential index m_2 for different values of the axial index m_1 (a) and wavenumber diagram of the $k-$space with the modal lattice (light grey rectangular grid) and iso-f_s curves (black lines) (b).

Figure 3.4 shows some of the structural modes described by equations (3.51); in particular plot (a) shows the mode characterized by the couple of indices $(1,0)$, plot (b) shows the $(1,1)$ mode, plot (c) shows the $(2,0)$ mode, plot (d) shows the $(2,2)$ mode, plot (e) shows the $(3,1)$ mode and finally plot (f) shows the $(3,3)$ structural natural mode. In every plot of figure 3.4, the left images

are axonometric views of the structural modes and the right images represent a cross section of the cylindrical shell, respectively of the symmetric component (top images) and of the anti-symmetric component (bottom images). For the cross-section images, the thick grey lines represent the undeformed surface of the cylinder while with the thin solid and dashed lines are shown the deformed surface of the cylinder during the flexural vibration.

The images in figure 3.4 are reported for illustrative purposes only. Indeed, the structural modes here presented are the ones for which the graphical representation is the most readable. This is due to the limited values (up to 3) of m_1 and m_2 that correspond to clearly observable patterns. On the other hand, higher values of m_1 and m_2 lead to an unreadable and misleading graphical representation. From figure 3.3 (a) it can be deduced that the lowest values of m_2 are associated with structural natural frequencies which are well above the frequency range considered in this study.

From plots (a) and (c) of figure 3.4 it can be clearly seen that when the circumferential index m_2 is zero, the anti-symmetric component of the flexural structural mode is everywhere zero, implying that this component does not contribute to the total vibration of the structure. Indeed, when the circumferential modal index m_2 is equal to zero, the flexural displacement is independent of the angular coordinate.

This can also be seen considering the nodal pattern of the symmetric and anti-symmetric components of the flexural structural modes, shown in figure 3.5 for the $(2, 3)$ mode. Considering the nodal positions, represented with the dash-dot lines, the following relationships can be gathered:

- The number of axial nodal lines is equal to $m_1 - 1$;

- The number of circumferential nodal lines is equal to $2m_2$.

Alternatively, the relationship between the modal indices and the axial and circumferential wavelengths can be established:

- the axial modal index m_1 represents the number of axial half-wavelengths;

- the circumferential modal index m_2 represents the number of circumferential wavelengths.

(a) $f_s = 628$ Hz

(b) $f_s = 506$ Hz

(c) $f_s = 629$ Hz

(d) $f_s = 505$ Hz

(e) $f_s = 611$ Hz

(f) $f_s = 507$ Hz
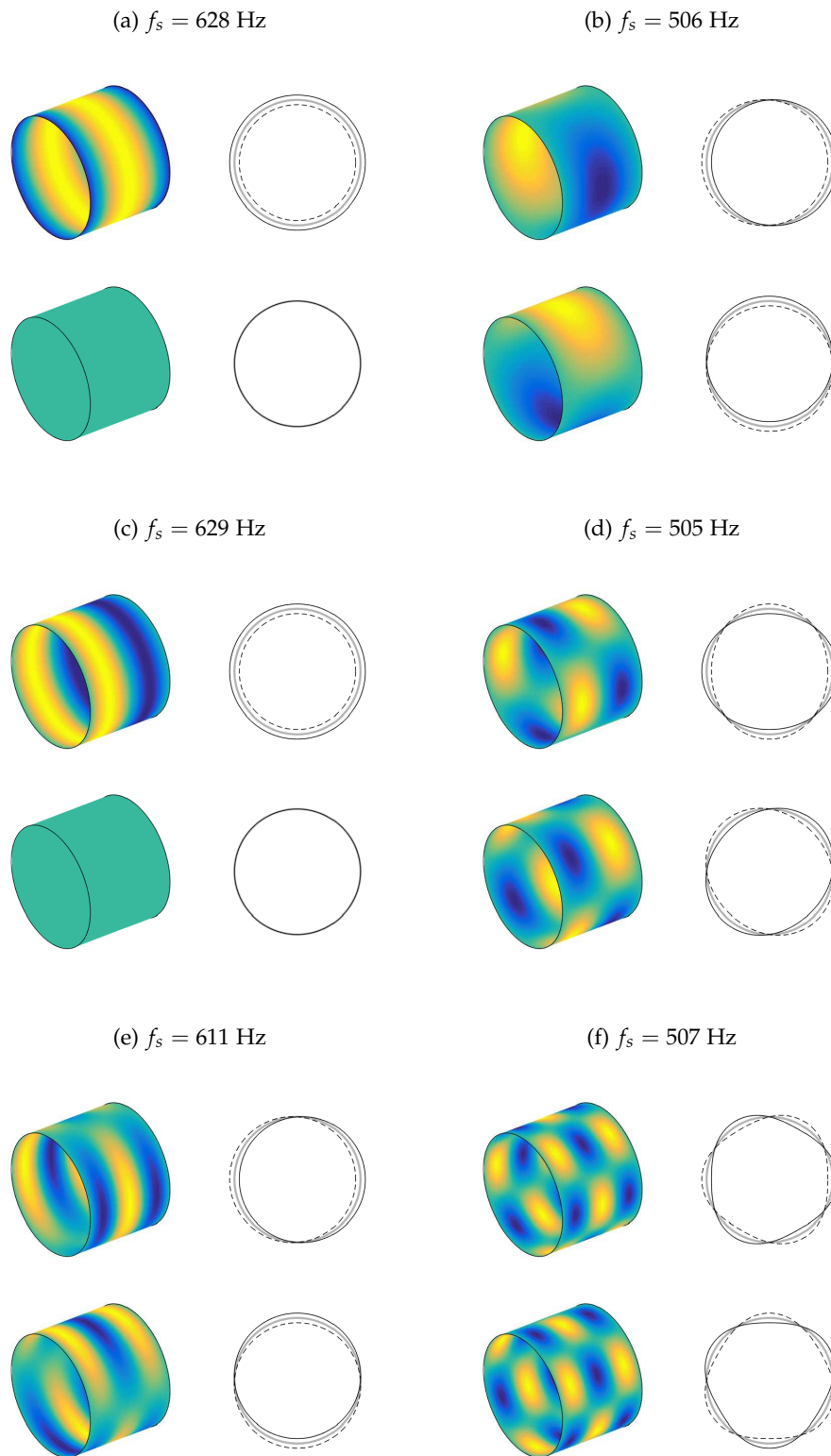
Figure 3.4: Axonometric (left images) and cross-section (right images) views of the symmetric (top images) and anti-symmetric (bottom images) of the structural natural mode shapes $(1,0)$ (a), $(1,1)$ (b), $(2,0)$ (c), $(2,2)$ (d), $(3,1)$ (e), $(3,3)$ (f).
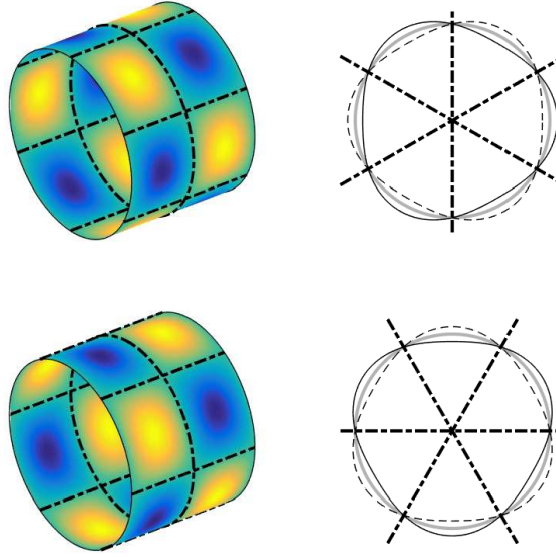
Figure 3.5: Nodal pattern for the symmetric (top plots) and for the anti-symmetric component (bottom plots) of the structural mode $(2, 3)$.

As shown in the right images of figure 3.5, where are shown the cross sections of the cylindrical shell, at a nodal cirumferential position for a mode component, correspond an anti-nodal circumferential position for the other component. The two components present the axial nodal lines at the same axial positions. The general position of nodal line are presented in Table 3.1.

Table 3.1: Nodal and anti-nodal positions for the cylindrical shell.

Direction		Symmetric component	Anti-symmetric component
Axial	nodal		$\alpha_1 \dfrac{L}{m_1}$
	anti - nodal		$\dfrac{L}{2m_1} + \alpha_2 \dfrac{L}{m_1}$
Circumferential	nodal	$\dfrac{\pi}{2m_2} + \beta \dfrac{\pi}{m_2}$	$\beta \dfrac{\pi}{m_2}$
	anti - nodal	$\beta \dfrac{\pi}{m_2}$	$\dfrac{\pi}{2m_2} + \beta \dfrac{\pi}{m_2}$

where $\alpha_1 = 0, 1, \ldots, m_1$, $\alpha_2 = 0, 1, \ldots, m_1 - 1$ and $\beta = 0, 1, \ldots, m_2 - 1$.

3.4   STRUCTURAL MODAL EQUATION OF MOTION

When a disturbance excites the cylindrical shell, the various mode are excited in various amounts, which may be limited little for certain modes and otherwise may assume large values for others, depending on the excitation field [101]. Assuming that the flexural displacement of the cylinder is separable in space and time [114], it can be represented in terms of the following modal summation:

$$w(\mathbf{x}_s, t) = \sum_{m=1}^{M} \varphi_m^s(\mathbf{x}_s) b_m^s(t) + \sum_{m=1}^{M} \varphi_m^a(\mathbf{x}_s) b_m^a(t), \qquad (3.53)$$

where $\varphi_m^s(\mathbf{x}_s)$ and $\varphi_m^a(\mathbf{x}_s)$ are the symmetric and anti-symmetric flexural natural mode shapes for the simply supported cylinder given in equations (3.51), $b_m^s(t)$ and $b_m^a(t)$ are the symmetric and anti-symmetric flexural modal amplitudes (sometimes also referred as modal participation factors [101]) and M is the number of flexural modes considered in the summation. This series expression can be rearranged in the following matrix form:

$$w(\mathbf{x}_s, t) = \begin{bmatrix} \boldsymbol{\varphi}^s(\mathbf{x}_s) & \boldsymbol{\varphi}^a(\mathbf{x}_s) \end{bmatrix} \begin{Bmatrix} \mathbf{b}^s(t) \\ \mathbf{b}^a(t) \end{Bmatrix} = \boldsymbol{\varphi}(\mathbf{x}_s)\mathbf{b}(t), \qquad (3.54)$$

where $\boldsymbol{\varphi}^s(\mathbf{x}_s)$ and $\boldsymbol{\varphi}^a(\mathbf{x}_s)$ are the row vectors with the symmetric and anti-symmetric structural flexural natural modes, whose dimensions are $1 \times M$, $\boldsymbol{\varphi}(\mathbf{x}_s) = \begin{bmatrix} \boldsymbol{\varphi}^s(\mathbf{x}_s) & \boldsymbol{\varphi}^a(\mathbf{x}_s) \end{bmatrix}$ is the $1 \times 2M$ vector of the structural flexural modes, $\mathbf{b}^s(t)$ and $\mathbf{b}^a(t)$ are the column vectors with the symmetric and anti-symmetric flexural modal amplitudes whose dimensions are $M \times 1$ and finally $\mathbf{b}(t) = \begin{bmatrix} \mathbf{b}^{s\,T}(t) & \mathbf{b}^{a\,T}(t) \end{bmatrix}^T$ is the $2M \times 1$ vector of the structural modal amplitudes.

Substitution the modal summation of equation (3.54) into the *in vacuo* equation of motion for the flexural displacement (3.35) yields:

$$\mathcal{L}_{\text{D-M},w} \left[\boldsymbol{\varphi}(\mathbf{x}_s) \right] \mathbf{b}(t) + \rho h \, \nabla_s^4 \boldsymbol{\varphi}(\mathbf{x}_s) \ddot{\mathbf{b}}(t) = \nabla_s^4 f_r(\mathbf{x}_s, t), \qquad (3.55)$$

where the symbol ¨ indicates the double derivative with respect to time. From the eigenvalue/eigenvector analysis of Section 3.3, it can be easily shown that:

$$\mathcal{L}_{\text{D-M},w} \left[\varphi_m(\mathbf{x}_s) \right] b_m(t) = \rho h \, \omega_{s,m}^2 \nabla_s^4 \varphi_m(\mathbf{x}_s) b_m(t). \qquad (3.56)$$

Inserting equation (3.56) into equation (3.55) leads:

$$\rho h \, \nabla_s^4 \boldsymbol{\varphi}(\mathbf{x}_s)\boldsymbol{\Omega}_s^2 \mathbf{b}(t) + \rho h \, \nabla_s^4 \boldsymbol{\varphi}(\mathbf{x}_s)\ddot{\mathbf{b}}(t) = \nabla_s^4 f_r(\mathbf{x}_s, t), \tag{3.57}$$

where $\boldsymbol{\Omega}_s$ is a $2M \times 2M$ diagonal matrix whose element are the structural natural frequencies such that:

$$\Omega_{s,(m,m)} = \Omega_{s,(m+M,m+M)} = \omega_{s,m} \tag{3.58}$$

where $m = 1, \ldots, M$ and $\omega_{s,m}$ is the m-th natural frequency of the cylinder given in equation (3.50).

After some algebraic manipulation, equation (3.57) can be rewritten in the following form:

$$\rho h \, \boldsymbol{\varphi}(\mathbf{x}_s)\ddot{\mathbf{b}}(t) + \rho h \, \boldsymbol{\varphi}(\mathbf{x}_s)\boldsymbol{\Omega}_s^2 \mathbf{b}(t) = f_r(\mathbf{x}_s, t). \tag{3.59}$$

Each term of equation (3.59) is then pre-multiplied by the column vector $\boldsymbol{\varphi}^T(\mathbf{x}_s)$ and integrated over the surface S of the cylindrical shell, yielding to the following matrix modal equation of motion:

$$\mathbf{M}_s\ddot{\mathbf{b}}(t) + \mathbf{K}_s\mathbf{b}(t) = \boldsymbol{\Phi}_s\mathbf{f}(t), \tag{3.60}$$

where $\mathbf{M}_s$ and $\mathbf{K}_s$ are the $2M \times 2M$ diagonal structural modal inertia and stiffness matrices, defined as:

$$\mathbf{M}_s = \rho h \int_S \boldsymbol{\varphi}^T(\mathbf{x}_s)\boldsymbol{\varphi}(\mathbf{x}_s)\mathrm{d}S = m_c\boldsymbol{\Lambda} \quad \text{and} \tag{3.61a}$$

$$\mathbf{K}_s = \rho h \int_S \boldsymbol{\varphi}^T(\mathbf{x}_s)\boldsymbol{\varphi}(\mathbf{x}_s)\boldsymbol{\Omega}_s^2\mathrm{d}S = \mathbf{M}_s\boldsymbol{\Omega}_s^2, \tag{3.61b}$$

where m_c is the mass of the cylinder and $\boldsymbol{\Lambda}$ is the $2M \times 2M$ diagonal matrix of the structural normalization coefficients whose elements are derived in appendix A. Also, $\boldsymbol{\Phi}_s$ and $\mathbf{f}(t)$ are the modal excitation matrix and the excitation vector.

The energy dissipation in the structure can be modelled in terms of an equivalent viscous damping factor [101, 114], thus the damped modal equation of motion for the cylinder can be written as:

$$\mathbf{M}_s\ddot{\mathbf{b}}(t) + \mathbf{C}_s\dot{\mathbf{b}}(t) + \mathbf{K}_s\mathbf{b}(t) = \boldsymbol{\Phi}_s\mathbf{f}(t), \tag{3.62}$$

where $\mathbf{C}_s$ is the $2M \times 2M$ diagonal modal damping matrix given by

$$\mathbf{C}_s = 2\zeta_s \mathbf{M}_s \mathbf{\Omega}_s, \tag{3.63}$$

where ζ_s is the structural damping ratio, assumed equal for all the structural modes.

3.4.1 Structural excitation field

The structural excitation field, shown in figure 2.1 (b), is assumed to be a uniform distribution of uncorrelated, stochastic, radial forces resembling a rain on the roof excitation [47, 72, 73]. The stochastic and uncorrelated nature of the rain on the roof excitation actuate all the structural modes efficiently, evening out the resonance response of all the structural modes [28]. The white noise rain on the roof excitation field is modelled with a uniform array of 24 uncorrelated point forces (8 in the circumferential direction and 3 in the axial direction) [64, 65]. The forcing term in equation (3.59) is then expressed as:

$$f_r(\mathbf{x}_s, t) = \sum_{i=1}^{N_R} f_{R,i}(t)\delta(\mathbf{x}_s - \mathbf{x}_{s,i}), \tag{3.64}$$

where $f_{R,i}(t)$ is the time-dependent amplitude of the i-th rain on the roof point force and $\delta(\mathbf{x}_s - \mathbf{x}_{s,i})$ is the two-dimensional Dirac delta function, which in cylindrical coordinate is given by [101]

$$\delta(\mathbf{x}_s - \mathbf{x}_{s,i}) = \delta(x - x_i)\frac{1}{R}\delta(\vartheta - \vartheta_i), \tag{3.65}$$

at the position $\mathbf{x}_{s,i} = (x_i, \vartheta_i)$ where the i-th force acts. The modal excitation matrix and the excitation vector of equation (3.62) are thus a $2M \times N_R$ matrix and a $N_R \times 1$ column vector respectively, where N_R is the total number of forces. Following the procedure described in the previous section, the first M rows of the modal excitation matrix $\mathbf{\Phi}_s$ are given by the symmetric structural modes evaluated at the forcing positions and the second M row are the anti-symmetric structural modes evaluated at the same points. Thus, the generic elements of the modal excitation matrix are given by:

$$\Phi_{s,(m,i)} = \varphi_m^s(\mathbf{x}_{s,i}) \quad \text{and} \tag{3.66a}$$

$$\Phi_{s,(m+M,i)} = \varphi_m^a(\mathbf{x}_{s,i}), \tag{3.66b}$$

where $m = 1, \ldots . M$. The excitation vector is thus of the form:

$$\mathbf{f}(t) = \begin{bmatrix} f_{R,1}(t) & f_{R,2}(t) & \ldots & f_{R,N_R}(t) \end{bmatrix}^T. \tag{3.67}$$

3.4.2 Frequency analysis of the structural response

Noise and vibration problems resulting from stationary random disturbances are normally studied in the frequency domain by considering the spectra of the responses [28]. Assuming harmonic motion, the time harmonic functions presented in the previous sections can be expressed in the form

$$g(t) = \mathrm{Re}[g(\omega)e^{j\omega t}], \tag{3.68}$$

where ω is the circular frequency, $g(\omega)$ is the frequency-dependent complex amplitude of the time-harmonic function $g(t)$, j is the imaginary unit such that $j^2 = -1$ and $\mathrm{Re}[\cdot]$ is the real part operator. Then, the differential equation (3.62) that describe the time-dependent flexural displacement of the cylinder can be expressed as

$$\left[-\omega^2 \mathbf{M}_s + j\omega \mathbf{C}_s + \mathbf{K}_s \right] \mathbf{b}(\omega) = \boldsymbol{\Phi}_s \mathbf{f}(\omega), \tag{3.69}$$

where $\mathbf{b}(\omega)$ and $\mathbf{f}(\omega)$ are the column vectors of the frequency-dependent complex amplitudes of the time-harmonic flexural modal displacements and excitation forces.

An appropriate measure of the global flexural response of the cylindrical structure is given by the Power Spectral Density of the total kinetic energy of the cylinder [22, 28, 64, 72], which, for brevity, will be stated as flexural kinetic energy PSD. This quantity can be derived with the following expression [124, 125]

$$S_K(\omega) = \frac{1}{2} \rho h \int_S \lim_{T \to \infty} E \left[\frac{1}{T} \dot{w}^*(\mathbf{x}_s, \omega) \dot{w}(\mathbf{x}_s, \omega) \right] dS, \tag{3.70}$$

where $E[\cdot]$ is the expectation operator, the superscript * indicates the complex conjugate operator and $\dot{w}(\mathbf{x}_s, \omega)$ is the frequency-dependent amplitude of the flexural velocity at a cylindrical surface point $\mathbf{x}_s$. According to equation (3.54), the flexural velocity is defined as

$$\dot{w}(\mathbf{x}_s, \omega) = \boldsymbol{\varphi}(\mathbf{x}_s) \dot{\mathbf{b}}(\omega), \tag{3.71}$$

where $\dot{\mathbf{b}}(\omega)$ is the $1 \times 2M$ column vector of the complex frequency-dependent amplitudes of the flexural modal velocities and may be obtained by equation (3.69) as

$$\dot{\mathbf{b}}(\omega) = \mathbf{Y}(\omega)\mathbf{\Phi}_s\mathbf{f}(\omega). \tag{3.72}$$

Here

$$\mathbf{Y}(\omega) = j\omega \left[-\omega^2\mathbf{M}_s + j\omega\mathbf{C}_s + \mathbf{K}_s \right]^{-1} \tag{3.73}$$

is the $2M \times 2M$ mobility matrix derived from equation (3.69). Substituting equation (3.72) into (3.71)and the resulting expression into equation (3.70) leads to

$$
\begin{aligned}
S_K(\omega) &= \frac{1}{2}\rho h \int_S \lim_{T \to \infty} E\left[\frac{1}{T}\mathbf{f}^T(\omega)\mathbf{\Phi}_s^T\mathbf{Y}^H(\omega)\boldsymbol{\varphi}^T(\mathbf{x}_s)\boldsymbol{\varphi}(\mathbf{x}_s)\mathbf{Y}(\omega)\mathbf{\Phi}_s\mathbf{f}(\omega) \right] dS \\
&= \frac{1}{2}m_c\operatorname{Tr}\left[\mathbf{S_{bb}}(\omega) \right],
\end{aligned}
\tag{3.74}
$$

where the superscript ^{H} indicates the Hermitian operator, $\operatorname{Tr}[\cdot]$ is the trace operator and $\mathbf{S_{bb}}(\omega)$ is the $2M \times 2M$ fully populated matrix with the PSD of the modal structural velocities given by:

$$
\begin{aligned}
\mathbf{S_{bb}}(\omega) &= \lim_{T \to \infty} E\left[\frac{1}{T}\mathbf{\Lambda}\mathbf{Y}(\omega)\mathbf{\Phi}_s\mathbf{f}(\omega)\mathbf{f}^T(\omega)\mathbf{\Phi}_s^T\mathbf{Y}^H(\omega) \right] \\
&= \mathbf{\Lambda}\mathbf{Y}(\omega)\mathbf{\Phi}_s\mathbf{S_{ff}}(\omega)\mathbf{\Phi}_s^T\mathbf{Y}^H(\omega),
\end{aligned}
\tag{3.75}
$$

where $\mathbf{S_{ff}}(\omega)$ is the $N_R \times N_R$ matrix with the PSD of the rain on the roof force excitations, which is assumed to be an identity matrix [64, 72]:

$$\mathbf{S_{ff}}(\omega) = \lim_{T \to \infty} E\left[\mathbf{f}(\omega)\mathbf{f}^T(\omega) \right] \equiv \mathbf{I}. \tag{3.76}$$

Thus, the PSD of the cylinder flexural kinetic energy is given by:

$$S_K(\omega) = \frac{1}{2}m_c\operatorname{Tr}\left[\mathbf{\Lambda}\mathbf{Y}(\omega)\mathbf{\Phi}_s\mathbf{I}\mathbf{\Phi}_s^T\mathbf{Y}^H(\omega) \right]. \tag{3.77}$$

From equations (3.53) and (3.54) it can be seen that the flexural displacement of the cylindrical shell can be thought as the sum of two components, the first related to the symmetric components of the motion and the second related to the anti-symmetric components of the motion:

$$w(\mathbf{x}_s, t) = w^s(\mathbf{x}_s, t) + w^a(\mathbf{x}_s, t), \tag{3.78}$$

where

$$w^s(\mathbf{x}_s, t) = \boldsymbol{\varphi}^s \mathbf{b}^s(t), \tag{3.79a}$$

$$w^a(\mathbf{x}_s, t) = \boldsymbol{\varphi}^a \mathbf{b}^a(t). \tag{3.79b}$$

In the same way the PSD of the flexural kinetic energy can be expressed as the sum of two terms, the former related with the symmetric and the latter related with the anti-symmetric motion:

$$S_K(\omega) = S_K^s(\omega) + S_K^a(\omega), \tag{3.80}$$

where the two terms are defined as:

$$S_K^s(\omega) = \frac{1}{2}\rho h \int_S \lim_{T\to\infty} E\left[\frac{1}{T}\dot{w}^{s*}(\mathbf{x}_s, \omega)\dot{w}^s(\mathbf{x}_s, \omega)\right] dS, \tag{3.81a}$$

$$S_K^a(\omega) = \frac{1}{2}\rho h \int_S \lim_{T\to\infty} E\left[\frac{1}{T}\dot{w}^{a*}(\mathbf{x}_s, \omega)\dot{w}^a(\mathbf{x}_s, \omega)\right] dS. \tag{3.81b}$$

Following the same procedure which leads to the expression of the PSD of the flexural kinetic energy of the cylinder given in equation (3.77), the PSDs related to the two components motion can be expressed as:

$$S_K^s(\omega) = \frac{1}{2}m_c \text{Tr}\left[\boldsymbol{\beta}^s \boldsymbol{\Lambda} \mathbf{Y}(\omega) \boldsymbol{\Phi}_s \mathbf{I} \boldsymbol{\Phi}_s^T \mathbf{Y}^H(\omega) \boldsymbol{\beta}^{sT}\right], \tag{3.82a}$$

$$S_K^a(\omega) = \frac{1}{2}m_c \text{Tr}\left[\boldsymbol{\beta}^a \boldsymbol{\Lambda} \mathbf{Y}(\omega) \boldsymbol{\Phi}_s \mathbf{I} \boldsymbol{\Phi}_s^T \mathbf{Y}^H(\omega) \boldsymbol{\beta}^{aT}\right], \tag{3.82b}$$

where $\boldsymbol{\beta}^s$ and $\boldsymbol{\beta}^a$ are the $M \times 2M$ matrices given by:

$$\boldsymbol{\beta}^s = \begin{bmatrix} \mathbf{I}_{M\times M} & \mathbf{0}_{M\times M} \end{bmatrix} \quad \text{and} \tag{3.83a}$$

$$\boldsymbol{\beta}^a = \begin{bmatrix} \mathbf{0}_{M\times M} & \mathbf{I}_{M\times M} \end{bmatrix}, \tag{3.83b}$$

being $\mathbf{I}_{M\times M}$ and $\mathbf{0}_{M\times M}$ the $M \times M$ identity and zero matrices respectively.

3.4.3 *Simulation results*

In figure 3.6 are shown the 20-100 Hz flexural kinetic energy PSD for the symmetric component defined in equation (3.82a), plot (a), for the anti-symmetric component defined in equation (3.82b), plot (b), and for the global response defined in equation (3.77), plot (c).
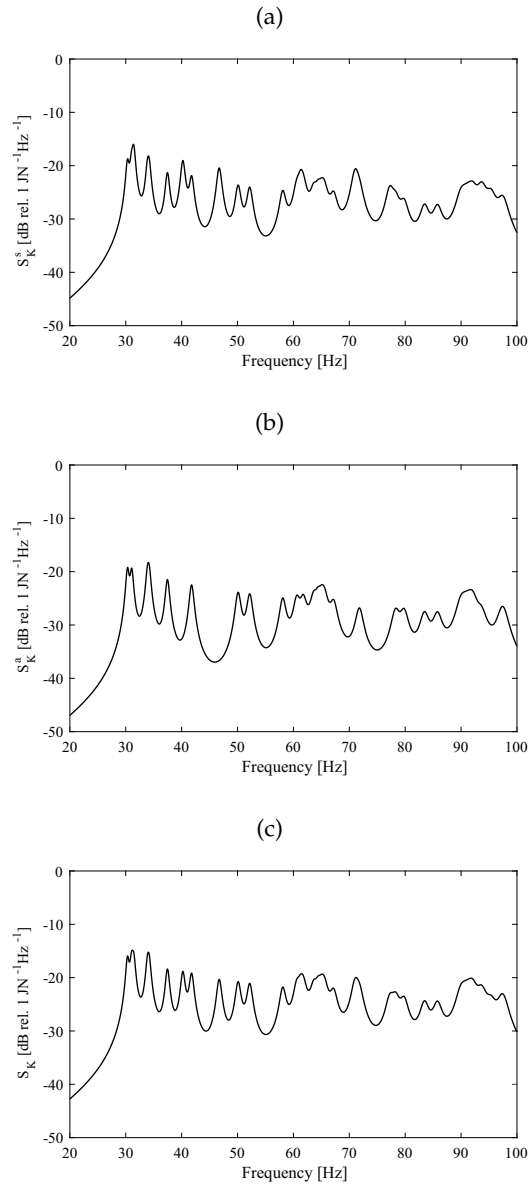
Figure 3.6: Spectra of the flexural kinetic energy of the symmetric component (a), the anti-symmetric component (b) and of the total response (c), which considers both the components.

From these figures appear quite clear two main characteristics. First, the uneven distribution of the resonance peaks, which straightforwardly derive from the expression of the structural natural frequencies given in equation (3.50). Second, the amplitudes of the resonance peaks are fairly even, since the rain on the roof equally excites all the modes.

The response is characterised by several resonance peaks, some of which are clustered in small band of few Hz. In particular, the response is characterised by almost separate peaks below about 60 Hz and by a more uniform and flat response above 60 Hz, due to the high modal overlap factor which characterise the cylindrical shells [99, 122, 123, 126].

3.4.4 *Effects of the spatial distribution of the excitation field*

In this section, the influence of the forcing field spatial distribution on the cylindrical shell response is analysed. The analysis is carried out considering for simplicity a single structural mode.

If just the single flexural mode shape $\tilde{m}$ is considered, the flexural displacement can be expressed as:

$$\tilde{w}(\mathbf{x}_s, t) = \varphi^s_{\tilde{m}}(\mathbf{x}_s)b^s_{\tilde{m}}(t) + \varphi^a_{\tilde{m}}(\mathbf{x}_s)b^a_{\tilde{m}}(t). \tag{3.84}$$

If a single point force is applied on the cylindrical shell at position $\mathbf{x}_F$, the equation of motion (3.69), considering just a single flexural mode shape, can be expressed as two uncoupled equations related to the symmetric and anti-symmetric component:

$$\left(-\omega^2 M^s_{\tilde{m}} + j\omega C^s_{\tilde{m}} + K^s_{\tilde{m}}\right) b^s_{\tilde{m}}(\omega) = \varphi^s_{\tilde{m}}(\mathbf{x}_F)f_R(\omega) \quad \text{and} \tag{3.85a}$$

$$\left(-\omega^2 M^a_{\tilde{m}} + j\omega C^a_{\tilde{m}} + K^a_{\tilde{m}}\right) b^a_{\tilde{m}}(\omega) = \varphi^a_{\tilde{m}}(\mathbf{x}_F)f_R(\omega), \tag{3.85b}$$

where M^s, C^s, K^s and M^a, C^a, K^a are respectively the $(\tilde{m}, \tilde{m})$ and the $(\tilde{m} + M, \tilde{m} + M)$ elements of the modal inertia, damping and stiffness matrices given in equations (3.61) and (3.63). As shown in appendix A, the symmetric and anti-symmetric terms are the same except for the case where the circumferential index is zero, $m_2 = 0$. But in this case, as shown in section 3.3, the anti-symmetric component of motion is zeros, and the motion is completely described by the symmetric component. Thus, assuming $\tilde{m}_2 \neq 0$, the dynamic stiffness [127] can be defined as :

$$\tilde{D}(\omega) = -\omega^2 \tilde{M} + j\omega \tilde{C} + \tilde{K} \tag{3.86}$$

where $\tilde{M} = M^s_{\tilde{m}} = M^a_{\tilde{m}}$, $\tilde{C} = C^s_{\tilde{m}} = C^a_{\tilde{m}}$ and $\tilde{K} = K^s_{\tilde{m}} = K^a_{\tilde{m}}$. Equations (3.85) can thus be solved for the modal amplitudes, yielding:

$$b^s_{\tilde{m}}(\omega) = \frac{\varphi^s_{\tilde{m}}(\mathbf{x}_F) f_R(\omega)}{\tilde{D}(\omega)} \quad \text{and} \tag{3.87a}$$

$$b^a_{\tilde{m}}(\omega) = \frac{\varphi^a_{\tilde{m}}(\mathbf{x}_F) f_R(\omega)}{\tilde{D}(\omega)}. \tag{3.87b}$$

The frequency-dependent flexural displacement due to the $\tilde{m}$-th flexural mode shape can be expressed from equation (3.84) as

$$\tilde{w}(\mathbf{x}_s, \omega) = \frac{\varphi^s_{\tilde{m}}(\mathbf{x}_s)\varphi^s_{\tilde{m}}(\mathbf{x}_F) f_R(\omega)}{\tilde{D}(\omega)} + \frac{\varphi^a_{\tilde{m}}(\mathbf{x}_s)\varphi^a_{\tilde{m}}(\mathbf{x}_F) f_R(\omega)}{\tilde{D}(\omega)}. \tag{3.88}$$

Expressing in an explicit manner the mode shapes as given in equations (3.51), the flexural displacement can be written as:

$$\tilde{w}(\mathbf{x}_s, \omega) = \frac{f_R(\omega)}{D(\omega)} \sin\left(\frac{\tilde{m}_1 \pi}{L} x\right) \sin\left(\frac{\tilde{m}_1 \pi}{L} x_F\right) [\cos(\tilde{m}_2 \vartheta_F) \cos(\tilde{m}_2 \vartheta) \tag{3.89}$$
$$+ \sin(\tilde{m}_2 \vartheta) \sin(\tilde{m}_2 \vartheta_F)],$$

and recalling the trigonometric identity

$$\cos(\alpha - \beta) = \cos(\alpha)\cos(\beta) + \sin(\alpha)\sin(\beta), \tag{3.90}$$

the flexural displacement can be written as:

$$\tilde{w}(\mathbf{x}_s, \omega) = \frac{f_R(\omega)}{D(\omega)} \sin\left(\frac{\tilde{m}_1 \pi}{L} x\right) \sin\left(\frac{\tilde{m}_1 \pi}{L} x_F\right) \cos\left[\tilde{m}_2(\vartheta - \vartheta_F)\right]. \tag{3.91}$$

This equation shows the fact that when a single force acts on the the cylinder, the flexural displacement related to a flexural mode tends to orientate itself in order to presents its maximum deflection at an orientation which coincides with the orientation of the force [22, 101].

This is shown in figure 3.7 where are shown the deflections of the structural modes characterised by modal indices $(1, 2)$, plot (a), and $(1, 3)$, plot (b), when they are excited by a single point force oriented at $\pi/6$ and $\pi/4$ respectively. The symmetric and anti-symmetric components, shown in the left and central graphs respectively, present an amplitude which depends on the position of the force thus that the resulting deflection, shown in the right graphs, presents its maximum deflection in correspondence to the orientation of the force.

(a)

(b)
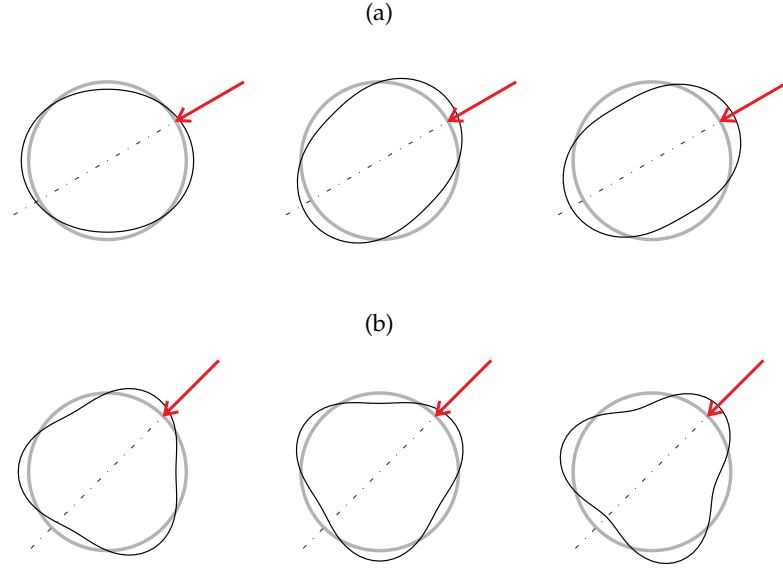
Figure 3.7: Circumferential orientation of the symmetric component (left graphs), anti-symmetric component (central graphs) and of the total flexural displacement (right graphs) at the mid-section of the cylindrical shell for the $(1,2)$ structural mode shape (plot (a)) and for the $(1,3)$ structural mode (plot (b)) when a single point force acts on the cylinder.

When two point forces act on the cylindrical shell, the equation of motion results in the following two equations:

$$\left(-\omega^2 M_{\tilde{m}}^s + j\omega C_{\tilde{m}}^s + K_{\tilde{m}}^s\right) b_{\tilde{m}}^s(\omega) = \varphi_{\tilde{m}}^s(\mathbf{x}_{F1})f_{R1}(\omega) + \varphi_{\tilde{m}}^s(\mathbf{x}_{F2})f_{R2}(\omega), \quad \text{(3.92a)}$$

$$\left(-\omega^2 M_{\tilde{m}}^a + j\omega C_{\tilde{m}}^a + K_{\tilde{m}}^a\right) b_{\tilde{m}}^a(\omega) = \varphi_{\tilde{m}}^a(\mathbf{x}_{F1})f_{R1}(\omega) + \varphi_{\tilde{m}}^a(\mathbf{x}_{F2})f_{R2}(\omega), \quad \text{(3.92b)}$$

and solving for the modal amplitudes, leads to

$$b_{\tilde{m}}^s(\omega) = \frac{\varphi_{\tilde{m}}^s(\mathbf{x}_{F1})f_{R1}(\omega)}{\tilde{D}(\omega)} + \frac{\varphi_{\tilde{m}}^s(\mathbf{x}_{F2})f_{R2}(\omega)}{\tilde{D}(\omega)} \quad \text{and} \quad \text{(3.93a)}$$

$$b_{\tilde{m}}^a(\omega) = \frac{\varphi_{\tilde{m}}^a(\mathbf{x}_{F1})f_{R1}(\omega)}{\tilde{D}(\omega)} + \frac{\varphi_{\tilde{m}}^a(\mathbf{x}_{F2})f_{R2}(\omega)}{\tilde{D}(\omega)}, \quad \text{(3.93b)}$$

where the assumption of $\tilde{m}_2 \neq 0$ is made. The flexural displacement due to the $\tilde{m}$-th mode can be written as:

$$\tilde{w}(\mathbf{x}_s, \omega) = \frac{1}{D(\omega)} \sin\left(\frac{\tilde{m}_1 \pi}{L} x\right) \left\{ f_{R1}(\omega) \sin\left(\frac{\tilde{m}_1 \pi}{L} x_{F1}\right) \cos\left[\tilde{m}_2(\vartheta - \vartheta_{F1})\right] + \right.$$

$$\left. f_{R2}(\omega) \sin\left(\frac{\tilde{m}_1 \pi}{L} x_{F2}\right) \cos\left[\tilde{m}_2(\vartheta - \vartheta_{F2})\right] \right\}$$

$$\text{(3.94)}$$

From this equation it can be seen that no explicit orientation of the flexural displacement derive from the orientation of the two applied forces. If the two forces are such that

$$f_{R1}(\omega)\sin\left(\frac{\tilde{m}_1\pi}{L}x_{F1}\right) = f_{R2}(\omega)\sin\left(\frac{\tilde{m}_1\pi}{L}x_{F2}\right) = \tilde{f}(\omega, x_{F1}, x_{F2}) \qquad (3.95)$$

equation (3.94) can be written as

$$\tilde{w}(\mathbf{x}_s, \omega) = \frac{\tilde{f}(\omega, x_{F1}, x_{F2})}{D(\omega)}\cos\left[\tilde{m}_2\left(\frac{\vartheta_{F1} - \vartheta_{F2}}{2}\right)\right]\sin\left(\frac{\tilde{m}_1\pi}{L}x\right)\cos\left[\tilde{m}_2\left(\vartheta - \frac{\vartheta_{F1} + \vartheta_{F2}}{2}\right)\right]$$

$$(3.96)$$

This equation shows that the displacement will orientate itself to present the maximum displacement at an circular position which corresponds to the mean orientation of the two forces.

Figure 3.8 shows the deflection of the cylindrical shell characterised by the structural mode with modal indices $(1, 3)$ when the two forces are uncorrelated in amplitude and position, plot (a), and when the two forces are such to satisfy equation (3.95), plot (b). The dot-dashed lines represent the mean orientation of the two forces. It is clearly observable that the condition shown in plot (a) does not lead to the orientation of the flexural deflection according to the mean orientation of the forces. Instead, for the condition shown in plot (b), the global deflection of the structure is oriented according to the mean orientation of the two forces.

It has to be highlighted that the condition given in equation (3.95) represents a more mathematical than practical condition. Indeed, also if the two force apply in two position which would satisfy the geometrical part of the equation, the amplitude of the two forces could vary over time, especially if the two forces have a stochastic nature.

This analysis could be enhanced considering a greater number of forces, but the analogous condition to the one expressed in equation (3.95) becomes more complex and loses any practical sense.

(a)

(b)
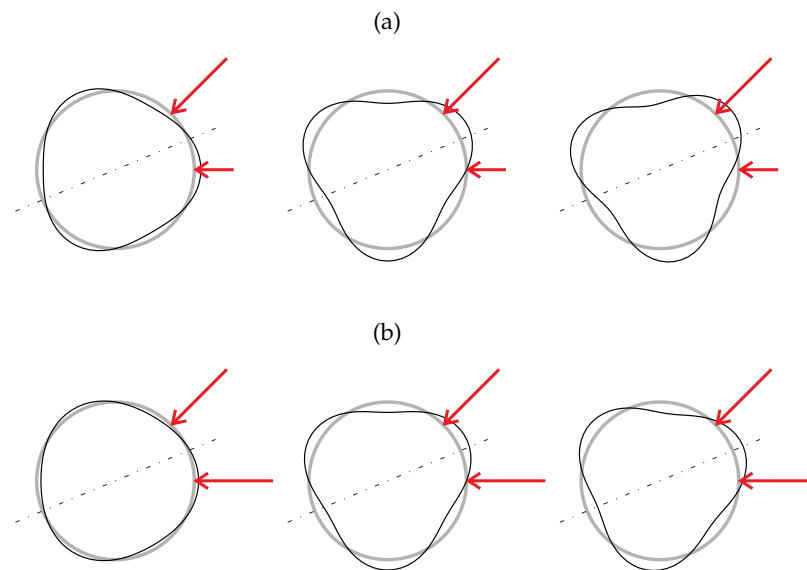
Figure 3.8: Circumferential orientation of the symmetric components (left graphs), of the anti-symmetric component (central graphs) and of the total flexural displacement (right graphs) at the mid-section of the cylindrical shell for the $(1,3)$ flexural mode shape when two forces act on the cylinder. Plot (a) represents the general case, plot (b) represents the case in which the two forces satisfy the condition of equation (3.95).

3.5 WAVE EQUATION FOR THE CYLINDRICAL ENCLOSURE

In this section the derivation of the acoustic wave equation expressed in terms of the acoustic pressure is presented. For simplicity, the acoustic wave equation is derived for the one-dimensional case and then it will be extended to the three-dimensional case considered in this study.

The derivation of the acoustic wave equation in terms of acoustic pressure for an acoustic volume follows three steps, which can be summarized as [128–130]:

1. Derivation of the continuity equation;

2. Derivation of the Euler's equation;

3. Derivation of the equation of state.

3.5.1   *Continuity equation*

The continuity equation connect the motion of a fluid with its compression or expansion. Considering the element shown in Figure 3.9, the net rate of mass which flows into the element through its surface must equal the net rate with which mass varies [128].
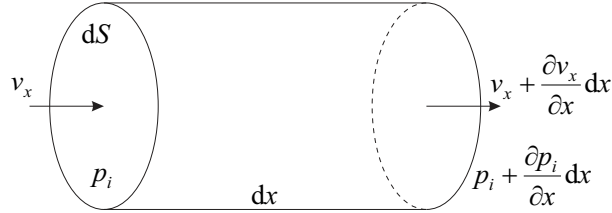
Figure 3.9: Fluid element subject to a pressure gradient in which fluid enters at the left and exits at the right.

The net influx of mass into the volume is given by:

$$\left[\rho_i v_x - \left(\rho_i v_x + \frac{\rho_i v_x}{\partial x} dx \right) \right] dS = -\frac{\rho_i v_x}{\partial x} dV, \tag{3.97}$$

where $\rho_i = \rho_0 + \tilde{\rho}$ is the instantaneous density of the fluid, given by the sum of the equilibrium density ρ_0 and of the acoustic density $\tilde{\rho}$, v_x is the particle velocity of the fluid element in the x direction, dx, dS and dV are the length, the transverse surface and the volume of the elemental volume of figure 3.9. The net influx must equal the rate with which mass increase $(\partial \rho_i / \partial t)\, dV$,

$$\frac{\partial \rho_i}{\partial t} + \frac{\rho_i v_x}{\partial x} = 0 \tag{3.98}$$

This exact continuity equation can be linearised considering that the definition of the instantaneous density,

$$\frac{\partial (\rho_0 + \tilde{\rho})}{\partial t} + \frac{(\rho_0 + \tilde{\rho})\, v_x}{\partial x} = 0, \tag{3.99}$$

and recognizing that the equilibrium density is constant with time $(\partial \rho_0 / \partial t = 0)$ and neglecting the product $\tilde{\rho} v_x$ since it is a second order term [128, 130], the linearised continuity equation can be written as

$$\frac{\partial \tilde{\rho}}{\partial t} + \rho_0 \frac{v_x}{\partial x} = 0. \tag{3.100}$$

If mass is injected into the volume, as for example in case where a loud-speaker is present in the volume, the linearised continuity equation can be expressed as [128, 129]

$$\frac{\partial \tilde{\rho}}{\partial t} + \rho_0 \frac{v_x}{\partial x} = \rho_0 \, q \tag{3.101}$$

where q is the fluctuating volume flow per unit volume and correspond to a monopole source.

3.5.2 *Euler's equation*

The Euler's equation represents the Newton's second law for the fluid case and, in absence of dissipations due to viscosity, it states that the net force on a fluid element due to an acoustic gradient equals the product of the acceleration and the mass of the fluid element. With reference to figure 3.9, the net force acting on the fluid element is

$$\left[p_i - \left(p_i + \frac{\partial p_i}{\partial x} \mathrm{d}x \right) \right] \mathrm{d}S = -\frac{\partial p_i}{\partial x} \mathrm{d}V. \tag{3.102}$$

where $p_i = p_0 + p$ is the instantaneous pressure, given by the sum of the equilibrium pressure p_0 and of the acoustic pressure p. This term must be equal to $(\partial v_x / \partial t) \, \rho_i \mathrm{d}V$, thus

$$-\frac{\partial p_i}{\partial x} = \rho_i \frac{\partial v_x}{\partial t} \tag{3.103}$$

This exact equation can be linearised assuming that the equilibrium pressure is homogeneous and neglecting the term $\tilde{\rho} v_x$ in the right hand side [130], yielding to

$$-\frac{\partial p}{\partial x} = \rho_0 \frac{\partial v_x}{\partial t}, \tag{3.104}$$

which represents the linear inviscid Euler's equation [128].

3.5.3 *Equation of state*

The equation of state represents a relation between the density and pressure in the form $p = p(\rho)$. Assuming that the acoustic precesses are isentropic [130, 131], the instantaneous and equilibrium pressure and density are related by the isentropic relation:

$$\frac{p_i}{p_0} = \left(\frac{\rho_i}{\rho_0} \right)^\gamma, \tag{3.105}$$

where γ represents the ratio of specific heats. The relation between the acoustic quantities can be obtained considering the Taylor's expansion of equation (3.105), in the form

$$p_i - p_0 = \left(\frac{\partial p_i}{\partial \rho_i}\right)_{s,\rho_0} (\rho_i - \rho_0) + \frac{1}{2}\left(\frac{\partial^2 p_i}{\partial \rho_i^2}\right)_{s,\rho_0} (\rho_i - \rho_0)^2 + \ldots, \qquad (3.106)$$

where the subscripts $_{s,\rho_0}$ indicate that the partial derivatives are determined for isentropic process about its equilibrium density. Retaining only the first term and recognising in $p_i - p_0$ the acoustic pressure p and in $\rho_i - \rho_0$ the acoustic density $\tilde{\rho}$, equation (3.106) can be expressed as

$$p = c_0^2 \tilde{\rho}, \qquad (3.107)$$

where

$$c_0^2 = \left(\frac{\partial p_i}{\partial \rho_i}\right)_{s,\rho_0} \qquad (3.108)$$

is the speed of sound [128].

3.5.4   Acoustic wave equation

The acoustic wave equation can be obtained combining together the equations (3.101), (3.104) and (3.107), leading to the well-known one dimensional inhomogeneous wave equation [128–130]:

$$\frac{\partial^2 p}{\partial x^2} - \frac{1}{c_0^2}\frac{\partial^2 p}{\partial t^2} = -\rho_0 \frac{\partial q}{\partial t}. \qquad (3.109)$$

This wave equation describing the behaviour of the acoustic pressure, can be easily extended for the three-dimensional case as

$$\nabla^2 p(\mathbf{x},t) - \frac{1}{c_0^2}\frac{\partial^2 p(\mathbf{x},t)}{\partial t^2} = -\rho_0 \frac{\partial q(\mathbf{x},t)}{\partial t}, \qquad (3.110)$$

where ∇^2 is the three dimensional Laplacian operator in cylindrical coordinates and $\mathbf{x} = (x, \vartheta, r)$ represent the generic position in the acoustic volume, given in the cylindrical coordinates shown in figure 2.1 (a).

3.6 ACOUSTIC NATURAL MODES AND FREQUENCIES

The acoustic natural modes for the acoustic pressure can be obtained assuming the free response of the acoustic volume, thus neglecting the source term in equation (3.110). Expressing the Laplacian operator in cylindrical coordinates, this equation can be rewritten as [128, 132]

$$\frac{\partial^2 p(\mathbf{x},t)}{\partial r^2} + \frac{1}{r}\frac{\partial p(\mathbf{x},t)}{\partial r} + \frac{1}{r^2}\frac{\partial^2 p(\mathbf{x},t)}{\partial \vartheta^2} + \frac{\partial^2 p(\mathbf{x},t)}{\partial x^2} - \frac{1}{c_0^2}\frac{\partial^2 p(\mathbf{x},t)}{\partial t^2} = 0. \quad (3.111)$$

As for the flexural displacement of the cylindrical shell, the acoustic pressure can be expressed using the separation of variables as a product of functions, each of which depending only upon a single variable [128, 129, 131, 132]:

$$p(\mathbf{x},t) = \psi(\mathbf{x})g(t) = \mathcal{X}(x)\Theta(\vartheta)\mathcal{R}(r)g(t). \quad (3.112)$$

Substitution of equation (3.112) into equation (3.111) yields:

$$\mathcal{X}\Theta g\frac{d^2\mathcal{R}}{dr^2} + \frac{\mathcal{X}\Theta g}{r}\frac{d\mathcal{R}}{dr} + \frac{\mathcal{X}\mathcal{R}g}{r^2}\frac{d^2\Theta}{d\vartheta^2} + \Theta\mathcal{R}g\frac{d^2\mathcal{X}}{dx^2} - \frac{\mathcal{X}\Theta\mathcal{R}}{c_0^2}\frac{d^2g}{dt^2} = 0. \quad (3.113)$$

where the dependence of the functions on the variables is omitted and the partial derivatives is substituted by ordinary derivatives. Dividing by $\mathcal{X}\Theta\mathcal{R}g$ gives

$$\frac{1}{\mathcal{R}}\frac{d^2\mathcal{R}}{dr^2} + \frac{1}{r\mathcal{R}}\frac{d\mathcal{R}}{dr} + \frac{1}{r^2\Theta}\frac{d^2\Theta}{d\vartheta^2} + \frac{1}{\mathcal{X}}\frac{d^2\mathcal{X}}{dx^2} - \frac{1}{g\,c_0^2}\frac{d^2g}{dt^2} = 0. \quad (3.114)$$

The only way that equation (3.114) can be satisfied by three independent functions is that each term depending upon a coordinate is equal to a constant and those constants sums to 0. Thus equation (3.114) can be expressed as four ordinary differential equations as

$$\frac{1}{g}\frac{d^2g}{dt^2} = -\omega^2, \quad (3.115a)$$

$$\frac{1}{\mathcal{X}}\frac{d^2\mathcal{X}}{dx^2} = -k_x^2, \quad (3.115b)$$

$$\frac{1}{\Theta}\frac{d^2\Theta}{d\vartheta^2} = -n_2^2 \quad \text{and} \quad (3.115c)$$

$$\frac{1}{\mathcal{R}}\frac{d^2\mathcal{R}}{dr^2} + \frac{1}{r\mathcal{R}}\frac{d\mathcal{R}}{dr} + \frac{n_2^2}{r^2} = -k_{\vartheta,r}^2, \quad (3.115d)$$

with

$$k_x^2 + k_{\vartheta,r}^2 = k^2 = \frac{\omega^2}{c_0^2}. \tag{3.116}$$

From equations (3.115c) and (3.115d) it can be seen that the radial and circumferential terms are related, since the term m_2 appears both in the radial and in the circumferential equation. The values for the constants in equations (3.115) can be determined solving the equations, once the boundary conditions are stated. The acoustic volume shown in figure 2.1 (a) is considered to be subject to rigid walled boundary conditions. For this boundary conditions, the particle velocity normal to the surface of the cylindrical enclosure must be zero [128, 129], thus:

$$v_x(x = 0, t) = v_x(x = L, t) = v_r(r = R, t) = 0, \tag{3.117}$$

where v_x and v_r are the components of the particle velocity in the axial and radial directions, respectively. According to the Euler's equation (3.104), these conditions can be written as [128]:

$$\left.\frac{\partial p(\mathbf{x}, t)}{\partial x}\right|_{x=0} = \left.\frac{\partial p(\mathbf{x}, t)}{\partial x}\right|_{x=L} = \left.\frac{\partial p(\mathbf{x}, t)}{\partial r}\right|_{r=R} = 0. \tag{3.118}$$

The solution to the equation for the function in the axial direction, (3.115b), is of the form

$$X(x) = \cos(k_x x), \tag{3.119}$$

where the axial wavenumber are of the form

$$k_x = \frac{n_1 \pi}{L}, \tag{3.120}$$

with the axial modal indices given by integer numbers, $n_1 = 0, 1, 2, \ldots$. As in the case of the cylindrical shell, no explicit boundary conditions are posed on the circumferential function $\Theta(\vartheta)$, except the fact that the acoustic pressure and the slope of the acoustic pressure be continuous with the circumferential angle. Thus solution to equations (3.115c) are of the form

$$\Theta(\vartheta) = \cos(n_2 \vartheta) + \sin(n_2 \vartheta), \tag{3.121}$$

where, due to the periodicity of the boundary condition, the circumferential modal indices assumes integers values, $n_2 = 0, 1, 2, \ldots$.

Equation (3.115d) can be rewritten in the more common form as

$$r^2 \frac{\mathrm{d}^2 \mathcal{R}}{\mathrm{d}r^2} + r \frac{\mathrm{d}\mathcal{R}}{\mathrm{d}r} + \left(k_{\vartheta,r}^2 r^2 - n_2^2 \right) \mathcal{R} = 0. \tag{3.122}$$

This equation for $\mathcal{R}(r)$ represent the Bessels's equation [129, 132], which, for each integer value of n_2, has two linearly independent solutions, the integer-order Bessel functions of the first and second kinds, also referred as Bessel functions, $J_{n_2}(k_{\vartheta,r} r)$, and Neumann functions, $Y_{n_2}(k_{\vartheta,r} r)$, where the subscript indicates the integer value of m_2 in the Bessel's equation (3.122). Since the Bessel functions of the second kind, $Y_{n_2}((k_{\vartheta,r} r)$, assume an infinite value for $r \to 0$, $Y_{n_2}(0) = -\infty$, [133, 134], this set of solutions must be neglect in order to obtain a solution which is continue at $r = 0$. In order to satisfy the rigid walled boundary condition given by equation (3.118), the argument of the Bessel function of the first kind must be such as:

$$\left. \frac{\mathrm{d}\mathcal{R}(r)}{\mathrm{d}r} \right|_{r=R} = \left. \frac{\mathrm{d}J_{m_2}(k_{\vartheta,r} r)}{\mathrm{d}r} \right|_{r=R} = 0. \tag{3.123}$$

The value of $\lambda_{n_2 n_3} = k_{\vartheta,r} R$, which is the $(n_3 + 1)$-th extremum of the n_2-th Bessel function of the first kind is generally tabulated and an expression is only available for the asymptotic values. Some of these values are reported in appendix A, where the Bessel functions of the first orders are also shown. The coupled circumferential-radial wavenumber can thus be expressed as

$$k_{\vartheta,r} = \frac{\lambda_{n_2 n_3}}{R} \tag{3.124}$$

and the radial function can be written as

$$\mathcal{R}(r) = J_{n_2}(k_{\vartheta,r} r). \tag{3.125}$$

The general solution of equation (3.115a) is of the form

$$g(t) = e^{j\omega t}, \tag{3.126}$$

yielding to the fact that the pressure oscillations can only be harmonic in absence of external sources. Substituting equations (3.120) and (3.124) into equa-

tion (3.116), the acoustic natural angular frequency can be expressed in terms of the modal indices n_1, n_2 and n_3 as [128–130]:

$$\omega_{a,n} = \sqrt{c_0^2 \left[\left(\frac{n_1 \pi}{L} \right)^2 + \left(\frac{\lambda_{n_2 n_3}}{R} \right)^2 \right]}, \tag{3.127}$$

where the subscript n indicates the combination of the three modal indices (n_1, n_2, n_3). Figure 3.10 shows the variation of the acoustic natural frequency with the circumferential index n_2 for different values of the axial index n_1 with $n_3 = 0$ plot (a), $n_3 = 1$ plot (b) and $n_3 = 2$ plot (c). From these plot it can be seen that the acoustic natural frequency $f_{a,n}$, obtained dividing the angular frequency $\omega_{a,n}$ in equation (3.127) by 2π, has an increasing behaviour as each of the modal indices increases. The lowest frequency corresponds to the case in which all the three modal indices are zero, and it assumes a value equal to zero. This particular mode is referred as compliant mode [23].

Another common representation of the variation of the acoustic natural frequency $f_{a,n}$ is shown in Figure 3.10 (d) where the iso-f_a lines (thick black lines) are plotted in the acoustic k-space. Despite the acoustic domain is a three-dimensional, due to the coupling between the radial and circumferential wavenumbers, the acoustic wavaspace for the cylindrical acoustic enclosure is a two-dimensional [131, 132, 135]. From equation (3.116), the iso-f_a curves in the k-space, whose coordinates are the acoustic axial wavenumber k_x and the coupled circumferential - radial wavenumber $k_{\vartheta, r}$, assume the form of quarters of circles.

Combining together the expressions given by equations (3.119), (3.121) and (3.125), the expression for the acoustic mode shapes can be derived. As in the case of the flexural displacements of the cylindrical shell, due to the circumferential symmetry of the cylindrical domain, the acoustic mode shapes can be written in terms of a symmetric and an anti-symmetric component [28, 128, 129]:

$$\psi_n^s(\mathbf{x}) = \cos\left(\frac{n_1 \pi}{L} x \right) \cos\left(n_2 \vartheta \right) J_{n_2}\left(\frac{\lambda_{n_2 n_3}}{R} r \right) \quad \text{and} \tag{3.128a}$$

$$\psi_n^a(\mathbf{x}) = \cos\left(\frac{n_1 \pi}{L} x \right) \sin\left(n_2 \vartheta \right) J_{n_2}\left(\frac{\lambda_{n_2 n_3}}{R} r \right). \tag{3.128b}$$

The presence of two modal shape components for each combination of the triplet of acoustic modal indices (n_1, n_2, n_3), yields to a twofold degeneracy of the acoustic modes [132], which is necessary to describe a general acoustic field in the cylindrical domain, which can have any arbitrary angular orientation, as will be discussed in section 3.7.4.
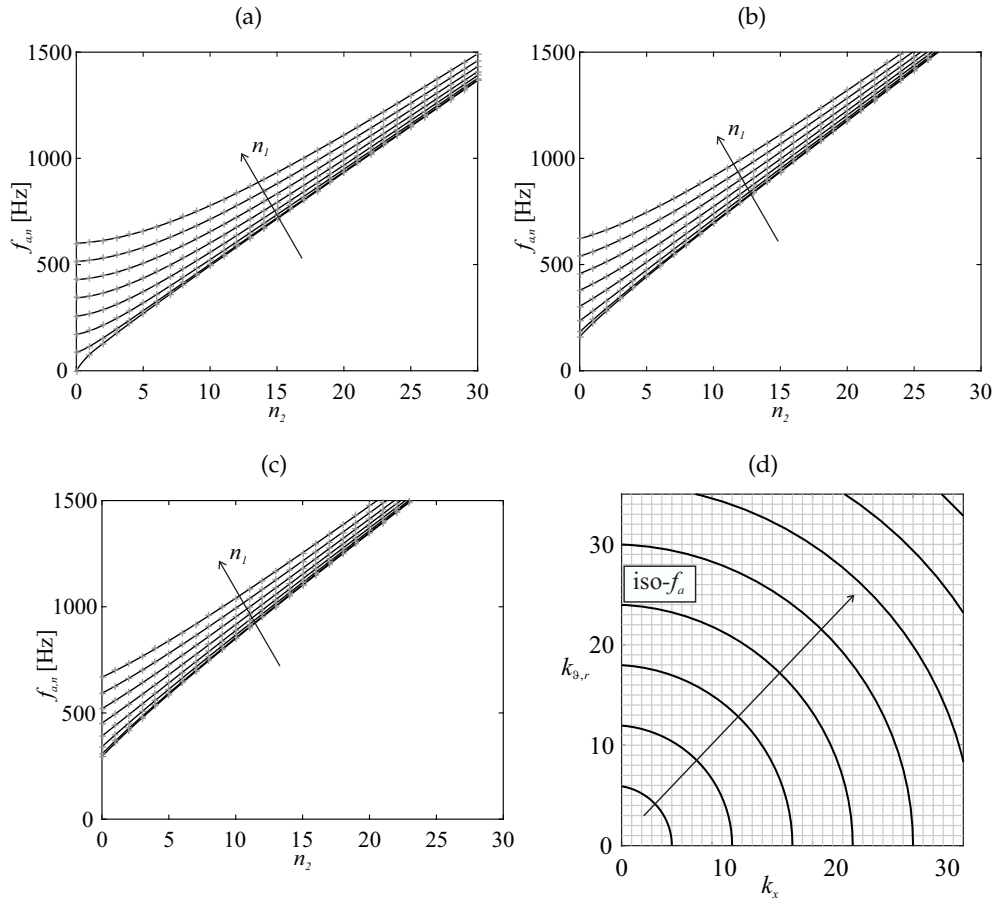
Figure 3.10: Variation of the acoustic natural frequency $f_{a,n}$ with the circumferential index n_2 for different values of the axial index n_1 for fixed value of the radial index, $n_3 = 0$ (a), $n_3 = 1$ (b), $n_3 = 2$ (c) and wavenumber diagram of the $k-$space with the modal lattice (light grey rectangular grid) and iso-f_a curves (black lines) (d).

Figure 3.11 shows some of the acoustic mode shapes given by equation (3.128), in particular in plot (a) is shown the $(0,0,0)$ (compliant) mode, in plot (b) is shown the $(1,0,0)$ mode, in plot (c) the $(0,1,0)$ mode, in plot (d) the $(0,0,1)$ mode, in plot (e) the $(3,1,1)$ mode and finally in plot (f) the $(3,1,3)$ acoustic mode. In each plot the image represents the symmetric component and the right image represents the anti-symmetric component. From the analysis of these plots it can be seen that when the circumferential index n_2 is zero, the anti-symmetric component of the mode is everywhere zero in the acoustic domain. This is a reasonable result since when the circumferential index is zero, the acoustic pressure does not present any variation along the circumferential direction, thus the symmetric component is sufficient to completely describe the acoustic field.
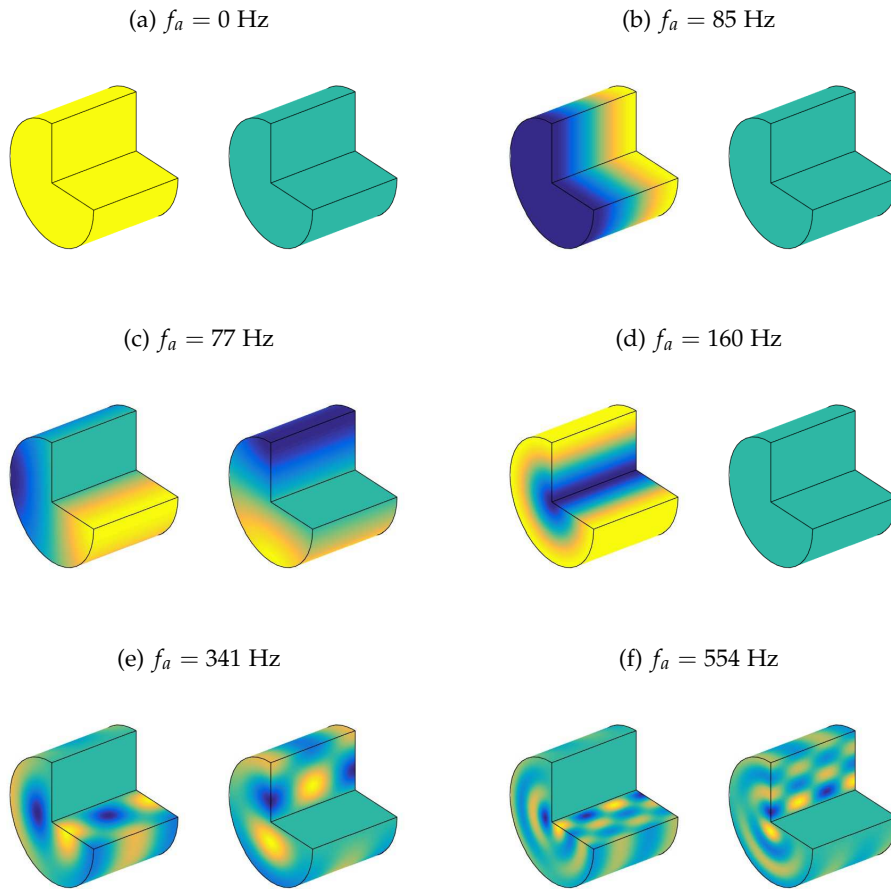
Figure 3.11: Axonometric view of the symmetric (left hand side) and anti-symmetric (right hand side) components of the acoustic mode shape $(0,0,0)$ (a), $(1,0,0)$ (b), $(0,1,0)$ (c), $(0,0,1)$ (d), $(3,1,1)$ (e), $(3,1,3)$ (f).

In figure 3.12 is shown the nodal pattern for the symmetric component (upper images) and for the anti-symmetric component (bottom images) of the acoustic mode shape $(1,3,2)$. From this figure it can be easily deduced the relationship between the acoustic modal index and the number of nodal lines in the three directions, in particular:

- the axial index n_1 corresponds to the number of axial nodal lines;

- the circumferential index n_2 corresponds to the number of nodal lines in the circumferential directions;

- the radial index n_3 indicates the number of radial nodal lines.

Alternatively, the acoustic modal indices can be related to the wavenumbers in the three directions as

- the axial index n_1 represents the number of axial half-wavelengths;

- the circumferential index n_2 represents to the number of wavelengths in the circumferential directions;

- the radial index n_3 indicates the number of radial half-wavelengths, at which one-fourth radial wavelength must be summed.
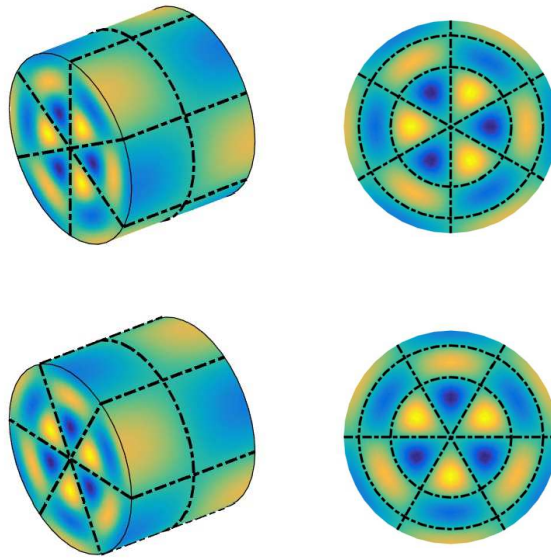
Figure 3.12: Nodal pattern for the symmetric (top plots) and for the anti-symmetric component (bottom plots) of the acoustic mode shape $(1, 3, 2)$.

It is interesting to note that the nodal positions in the axial and radial directions correspond for the two components, while a nodal position in the circumferential direction correspond an anti-nodal position for the other component. The positions of the nodal and anti-nodal points for the cylindrical enclosure are reported in table 3.2, where $\gamma_{n_2\delta}$ is the δ-th zero of the first kind Bessel function of order n_2, such that $J_{n_2}(\gamma_{n_2\delta}) = 0$.

A final consideration about the acoustic mode shapes regards the classification of the mode shapes [131]. Apart from the complaint mode and the axial modes, which have only axial dependence, it is not possible to separate the modes into purely axial and tangential modes, due to the coupling between the radial and the circumferential directions. This can be particular appreciated considering again figure 3.11 (c), which presents the mode with the only circumferential index different than zero. According to the classical classification

Table 3.2: Nodal and anti-nodal positions for the cylindrical enclosure.

Direction		Symmetric component	Anti-symmetric component
Axial	nodal	$\dfrac{L}{2n_1} + \alpha_1 \dfrac{L}{n_1}$	
	anti - nodal	$\alpha_2 \dfrac{L}{n_1}$	
Circumferential	nodal	$\dfrac{\pi}{2n_2} + \beta \dfrac{\pi}{n_2}$	$\beta \dfrac{\pi}{n_2}$
	anti - nodal	$\beta \dfrac{\pi}{n_2}$	$\dfrac{\pi}{2n_2} + \beta \dfrac{\pi}{n_2}$
Radial	nodal	$R \dfrac{\gamma_{n_2 \delta}}{\lambda_{n_2 n_3}}$	
	anti - nodal	$R \dfrac{\lambda_{n_2 \delta}}{\lambda_{n_2 n_3}}$	

where $\alpha_1 = 0, 1, \ldots, n_1 - 1$, $\alpha_2 = 0, 1, \ldots, n_1$, $\beta = 0, 1, \ldots, m_2 - 1$
and $\delta = 0, \ldots, n_3$.

[129, 131], this should be defined a ϑ-axial mode, but it can be clearly seen that the acoustic pressure is not independent of the radial position [132].

3.7 ACOUSTIC MODAL EQUATION OF MOTION

The acoustic pressure at the generic position $\mathbf{x}$ is approximate into the following finite modal summation [28, 30, 99, 129]

$$p(\mathbf{x}, t) = \sum_{n=1}^{N} \psi_n^s(\mathbf{x}) a_n^s(t) + \sum_{n=1}^{N} \psi_n^a(\mathbf{x}) a_n^a(t), \tag{3.129}$$

where $\psi_n^s(\mathbf{x})$ and $\psi_n^a(\mathbf{x})$ are the rigid-walled symmetric and anti-symmetric acoustic natural mode shapes given in equations (3.128), $a_n^s(t)$ and $a_n^a(t)$ are the symmetric and anti-symmetric acoustic modal amplitudes and N is the number of flexural modes considered in the summation. This series expression can be rearranged in the following matrix form:

$$p(\mathbf{x}, t) = \begin{bmatrix} \boldsymbol{\psi}^s(\mathbf{x}) & \boldsymbol{\psi}^a(\mathbf{x}) \end{bmatrix} \begin{Bmatrix} \mathbf{a}^s(t) \\ \mathbf{a}^a(t) \end{Bmatrix} = \boldsymbol{\psi}(\mathbf{x}) \mathbf{a}(t), \tag{3.130}$$

where $\boldsymbol{\psi}^s(\mathbf{x})$ and $\boldsymbol{\psi}^a(\mathbf{x})$ are the $1 \times N$ row vectors with the symmetric and anti-symmetric acoustic natural modes, $\boldsymbol{\psi}(\mathbf{x}) = \begin{bmatrix} \boldsymbol{\psi}^s(\mathbf{x}) & \boldsymbol{\psi}^a(\mathbf{x}) \end{bmatrix}$ is the $1 \times 2N$ vector of the acoustic modes, $\mathbf{a}^s(t)$ and $\mathbf{a}^a(t)$ are the column vectors with the symmetric and anti-symmetric acoustic modal amplitudes whose dimensions are $N \times 1$

and finally $\mathbf{a}(t) = \begin{bmatrix} \mathbf{a}^{s\,T}(t) & \mathbf{a}^{a\,T}(t) \end{bmatrix}^T$ is the $2N \times 1$ vector of the acoustic modal amplitudes.

Substituting the modal summation given in equation (3.130) into the three-dimensional wave equation (3.110) yields to

$$\nabla^2 \boldsymbol{\psi}(\mathbf{x})\mathbf{a}(t) - \frac{1}{c^2}\boldsymbol{\psi}(\mathbf{x})\ddot{\mathbf{a}}(t) = -\rho_0 \frac{\partial q(\mathbf{x},t)}{\partial t}. \tag{3.131}$$

From the analysis presented in section 3.6, the acoustic natural modes satisfy the following eigenvalue-eigenvector relation:

$$\nabla^2 \boldsymbol{\psi}(\mathbf{x}) = -\frac{1}{c_0^2}\boldsymbol{\psi}(\mathbf{x})\boldsymbol{\Omega}_a^2, \tag{3.132}$$

where $\boldsymbol{\Omega}_a$ is the $2N \times 2N$ diagonal matrix of the acoustic natural frequencies whose diagonal elements are given by

$$\Omega_{a,(n,n)} = \Omega_{a,(n+N,n+N)} = \omega_{a,n}, \tag{3.133}$$

where $n = 1, 2, \ldots, N$ and $\omega_{a,n}$ is the acoustic natural frequency given in equation (3.127). Thus equation (3.131) can be rewritten as

$$\boldsymbol{\psi}(\mathbf{x})\ddot{\mathbf{a}}(t) + \boldsymbol{\psi}(\mathbf{x})\boldsymbol{\Omega}_a^2\mathbf{a}(t) = \rho_0 c_0^2 \dot{q}(\mathbf{x},t), \tag{3.134}$$

where $\dot{}$ and $\ddot{}$ indicate the first and the second time derivative, respectively. Assuming a viscous damping, the energy dissipation can be modelled as a term proportional to the time derivative of the acoustic pressure [23, 99], thus:

$$\boldsymbol{\psi}(\mathbf{x})\ddot{\mathbf{a}}(t) + \boldsymbol{\psi}(\mathbf{x})\mathbf{d}\dot{\mathbf{a}}(t) + \boldsymbol{\psi}(\mathbf{x})\boldsymbol{\Omega}_a^2\mathbf{a}(t) = \rho_0 c_0^2 \frac{\partial q(\mathbf{x},t)}{\partial t}, \tag{3.135}$$

where $\mathbf{d}$ is a $2N \times 2N$ diagonal matrix whose diagonal elements are the equivalent acoustical damping terms given by:

$$d_{(n,n)} = d_{(n+N,n+N)} = 2\zeta_0\,\omega_{a,n}, \tag{3.136}$$

where ζ_0 is the acoustic modal damping ratio given in table 2.1, which is assumed equal for all the acoustic modes [28, 64, 99]. Pre-multiplying both sides of equation (3.135) by the column vector with the acoustic mode shapes $\boldsymbol{\psi}^T(\mathbf{x})$

and integrating over the acoustic volume of the cylindrical enclosure lead to the following matrix equation:

$$\mathbf{Q}\ddot{\mathbf{a}}(t) + \mathbf{D}\dot{\mathbf{a}}(t) + \mathbf{H}\mathbf{a}(t) = \mathbf{\Psi}\dot{\mathbf{q}}(t), \tag{3.137}$$

where $\mathbf{Q}$, $\mathbf{D}$ and $\mathbf{H}$ are the $2M \times 2M$ diagonal acoustic modal inertia, damping and stiffness matrices [99], given by:

$$\mathbf{Q} = \int_{V_c} \boldsymbol{\psi}^T(\mathbf{x})\boldsymbol{\psi}(\mathbf{x})\, dV = V_c\mathbf{\Gamma}, \tag{3.138a}$$

$$\mathbf{D} = \int_{V_c} \boldsymbol{\psi}^T(\mathbf{x})\boldsymbol{\psi}(\mathbf{x})\mathbf{d}\, dV = 2\zeta_0 V_c\mathbf{\Omega}_a\mathbf{\Gamma} \quad \text{and} \tag{3.138b}$$

$$\mathbf{H} = \int_{V_c} \boldsymbol{\psi}^T(\mathbf{x})\boldsymbol{\psi}(\mathbf{x})\mathbf{\Omega}_a^2\, dV = \mathbf{Q}\mathbf{\Omega}_a^2, \tag{3.138c}$$

where V_c is the volume of the cylindrical enclosure and $\mathbf{\Gamma}$ is the $2N \times 2N$ diagonal matrix of the acoustic normalization coefficient whose elements are derived in appendix A. Also, $\mathbf{\Psi}$ and $\dot{\mathbf{q}}(t)$ are the modal source matrix and the source vector.

3.7.1 Acoustic source field

The source distribution presented here will be considered only in this section since, as will be described in section 3.8, in the remaining of this thesis the only excitation source for the acoustic domain will be flexural displacement of the cylindrical shell.

In order to obtain the most general response of the acoustic domain, the source distribution considered is of the rain on the roof type [28], which is a modelled with an array of 27 point force (equally distributed in three axial, three circumferential and three radial positions). The source term in equation (3.110) can thus be expressed as

$$q(\mathbf{x}, t) = \sum_{k=1}^{N_s} q_k(t)\delta(\mathbf{x} - \mathbf{x}_k), \tag{3.139}$$

where $q_k(t)$ is the time-dependent amplitude of the k-th rain on the roof point source, N_s is the number of sources considered and $\delta(\mathbf{x} - \mathbf{x}_k)$ is the three-dimensional Dirac delta function given by [23]

$$\delta(\mathbf{x} - \mathbf{x}_k) = \delta(x - x_k)\frac{1}{R}\delta(\vartheta - \vartheta_k)\delta(r - r_k) \tag{3.140}$$

at the position $\mathbf{x}_k = (x_k, \vartheta_k, r_k)$ where the k-th point source is placed. Premultiplying the right hand side of equation (3.135), given the expression (3.139), the modal source matrix results in $2N \times N_s$ matrix whose columns are the acoustic natural mode shapes evaluated at the source position, multiplied by the fluid density and the speed of sound at the second power,

$$\Psi_{(n,k)} = \rho_0 c_0^2 \psi_n^s(\mathbf{x}_k) \quad \text{and} \tag{3.141a}$$

$$\Psi_{(n+N,k)} = \rho_0 c_0^2 \psi_n^a(\mathbf{x}_k), \tag{3.141b}$$

where $n = 1, 2, \ldots, N$. The $N_s \times 1$ column vector $\dot{\mathbf{q}}(t)$ is composed by the time-dependent amplitudes of the N_s point sources $q_k(t)$, with $k = 1, 2, \ldots, N_s$.

3.7.2 *Frequency analysis of the acoustic response*

Expressing the time-harmonic functions as in equation (3.68), the time-dependent equation (3.137) can be expressed in the frequency domain as:

$$\left[-\omega^2 \mathbf{Q} + j\omega \mathbf{D} + \mathbf{H} \right] \mathbf{a}(\omega) = j\omega \Psi \mathbf{q}(\omega), \tag{3.142}$$

where $\mathbf{a}(\omega)$ and $\mathbf{q}(\omega)$ are the column vectors of the frequency-dependent complex amplitudes of the time-harmonic acoustic modal pressures and excitation sources.

The overall sound field in the acoustic enclosure can be established in terms of the Power Spectral Density of the total acoustic potential energy [28, 60, 64, 65], which, for brevity, will be referred as acoustic potential energy PSD, defined as:

$$S_P(\omega) = \frac{1}{2\rho_0 c_0^2} \int_{V_c} \lim_{T \to \infty} E\left[\frac{1}{T} p^*(\mathbf{x}, \omega) p(\mathbf{x}, \omega) \right] dV, \tag{3.143}$$

where, as in section 3.4.2, $E[\cdot]$ is the expectation operator, the superscript * indicates the complex conjugate operator and $p(\mathbf{x}, \omega)$ is the frequency-dependent amplitude of the acoustic pressure in the point $\mathbf{x}$ which, from equation (3.130), can be expressed as

$$p(\mathbf{x}, \omega) = \boldsymbol{\psi}(\mathbf{x}) \mathbf{a}(\omega). \tag{3.144}$$

The vector of the frequency-dependent complex amplitude of the time-harmonic acoustic modal pressures $\mathbf{a}(\omega)$ is given by equation (3.142) as

$$\mathbf{a}(\omega) = j\omega \mathbf{A}(\omega) \Psi \mathbf{q}(\omega). \tag{3.145}$$

Here $\mathbf{A} = \left[-\omega^2\mathbf{Q} + j\omega\mathbf{D} + \mathbf{H}\right]^{-1}$ is the acoustic modal admittance matrix [28, 127]. The PSD function in equation (3.143) can be rewritten as:

$$
\begin{aligned}
S_P(\omega) &= \frac{1}{2\rho_0 c_0^2}\int_{V_c}\lim_{T\to\infty} E\left[\frac{1}{T}\mathbf{a}^H(\omega)\boldsymbol{\psi}^T(\mathbf{x})\boldsymbol{\psi}(\mathbf{x})\mathbf{a}(\omega)\right]\,\mathrm{d}V \\
&= -\frac{\omega^2}{2\rho_0 c_0^2}\int_{V_c}\lim_{T\to\infty} E\left[\frac{1}{T}\mathbf{q}^T(\omega)\boldsymbol{\Psi}^T\mathbf{A}^H(\omega)\boldsymbol{\psi}^T(\mathbf{x})\boldsymbol{\psi}(\mathbf{x})\mathbf{A}(\omega)\boldsymbol{\Psi}\mathbf{q}(\omega)\right]\,\mathrm{d}V \\
&= -\omega^2\frac{V_c}{2\rho_0 c_0^2}\,\mathrm{Tr}\left[\mathbf{S_{aa}}(\omega)\right],
\end{aligned}
$$

(3.146)

where $\mathbf{S_{aa}}(\omega)$ is the fully populated matrix with the PSDs of the modal pressure amplitudes which, after some mathematical manipulations, result given by:

$$
\begin{aligned}
\mathbf{S_{aa}}(\omega) &= \lim_{T\to\infty} E\left[\boldsymbol{\Gamma}\mathbf{A}(\omega)\boldsymbol{\Psi}\mathbf{q}(\omega)\mathbf{q}^T(\omega)\boldsymbol{\Psi}^T\mathbf{A}^H(\omega)\right] \\
&= \boldsymbol{\Gamma}\mathbf{A}(\omega)\boldsymbol{\Psi}\mathbf{S_{qq}}(\omega)\boldsymbol{\Psi}^T\mathbf{A}^H(\omega),
\end{aligned}
$$

(3.147)

where $\mathbf{S_{qq}}(\omega)$ is the $N_s \times N_s$ matrix with the PSD of the rain on the roof monopole sources, which, in analogy with references [64, 72] is assumed to be an identity matrix:

$$
\mathbf{S_{qq}}(\omega) = \lim_{T\to\infty} E\left[\mathbf{q}(\omega)\mathbf{q}^T(\omega)\right] \equiv \mathbf{I}.
$$

(3.148)

Finally, the PSD of the acoustic potential energy is given by:

$$
S_P(\omega) = -\omega^2\frac{V_c}{2\rho_0 c_0^2}\,\mathrm{Tr}\left[\boldsymbol{\Gamma}\mathbf{A}(\omega)\boldsymbol{\Psi}\mathbf{S_{qq}}(\omega)\boldsymbol{\Psi}^T\mathbf{A}^H(\omega)\right].
$$

(3.149)

As for the case of the PSD of the flexural kinetic energy, which can be expressed as the sum of two terms due to the fact that the flexural displacements can be as well expressed as the sum of two components, also the PSD of the acoustic potential energy can be expressed as the sum of two terms, the former related with the symmetric and the latter related with the anti-symmetric component of the acoustic pressure:

$$
S_P(\omega) = S_P^s(\omega) + S_P^a(\omega),
$$

(3.150)

where the two terms are defined as:

$$S_P^s(\omega) = \frac{1}{2\rho_0 c_0^2} \int_{V_c} \lim_{T \to \infty} E\left[\frac{1}{T}p^{s*}(\mathbf{x},\omega)p^s(\mathbf{x},\omega)\right] \mathrm{d}V \quad \text{and} \tag{3.151a}$$

$$S_P^a(\omega) = \frac{1}{2\rho_0 c_0^2} \int_{V_c} \lim_{T \to \infty} E\left[\frac{1}{T}p^{a*}(\mathbf{x},\omega)p^a(\mathbf{x},\omega)\right] \mathrm{d}V. \tag{3.151b}$$

Following the same mathematical manipulation procedure which leads to equation (3.149), the PSDs related to the two components of the acoustic pressure can be expressed as:

$$S_P^s(\omega) = -\omega^2 \frac{V_c}{2\rho_0 c_0^2}\mathrm{Tr}\left[\boldsymbol{\alpha}^s \Gamma \mathbf{A}(\omega)\boldsymbol{\Psi}\mathbf{S}_{\mathbf{qq}}(\omega)\boldsymbol{\Psi}^T \mathbf{A}^H(\omega)\boldsymbol{\alpha}^{sT}\right] \quad \text{and} \tag{3.152a}$$

$$S_P^a(\omega) = -\omega^2 \frac{V_c}{2\rho_0 c_0^2}\mathrm{Tr}\left[\boldsymbol{\alpha}^a \Gamma \mathbf{A}(\omega)\boldsymbol{\Psi}\mathbf{S}_{\mathbf{qq}}(\omega)\boldsymbol{\Psi}^T \mathbf{A}^H(\omega)\boldsymbol{\alpha}^{aT}\right], \tag{3.152b}$$

where $\boldsymbol{\alpha}^s$ and $\boldsymbol{\alpha}^a$ are the $N \times 2N$ matrices given by:

$$\boldsymbol{\alpha}^s = \begin{bmatrix} \mathbf{I}_{N \times N} & \mathbf{0}_{N \times N} \end{bmatrix} \quad \text{and} \tag{3.153a}$$

$$\boldsymbol{\alpha}^a = \begin{bmatrix} \mathbf{0}_{N \times N} & \mathbf{I}_{N \times N} \end{bmatrix}, \tag{3.153b}$$

being $\mathbf{I}_{N \times N}$ and $\mathbf{0}_{N \times N}$ the $N \times N$ identity and zero matrices, respectively.

3.7.3 *Simulation results*

Figure 3.13 the 20-100 Hz spectra of the acoustic potential energy PSD of the cylindrical enclosure, when only the symmetric component is considered (plot (a)), when the anti-symmetric component is considered (plot (b)) and when the total response is considered (plot (c)). In the frequency range considered the acoustic enclosure is characterised by three natural frequency, the first due to the compliant mode. The acoustic response is thus characterised by a resonant peak at frequency close to zero. Comparing plots (a) and (b), the response related to the anti-symmetric component presents just one resonant peak, while the response related to the symmetric component presents three resonant peaks, related to the three resonant frequencies of the enclosure. This is due to the fact that the first (compliant) and the third resonant modes are characterised by a circumferential index which is equal to zero. Due to the value of the modal damping ratio chosen, ζ_0, the resonant peaks are particularly smooth. The results are expressed in decibels, where the reference value

is considered 1 J s, since the rain on the roof sources are assumed to have unity amplitude, equation (3.148), and their dimensions are $[s^{-1}]$.

(a)

(b)

(c)
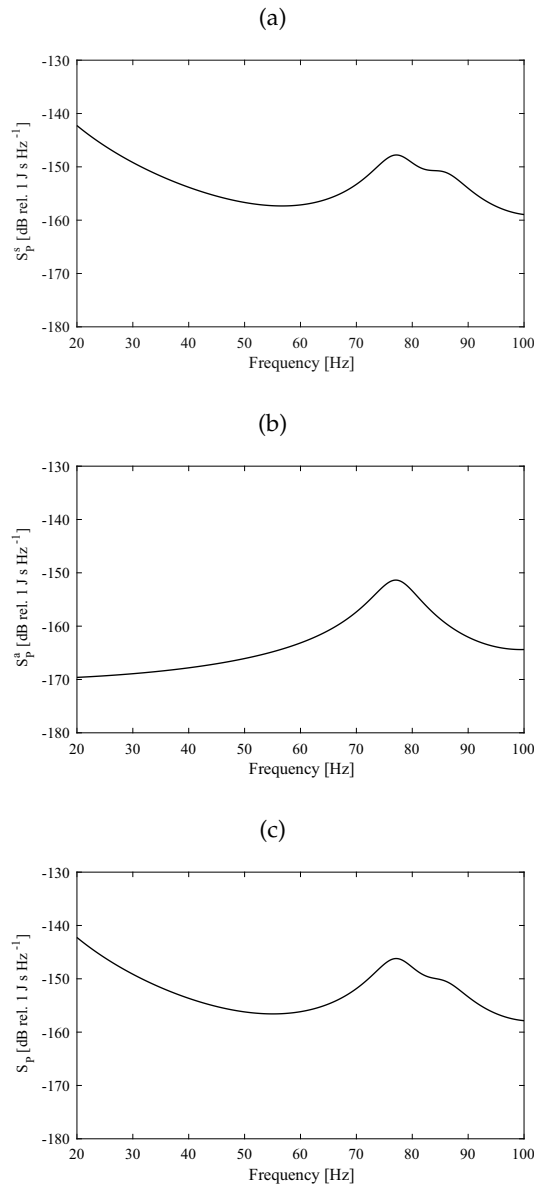
Figure 3.13: Spectra of the acoustic potential energy PSD due to the symmetric component (a), the anti-symmetric component (b) and the total response, which considers both components (c).

3.7.4 *Effects of the spatial distribution of the source field*

In analogy of the circumferential orientation of the flexural displacement due to the excitation field presented in section 3.4.4, in this section the effect of

the spatial distribution of the acoustic sources on the spatial orientation of the acoustic domain is presented. The acoustic pressure considering just the $\tilde{n}$-th acoustic mode shapes in equation (3.129), $\tilde{p}(\mathbf{x}, t)$, can be expressed as

$$\tilde{p}(\mathbf{x}, t) = \psi_{\tilde{n}}^s(\mathbf{x}) a_{\tilde{n}}^s(t) + \psi_{\tilde{n}}^a(\mathbf{x}) a_{\tilde{n}}^a(t). \tag{3.154}$$

If a single point source acting at position $\mathbf{x}_q = \left(x_q, \vartheta_q, r_q \right)$ is considered, the matrix equation (3.142) can be rewritten as two uncoupled equations related to the symmetric and anti-symmetric component of the acoustic pressure:

$$\left(-\omega^2 Q_{\tilde{n}}^s + j\omega D_{\tilde{n}}^s + H_{\tilde{n}}^s \right) a_{\tilde{n}}^s(\omega) = j\omega \rho_0 c_0^2 \psi_{\tilde{n}}^s(\mathbf{x}_q) q(\omega) \tag{3.155a}$$

$$\left(-\omega^2 Q_{\tilde{n}}^a + j\omega D_{\tilde{n}}^a + H_{\tilde{n}}^a \right) a_{\tilde{n}}^a(\omega) = j\omega \rho_0 c_0^2 \psi_{\tilde{n}}^a(\mathbf{x}_q) q(\omega) \tag{3.155b}$$

where $Q_{\tilde{n}}^s$, $D_{\tilde{n}}^s$, $H_{\tilde{n}}^s$ and $Q_{\tilde{n}}^a$, $D_{\tilde{n}}^a$, $H_{\tilde{n}}^a$ are respectively the $(\tilde{n}, \tilde{n})$ and the $(\tilde{n} + N, \tilde{n} + N)$ elements of the modal acoustic inertia, damping and stiffness matrices given in equations (3.138). Assuming that the circumferential index n_2 is different than zero, as shown in appendix A, each symmetric term corresponds to the the anti-symmetric one. Thus the following terms can be defined:

$$\tilde{Q} = Q_{\tilde{n}}^s = Q_{\tilde{n}}^a, \tag{3.156a}$$

$$\tilde{D} = D_{\tilde{n}}^s = D_{\tilde{n}}^a, \tag{3.156b}$$

$$\tilde{H} = H_{\tilde{n}}^s = H_{\tilde{n}}^a \quad \text{and} \tag{3.156c}$$

$$\tilde{\alpha}(\omega) = -\omega^2 \tilde{Q} + j\omega \tilde{D} + \tilde{H}. \tag{3.156d}$$

Defining for brevity $\beta(\omega) = \rho_0 c_0^2 q(\omega)$, the solutions of equations (3.155) are of the form:

$$a_{\tilde{n}}^s(\omega) = \frac{j\omega \psi_{\tilde{n}}^s(\mathbf{x}_q) \beta(\omega)}{\tilde{\alpha}(\omega)} \quad \text{and} \tag{3.157a}$$

$$a_{\tilde{n}}^a(\omega) = \frac{j\omega \psi_{\tilde{n}}^a(\mathbf{x}_q) \beta(\omega)}{\tilde{\alpha}(\omega)}, \tag{3.157b}$$

and the acoustic pressure due to the $\tilde{n}$-th mode results:

$$\begin{aligned}
\tilde{p}(\mathbf{x}, \omega) &= \frac{j\omega \psi_{\tilde{n}}^s(\mathbf{x}) \psi_{\tilde{n}}^s(\mathbf{x}_q) \beta(\omega)}{\tilde{\alpha}(\omega)} + \frac{j\omega \psi_{\tilde{n}}^a(\mathbf{x}) \psi_{\tilde{n}}^a(\mathbf{x}_q) \beta(\omega)}{\tilde{\alpha}(\omega)} \\
&= \frac{j\omega \beta(\omega)}{\tilde{\alpha}(\omega)} \left[\psi_{\tilde{n}}^s(\mathbf{x}) \psi_{\tilde{n}}^s(\mathbf{x}_q) + \psi_{\tilde{n}}^a(\mathbf{x}) \psi_{\tilde{n}}^a(\mathbf{x}_q) \right].
\end{aligned} \tag{3.158}$$

Expressing the acoustic mode shapes in the explicit manner given in equations (3.128) , the acoustic pressure can be written as:

$$\tilde{p}(\mathbf{x}, \omega) = \frac{j\omega\beta(\omega)}{\tilde{\alpha}(\omega)} \cos\left(\frac{\tilde{n}_1\pi}{L}x\right) \cos\left(\frac{\tilde{n}_1\pi}{L}x_q\right) J_{\tilde{n}_2}\left(\frac{\lambda_{\tilde{n}_2\tilde{n}_3}}{R}r\right) J_{\tilde{n}_2}\left(\frac{\lambda_{\tilde{n}_2\tilde{n}_3}}{R}r_q\right) \cdot$$
$$\left[\cos(\tilde{n}_2\vartheta)\cos(\tilde{n}_2\vartheta_q) + \sin(\tilde{n}_2\vartheta)\sin(\tilde{n}_2\vartheta_q)\right]. \tag{3.159}$$

Recalling the trigonometric identity (3.90), the acoustic pressure due to the $\tilde{n}$-th acoustic mode shape can be expressed as

$$\tilde{p}(\mathbf{x}, \omega) = \frac{j\omega\beta(\omega)}{\tilde{\alpha}(\omega)} \cos\left(\frac{\tilde{n}_1\pi}{L}x\right) \cos\left(\frac{\tilde{n}_1\pi}{L}x_q\right) \cdot$$
$$J_{\tilde{n}_2}\left(\frac{\lambda_{\tilde{n}_2\tilde{n}_3}}{R}r\right) J_{\tilde{n}_2}\left(\frac{\lambda_{\tilde{n}_2\tilde{n}_3}}{R}r_q\right) \cos\left[\tilde{n}_2\left(\vartheta - \vartheta_q\right)\right]. \tag{3.160}$$

Equation (3.160) proves that each acoustic mode shape orients itself such that it presents an anti-nodal position at an orientation which corresponds to the orientation of the source. The angular positions of the nodal and anti-nodal lines can be thus be expressed with reference to the orientation of the source ϑ_q as

$$\vartheta_N = \vartheta_q + \alpha\frac{\pi}{n_2} \quad \text{and} \tag{3.161a}$$

$$\vartheta_{AN} = \vartheta_q + \frac{\pi}{2n_2} + \alpha\frac{\pi}{n_2}, \tag{3.161b}$$

where the subscripts $_N$ and $_{AN}$ identify the nodal and anti-nodal angular coordinate and α is an integer such that $\alpha = 0, 1, \ldots, 2n_2 - 1$.

Figure 3.14 shows the acoustics pressure distribution of $(1, 1, 1)$ mode, plot (a), and of $(1, 2, 2)$ mode, plot (b), at the base of the cylindrical enclose when a single monopole source (indicated with red circle) is considered. The dash-dotted lines are oriented as the sources, which are at an angular coordinate equals to $\pi/6$ for the case considered in plot (a) and $3\pi/8$ for the case considered in plot (b). The orientation of the symmetric and anti-symmetric components of the acoustic mode, left graphs and central graphs respectively, are not dependent on the source orientation, indeed present nodal and anti-nodal circumferential positions as given in table 3.2. The source position influence the amplitude of the components, which is represented by the intensity of the colours. The total response, given by the sum of the two components and shown in the right graphs, is instead oriented as the source, presenting nodal and anti-nodal circumferential positions at the angles given by equations (3.161).

(a)

(b)
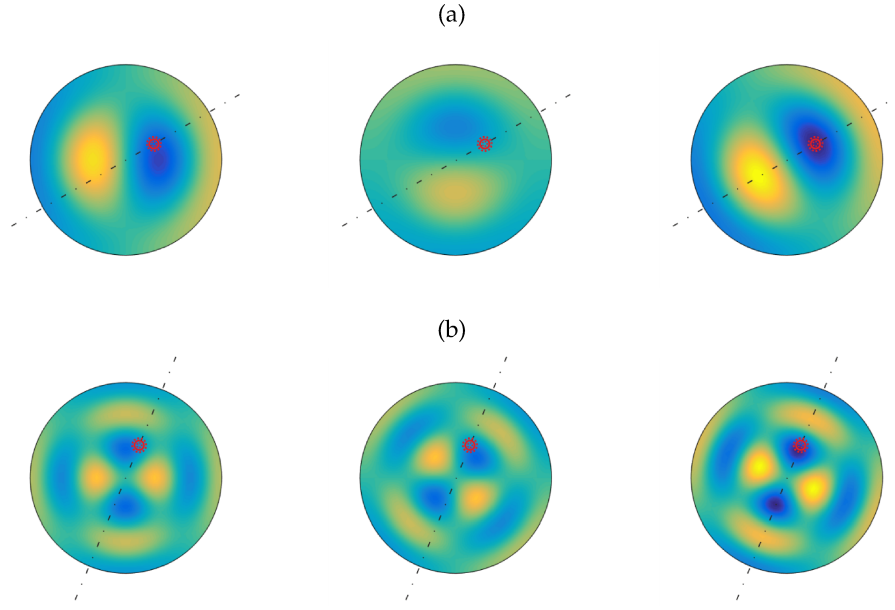
Figure 3.14: Orientation of the symmetric component (left graphs), anti-symmetric component (central graphs) and total acoustic pressure (right graphs) at the base of the cylindrical enclosure of the $(1,1,1)$ mode shape (plot (a)) and of the $(1,2,2)$ mode shape (plot (b)) when a single source is considered.

If two point monopole sources are considered to act in the acoustic enclosure, the modal amplitudes of the two components of the acoustic pressure can be obtained as:

$$a_{\tilde{n}}^s(\omega) = \frac{j\omega\psi_{\tilde{n}}^s(\mathbf{x}_{q1})\beta_1(\omega)}{\tilde{\alpha}(\omega)} + \frac{j\omega\psi_{\tilde{n}}^s(\mathbf{x}_{q2})\beta_2(\omega)}{\tilde{\alpha}(\omega)} \quad \text{and} \tag{3.162a}$$

$$a_{\tilde{n}}^a(\omega) = \frac{j\omega\psi_{\tilde{n}}^a(\mathbf{x}_{q1})\beta_1(\omega)}{\tilde{\alpha}(\omega)} + \frac{j\omega\psi_{\tilde{n}}^a(\mathbf{x}_{q2})\beta_2(\omega)}{\tilde{\alpha}(\omega)}, \tag{3.162b}$$

where $\mathbf{x}_{q1} = (x_{q1}, \vartheta_{q1}, r_{q1})$ and $\mathbf{x}_{q2} = (x_{q2}, \vartheta_{q2}, r_{q2})$ are the points where the two sources are considered to act, $\beta_1(\omega) = \rho_0 c_0^2 q_1(\omega)$ and $\beta_2(\omega) = \rho_0 c_0^2 q_2(\omega)$, being $q_1(\omega)$ and $q_2(\omega)$ the frequency-dependent amplitudes of the two sources.

The acoustic pressure related to the $\tilde{n}$-th acoustic mode shapes results given by:

$$\tilde{p}(\mathbf{x}, \omega) = \frac{j\omega}{\tilde{\alpha}(\omega)} \left\{ \beta_1(\omega) \left[\psi_{\tilde{n}}^s(\mathbf{x})\psi_{\tilde{n}}^s(\mathbf{x}_{q1}) + \psi_{\tilde{n}}^a(\mathbf{x})\psi_{\tilde{n}}^a(\mathbf{x}_{q1}) \right] + \right.$$
$$\left. \beta_2(\omega) \left[\psi_{\tilde{n}}^s(\mathbf{x})\psi_{\tilde{n}}^s(\mathbf{x}_{q2}) + \psi_{\tilde{n}}^a(\mathbf{x})\psi_{\tilde{n}}^a(\mathbf{x}_{q2}) \right] \right\}. \tag{3.163}$$

Expressing the natural mode shapes in the explicit manner given by equation (3.128) and considering the trigonometric identity given in equation (3.90), after

some cumbersome algebraic manipulation, equation (3.163) can be expressed as

$$
\begin{aligned}
\tilde{p}(\mathbf{x}, \omega) = {} & \frac{j\omega}{\tilde{\alpha}(\omega)} \cos\left(\frac{\tilde{n}_1 \pi}{L} x\right) J_{\tilde{n}_2}\left(\frac{\lambda_{\tilde{n}_2 \tilde{n}_3}}{R} r\right) \cdot \\
& \left\{ \beta_1(\omega) \cos\left(\frac{\tilde{n}_1 \pi}{L} x_{q1}\right) J_{\tilde{n}_2}\left(\frac{\lambda_{\tilde{n}_2 \tilde{n}_3}}{R} r_{q1}\right) \cos\left[\tilde{n}_2 \left(\vartheta - \vartheta_{q1}\right)\right] + \right. \\
& \left. \beta_2(\omega) \cos\left(\frac{\tilde{n}_1 \pi}{L} x_{q2}\right) J_{\tilde{n}_2}\left(\frac{\lambda_{\tilde{n}_2 \tilde{n}_3}}{R} r_{q2}\right) \cos\left[\tilde{n}_2 \left(\vartheta - \vartheta_{q2}\right)\right] \right\},
\end{aligned}
\tag{3.164}
$$

where no explicit angular orientation appears, since this depend upon the circumferential position of the sources and also on the axial and radial positions and on the amplitudes. If the two sources are such that:

$$
\beta_1(\omega) \cos\left(\frac{\tilde{n}_1 \pi}{L} x_{q1}\right) J_{\tilde{n}_2}\left(\frac{\lambda_{\tilde{n}_2 \tilde{n}_3}}{R} r_{q1}\right) = \beta_2(\omega) \cos\left(\frac{\tilde{n}_1 \pi}{L} x_{q2}\right) J_{\tilde{n}_2}\left(\frac{\lambda_{\tilde{n}_2 \tilde{n}_3}}{R} r_{q2}\right) = \tilde{c}(\omega),
\tag{3.165}
$$

the acoustic pressure can be expressed as:

$$
\tilde{p}(\mathbf{x}, \omega) = \frac{j\omega \tilde{c}(\omega)}{\tilde{\alpha}(\omega)} \cos\left(\frac{\tilde{n}_1 \pi}{L} x\right) J_{\tilde{n}_2}\left(\frac{\lambda_{\tilde{n}_2 \tilde{n}_3}}{R} r\right) \cos\left[\tilde{n}_2 \frac{\vartheta_{q2} - \vartheta_{q1}}{2}\right] \cos\left[\tilde{n}_2 \left(\vartheta - \frac{\vartheta_{q1} + \vartheta_{q2}}{2}\right)\right].
\tag{3.166}
$$

This equation shows that, when the two sources are such that equation (3.165) is satisfied, the resulting acoustic mode is oriented in a way to present the antinodal position at an orientation which corresponds to the mean orientation of the two sources. These results are graphically presented in figure 3.15, where the acoustic pressure distribution at the base of the cylindrical enclosure is shown. The two sources, represented by the two red circles, are considered in the general case, plot (a), and in the case in which equation (3.165) is satisfied, plot (b). As in the case of a single source, the orientation of the symmetric component (left graphs) and of the anti-symmetric component (central plots) are not affected by the orientation of the two sources, presenting nodal and anti-nodal angular positions given by the values reported in table 3.2. The positions and the amplitudes of the two sources affect instead the amplitudes of the two components, as can be deduced by the intensity of the colours. It is indeed the relative amplitude the two components that lead to the orientation of the total acoustic pressure (right graphs) which, as expected, does not coincide with the mean orientation of the two sources (shown with the dash-dotted black line) in plot (a) while in plot (b) the total acoustic orientation is oriented as the mean orientation of the two sources.

The considerations about the orientation of the acoustic pressure with reference to the orientation of the sources can be extended to a larger number of
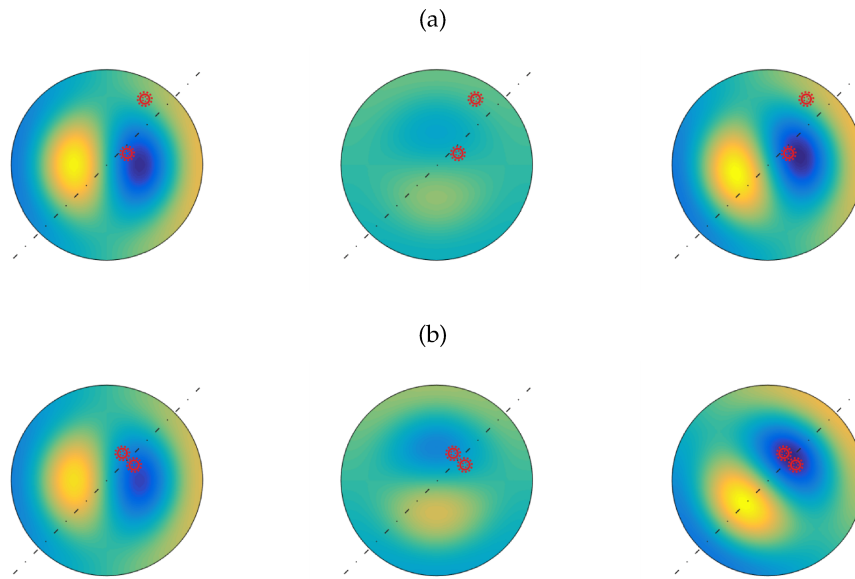
Figure 3.15: Orientation of the symmetric component (left graphs), anti-symmetric component (central graphs) and total acoustic pressure (right graphs) at the base of the cylindrical enclosure of the $(1,1,1)$ mode shape when two sources are considered. Plot (a) represents the general case, while plot (b) represents the case in which the two sources satisfy the condition of equation (3.165).

sources. This will lead to results similar to the one obtained in equation (3.164), where no particular orientation appears explicit. Furthermore equations analogous to equation (3.166) can be applied, but this would be more a mathematical problem than a physical and engineering one.

3.8 COUPLED STRUCTURAL-ACOUSTIC EQUATION OF MOTION

This section presents the coupled structural-acoustic response of the cylindrical shell and of the acoustic enclosure, which will be studied in the low frequency range in terms of the flexural kinetic energy PSD for the flexural vibration of the cylindrical wall and of the acoustic potential energy PSD for the interior sound field.

The fully coupled equations of motion for the structural-acoustic response of the system is derived using the *Modal-Interaction-Model* [28, 30, 99] in which, since the coupled system is studied in the low frequency range, the flexural vibration of the cylindrical wall and the interior sound field is conveniently modelled with finite summations of the structural and acoustic modes, respectively.

The flexural response of the cylinder is derived from the modal expansion of the *in-vacuo* flexural modes of the simply-supported cylinder, equations (3.51) and (3.53), and the interior acoustic field is derived from the modal summation of the acoustic pressure natural modes for the cylindrical cavity with *rigid-walled* boundary conditions, as presented in equations (3.128) and (3.129), as presented for example in references [30, 100, 120, 136, 137]. As discussed in reference [99], the use of the rigid walled acoustic modes guarantees the convergence to the correct acoustic pressure on the interior and on the wall surface of the cylindrical cavity but not to the normal acoustic particle velocity at the flexible walls of the cavity. However, only the former acoustic quantity is considered in the formulation while the latter is not considered, thus the rigidly-walled acoustic modes can be suitably used in the model.

The interactions between the structural and acoustic domain are formulated in terms of acoustic-structural and structural-acoustic modal coupling factors [30, 64, 94, 99, 136, 138], which represent the coupling mechanism between the structural cylindrical shell and the acoustic enclosure. Since the coupling between this two domains is severely selective [64, 69, 136], a convergence study is presented in appendix B.

The only excitation field at which the coupled system is exposed is the white noise rain on the roof force excitation described in section 3.4.1 and shown in figure 2.1 (b). Thus the flexural vibration of the cylindrical shell represent the only source for the acoustic domain.

3.8.1 *Coupled structural-acoustic modal equation of motion*

The derivation of the modal equation of motion for the structural domain presented in section 3.4 can be used as the basis for the derivation of the coupled modal equation for the structural side. Indeed the procedure is the same, as long as the acoustic effect on the cylindrical shell is considered. The forcing term given in equation (3.64) must thus be substituted by the sum of the forces exerted by the rain on the roof point forces $f_{R,i}(t)\delta(\mathbf{x}_s - \mathbf{x}_{s,i})$ and the pressure distribution due to the acoustic pressure at the shell walls $p(\mathbf{x}_s, t)$:

$$f_r(\mathbf{x}_s, t) = \sum_{i=1}^{N_R} f_{R,i}(t)\delta(\mathbf{x}_s - \mathbf{x}_{s,i}) + p(\mathbf{x}_s, t). \tag{3.167}$$

Expressing the acoustic pressure in terms of its modal summation (3.130), equation (3.167) can be written as

$$f_r(\mathbf{x}_s, t) = \sum_{i=1}^{N_R} f_{R,i}(t)\delta(\mathbf{x}_s - \mathbf{x}_{s,i}) + \boldsymbol{\psi}(\mathbf{x}_s)\mathbf{a}(t), \tag{3.168}$$

where the acoustic mode shapes are evaluated at the position $\mathbf{x}_s = (x, \vartheta, R)$ on the cylindrical walls.

Analogously, the coupled modal equation for the coupled system for the acoustic side can be obtained according to the derivation presented in section 3.7. The difference with the results obtained considering the uncoupled acoustic domain is that, in the fully coupled system, the only acoustic source is the flexural displacement of the cylindrical shell. Thus, the source term given in equation (3.139), for the fully coupled system without acoustic sources can be written as [64, 99]:

$$q(\mathbf{x}, t) = -2\dot{w}(\mathbf{x}_s, t)\delta(r - R), \tag{3.169}$$

where $\dot{w}(\mathbf{x}_s, t)$ is the flexural velocity of the cylindrical wall, directed outwards from the cavity and $\delta(\cdot)$ is the one-dimensional Dirac delta function. Expressing the flexural velocity with the finite modal summation given in equation (3.54), equation (3.169) can be written as:

$$q(\mathbf{x}, t) = -2\boldsymbol{\varphi}(\mathbf{x}_s)\dot{\mathbf{b}}(t)\delta(r - R). \tag{3.170}$$

To obtain the fully coupled equation of motion for the flexural vibration and the acoustic pressure, the following procedure is implemented:

1. the modal summation for the flexural displacement given in equation (3.54) and the expression for the forcing term of equation (3.168) are substituted into the structural equation of motion for the cylinder, equation (3.55);

2. both sides of the resulting equation (3.55) are pre-multiplied by the column vector with the flexural modes $\boldsymbol{\varphi}^T(\mathbf{x}_s)$ and integrated over the surface of the cylindrical wall;

3. the modal summation for the acoustic pressure given in equation (3.130) and the acoustic source term of equation (3.170) are inserted into the three-dimensional wave equation for the cylindrical enclosure, equation (3.110);

4. both sides of the resulting equation (3.110) are pre-multiplied by the column vector with the acoustic modes $\boldsymbol{\psi}^T(\mathbf{x})$ and integrated over the acoustic volume of the cylindrical enclosure.

This mathematical procedure leads to the following set of $2M + 2N$ ordinary differential equations, given in matrix form as:

$$\begin{bmatrix} \mathbf{M}_s & \mathbf{0} \\ \mathbf{R} & \mathbf{Q} \end{bmatrix} \begin{Bmatrix} \ddot{\mathbf{b}}(t) \\ \ddot{\mathbf{a}}(t) \end{Bmatrix} + \begin{bmatrix} \mathbf{C}_s & \mathbf{0} \\ \mathbf{0} & \mathbf{D} \end{bmatrix} \begin{Bmatrix} \dot{\mathbf{b}}(t) \\ \dot{\mathbf{a}}(t) \end{Bmatrix} + \begin{bmatrix} \mathbf{K}_s & -\mathbf{S} \\ \mathbf{0} & \mathbf{H} \end{bmatrix} \begin{Bmatrix} \mathbf{b}(t) \\ \mathbf{a}(t) \end{Bmatrix} = \begin{Bmatrix} \boldsymbol{\Phi}_s \\ \mathbf{0} \end{Bmatrix} \mathbf{f}(t),$$

(3.171)

where $\mathbf{M}_s, \mathbf{C}_s$ and $\mathbf{K}_s$ are the structural modal inertia, damping and stiffness matrices given in equations (3.61) and (3.63), $\mathbf{Q}$, $\mathbf{D}$ and $\mathbf{H}$ are the acoustic modal inertia, damping and stiffness matrices given in equations (3.138) and $\mathbf{b}(t)$ and $\mathbf{a}(t)$ are the column vectors containing respectively the flexural modal amplitudes and the acoustic modal amplitudes. Also, $\boldsymbol{\Phi}_s$ and $\mathbf{f}(t)$ are the modal excitation matrix and the excitation vector given by equations (3.66) and (3.67). Finally, the off-diagonal matrices $\mathbf{R}$ and $\mathbf{S}$ are the acoustic-structural and the structural-acoustic coupling matrices [99], whose detailed expressions are given in appendix B. It is again important to highlight that the presence of this two terms, which actually couple the two sets of equations, are introduced by the fact the flexural vibration is modelled in terms of the *in vacuo* flexural modes and the interior acoustic field is modelled in terms of the *rigidly-walled* acoustic modes.

Equation (3.171) can be written in the following compact form:

$$\hat{\mathbf{M}}\ddot{\hat{\mathbf{q}}}(t) + \hat{\mathbf{C}}\dot{\hat{\mathbf{q}}}(t) + \hat{\mathbf{K}}\hat{\mathbf{q}}(t) = \hat{\boldsymbol{\Phi}}\mathbf{f}(t),$$

(3.172)

where $\hat{\mathbf{M}}$, $\hat{\mathbf{C}}$ and $\hat{\mathbf{K}}$ are the global inertia, damping and stiffness modal matrices of the fully coupled structural-acoustic system and $\hat{\boldsymbol{\Phi}}$ is the excitation modal matrix for the fully coupled system. The definitions of these matrices can be straightforwardly obtained from equation (3.171). Finally $\hat{\mathbf{q}}(t) = \begin{bmatrix} \mathbf{b}^T(t) & \mathbf{a}^T(t) \end{bmatrix}^T$ is the $(2M + 2N) \times 1$ column vector of the modal amplitudes for the coupled system.

3.8.2 *Frequency analysis of the coupled structural-acoustic response*

As presented in the previous sections 3.4.2 and 3.7.2, the global flexural response and the global interior sound response could be established by the flexural kinetic energy PSD and by the acoustic potential energy PSD. The use of

these two energy functions is particularly convenient since it allows the representation of the spatially distributed characteristic of the structural vibration and sound fields with just two terms [28]. From the definitions given in equations (3.70) and (3.143), the two PSD functions can be written as:

$$S_K(\omega) = \frac{1}{2}\rho h \int_S \lim_{T\to\infty} E\left[\frac{1}{T}\dot{w}^*(\mathbf{x}_s,\omega)\dot{w}(\mathbf{x}_s,\omega)\right]\mathrm{d}S \quad \text{and} \tag{3.173a}$$

$$S_P(\omega) = \frac{1}{2\rho_0 c_0^2} \int_{V_c} \lim_{T\to\infty} E\left[\frac{1}{T}p^*(\mathbf{x},\omega)p(\mathbf{x},\omega)\right]\mathrm{d}V, \tag{3.173b}$$

where S and V_c represents the lateral surface and the volume of the cylindrical enclosure, $E[\cdot]$ is the expectation operator and the superscript * indicates the complex conjugate operator. As in equations (3.70) and (3.143), $\dot{w}(\mathbf{x}_s,\omega)$ represents the frequency-dependent complex amplitude of the time-harmonic flexural velocity at a point $\mathbf{x}_s$ of the cylindrical shell and $p(\mathbf{x},\omega)$ is the frequency-dependent complex amplitude of the time-harmonic acoustic pressure at a point $\mathbf{x}$ inside the acoustic enclosure. According to equations (3.71) and (3.144), these two quantities may be expressed as:

$$\dot{w}(\mathbf{x}_s,\omega) = \boldsymbol{\varphi}(\mathbf{x}_s)\dot{\mathbf{b}}(\omega) \quad \text{and} \tag{3.174a}$$

$$p(\mathbf{x},\omega) = \boldsymbol{\psi}(\mathbf{x})\mathbf{a}(\omega), \tag{3.174b}$$

where $\boldsymbol{\varphi}(\mathbf{x}_s), \boldsymbol{\psi}(\mathbf{x})$ are the row vectors of the flexural structural modes and of the the acoustic mode shapes defined in equations (3.54) and (3.130) respectively and $\dot{\mathbf{b}}(\omega), \mathbf{a}(\omega)$ are the column vector with the frequency-dependent complex amplitudes of the flexural modal velocities and acoustic modal pressures. These vectors are given by the finite Fourier transform of equation (3.172), which gives:

$$\dot{\mathbf{b}}(\omega) = \hat{\boldsymbol{\beta}}\hat{\mathbf{Y}}(\omega)\hat{\boldsymbol{\Phi}}\mathbf{f}(\omega) \quad \text{and} \tag{3.175a}$$

$$\mathbf{a}(\omega) = \frac{1}{j\omega}\hat{\boldsymbol{\alpha}}\hat{\mathbf{Y}}(\omega)\hat{\boldsymbol{\Phi}}\mathbf{f}(\omega). \tag{3.175b}$$

Here

$$\hat{\mathbf{Y}}(\omega) = j\omega\left[-\omega^2\hat{\mathbf{M}} + j\omega\hat{\mathbf{C}} + \hat{\mathbf{K}}\right]^{-1} \tag{3.176}$$

is the modal mobility matrix of the coupled structural-acoustic system derived from the Fourier transform of equation (3.172) and

$$\hat{\beta} = \begin{bmatrix} \mathbf{I}_{2M \times 2M} & \mathbf{0}_{2M \times 2N} \end{bmatrix} \quad \text{and} \tag{3.177a}$$

$$\hat{\alpha} = \begin{bmatrix} \mathbf{0}_{2N \times 2M} & \mathbf{I}_{2N \times 2N} \end{bmatrix}, \tag{3.177b}$$

where $\mathbf{I}$ and $\mathbf{0}$ are identity and zero matrices with the dimensions indicated by the subscripts.

Substitution of equations (3.174) into equations (3.173) gives

$$\begin{aligned} S_K(\omega) &= \frac{1}{2}\rho h \int_S \lim_{T \to \infty} E\left[\frac{1}{T}\dot{\mathbf{b}}^H(\omega)\boldsymbol{\varphi}^T(\mathbf{x}_s)\boldsymbol{\varphi}(\mathbf{x}_s)\dot{\mathbf{b}}(\omega)\right]\mathrm{d}S \\ &= \frac{1}{2}m_c \mathrm{Tr}\left[\hat{\mathbf{S}}_{\mathbf{bb}}(\omega)\right], \end{aligned} \tag{3.178a}$$

$$\begin{aligned} S_P(\omega) &= \frac{1}{2\rho_0 c_0^2} \int_{V_c} \lim_{T \to \infty} E\left[\frac{1}{T}\mathbf{a}^H(\omega)\boldsymbol{\psi}^T(\mathbf{x})\boldsymbol{\psi}(\mathbf{x})\mathbf{a}(\omega)\right]\mathrm{d}V \\ &= \frac{V_c}{2\rho_0 c_0^2}\mathrm{Tr}\left[\hat{\mathbf{S}}_{\mathbf{aa}}(\omega)\right], \end{aligned} \tag{3.178b}$$

where the superscript ^{H} indicates the Hermitian operator, m_c and V_c are the mass of the cylindrical shell and the volume of the acoustic enclosure and $\mathrm{Tr}[\cdot]$ is the trace matrix operator. Finally, $\hat{\mathbf{S}}_{\mathbf{bb}}(\omega)$ and $\hat{\mathbf{S}}_{\mathbf{aa}}(\omega)$ are the fully populated populated matrices with the PSD of the modal structural velocities and of the modal pressure amplitudes given by

$$\hat{\mathbf{S}}_{\mathbf{bb}}(\omega) = \lim_{T \to \infty} E\left[\frac{1}{T}\boldsymbol{\Lambda}\dot{\mathbf{b}}^H(\omega)\dot{\mathbf{b}}(\omega)\right] \quad \text{and} \tag{3.179a}$$

$$\hat{\mathbf{S}}_{\mathbf{aa}}(\omega) = \lim_{T \to \infty} E\left[\frac{1}{T}\boldsymbol{\Gamma}\mathbf{a}^H(\omega)\mathbf{a}(\omega)\right], \tag{3.179b}$$

where $\boldsymbol{\Lambda}$ and $\boldsymbol{\Gamma}$ are the diagonal matrices with the normalization coefficients whose expressions are given in appendix A. Substitution of equations (3.175) into equations (3.179) and using the cyclic property of the trace matrix operator, follows:

$$\hat{\mathbf{S}}_{\mathbf{bb}}(\omega) = \lim_{T \to \infty} E\left[\frac{1}{T}\boldsymbol{\Lambda}\hat{\boldsymbol{\beta}}\hat{\mathbf{Y}}(\omega)\hat{\boldsymbol{\Phi}}\mathbf{f}(\omega)\mathbf{f}^H(\omega)\hat{\boldsymbol{\Phi}}^T\hat{\mathbf{Y}}^H(\omega)\hat{\boldsymbol{\beta}}^T\right]$$

$$= \boldsymbol{\Lambda}\hat{\boldsymbol{\beta}}\hat{\mathbf{Y}}(\omega)\hat{\boldsymbol{\Phi}}\mathbf{S}_{\mathbf{ff}}(\omega)\hat{\boldsymbol{\Phi}}^T\hat{\mathbf{Y}}^H(\omega)\hat{\boldsymbol{\beta}}^T, \tag{3.180a}$$

$$\hat{\mathbf{S}}_{\mathbf{aa}}(\omega) = \frac{1}{\omega^2}\lim_{T \to \infty} E\left[\frac{1}{T}\boldsymbol{\Gamma}\hat{\boldsymbol{\alpha}}\hat{\mathbf{Y}}(\omega)\hat{\boldsymbol{\Phi}}\mathbf{f}(\omega)\mathbf{f}^H(\omega)\hat{\boldsymbol{\Phi}}^T\hat{\mathbf{Y}}^H(\omega)\hat{\boldsymbol{\alpha}}^T\right]$$

$$= \frac{1}{\omega^2}\boldsymbol{\Gamma}\hat{\boldsymbol{\alpha}}\hat{\mathbf{Y}}(\omega)\hat{\boldsymbol{\Phi}}\mathbf{S}_{\mathbf{ff}}(\omega)\hat{\boldsymbol{\Phi}}^T\hat{\mathbf{Y}}^H(\omega)\hat{\boldsymbol{\alpha}}^T. \tag{3.180b}$$

In these two equations $\mathbf{S}_{\mathbf{ff}}(\omega)$ is the matrix with the PSDs of the excitation forces, which, as discussed in section 3.4.1, for the uncorrelated rain on the roof force considered are assumed to one such that [64, 72]:

$$\mathbf{S}_{\mathbf{ff}}(\omega) = \lim_{T \to \infty} E\left[\mathbf{f}(\omega)\mathbf{f}^T(\omega)\right] \equiv \mathbf{I}, \tag{3.181}$$

where $\mathbf{I}$ is the $N_R \times N_R$ identity matrix.

Substitution of equation (3.181) into equations (3.180), and the resulting equations into equations (3.178) lead to the final expressions of the PSDs functions of the cylindrical flexural kinetic energy and of the acoustic potential energy, which result given by

$$S_K(\omega) = \frac{1}{2}m_c\text{Tr}\left[\boldsymbol{\Lambda}\hat{\boldsymbol{\beta}}\hat{\mathbf{Y}}(\omega)\hat{\boldsymbol{\Phi}}\mathbf{I}\hat{\boldsymbol{\Phi}}^T\hat{\mathbf{Y}}^H(\omega)\hat{\boldsymbol{\beta}}^T\right] \quad \text{and} \tag{3.182a}$$

$$S_P(\omega) = \frac{V_c}{2\rho_0 c_0^2\omega^2}\text{Tr}\left[\boldsymbol{\Gamma}\hat{\boldsymbol{\alpha}}\hat{\mathbf{Y}}(\omega)\hat{\boldsymbol{\Phi}}\mathbf{I}\hat{\boldsymbol{\Phi}}^T\hat{\mathbf{Y}}^H(\omega)\hat{\boldsymbol{\alpha}}^T\right]. \tag{3.182b}$$

3.8.3 *Simulation study*

Figure 3.16 show the 20-100 Hz spectra of the flexural kinetic energy PSD (plot (a)) and of the acoustic potential energy PSD (plot (b)) of the coupled cylinder shell structure and acoustic enclosure.

The coupled structural response correspond with the one obtained considering the *in vacuo* structure, as shown in plot (a) of figure 3.18, where is shown the overlay of the coupled (thin solid black line) and of the *in vacuo* (thick solid cyan line) responses.

The several resonance peaks of the coupled acoustic response in figure 3.16 (b) are due to to the cavity acoustic natural modes, which are specified by the thick-cyan triangles at about 78 and 85 Hz and to the resonances of the flexural modes of the cylinder, which are effectively coupled with the interior sound field in the 20-100 Hz frequency band.

(a)

(b)
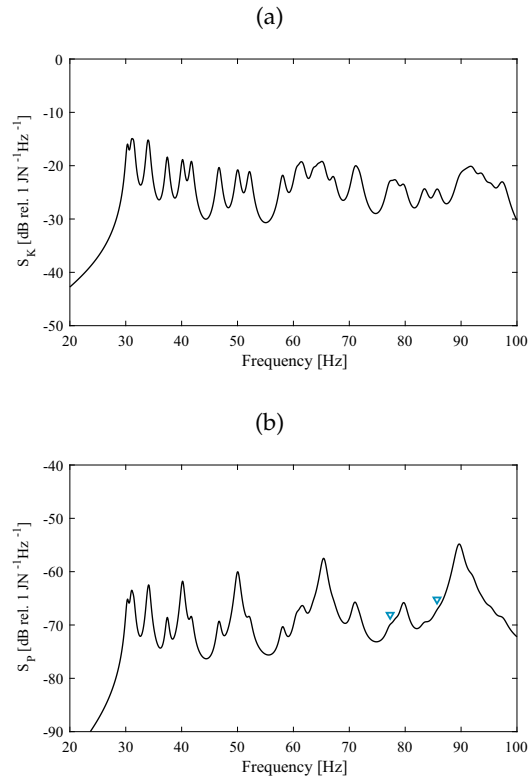
Figure 3.16: Spectra of the flexural kinetic energy PSD (plot (a)) and of the acoustic potential energy PSD (plot (b)) for the fully coupled structural-acoustic system in the 20-100 Hz frequency range.

The correspondence of the resonance peaks in the structural and acoustic response could be assessed in figure 3.17, which shows the overlay of the coupled structural (thin solid black line) and of the acoustic (thick solid cyan line) response. In this figure it is also possible to observe that the structural resonance peaks are fairly even in amplitude while the amplitudes of the resonance peaks of the acoustic response are somewhat uneven compared to those in the flexural kinetic energy PSD. This is because, despite all structural modes are equally excited by the rain on the roof disturbance, the coupling between the structural domain and the acoustic domain varies a lot for each structural mode, as can be deduced from table B.1 of appendix B.

Finally, in figure 3.18 (b) is shown the overlay of the coupled (thin solid black line) and of the *rigidly-walled* cylindrical enclosure (thick solid cyan line) acoustic potential energy PSDs. Also in this figure it appears that the coupling with the structural domain yields to the presence of resonance peaks in the coupled response which correspond to the structural resonance frequencies.
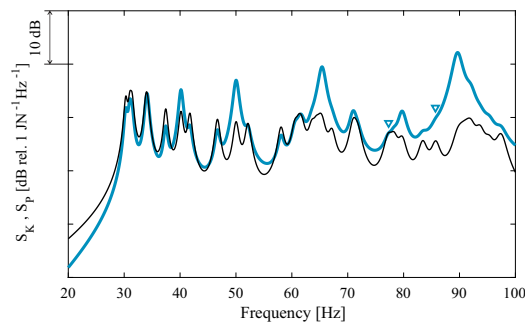
Figure 3.17: Overlay of the spectra of the flexural kinetic energy PSD (thin solid black line) and of the acoustic potential energy PSD (thick cyan line) in the 20-100 Hz frequency range. The cyan triangles point at the response in correspondence of the natural frequency of the uncoupled acoustic cavity.

(a)

(b)
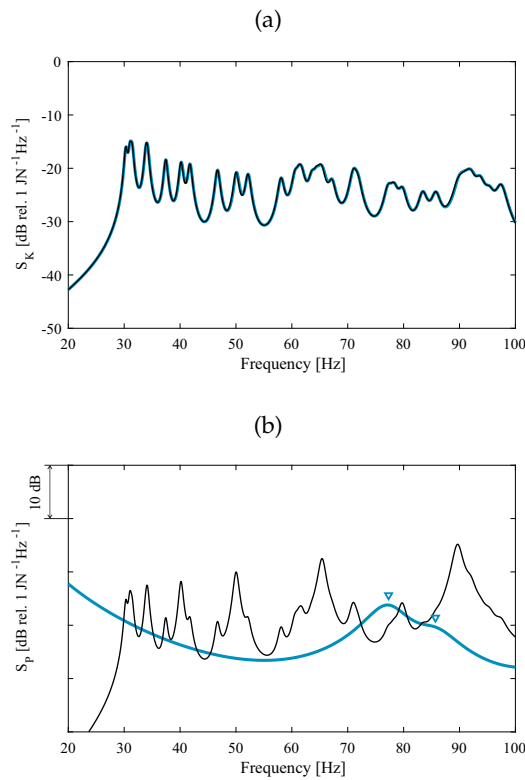
Figure 3.18: Overlay of the spectra of the flexural kinetic energy PSD considering the uncoupled (thick cyan lines) and coupled (thin black line) cylindrical shell (plot (a)), and overlay of the spectra of the acoustic potential enelgy PSD considering the uncloupled (thick cyan line) and the coupled (thin black line) acoustic enclosure (plot (b)). The cyan triangles point at the response in correspondence of the natural frequency of the uncoupled acoustic cavity.

3.9 CHAPTER CONCLUDING REMARKS

The study presented in this chapter is devoted to the derivation of the fully coupled structural-acoustic response which constitute the fundamental model

for the assessment of the noise and vibration properties of the Tuned Vibration Absorbers presented in the following chapters. The uncoupled structural and acoustic responses are first presented in order to highlight the peculiarity of each domain, focusing on a deep description of the procedures which lead to the structural equation of motion and the acoustic wave equation.

A common characteristic for both the domains is related to the cylindrical geometry. Indeed, for each natural shape of both the flexural vibration and the acoustic pressure, two orthogonal components are needed to obtain a full representation of the oscillatory quantities. Furthermore, a simplified model shown that both structural and responses are influenced by the particular orientation of the related excitation field.

Finally, the fully coupled structural-acoustic system is presented. The responses of the flexural vibration and of the internal acoustic field are expressed with the flexural kinetic energy PSD and the acoustic potential energy PSD. The study showed that when the coupled system is subject to an array of white noise rain on the roof uncorrelated point forces, both the structural and acoustic domain are excited and that the acoustic response is strongly affected by the structural response.

4

FIXED TUNED VIBRATION ABSORBER: MECHANICAL ABSORBER

This chapter studies the noise and flexural vibration control effect produced on a thin cylindrical shell and acoustic enclosure by a mechanical fixed Tuned Vibration Absorber. In particular, the dynamic characteristics of a mechanical TVA are first presented, showing the principal operating issues of the classical mechanical fixed tuned device and reporting the optimal tuning criteria.

A coupled structural-TVA simplified model is also presented in which general guidelines for the positioning of the TVA on cylindrical structures are provided.

Contents

4.1   INTRODUCTION

The control of vibration and acoustic noise over the last years have received a lot of interest. This is principally due to the attempt of increase payload size and increase the efficiency of aerospace structures, which lead them to become progressively lighter, with the drawback of a low frequency decrease of the transmission loss, where passive sound absorption treatments are ineffective. A review of the applications of vibration absorbers in propeller aircraft was given by Wright and Kidner [139]. Most of the recent works are related to active techniques, in particular to Active Vibration Control (AVC) [140–142] and Active Noise Control (ANC) [23, 67, 68]. Active Structural Acoustic Control (ASAC), in which the vibration control is obtained in conjunction with sound sensors, has also been studied [93, 140, 142, 143].

Despite the huge effort on the study of active techniques, limited literature is available on passive vibration and noise control of cylindrical shells [69, 139]. Some theoretical results can be found in references [69, 138, 144] while the experimental results of the application of passive TVAs can be found in references [145–147].

In this chapter the use of fixed Tuned Vibration Absorbers to control the flexural and internal acoustic response of a coupled cylindrical shell and enclosure is considered.

Tuned Vibration Absorbers [148] are passive devices composed by a seismic mass suspended on a spring and damper system. The suspension system is attached to a base mass which allows the connection with the hosting structure. Since this base mass is usually small, it is sometimes neglected in the analysis of the TVA. Since their invention [74], the devices were largely studied and employed in a wide rage of application, from high precision mechanical systems to civil engineering [29]. They are known under several names and acronyms, such as, for example, Tuned Vibration Absorber (TVA) [148–150], Dynamic Vibration Absorber (DVA) [31, 32, 151–153], Vibration Neutralizer [7, 17, 18, 37] and Tuned Mass Dampers (TMD) [34, 149]. This is partially due to the fact that the same system can tackle the problem of reduce the vibration of the hosting structure due either to tonal or broadband disturbance.

In the former case, shown in plot (a) of figure 4.1, the TVA is usually called DVA or Vibration Neutralizer and it is used to reduce the amplitude of the response of the hosting (often also called primary) system subject to a tonal disturbance. The natural frequency of the absorber should be tuned to the excitation frequency and the damping should be as low as possible.

(a)

(b)
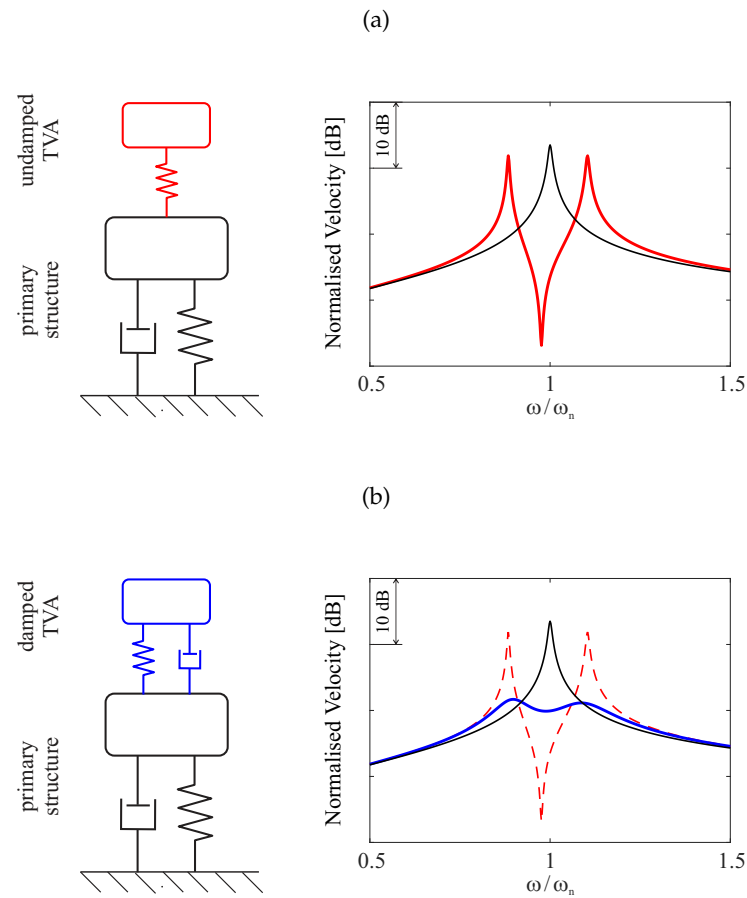
Figure 4.1: Schematic representation and amplitude of the response per unit excitation of a sdof primary system equipped with a Vibration Neutralizer (plot (a)) and with a TVA (plot (b)).

In this way, the device offers the greatest mechanical impedance at the exact frequency at which it is tuned. Figure 4.1 (a) shows on the right the spectrum of the velocity response per unit excitation of the primary system, considered as a single-degree-of-freedom (sdof) system without any control system (thin solid black line) and with a Vibration Neutralizer (undamped TVA) tuned at the resonance frequency of the primary system (thick solid red line). The response of the system equipped with the Vibration Neutralizer presents two resonance peaks and a sharp anti-resonance at the frequency at which the device is tuned.

In the latter case, shown in figure 4.1 (b), the TVA is often referred as TVA or TMD. In this case it operates with optimal levels of damping to reduce the broadband vibration response of the hosting structure subject to broad frequency band random disturbances. In this case the natural frequency of the device and the damping should be tuned in order to minimise the resonant

response of a target mode of the hosting structure over a broad frequency band. The normalised response of the primary system without TVA (thin solid black line), with an undamped TVA (thin dashed red line) and with an optimally damped TVA (thick solid blue line) are compared in the right graph in plot (b) of figure 4.1. The response of the primary system equipped with the optimally damped TVA presents the two resonance peaks, but these are smooth due to the damping effects. Also, the response is no more characterised by the anti-resonance in correspondence of the frequency at which the device is tuned.

The first part of the chapter is devoted to the analysis of the TVA. The dynamic response is first described in terms of the base impedance. Then, a review of the tuning criteria is provided. The principal operation limitations of the classical mechanical TVA are presented considering both the effects of a mistuned TVA and the ones of a single TVA on a multi-degrees-of-freedom system. A simplified model, composed by just one structural mode of the cylindrical shell and a simplified TVA is used to obtain general guidelines for the positioning of the TVAs on cylindrical shells.

The last part of the chapter presents the simulation study on the control effects produced by arrays of 12 and 18 TVAs.

4.2 CHARACTERIZATION OF THE TVA

In a recent study, Rohlfing *et al.* [154] described the response of a velocity feedback control unit in terms of the open- and closed-loop base impedance. They defined the base impedance of the device as

$$Z_b(\omega) = \frac{f_b(\omega)}{\dot{w}_b(\omega)}, \qquad (4.1)$$

where $f_b(\omega)$ and $\dot{w}_b(\omega)$ are the complex amplitudes of the time-harmonic force and velocity at the base of the device. This equation allows for a straightforward physical interpretation of both stability and control performances. This approach has been used also in other studies, as for example [155, 156]. The base impedance can also be used to assess the dynamic behaviour of a TVA [157].
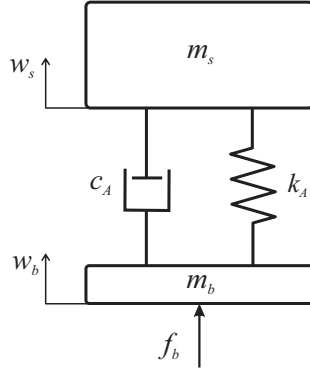
Figure 4.2: Lumped parameter model for the classical mechanical TVA.

Table 4.1: Reference parameters for the mechanical TVA.

Parameter	Symbol	Value	
Seismic mass	m_s	115	[g]
Base mass	m_b	185	[g]
Natural frequency	f_A	20	[Hz]
Damping ratio	ζ_A	2	[%]

Considering the notation shown in the lumped parameter model depicted in figure 4.2, the Newton's law for the base and seismic masses can be written as:

$$m_b \ddot{w}_b(t) = k_A(w_s(t) - w_b(t)) + c_A(\dot{w}_s(t) - \dot{w}_b(t)) + f_b(t), \quad (4.2a)$$

$$m_s \ddot{w}_s(t) = -k_A(w_s(t) - w_b(t)) - c_A(\dot{w}_s(t) - \dot{w}_b(t)), \quad (4.2b)$$

where $w_s(t)$, $w_b(t)$ are the time-dependent displacements of the seismic and base masses m_s and m_b, c_A and k_A are the damping and stiffness elements of the TVA and $f_b(t)$ is the time-dependent amplitude of the force acting on the base mass. Assuming time harmonic dependence, these equations can be written in terms of the complex amplitudes of the time-harmonic velocities of the two masses $\dot{w}_s(\omega)$ and $\dot{w}_b(\omega)$ and of the force $f_b(\omega)$ as

$$(Z_{mb}(\omega) + Z_s(\omega)) \dot{w}_b(\omega) = Z_s(\omega)\dot{w}_s(\omega) + f_b(\omega), \quad (4.3a)$$

$$(Z_{ms}(\omega) + Z_s(\omega)) \dot{w}_s(\omega) = Z_s(\omega)\dot{w}_b(\omega), \quad (4.3b)$$

where $Z_{mb}(\omega) = j\omega m_b$ is the impedance of the base mass, $Z_{ms}(\omega) = j\omega m_s$ is the impedance of the seismic mass and $Z_s(\omega) = c_A + k_A/(j\omega)$ is the impedance of the mechanical suspension [127, 158]. The complex amplitude of the velocity of the seismic mass can be obtained from equation (4.3b) as

$$\dot{w}_s(\omega) = \frac{Z_s(\omega)}{Z_{ms}(\omega) + Z_s(\omega)}\dot{w}_b(\omega), \quad (4.4)$$

which, substituted in equation (4.3a), gives

$$\left(Z_{mb}(\omega) + \frac{Z_{ms}(\omega)Z_s(\omega)}{Z_{ms}(\omega) + Z_s(\omega)} \right) \dot{w}_b(\omega) = f_b(\omega). \tag{4.5}$$

Thus, the base impedance of the mechanical TVA results given by:

$$Z_b(\omega) = Z_{mb}(\omega) + \frac{Z_{ms}(\omega)Z_s(\omega)}{Z_{ms}(\omega) + Z_s(\omega)}. \tag{4.6}$$

Figure 4.3 shows the magnitude (upper plot) and phase (lower plot) of $Z_b(\omega)$, calculated considering the TVA parameters listed in table 4.1. At low frequencies the two masses move nearly in phase and thus the TVA produces a mass impedance effect $Z(\omega) = Z_{mb}(\omega) + Z_{ms}(\omega)$. At higher frequencies, above the resonance frequency of the TVA, the top mass is characterized by little oscillations and behaves like a seismic reference system. Thus the TVA produces a mass impedance effect $Z(\omega) = Z_{mb}(\omega)$. At frequencies around the fundamental natural frequency at 20 Hz, the spring mass system resonates and produces a sharp resonance peak followed by a sharp low, respectively with -180 phase lag and $+180$ phase lead. This indicates that, at the resonance frequency, the
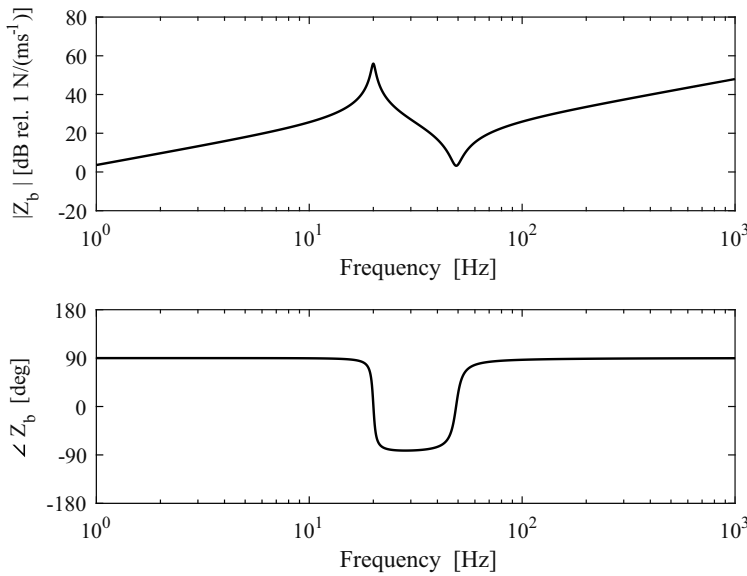
Figure 4.3: Base impedance FRFs (amplitude in the top plot and phase in the bottom plot) of the classical mechanical TVA.

absorber is characterized by a large dissipative impedance, that is, a large vibration absorption effect. TVA systems can therefore be used to effectively absorb vibration energy. They can be used, for instance, to attenuate the response pro-

duced by a resonant mode of a flexible structure by properly tuning the TVA fundamental resonance frequency and damping ratio.

4.3 TUNING LAWS FOR THE TVA

The first optimisation criterion, proposed by Omondroyd and Den Hartog in 1928 [75], sets the natural frequency of the vibration absorber such that the two peaks in the coupled displacement response of the primary system have the same amplitude. Also, the damping ratio is set such that the derivative at the two peaks is zero. Several others optimisation criteria have been proposed, as summarised in references [159, 160], for the broadband control of the resonant response of structures. In general, they can be categorised in two groups, which either consider H_∞ (e.g. [34, 75, 161]) or H_2 (e.g. [159, 162–164]) cost functions [165].
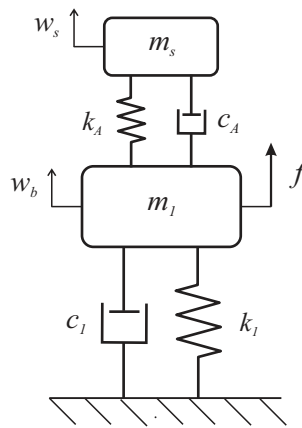
Figure 4.4: Lumped parameter model of a sdof system equipped with the fixed TVA.

The optimisation parameters are derived considering a hosting structure (also referred as primary structure) modelled as a single-degree-of-freedom (sdof) system characterised by mass, stiffness and damping parameters denoted by m_1, k_1 and c_1, as shown in figure 4.4. The fixed Tuned Vibration Absorber is modelled as a single-mass-dashpot-spring system, with mass, stiffness and damping elements denoted by m_s, k_A and c_A. The optimisation criteria are derived with reference to the ratio

$$\mu = \frac{m_s}{m_1} \tag{4.7}$$

Table 4.2: Optimisation criteria of the Tuned Vibration Absorber. Adapted from [159]

	Optimisation	Objective	Proposed by	Optimal parameters
1	H_∞	Minimisation of the maximum displacement of the primary mass	Ormondroyd & Den Hartog [75], Nishihara & Asami [161]	$\zeta_{opt} = \sqrt{\dfrac{3\mu}{8(1+\mu)}}$ $\nu_{opt} = \dfrac{1}{1+\mu}$
2	H_2	Minimisation the transient vibration of the system	Iwata [164], Warburton[163]	$\zeta_{opt} = \sqrt{\dfrac{\mu(4+3\mu)}{8(1+\mu)(2+\mu)}}$ $\nu_{opt} = \sqrt{\dfrac{2+\mu}{2(1+\mu)^2}}$
3	Stability maximisation	Minimisation of the total displacement of the primary mass over all frequency	Miller *et al.* [166], Yamaguchi[167]	$\zeta_{opt} = \sqrt{\dfrac{\mu}{1+\mu}}$ $\nu_{opt} = \dfrac{1}{1+\mu}$
4	H_∞	Minimisation of the displacement of the primary and the relative displacement	Krenk [34]	$\zeta_{opt} = \sqrt{\dfrac{\mu}{2(1+\mu)}}$ $\nu_{opt} = \dfrac{1}{1+\mu}$
5	H_2	Minimisation of the total kinetic energy of the primary mass over all frequencies	Warburton [163]	$\zeta_{opt} = \dfrac{\sqrt{\mu}}{2}$ $\nu_{opt} = \dfrac{1}{\sqrt{1+\mu}}$
6	H_2	Maximisation of the power dissipated by the absorber	Zilletti *et al.* [159]	$\zeta_{opt} = \dfrac{\sqrt{\mu}}{2}$ $\nu_{opt} = \dfrac{1}{\sqrt{1+\mu}}$

between the TVA seismic mass and the mass of the the primary system. As summarised in table 4.2, the objective of the several optimisation criteria is to provide the optimal value of the TVA damping ratio, defined as

$$\zeta_A = \frac{c_A}{2m_s\omega_A} \tag{4.8}$$

and of the frequency ratio ν,

$$\nu = \frac{\omega_A}{\omega_1} \tag{4.9}$$

between the fundamental natural frequency of the TVA, ω_A, and the natural frequency of the primary structure, ω_1. These are defined as

$$\omega_A = \sqrt{\frac{k_A}{m_s}} \quad \text{and} \tag{4.10a}$$

$$\omega_1 = \sqrt{\frac{k_1}{m_1}}. \tag{4.10b}$$
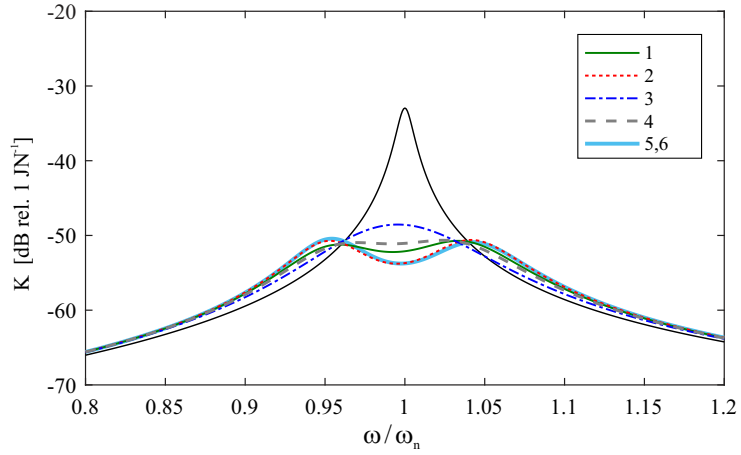
Figure 4.5: Kinetic energy spectrum of the primary system without TVA (thin black line) and with a TVA whose parameters are tuned according to the six optimisation criteria of table 4.2.

In figure 4.5 are shown the kinetic energy spectra of the primary system without TVA (thin solid black line) and equipped with a fixed TVA. The parameters of the TVA are selected according to the theory proposed by Ormondroyd and Den Hartog [75] (thick solid green line), by Iwata [164] (thin dotted red line), by Miller *et al.* [166] (thin dash-dot blue line), by Krenk [34] (thick dashed grey line) and by Warburton [163], whose parameters corresponds to the ones proposed by the theory derived by Zilletti *et al.* [159], (thick solid cyan line).

In this thesis, the time-averaged kinetic energy minimisation criterion proposed by Zilletti *et al.* [159] is adopted. The optimal damping ratio and the optimal frequency ratio are therefore given by:

$$\zeta_{opt} = \frac{\sqrt{\mu}}{2} \quad \text{and} \tag{4.11a}$$

$$\nu_{opt} = \frac{1}{\sqrt{1+\mu}}. \tag{4.11b}$$

When the TVA is applied on a distributed structure, such as the cylinder considered in this thesis, the mass ratio given in equation (4.7) has to be substituted by the following relation [29, 56]:

$$\mu = \frac{m_s}{m_m} \varphi_m^2(\mathbf{x}_A),$$ (4.12)

where m_m is the modal mass of the controlled mode of the structure and $\varphi_m(\mathbf{x}_A)$ is the amplitude of the targeted mode at the TVA position $\mathbf{x}_A$. It is interesting to note how, for distributed structures, the mass ratio is defined in a comparable manner as the coupling parameter between an acoustic mode of an acoustic cavity and a Helmholtz Resonator [168].

4.4   ISSUES OF THE TVA

As highlighted in the previous section, the values of the optimal parameters depend on the mass ratio, given in equations (4.7) and (4.12) for the case of a sdof or distributed hosting structure, respectively. To limit the problems related to an excessive weight of the TVA, the mass ration is typically $\mu \simeq 1 - 8\%$, thus the frequency ratio ν_{opt} is given normally by a value close to one. According to equation (4.9), the natural frequency of the TVA should be tuned to a value close to the natural frequency of the controlled mode. This implies that a precise knowledge of the dynamic response of the hosting system is required. This *a priori* knowledge of the dynamic response of the system is difficult to obtain for engineering system and becomes of little use when operation conditions of the structure, such as for example temperature, pressuring or tensioning effects, modify the dynamic behaviour of the structure. In plot (a) of figure 4.6 is shown the effect of a mistuned of the TVA. A sdof system is considered as the hosting structure. The left graph shows the velocity response of the system when it presents a resonance frequency which coincides with the nominal value ω_n, without TVA (thin black line) and when the system is equipped with a TVA tuned to ω_n (thick solid blue line). In this case, the TVA effectively control the resonant response of the hosting structure. In the central and right graphs are considered the cases in which, due to operation conditions, the structure changes its dynamic behaviour and as a consequence it presents a resonance frequency which is 5% lower (central graph) or higher (right graph) than the nominal value ω_n. If a classical mechanical fixed TVA is considered, the change of the dynamic response of the hosting structure is not tracked by the passive control device, which, being tuned to the nominal value ω_n, results mistuned
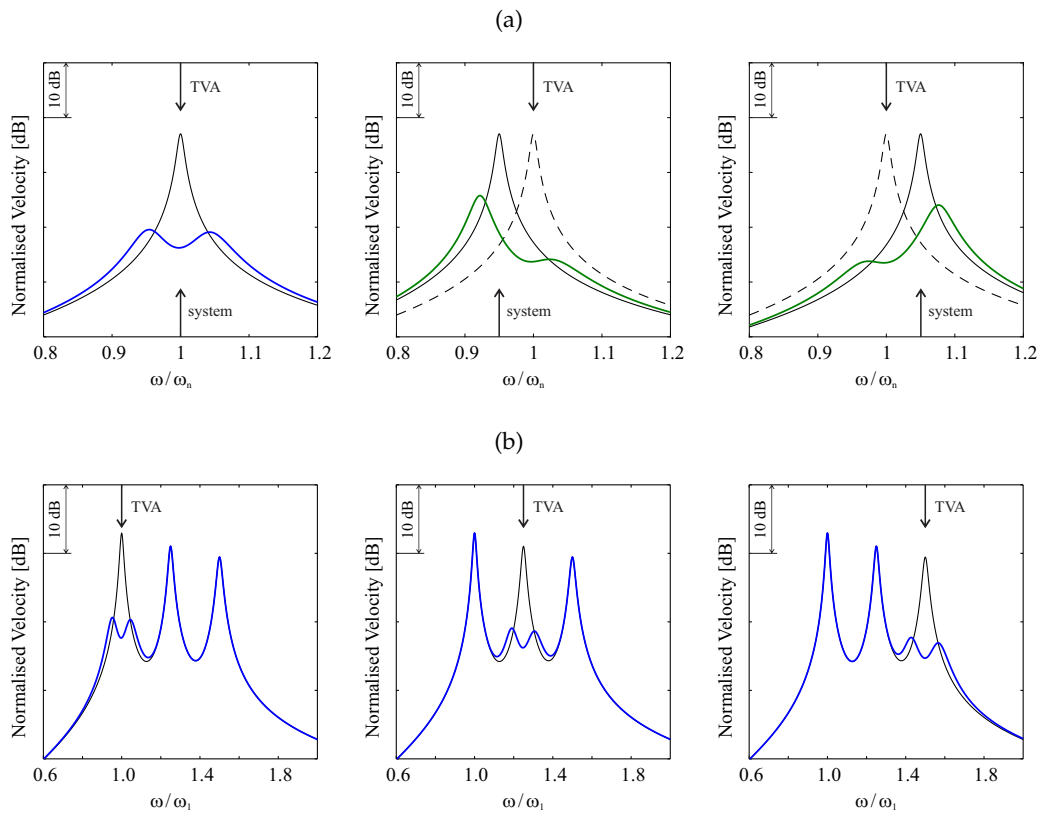
Figure 4.6: Amplitude of the velocity response per unit excitation of a sdof primary system with no TVA (thin solid black lines and thin dashed black lines) and with the TVA tuned to the the nominal value of ω_n (thick blue line and thick green lines) (plot (a)) when the resonance frequency coincides with ω_n (left graph) and when the resonance frequency is 5% lower (central graph) and 5% higher (right graph) of the nominal value and velocity spectra per unit excitation of a three-degrees-of-freedom system (plot (b)) with no TVA (thin solid black lines) and with the TVA (thick solid blue lines) tuned to the first (left graph), the second (central graph) and the third (right graph) natural frequency.

to the actual resonance frequency of the primary system. The velocity response per unit excitation of the primary system subject to operation conditions is shown in the central and right graphs of figure 4.6 (a) with the thin solid black lines and the nominal velocity response is shown with the thin dashed black lines. The responses of the primary system equipped with the mistuned TVA are shown with the thick solid green lines. The set of the three graphs in plot (a) shows how the TVA loses its control performances when the primary system is subject to operation effects which modify its dynamic response.

Plot (b) of figure 4.6 presents the normalised amplitude velocity response of a three-degrees-of-freedom primary system without TVA (thin black lines) and when the primary system is equipped with a TVA (thick blue lines) tuned

to the first (left graph), to the second (central graph) and to the third (right graph) natural frequency of the hosting structure. The set of the three graphs of plot (b) shows how, when a multi-degrees-of-freedom system is equipped with a single TVA, the control effect is achieved only for the resonance peak which correspond to the natural frequency at which the device is tuned.

From the former analysis, the principal operative drawbacks of the TVAs can be summarised as:

- The TVA requires a precise tuning to the natural frequency corresponding to the targeted resonance peak; this implies that

- A precise knowledge of the dynamic response of the hosting structure is required;

- The control effect of the TVA is achieved only at a targeted resonance peak, thus to control several resonance peaks of a mdof (or distributed) system a huge number of devices is needed.

4.5 POSITIONING CRITERIA

In this section the positioning of the TVA on cylindrical structures is analysed. Indeed, as well as the tuning, the positioning of a TVA plays a key role in the effectiveness of the device in the vibration control, since a misplaced TVA would give similar effects as a mistuned TVA.

For structures that do not present the twofold modal degeneracy presented in section 3.3 of the previous chapter, *e.g.* beams and rectangular plates, the positioning is a relatively simple task, since the TVA should be place as close as possible to the anti-nodal positions of the target mode to maximise the vibration absorption effect [169]. Some initial results on the positioning of the TVA on a cylindrical structure are given by Huang and Fuller [69]. They compared the results obtained considering several configurations of the TVAs when the cylindrical shell subject to both point and distributed forces.

In this section, a simplified model of the cylindrical shell, composed by just a single structural mode, is used to assess the control effects of a single TVA or the combination of two TVAs. Furthermore, also a simplified model of the TVA is considered, in which the base mass is neglected.

In section 3.4.4 of the previous chapter is shown that the frequency-dependent modal equation of motion considering just a single flexural mode results in two

uncoupled modal equation, related to the symmetric and anti-symmetric component of the selected mode:

$$\left(-\omega^2 \tilde{M} + j\omega \tilde{C} + \tilde{K}\right) b_{\tilde{m}}^s(\omega) = \varphi_{\tilde{m}}^s(\mathbf{x}_F) f_R(\omega), \qquad (4.13\text{a})$$

$$\left(-\omega^2 \tilde{M} + j\omega \tilde{C} + \tilde{K}\right) b_{\tilde{m}}^a(\omega) = \varphi_{\tilde{m}}^a(\mathbf{x}_F) f_R(\omega), \qquad (4.13\text{b})$$

where $\tilde{M}$, $\tilde{C}$ and $\tilde{K}$ are the modal inertia, damping and stiffness coefficients for the $\tilde{m}$-th mode, assuming $m_2 \neq 0$. Also, $f_R(\omega)$ is the frequency-dependent amplitude of the single point force acting on the cylinder and $\varphi_{\tilde{m}}^s(\mathbf{x}_F)$, $\varphi_{\tilde{m}}^a(\mathbf{x}_F)$ are the symmetric and anti-symmetric mode shapes of the $\tilde{m}$-th structural mode at the position $\mathbf{x}_F$ where the force is applied. When on the cylinder is applied a single TVA at the position $\mathbf{x}_A = (x_A, \vartheta_A)$, the force due to the TVA must be included in the right-hand-side of equations (4.13). From the definition of the base impedance given in equation (4.1), the frequency-dependent amplitude of the point force that the TVA exerts on the structure can be expressed as

$$f_{TVA}(\mathbf{x}, \omega) = -Z_A(\omega) \dot{\tilde{w}}(\mathbf{x}_A, \omega) \delta(\mathbf{x}_s - \mathbf{x}_A), \qquad (4.14)$$

where $Z_A(\omega)$ is the impedance of the simplified TVA given by:

$$Z_A(\omega) = \frac{Z_{ms}(\omega) Z_s(\omega)}{Z_{ms}(\omega) + Z_s(\omega)} = \frac{j\omega m_s \left(c_A + k_A/(j\omega)\right)}{j\omega m_s + c_A + k_A/(j\omega)}. \qquad (4.15)$$

Substituting in equation (4.14) the expression for the flexural displacement due to the $\tilde{m}$-th mode,

$$\tilde{w}(\mathbf{x}_s, \omega) = \varphi_{\tilde{m}}^s(\mathbf{x}_s) b_{\tilde{m}}^s(\omega) + \varphi_{\tilde{m}}^a(\mathbf{x}_s) b_{\tilde{m}}^a(\omega), \qquad (4.16)$$

and integrating the resulting equation over the surface of the cylinder, pre-multiplied by the symmetric or anti-symmetric structural mode shape, the two modal forces due to the TVA are given by:

$$f_{TVA}^s(\omega) = -j\omega \varphi_{\tilde{m}}^s(\mathbf{x}_A) Z_A(\omega) \varphi_{\tilde{m}}^s(\mathbf{x}_A) b_{\tilde{m}}^s(\omega) - j\omega \varphi_{\tilde{m}}^s(\mathbf{x}_A) Z_A(\omega) \varphi_{\tilde{m}}^a(\mathbf{x}_A) b_{\tilde{m}}^a(\omega),$$
$$(4.17\text{a})$$

$$f_{TVA}^s(\omega) = -j\omega \varphi_{\tilde{m}}^a(\mathbf{x}_A) Z_A(\omega) \varphi_{\tilde{m}}^s(\mathbf{x}_A) b_{\tilde{m}}^s(\omega) - j\omega \varphi_{\tilde{m}}^a(\mathbf{x}_A) Z_A(\omega) \varphi_{\tilde{m}}^a(\mathbf{x}_A) b_{\tilde{m}}^a(\omega).$$
$$(4.17\text{b})$$

These expression can be written in a compact form by defining

$$Z_A^{ss}(\omega) = \varphi_{\tilde{m}}^s(\mathbf{x}_A) Z_A(\omega) \varphi_{\tilde{m}}^s(\mathbf{x}_A), \tag{4.18a}$$

$$Z_A^{sa}(\omega) = \varphi_{\tilde{m}}^s(\mathbf{x}_A) Z_A(\omega) \varphi_{\tilde{m}}^a(\mathbf{x}_A), \tag{4.18b}$$

$$Z_A^{as}(\omega) = \varphi_{\tilde{m}}^a(\mathbf{x}_A) Z_A(\omega) \varphi_{\tilde{m}}^s(\mathbf{x}_A), \tag{4.18c}$$

$$Z_A^{aa}(\omega) = \varphi_{\tilde{m}}^a(\mathbf{x}_A) Z_A(\omega) \varphi_{\tilde{m}}^a(\mathbf{x}_A), \tag{4.18d}$$

which, substituted into equations (4.17) and the resulting equations inserted in equations (4.13), yield to coupled modal equations of motion for the $\tilde{m}$ mode of the cylinder subject to a single force and equipped with a single TVA:

$$\left(-\omega^2 \tilde{M} + j\omega \tilde{C} + j\omega Z_A^{ss}(\omega) + \tilde{K}\right) b_{\tilde{m}}^s(\omega) + j\omega Z_A^{sa}(\omega) b_{\tilde{m}}^a(\omega) = \varphi_{\tilde{m}}^s(\mathbf{x}_F) f_R(\omega), \tag{4.19a}$$

$$j\omega Z_A^{as}(\omega) b_{\tilde{m}}^s(\omega) + \left(-\omega^2 \tilde{M} + j\omega \tilde{C} + j\omega Z_A^{aa}(\omega) + \tilde{K}\right) b_{\tilde{m}}^a(\omega) = \varphi_{\tilde{m}}^a(\mathbf{x}_F) f_R(\omega), \tag{4.19b}$$

Defining the dynamic stiffness [127] as :

$$\tilde{D}(\omega) = -\omega^2 \tilde{M} + j\omega \tilde{C} + \tilde{K}, \tag{4.20}$$

equations (4.19) could be rewritten as:

$$\left[\tilde{D}(\omega) + j\omega Z_A^{ss}(\omega)\right] b_{\tilde{m}}^s(\omega) + j\omega Z_A^{sa}(\omega) b_{\tilde{m}}^a(\omega) = \varphi_{\tilde{m}}^s(\mathbf{x}_F) f_R(\omega), \tag{4.21a}$$

$$j\omega Z_A^{as}(\omega) b_{\tilde{m}}^s(\omega) + \left[\tilde{D}(\omega) + j\omega Z_A^{aa}(\omega)\right] b_{\tilde{m}}^a(\omega) = \varphi_{\tilde{m}}^a(\mathbf{x}_F) f_R(\omega), \tag{4.21b}$$

Comparing equations (4.21) with equations (3.85) given in section 3.4.4 of the previous chapter, one can clearly see that the TVA couples the two modal equations of motion for the $\tilde{m}$-th structural mode.

The modal amplitudes of the $\tilde{m}$-th structural mode, for the symmetric and anti-symmetric component can be obtained by solving equations (4.21) as:

$$b_{\tilde{m}}^s(\omega) = \frac{\left[\tilde{D}(\omega) + j\omega Z_A^{aa}(\omega)\right] \varphi_{\tilde{m}}^s(\mathbf{x}_F) + j\omega Z_A^{sa}(\omega) \varphi_{\tilde{m}}^a(\mathbf{x}_F)}{\tilde{D}(\omega) \left[\tilde{D}(\omega) + j\omega Z_A^{ss}(\omega) + j\omega Z_A^{aa}(\omega)\right]} f_R(\omega), \tag{4.22a}$$

$$b_{\tilde{m}}^a(\omega) = \frac{j\omega Z_A^{as}(\omega) \varphi_{\tilde{m}}^s(\mathbf{x}_F) + \left[\tilde{D}(\omega) + j\omega Z_A^{ss}(\omega)\right] \varphi_{\tilde{m}}^a(\mathbf{x}_F)}{\tilde{D}(\omega) \left[\tilde{D}(\omega) + j\omega Z_A^{ss}(\omega) + j\omega Z_A^{aa}(\omega)\right]} f_R(\omega). \tag{4.22b}$$

The frequency-dependent amplitude of the flexural displacement due to the $\tilde{m}$ structural mode could thus be obtained from the expression given in equation (4.16).

In section 3.4.4 it was shown that the effect of a single point force on a cylindrical shell is to orient the resulting deflection such that the shell presents the maximum displacement at an angular orientation that corresponds to the orientation of the force. Thus, in order to maximise the vibration control effect of the TVA, it should be located in an anti-nodal position for the resulting deflection, as shown in figure 4.7. In plot (a) are shown the reference undeformed cylindrical shell (thick solid grey lines), the deflection of the cylindrical shell due to a point force without the TVA (thin dashed blue lines) and with the TVA (thin solid blue lines). In plot (b) are shown the spectra of the flexural kinetic energy PSD versus the normalised frequency of the plain cylindrical shell (thin solid black lines) and of the cylinder equipped with the TVA (thick solid blue lines) for the symmetric (left), anti-symmetric (central) and resulting (right graphs) components. When the TVA is positioned in an angular position which corresponds to an anti-nodal circumferential position of the resulting deflection, both the symmetric and anti-symmetric components are effectively controlled, thus the global response is controlled.

As highlighted in section 3.4.4, the positions of the nodal and anti-nodal lines could be derived only if one single point force acts on the cylindrical shell and the direction of this force is known. In the general case, the distribution of forces could be unknown or the forces are characterised by a stochastic nature. In these case the position of the nodal and anti-nodal lines could not be predicted. This condition is shown in figure 4.8, where the TVA results misplaced with respect to the anti-nodal positions of the resulting deflection due to a single point force. In this case both the symmetric and anti-symmetric components, and thus also the global deflection, are only slightly affected by the presence of the TVA. This can be seen both in plots (a) and (b) of figure 4.8, where are shown the deflection of the middle-surface of the cylindrical shell and the spectra of the flexural kinetic energy for the symmetric (left), anti-symmetric (central) and global (right graphs) deflection.

(a)

(b)
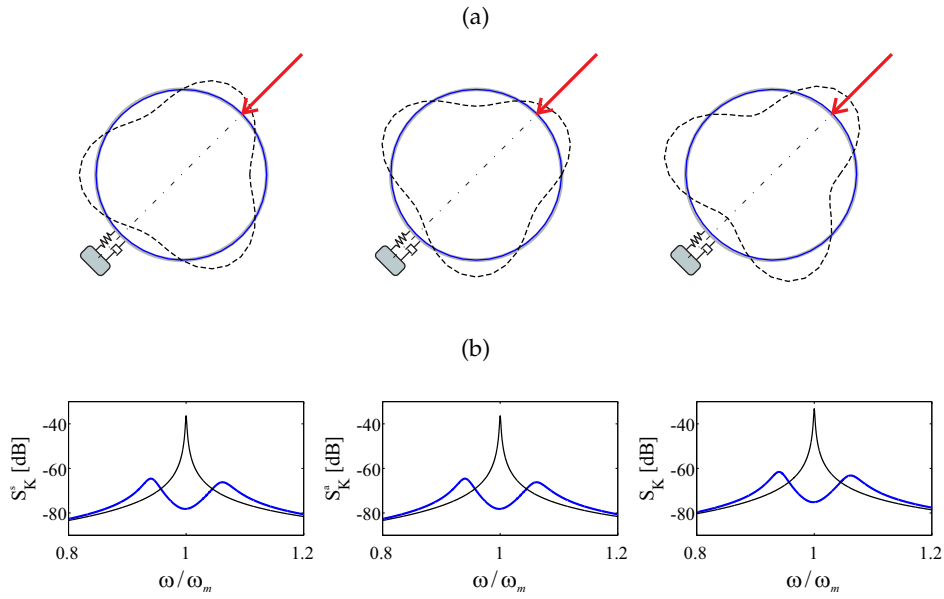
Figure 4.7: Middle-section deformation of the cylindrical shell, plot (a), and spectra of the flexural kinetic energy PSD, plot (b) for the symmetric (left), anti-symmetric (central) and global (right graphs) components when the TVA is placed in an anti-nodal position of the global deflection.

(a)

(b)
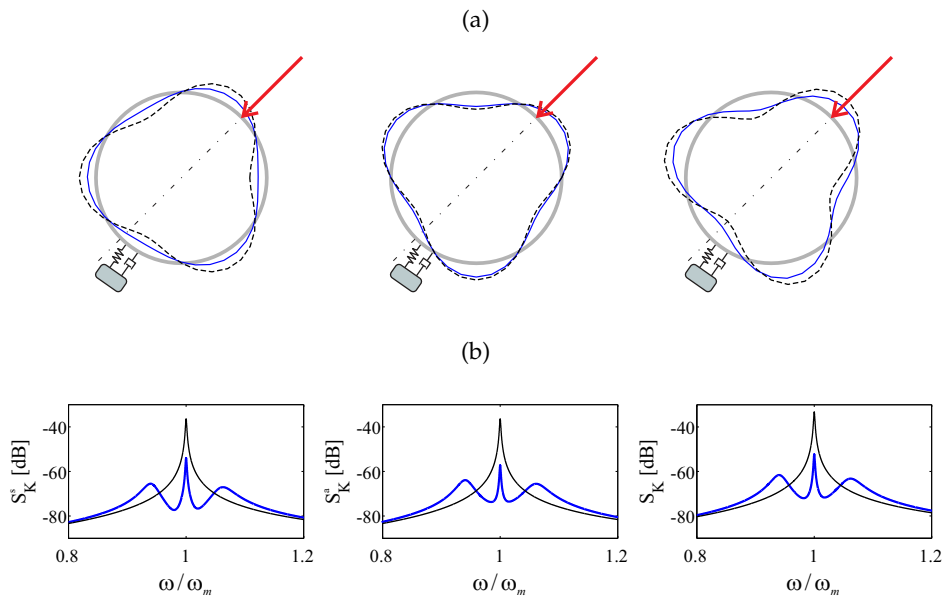
Figure 4.8: Middle-section deformation of the cylindrical shell, plot (a), and spectra of the flexural kinetic energy PSD, plot (b) for the symmetric (left), anti-symmetric (central) and global (right graphs) components when the TVA is misplaced with respect to the anti-nodal position of the global deflection.

Figure 4.9 and 4.10 show the control effect on the middle-surface deflection (plots (a)) and on the spectra of the flexural kinetic energy PSDs (plots (b)) of a single TVA placed in an anti-nodal position of the symmetric and anti-symmetric components, respectively. The two figures show that when the TVA is located on an anti-nodal position of a given component, it can effectively control the flexural response of only that component. This is confirmed by considering equations (4.22). Indeed, if the TVA is placed on an anti-nodal position for a symmetrical component, the mode shapes are such that $\varphi_{\tilde{m}}^{s}(\mathbf{x}_A) \neq 0$ and $\varphi_{\tilde{m}}^{a}(\mathbf{x}_A) = 0$, thus only the term $Z_A^{ss}(\omega)$ in equations (4.18) results different than zero, while the terms $Z_A^{sa}(\omega)$, $Z_A^{as}(\omega)$ and $Z_A^{aa}(\omega)$ are zero. The frequency-dependent modal amplitudes for the two components given in equations (4.22) result:

$$b_{\tilde{m}}^{s}(\omega) = \frac{\varphi_{\tilde{m}}^{s}(\mathbf{x}_F)}{\left[\tilde{D}(\omega) + j\omega Z_A^{ss}(\omega)\right]} f_R(\omega), \qquad (4.23a)$$

$$b_{\tilde{m}}^{a}(\omega) = \frac{\varphi_{\tilde{m}}^{a}(\mathbf{x}_F)}{\tilde{D}(\omega)} f_R(\omega), \qquad (4.23b)$$

thus only the response of the symmetric component is affected by the presence of the TVA. When the TVA is placed on an anti-nodal position for the anti-symmetrical mode shape, the amplitudes of the two components of the mode shape at the TVA position are $\varphi_{\tilde{m}}^{s}(\mathbf{x}_A) = 0$ and $\varphi_{\tilde{m}}^{a}(\mathbf{x}_A) \neq 0$, thus the terms in equations (4.18) result $Z_A^{aa}(\omega) \neq 0$ and $Z_A^{ss}(\omega) = Z_A^{sa}(\omega) = Z_A^{as}(\omega) = 0$. The frequency-dependent modal amplitudes are given by:

$$b_{\tilde{m}}^{s}(\omega) = \frac{\varphi_{\tilde{m}}^{s}(\mathbf{x}_F)}{\tilde{D}(\omega)} f_R(\omega), \qquad (4.24a)$$

$$b_{\tilde{m}}^{a}(\omega) = \frac{\varphi_{\tilde{m}}^{a}(\mathbf{x}_F)}{\left[\tilde{D}(\omega) + j\omega Z_A^{aa}(\omega)\right]} f_R(\omega), \qquad (4.24b)$$

and in this case only the anti-symmetric response is affected by the presence of the TVA.

(a)

(b)
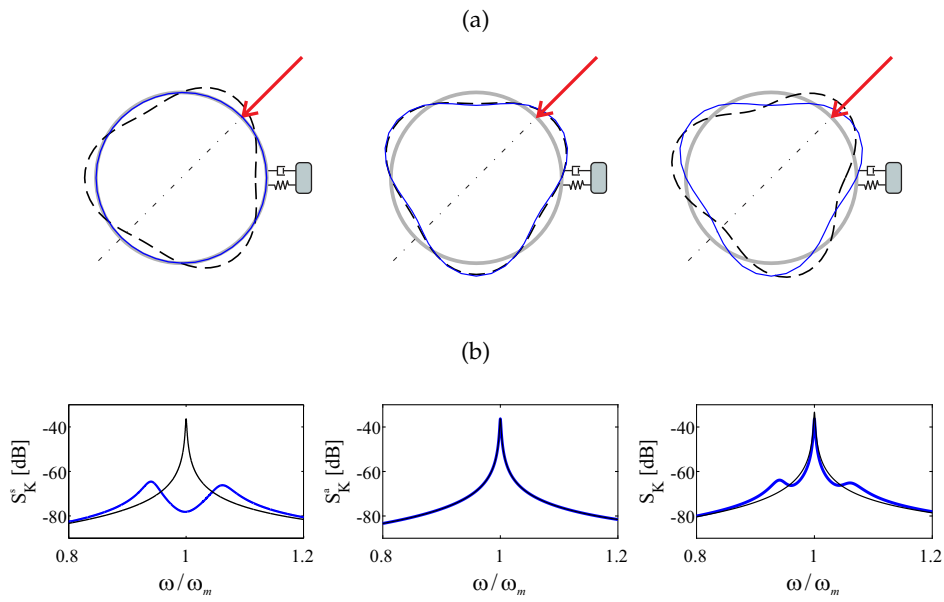
Figure 4.9: Middle-section deformation of the cylindrical shell, plot (a), and spectra of the flexural kinetic energy PSD, plot (b) for the symmetric (left), anti-symmetric (central) and global (right graphs) components when the TVA is placed on an anti-nodal position for the symmetric component.

(a)

(b)
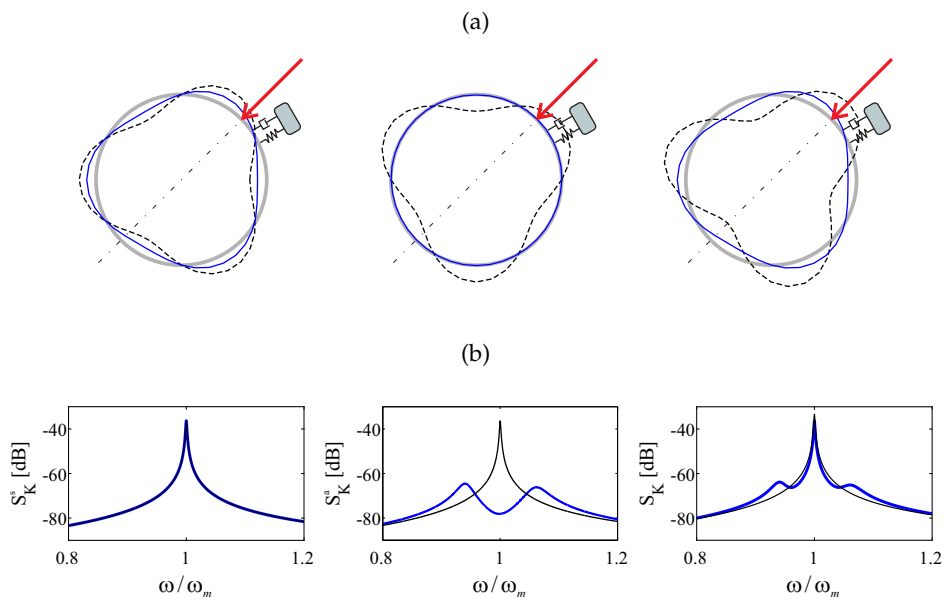
Figure 4.10: Middle-section deformation of the cylindrical shell, plot (a), and spectra of the flexural kinetic energy PSD, plot (b) for the symmetric (left), anti-symmetric (central) and global (right graphs) components when the TVA is placed on an anti-nodal position for the anti-symmetrical component.

This analysis suggests the use of two TVA, each of them placed on an anti-nodal position of the two components. The positions of the nodal and anti-nodal lines for a cylindrical shell are given in table 3.1 with reference of the zero angle coordinate shown in figure 2.1 (a). The definition of the origin of the circumferential coordinate is totally arbitrary, since the cylindrical shell has an infinite number of circumferential symmetry axes. The values of the nodal and anti-nodal circumferential positions given in table 3.1 are thus not absolute values, but relative values, since they depend on the circumferential position selected as the origin. The angular distance between two consecutive nodal and anti-nodal positions remains instead constant and does not depend on the circumferential position selected as the origin, but depends only on the circumferential modal index m_2.

Therefore two TVA are needed for the flexural control of a cylindrical shell when the excitation field does not allow the identification of the resulting orientation. Furthermore, the absolute angular positions of the two TVA are not important, but the relative position between them is fundamental. From the values reported in table 3.1, the angular distance between the TVA should be:

$$\Delta \vartheta_{Ak} = \left(k + \frac{1}{2} \right) \frac{\pi}{m_2}, \tag{4.25}$$

with $k = 0, 1, \ldots, m_2 - 1$. As an example, for the structural mode with $m_2 = 3$ shown in figures 4.7-4.12, the two TVAs should be separated along the circumference by an arc with angular aperture of either $\pi/6$ (30°), $\pi/2$ (90°) or $5\pi/6$ (150°). The vibration control effects of the two TVA placed on the cylinder with an angular distance given by equation (4.25) are shown in figure 4.11. Plot (a) shows the flexural displacement of the middle-section of the cylinder for the three possible configurations of the three TVA. With the two TVA optimally located, the displacements due to both components are reduced, and thus the resulting displacement is also reduced. This can also be seen in plot (b), where are shown the spectra of the flexural kinetic energy PSDs for the two components and for the resulting response. In this plot, since the three TVAs configurations give exactly the same spectra results, only the results due to one configuration is reported.

In figure 4.12 are shown the effects on the middle-section deflection (plot (a)) and on the spectra of the flexural kinetic energy PSD (plot (b))when two TVA are applied on the cylindrical shell but these are not separate by an angular aperture given by equation (4.25). The vibration control effect is slightly increased compared with the case of a single misplaced TVA, due to the addi-

(a)

(b)
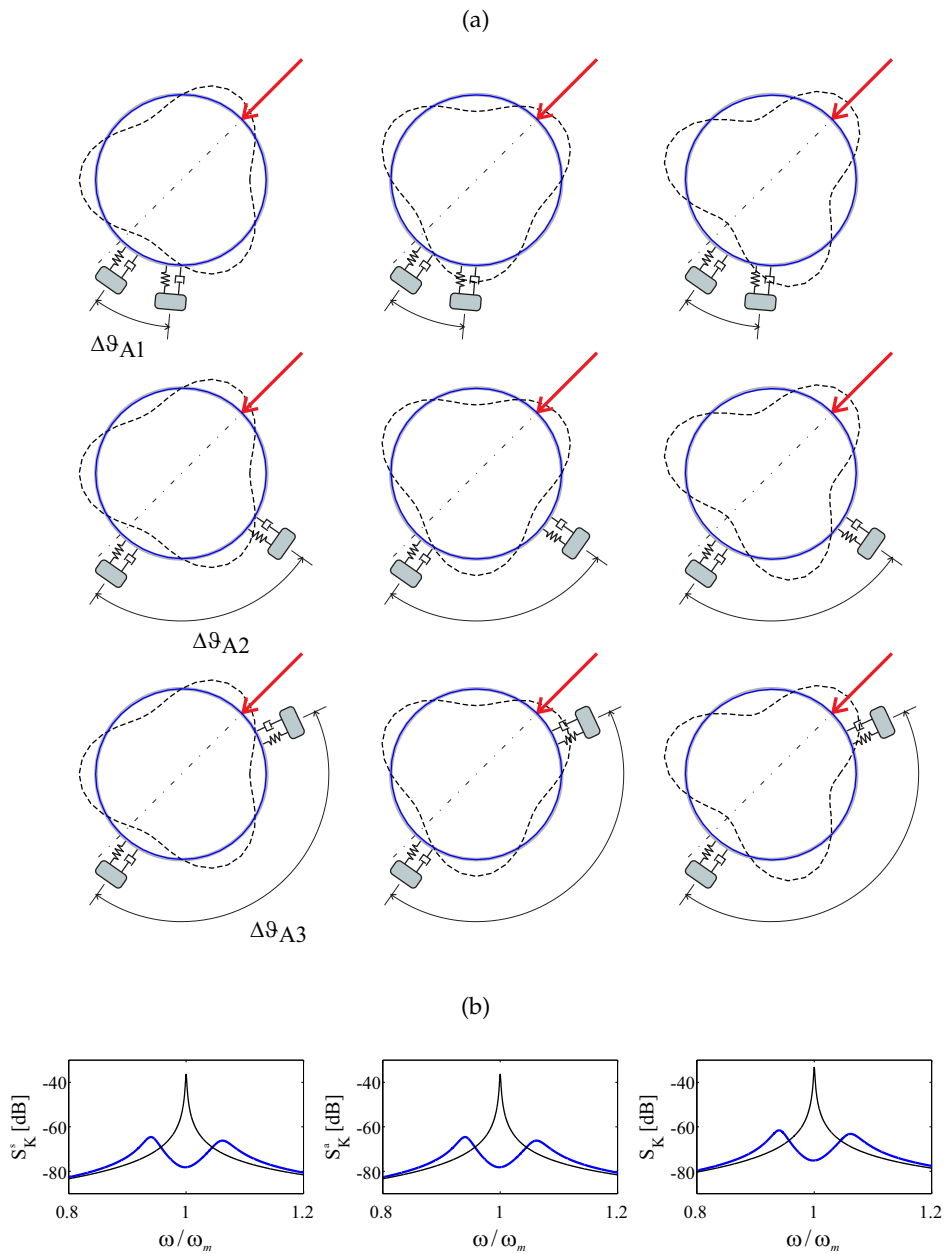
Figure 4.11: Middle-section deformation of the cylindrical shell, plot (a), and spectra of the flexural kinetic energy PSD, plot (b) for the symmetric (left), anti-symmetric (central) and global (right graphs) components when the two TVA are optimally positioned.

tional mass effect related to the mass of the second TVA. The two misplaced TVAs are not able to control the resonance peak of the structural mode, but they just reduce the amplitude of the resonance peak.

(a)

(b)
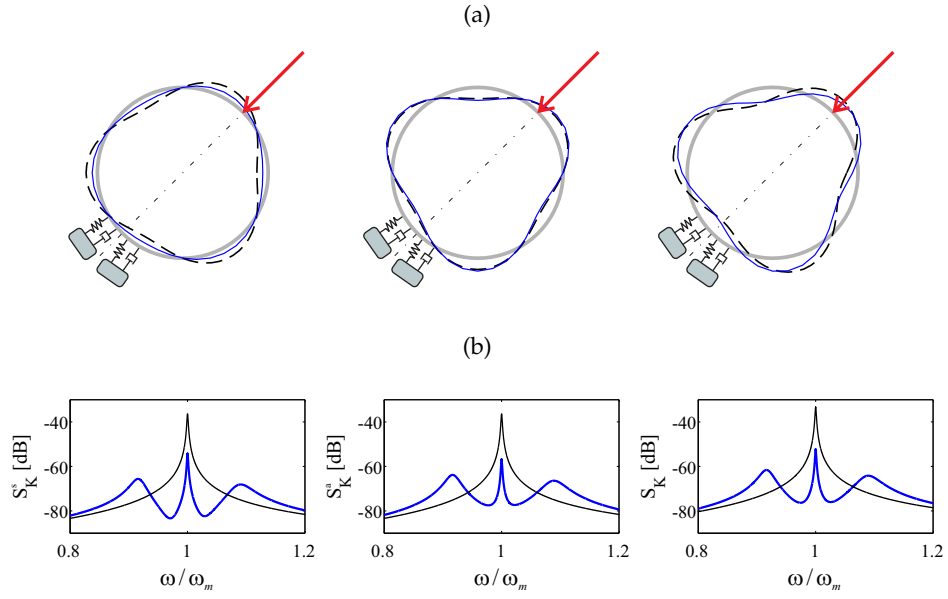
Figure 4.12: Middle-section deformation of the cylindrical shell, plot (a), and spectra of the flexural kinetic energy PSD, plot (b) for the symmetric (left), anti-symmetric (central) and global (right graphs) components when the two TVA are not optimally positioned.

4.6 COUPLED STRUCTURAL-ACOUSTIC-TVA RESPONSE

The derivation of the fully coupled structural-acoustic-TVA equation of motion is based on the mathematical procedure presented in section 3.8. For the sake of comprehensiveness, the structural equation of motion for the flexural displacement and the acoustic wave equation for the acoustic pressure is presented again.

According to the Donnell-Mushtari shell theory presented in chapter 3, the equation of motion for the flexural displacement of the cylindrical shell can be written as

$$D\nabla_s^8 w(\mathbf{x}_s,t) + \frac{Eh}{R^2}\frac{\partial^4 w(\mathbf{x}_s,t)}{\partial x^4} + \rho\, h\nabla_s^4\frac{\partial^2 w(\mathbf{x}_s,t)}{\partial t^2} = \nabla_s^4 f_r(\mathbf{x}_s,t), \qquad (4.26)$$

where $w(\mathbf{x}_s,t)$ is the flexural displacement of a point $\mathbf{x}_s = (x,\vartheta)$ on the cylindrical shell, ∇_s^2 is the two-dimensional Laplace operator in cylindrical coordinate defined in equation (3.19) and f_r represents the force term acting in the radial direction. The flexural displacements can be expressed with the finite modal summation of the *in vacuo* symmetric and anti-symmetric flexural mode shapes

for the simply supported cylinder, which can be arranged in the following matrix form:

$$w(\mathbf{x}_s, t) = \begin{bmatrix} \boldsymbol{\varphi}^s(\mathbf{x}_s) & \boldsymbol{\varphi}^a(\mathbf{x}_s) \end{bmatrix} \begin{Bmatrix} \mathbf{b}^s(t) \\ \mathbf{b}^a(t) \end{Bmatrix} = \boldsymbol{\varphi}(\mathbf{x}_s)\mathbf{b}(t), \qquad (4.27)$$

where the symmetric and anti-symmetric flexural natural modes are given in equations (3.51).

When the cylindrical structure is equipped with an array of TVA, the radial forcing term given in equation (4.26) is due to three components: first, the localised pressure exerted by the external rain-on-the-roof point forces $f_{R,i}(t)\delta(\mathbf{x}_s - \mathbf{x}_{s,i})$, with $i = 1, \ldots, N_R$, being N_R the number of uncorrelated rain-on-the-roof forces; second, the pressure distribution $p(\mathbf{x}_s, t)$ due to the cavity acoustic pressure and third, the localised forces generated at the absorbers footprints $f_{A,j}(t)\delta(\mathbf{x}_s - \mathbf{x}_{s,Aj})$, with $j = 1, \ldots, N_A$ being N_A the number of TVAs. Thus, the radial force per unit area exerted on the cylindrical shell can be expressed as follows:

$$f_r(\mathbf{x}_s, t) = \sum_{i=1}^{N_R} f_{R,i}(t)\delta(\mathbf{x}_s - \mathbf{x}_{s,i}) + p(\mathbf{x}_s, t) + \sum_{j=1}^{N_A} f_{A,j}(t)\delta(\mathbf{x}_s - \mathbf{x}_{s,Aj}), \qquad (4.28)$$

where $f_{R,i}$ and $f_{A,j}$ are the point forces produced by the rain-on-the-roof excitation field and by the TVAs, $\mathbf{x}_{s,i}$ and $\mathbf{x}_{s,Aj}$ are the position where the forces due to the excitation field and due to the TVA act and $\delta(\cdot)$ is the two-dimensional Dirac delta function in cylindrical coordinate whose definition is given in equation (3.65). As shown in figure 4.2, the mechanical fixed TVA is modelled as a base and seismic lumped masses, m_{bj} and m_{sj}, connected by the suspension spring, k_{Aj}, and damper, c_{Aj}, mechanical elements arranged in parallel. Thus, the forces produced by the TVAs on the cylinder are given by:

$$f_{A,j}(t) = -m_{bj}\ddot{w}_{bj}(t) + c_{Aj}\Delta\dot{w}_{Aj}(t) + k_{Aj}\Delta w_{Aj}(t), \qquad (4.29)$$

where

$$\Delta w_{Aj}(t) = w_{sj}(t) - w_{bj}(t) \qquad (4.30)$$

is the relative displacement between the base and seismic mass of the j-th TVA, being w_{sj} the displacement of the seismic mass and

$$w_{bj}(t) \equiv w(\mathbf{x}_{s,Aj}, t) \qquad (4.31)$$

the displacement of the base mass, which coincides with the radial displacement of the cylinder $w(\mathbf{x}_{s,Aj}, t)$ at the position $\mathbf{x}_{s,Aj}$ of the j-th TVA.

The acoustic wave equation for the cylindrical enclosure can be written as:

$$\nabla^2 p(\mathbf{x}, t) - \frac{1}{c_0^2} \frac{\partial^2 p(\mathbf{x}, t)}{\partial t^2} = -\rho_0 \frac{\partial q(\mathbf{x}, t)}{\partial t},$$ (4.32)

where $p(\mathbf{x}, t)$ is the acoustic pressure at a point $\mathbf{x} = (x, \vartheta, r)$ in the cylindrical enclosure, ∇^2 is the three-dimensional Laplace operator in cylindrical coordinates defined in equation (3.111) and $q(\mathbf{x}, t)$ is the monopole-type source term. The acoustic pressure is expressed with the finite modal summation of the symmetric and anti-symmetric acoustic mode shapes for the *rigidly-walled* cylindrical enclosure, which can be arranged in the following matrix form:

$$p(\mathbf{x}, t) = \begin{bmatrix} \boldsymbol{\psi}^s(\mathbf{x}) & \boldsymbol{\psi}^a(\mathbf{x}) \end{bmatrix} \begin{Bmatrix} \mathbf{a}^s(t) \\ \mathbf{a}^a(t) \end{Bmatrix} = \boldsymbol{\psi}(\mathbf{x}) \mathbf{a}(t)$$ (4.33)

where the symmetric and anti-symmetric acoustic natural modes are given in equations (3.128). In absence of any acoustic source in the enclosure, the source term $q(\mathbf{x}, t)$ in equation (4.32) is due to the flexural displacement of the cylindrical surface:

$$q(\mathbf{x}, t) = -2\ddot{w}(\mathbf{x}_s, t)\delta(r - R).$$ (4.34)

In addition to the structural equation of motion and the acoustic wave equation, also a set of equations of motion for the TVAs must be included in the fully coupled structural-acoustic-TVA equation of motion. Newton's second law applied to the seismic mass of the j-th TVA can be expressed as:

$$m_{sj}\ddot{w}_{sj}(t) = -c_{Aj}\Delta\dot{w}_{Aj}(t) - k_{Aj}\Delta w_{Aj}(t),$$ (4.35)

with $j = 1, 2, \ldots, N_A$.

To solve the equations of motion for the flexural structural waves, the acoustic waves and the TVA seismic masses given in equations (4.26), (4.32) and (4.35) , the following procedure is implemented:

1. the truncated modal summation expression for the flexural displacement given in equation (4.27) is inserted into equations (4.26), (4.29), (4.34) and (4.35);

2. the truncated modal summation expression for the acoustic pressure given in equation (4.33) is inserted into equations (4.28) and (4.32);

3. the resulting equation (4.29) is substituted into equation (4.28), which is then inserted into equation (4.26);

4. the resulting equation (4.34) is substituted into equation (4.32);

5. both sides of the resulting equation (4.26) are pre-multiplied by the column vector with the flexural modes $\boldsymbol{\varphi}(\mathbf{x}_s)$ and integrated over the surface of the cylindrical wall;

6. both sides of the resulting equation (4.32) are pre-multiplied by the column vector with the acoustic modes $\boldsymbol{\psi}^T(\mathbf{x})$ and integrated over the acoustic volume of the cylindrical enclosure.

This mathematical procedure leads to the following set of $2M + 2N + N_A$ ordinary differential equations, given in matrix form as:

$$
\begin{bmatrix} \overline{\mathbf{M}}_s & \mathbf{0} & \mathbf{0} \\ \mathbf{R} & \mathbf{Q} & \mathbf{0} \\ \mathbf{0} & \mathbf{0} & \mathbf{M}_A \end{bmatrix} \begin{Bmatrix} \ddot{\mathbf{b}}(t) \\ \ddot{\mathbf{a}}(t) \\ \ddot{\mathbf{w}}_A(t) \end{Bmatrix} + \begin{bmatrix} \overline{\mathbf{C}}_s & \mathbf{0} & -\mathbf{c}_A \\ \mathbf{0} & \mathbf{D} & \mathbf{0} \\ -\mathbf{c}_A^T & \mathbf{0} & \mathbf{C}_A \end{bmatrix} \begin{Bmatrix} \dot{\mathbf{b}}(t) \\ \dot{\mathbf{a}}(t) \\ \dot{\mathbf{w}}_A(t) \end{Bmatrix}
$$

$$
+ \begin{bmatrix} \overline{\mathbf{K}}_s & -\mathbf{S} & -\mathbf{k}_A \\ \mathbf{0} & \mathbf{H} & \mathbf{0} \\ -\mathbf{k}_A^T & \mathbf{0} & \mathbf{K}_A \end{bmatrix} \begin{Bmatrix} \mathbf{b}(t) \\ \mathbf{a}(t) \\ \mathbf{w}_A(t) \end{Bmatrix} = \begin{Bmatrix} \boldsymbol{\Phi}_s \\ \mathbf{0} \\ \mathbf{0} \end{Bmatrix} \mathbf{f}(t). \tag{4.36}
$$

Here

$$
\overline{\mathbf{M}}_s = \mathbf{M}_s + \boldsymbol{\Phi}_A^T \mathbf{m}_b \boldsymbol{\Phi}_A, \tag{4.37a}
$$

$$
\overline{\mathbf{C}}_s = \mathbf{C}_s + \boldsymbol{\Phi}_A^T \mathbf{C}_A \boldsymbol{\Phi}_A, \tag{4.37b}
$$

$$
\overline{\mathbf{K}}_s = \mathbf{K}_s + \boldsymbol{\Phi}_A^T \mathbf{K}_A \boldsymbol{\Phi}_A, \tag{4.37c}
$$

where $\mathbf{M}_s, \mathbf{C}_s$ and $\mathbf{K}_s$ are the structural modal inertia, damping and stiffness matrices given in equations (3.61) and (3.63), $\mathbf{m}_b$, $\mathbf{C}_A$ and $\mathbf{K}_A$ are the $N_A \times N_A$ diagonal matrices with the base masses m_{bj}, the damping parameters c_{Aj} and the stiffness parameters k_{Aj} of the N_A TVAs and

$$
\boldsymbol{\Phi}_A = \begin{bmatrix} \boldsymbol{\varphi}(\mathbf{x}_{s,A1}) \\ \vdots \\ \boldsymbol{\varphi}(\mathbf{x}_{s,AN_A}) \end{bmatrix} \tag{4.38}
$$

is the $N_A \times 2M$ matrix whose rows are formed by the modal amplitudes of the symmetric and anti-symmetric flexural structural modes at the positions $\mathbf{x}_{s,Aj}$ of the N_A TVAs. Also, $\mathbf{M}_A$ is the $N_A \times N_A$ diagonal matrix with the seismic masses

m_{sj} of the N_A TVAs, $\mathbf{Q}$, $\mathbf{D}$ and $\mathbf{H}$ are the acoustic modal inertia, damping and stiffness matrices given in equations (3.138), $\mathbf{R}$ and $\mathbf{S}$ are the acoustic-structural and the structural-acoustic coupling matrices and

$$\mathbf{c}_A = \mathbf{\Phi}_A^T \mathbf{C}_A, \tag{4.39a}$$

$$\mathbf{k}_A = \mathbf{\Phi}_A^T \mathbf{K}_A \tag{4.39b}$$

are the $2M \times N_A$ damping and stiffness coupling matrices between the structure and the TVAs. Finally, $\mathbf{\Phi}_s$, $\mathbf{f}(t)$ are the modal excitation matrix and the vector with the N_R rain on the roof force vector, given by equations (3.66) and (3.67) and the column vectors $\mathbf{b}(t)$, $\mathbf{a}(t)$, $\mathbf{w}_A(t)$ contain respectively the flexural modal amplitudes, the acoustic modal amplitudes and the displacements of the TVA seismic masses.

Equation (4.36) can be written in the following compact form:

$$\mathbf{M}\ddot{\mathbf{q}}(t) + \mathbf{C}\dot{\mathbf{q}}(t) + \mathbf{K}\mathbf{q}(t) = \mathbf{\Phi}\mathbf{f}(t) \tag{4.40}$$

where $\mathbf{q}(t) = \begin{bmatrix} \mathbf{b}^T(t) & \mathbf{a}^T(t) & \mathbf{w}_A^T(t) \end{bmatrix}^T$ and $\mathbf{M}$, $\mathbf{C}$, $\mathbf{K}$, $\mathbf{\Phi}$ are the global inertia, damping, stiffness and excitation modal matrices of the fully coupled structural-acoustic-TVA system.

4.6.1 Frequency domain formulation

As shown in section 3.8.2 of the previous chapter, a frequency domain formulation is derived from the time response of the coupled structural-acoustic-TVA system. The frequency domain analysis is usually adopted for noise and vibration problems subject to stationary random disturbances [28, 72, 99] and in this thesis the flexural kinetic energy PSD and the acoustic potential energy PSD [124, 125, 162] are used to established the global flexural and interior sound responses. The two PSD functions can be written as [28, 60, 64, 65]:

$$S_K(\omega) = \frac{1}{2}\rho h \int_S \lim_{T \to \infty} E\left[\frac{1}{T}\dot{w}^*(\mathbf{x}_s, \omega)\dot{w}(\mathbf{x}_s, \omega)\right] \mathrm{d}S \quad \text{and} \tag{4.41a}$$

$$S_P(\omega) = \frac{1}{2\rho_0 c_0^2} \int_{V_c} \lim_{T \to \infty} E\left[\frac{1}{T}p^*(\mathbf{x}, \omega)p(\mathbf{x}, \omega)\right] \mathrm{d}V. \tag{4.41b}$$

Equations (4.41) are analogous to (3.173) and the mathematical procedure is the same as in section 3.8.2, therefore a reduced formulation is presented here

to highlight the differences with the previous formulation. Equations (4.41) can be expressed as

$$S_K(\omega) = \frac{1}{2} m_c \mathrm{Tr}\left[\mathbf{S_{bb}}(\omega)\right] \quad \text{and} \tag{4.42a}$$

$$S_P(\omega) = \frac{V_c}{2\rho_0 c_0^2} \mathrm{Tr}\left[\mathbf{S_{aa}}(\omega)\right], \tag{4.42b}$$

where, for a linear and time invariant system, the matrices $\mathbf{S_{bb}}(\omega)$ and $\mathbf{S_{aa}}(\omega)$ containing the PSDs of modal structural velocities and the modal pressure amplitudes. These matrices are defined as

$$\mathbf{S_{bb}}(\omega) = \boldsymbol{\Lambda}\boldsymbol{\beta}\mathbf{Y}(\omega)\boldsymbol{\Phi}\mathbf{S_{ff}}(\omega)\boldsymbol{\Phi}^T\mathbf{Y}^H(\omega)\boldsymbol{\beta}^T \quad \text{and} \tag{4.43a}$$

$$\mathbf{S_{aa}}(\omega) = \frac{1}{\omega^2}\boldsymbol{\Gamma}\boldsymbol{\alpha}\mathbf{Y}(\omega)\boldsymbol{\Phi}\mathbf{S_{ff}}(\omega)\boldsymbol{\Phi}^T\mathbf{Y}^H(\omega)\boldsymbol{\alpha}^T. \tag{4.43b}$$

Here $\mathbf{Y}(\omega)$ is the modal mobility matrix of the coupled structural-acoustic-TVA system, obtained from the Fourier transform of equation (4.40) as:

$$\mathbf{Y}(\omega) = j\omega\left[-\omega^2\mathbf{M} + j\omega\mathbf{C} + \mathbf{K}\right]^{-1} \tag{4.44}$$

and

$$\boldsymbol{\beta} = \begin{bmatrix} \mathbf{I}_{2M\times 2M} & \mathbf{0}_{2M\times 2N} & \mathbf{0}_{2M\times N_A} \end{bmatrix} \tag{4.45a}$$

$$\boldsymbol{\alpha} = \begin{bmatrix} \mathbf{0}_{2N\times 2M} & \mathbf{I}_{2N\times 2N} & \mathbf{0}_{2N\times N_A} \end{bmatrix}, \tag{4.45b}$$

where $\mathbf{I}$ and $\mathbf{0}$ are respectively identity and zero matrices with the dimensions indicated by the subscripts. Finally, the matrix $\mathbf{S_{ff}}(\omega)$ contains the PSD functions of the 24 uncorrelated white noise forces acting on the cylindrical shell and is given by the 24×24 identity matrix $\mathbf{I}$.

By substituting equations (4.43) into equations (4.42), the cylinder flexural kinetic energy and the acoustic potential energy PSDs are given by:

$$S_K(\omega) = \frac{1}{2} m_c \mathrm{Tr}\left[\boldsymbol{\Lambda}\boldsymbol{\beta}\mathbf{Y}(\omega)\boldsymbol{\Phi}\mathbf{I}\boldsymbol{\Phi}^T\mathbf{Y}^H(\omega)\boldsymbol{\beta}^T\right] \quad \text{and} \tag{4.46a}$$

$$S_P(\omega) = \frac{V_c}{2\rho_0 c_0^2 \omega^2} \mathrm{Tr}\left[\boldsymbol{\Gamma}\boldsymbol{\alpha}\mathbf{Y}(\omega)\boldsymbol{\Phi}\mathbf{I}\boldsymbol{\Phi}^T\mathbf{Y}^H(\omega)\boldsymbol{\alpha}^T\right]. \tag{4.46b}$$

4.6.2 *Simulation study*

This section discusses the vibration and sound control effects produced by arrays of 12 and 18 fixed TVAs. The values of the base and seismic mass of each TVA are reported in table 4.1, thus the total mass for the two arrays the TVAs corresponds respectively to 5% and 8% of the cylinder total mass.

The 12 TVAs are tuned in pairs to control the 3rd, 5th, 7th, 10th, 19th and 29th structural modes, whose resonance frequencies are highlighted by the orange arrows in plots (a) and (c) of figure 4.14. The 18 TVAs are instead tuned in pairs to control the 1st, 3rd, 5th, 7th, 10th, 19th, 25th, 29th and 35th structural flexural modes, whose resonance frequencies are highlighted by the cyan arrows in plots (b) and (d) of figure 4.14. These modes were chosen since, as reported in table B.1 of appendix B, where the structural-acoustic coupling is analysed, they are characterised by the highest coupling coefficient. The coupling effects between these structural modes and the associated acoustic ones give rise to the highest resonance peaks in the acoustic response, as discussed in section 3.8.3 and shown in the bottom plots of figure 4.14.

The damping and stiffness parameters of the 12 and 18 TVAs, c_{Aj} and k_{Aj}, are derived from the optimal damping and frequency ratio given in equations (4.11), according to the time-averaged kinetic energy minimisation criterion proposed by Zilletti *et al.* [159]. For each TVA these parameters are thus given by

$$c_{Aj} = 2\,\zeta_{opt,j}\,m_s\,\omega_{Aj} \quad \text{and} \tag{4.47a}$$
$$k_{Aj} = m_s\,\omega_{Aj}^2, \tag{4.47b}$$

where ω_{Aj} is the angular tuning frequency, given by

$$\omega_{Aj} = \nu_{opt,j}\,\omega_{s,T}, \tag{4.48}$$

being $\omega_{s,T}$ the structural natural frequency of the target modes. The tuning frequencies and the damping ratios for the fixed tuned Vibration Absorbers are reported in table 4.3. The positions of the TVAs are here reported as well. These positions where chosen in order to locate the TVAs in two axial sectors, corresponding at 0.4 and 0.6 times the length of the cylinder. The circumferential position of each couple of TVAs are selected in order to satisfy the conditions discussed in section 4.5. The positions of the TVAs are also schematically shown in Figure 4.13.

Table 4.3: TVA parameters for the fixed tuned operation mode.

TVA n	Reference mode m	Position (x_A, ϑ_A)	Tuning frequency f_A [Hz]	Damping ratio ζ_A [%]
1	10	$(0.4L, \pi/7)$	49.8	5.8
2		$(0.6L, 15\pi/14)$		
3	19	$(0.4L, 0)$	65.1	5.8
4		$(0.6L, 13\pi/12)$		
5	29	$(0.4L, -\pi/5)$	89.2	5.8
6		$(0.6L, 9\pi/10)$		
7	3	$(0.4L, \pi/2)$	31.2	5.8
8		$(0.6L, 37\pi/24)$		
9	5	$(0.4L, 4\pi/9)$	33.9	5.8
10		$(0.6L, 3\pi/2)$		
11	7	$(0.4L, 5\pi/8)$	39.9	5.8
12		$(0.6L, 23\pi/16)$		
13	1	$(0.6L, -\pi/11)$	30.1	5.8
14		$(0.4L, 21\pi/22)$		
15	25	$(0.6L, 0)$	77.7	5.8
16		$(0.4L, 43\pi/42)$		
17	35	$(0.6L, \pi/23)$	92.9	5.8
18		$(0.4L, 45\pi/46)$		
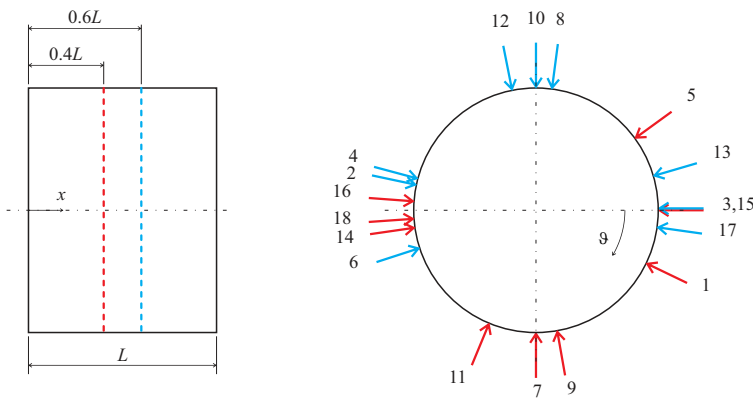
Figure 4.13: Schematic representation of the positions of the TVAs on the cylindrical structure. On the left image the two axial positions of the TVAs are represented with the red ($0.4L$) and blue ($0.6L$) dashed lines. The red and blue arrows on the right image indicated the angular position of the TVAs placed at $0.4L$ and $0.6L$, respectively.

In figure 4.14 are shown the 20 - 100 Hz flexural kinetic energy PSDs (top plots) and the 20 - 100 Hz acoustic potential energy PSDs of the plain cylinder (thin black lines) and of the cylinder equipped with an array of 12 (thick orange lines in left plots) and 18 (thick cyan lines in right plots) fixed TVAs.

The thick orange line in plot (a) of figure 4.14 shows that, when the cylinder is equipped with 12 fixed TVAs, the structural response is effectively reduced by 7 to 10 dB at the targeted resonance frequencies below 60 Hz. Instead, smaller reductions of the order of 2 dB are produced at the targeted resonance frequencies above 60 Hz. This effect could be due to the high modal overlap factor [99, 123, 126] that characterises thin cylindrical structures. The thick orange line in plot (c) of figure 4.14 shows that the 12 fixed TVAs effectively control the acoustic response at all the target resonance frequencies in the 20-100 Hz band by values comprised between 5 and 12 dB. This is because the targeted frequencies were selected considering those structural modes that better couple to the interior acoustic field.
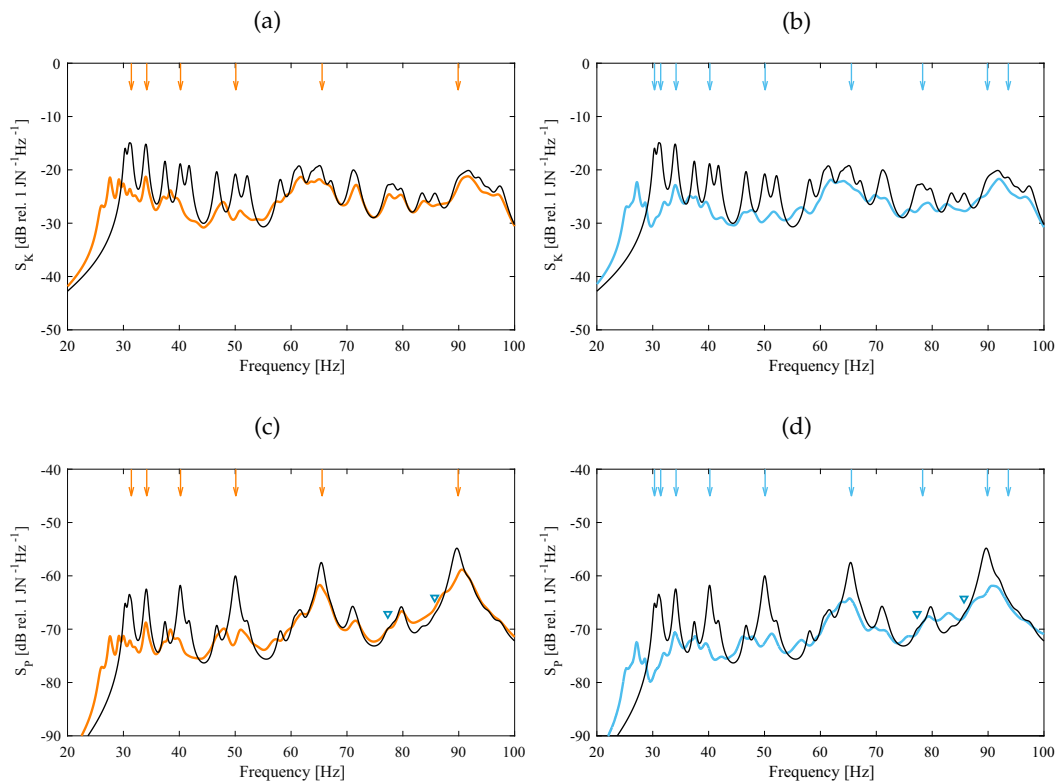
Figure 4.14: Spectra of the flexural kinetic energy PSD (top plots) and acoustic potential energy PSD (bottom plots) without TVAs (thin solid black lines), with 12 fixed Tuned Vibration Absorbers (thick orange lines in plots (a) and (c)) and with 18 fixed Tuned Vibration Absorbers (thick cyan lines in plots (b) and (d)).

The thick cyan line in plot (b) of figure 4.14 shows the effects produced by the array of 18 fixed TVAs. Compared to the 12 TVAs, the 18 fixed tuned TVAs further reduce the flexural response to values comprised between 10 and 15 dB at the target frequencies below 60 Hz and to values comprised between 3 to 5 dB at the target resonance frequencies above 60 Hz. Moreover, as shown by the thick cyan line in plot (d) of figure 4.14, the 18 fixed TVA substantially reduce the acoustic response at all targeted resonance frequencies by values comprised between 8 and 20 dB. Also in this case, this has to be attributed to the fact that the target resonances of the 18 fixed TVA were selected considering those structural modes that better couple to the interior acoustic field.

It is worth noting two peculiar characteristics of the structural and acoustic responses when the cylinder is equipped with the TVAs. Firstly, the spectra of both the structural and the acoustic responses are characterised by shifts to lower frequencies of the first few resonances. This effect could be explained considering the mass effect produced by the TVAs, which occurs at frequencies both below and above the fundamental natural frequency of the TVA, as discussed in section 4.2. Secondly, both structural and acoustic spectra are characterised by control spillover effects, which however have little impact on the overall control performances of the TVAs since they occur in correspondence to the troughs between resonances.

It is again important to highlight that these results are obtained by accurately tuning the TVAs to the structural resonant modes in the 20-100 Hz frequency band that better couple to the acoustic modes of the interior pressure field. This is relative simple to implement in a simulation study as the one proposed in this thesis. On the contrary, it turns out to be a cumbersome and impracticable task in real applications because it would require a sophisticated system identification procedure during the installation of the TVAs. Furthermore, in most practical applications, an online tuning system is needed to track the variations of the dynamic response of the cylinder due to changes of the working conditions, such as temperature changes, pressuring and tensioning effects.

4.7 CHAPTER CONCLUDING REMARKS

This chapter presented a theoretical and simulation study on classical mechanical fixed tuned vibration absorbers connected to a thin cylindrical shell to control its flexural and internal acoustic response. A fully coupled structural-acoustic-TVA analytical model was presented, which was developed considering the Modal Interaction Model.

The first part of the chapter was devoted to analyse the dynamic characteristic of the fixed TVA. The dynamic response of the device was presented in terms of the base impedance, which results an appropriate feature to describe the mechanical behaviour of TVA. Several tuning criteria presented in literature are reported and the differences between them was shown.

A simplified model composed by a single mode of the cylindrical shell and a TVA was used to obtain general guidelines for the positioning of TVAs in cylindrical structures. This study shows that when a cylindrical structure is subject to an excitation field which orients the flexural deflection of the structure in an unpredictable direction, two TVAs are needed to control the response at each resonance frequency of the cylinder. A simple relation for the angular positioning of the TVA was derived.

Finally, the last part of the chapter deals with the simulation study of the structural and acoustic responses of the cylindrical shell and enclosure. The effects produced by arrays of 12 and 18 fixed tuned absorbers were examined. The TVAs were accurately tuned in pairs to structural frequencies related to flexural modes characterised by the highest structural-acoustic coupling effects in the 20-100 Hz frequency band. The simulation results show how the fixed TVA can be used to effectively control both the structural and the acoustic responses.

5

TIME-VARYING TUNEABLE VIBRATION ABSORBER: RL
SHUNTED ELECTROMAGNETIC TRANSDUCER

This chapter deals with the simulation study concerning the low frequency control of the flexural vibration and internal acoustic field of a thin cylindrical structure subject to a rain on the roof white noise excitation and equipped with an array of time-varying shunted electro-magnetic vibration absorbers.

The constitutive equation governing the electro-magnetic transducer is first presented. An idealised transducer is used to derive the electro-mechanical analogies, which allows to describe in mechanical terms the effect of an electrical element used to shunt the electro-magnetic transducer.

The sweeping operation mode is then described, focusing on the description of the period law by which the natural frequency of the transducer is varied. The time variations of the shunt parameters is then derived.

Contents

5.1   INTRODUCTION

During the last years several studies have considered the possibility of using time-varying vibration absorbers to control the flexural response of thin structures in a broadband frequency range [47, 56, 57, 59, 62].

Two operation modes were presented. In the first one, called switching operation mode, the stiffness and damping parameters are iteratively set to pairs of values so that the natural frequency and the damping ratio of the absorber are switched to cyclically control the response of multiple resonant modes. In the second operation mode, referred as sweeping operation mode, the parameters are continuously swept between given ranges to control the resonance response of all the natural modes of the hosting structure in a given frequency band.

Also if the two operation modes appear very similar, they require a different *a priori* knowledge of the hosting structure. Indeed, for the switching operation mode a fully knowledge of the dynamic response of the hosting structure is required in order to tune the various steps of the switch to the targeted resonance responses. On the other hand, the sweeping operation mode can blindly operate in a given frequency range, without the need of a precise system identification of the hosting structure.

Electro-magnetic transducers are well-known device used mainly for active control [155, 170–176] but they have also been used for vibration isolation [177] and for adaptive and passive vibration control using a RC shunt circuit [178–180]. Also, a recent study showed some preliminary results on the possibility of using a voice coil transducer for the realisation of a time-varying mechanical vibration absorber [57].

In this chapter the implementation of time-varying shunted electro-magnetic vibration absorbers for broadband noise and vibration control is considered. The chapter begins with a description of the model of the electro-magnetic transducer, recalling the fundamental physical laws that govern the electro-mechanical transduction phenomenon. The mechanical response of the transducer is then assessed in terms of the transducer base impedance introduced in the previous chapter. This mechanical property is expressed in terms of the electrical parameters that characterise the shunt circuit.

An idealised coil-magnet transducer is used to obtain an electro-mechanical analogy scheme, which allows the derivation of the equivalent mechanical effect produced by electrical shunt elements. The elementary passive components are first considered and the results are used to obtain the mechanical equivalent effect of series and parallel of these elements.

The results of the electro-mechanical analogy study lead to the design of an optimal RL shunt circuit, which permits an independent tuning of the damping and stiffness parameters of the shunted TVA. Simple formulas are derived for the selection of the proper electrical parameters of the shunt for a given mechanical resonance frequency and damping ratio of the device.

The last part of the chapter is devoted to the analysis of the shunted electro-magnetic absorber operating in the sweeping mode. A control law for the time variation of the resonance frequency of the absorber is presented, which leads to a particular time variation of the shunt inductance and resistance. The effectiveness of noise and control properties of the sweeping TVA are assessed considering arrays of 12 and 18 devices mounted on the thin cylindrical shell coupled with the interior sound field presented in the previous chapters.

In reference [56] the authors suggest to use the prefix *tuneable* to describe the semi-active or adaptive absorbers. To avoid confusion and misinterpretations, in this chapter the electro-magnetic transducers operating in the sweeping mode are referred as sweeping TVA.

5.2 ELECTRO-MAGNETIC TRANSDUCER MODEL

An electro-mechanical transducer is a device which converts energy from mechanical to electrical form and vice versa. There exist two main categories of transducers, in the first type energy can only be transferred from one form to the other and in the second type energy can also be stored, either in mechanical or electrical form [181].

An electro-magnetic transducer (also called voice-coil or moving-coil transducer) is an energy transformer in which energy is converted from electrical to mechanical (and vice versa) through the interaction of a permanent magnet and a coil. Over the years, several configurations have been adopted to the practical realisation of the electro-magnetic transducer [182]. As shown in figure 5.1 (a), the electro-magnetic transducer considered in this thesis is composed by a cylindrical permanent magnet which is encircled by a ferromagnetic cylindrical element in which the coil is rigidly fixed. The two elements are connected *via* torsional springs, which provide a soft axial stiffness and a much higher transverse stiffness [183]. Figure 5.1 (b) shows the lumped parameter scheme used to model the electro-magnetic transducer. It is composed by base and seismic masses, m_b and m_s, which represent the mass of the inner magnet and the mass of the outer yoke and coil assembly, respectively. The stiffness and

damping effects are modelled with a spring and damper elements in parallel having stiffness k and damping c respectively.
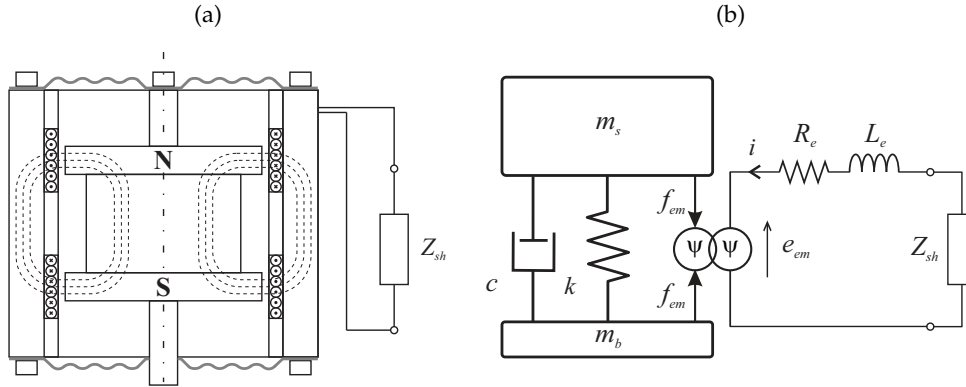
Figure 5.1: Sketch (a) and equivalent lumped parameter model (b) for the shunted electro-magnetic transducer.

The transduction effect is modelled with the electro-mechanical coupling coefficient ψ [184–186], furthermore the resistive and inductive effects of the coil are modelled with a resistance R_e and inductance L_e connected in series [181, 186, 187]. The mechanical and electrical properties of the transducer are reported in table 5.1.

Table 5.1: Physical properties of the open-circuited electro-magnetic transducer.

Parameter	Symbol	Value	
Seismic mass	m_s	115	[g]
Base mass	m_b	185	[g]
Natural frequency	f_A	20	[Hz]
Damping ratio	ζ_A	0.2	[-]
Coil resistance	R_e	12	[Ω]
Coil inductance	L_e	4.35	[mH]
Transduction coefficient	ψ	22.5	[N/A]

The constitutive equations which describe the two transduction effects follow from Faraday and Lorentz force laws [186]. Faraday's law stated that the potential increment $\mathrm{d}e_{em}$ over the elementary length $\mathrm{d}\mathbf{l}$ of the coil, induced by the relative motion between the coil and the magnet is:

$$\mathrm{d}e_{em} = \Delta\dot{\mathbf{w}}_A \times \mathbf{B} \cdot \mathrm{d}\mathbf{l}, \tag{5.1}$$

where $\Delta\dot{\mathbf{w}}_A = \dot{\mathbf{w}}_s - \dot{\mathbf{w}}_b$ is the relative velocity of the coil and the magnet, being $\dot{\mathbf{w}}_s$ and $\dot{\mathbf{w}}_b$ the velocities of the seismic and base masses, and $\mathbf{B}$ is the permanent magnetic flux. As shown in plot (a) of figure 5.1, the magnetic flux is radial, the two elements are allowed to move only in the axial direction and the coil is winded up along the circumference of the cylindrical outer case, thus the three quantity in equation (5.1) are mutually orthogonal, yielding:

$$\mathrm{d}e_{em} = -\Delta\dot{w}_A B \mathrm{d}l. \tag{5.2}$$

According to Lorentz's force law, when a small charge $\mathrm{d}q$ moves with a velocity $\mathbf{v}$ in an magnetic field $\mathbf{B}$, it results subject to a force given by:

$$\mathrm{d}\mathbf{f}_{em} = \mathrm{d}q\,\mathbf{v} \times \mathbf{B}. \tag{5.3}$$

Assuming that the small charge is constrained to move in a conductor, the product of the charge and velocity is equal to the electric current flowing in the conductor multiplied by the elementary length of the conductor:

$$\mathrm{d}\mathbf{f}_{em} = i\mathrm{d}\mathbf{l} \times \mathbf{B}. \tag{5.4}$$

Considering again the sketch of the electro-magnetic transducer shown in figure 5.1 (a), the Lorentz force results in the axial direction, thus equation (5.4) could be written as:

$$\mathrm{d}f_{em} = -iB\mathrm{d}l. \tag{5.5}$$

Integrating equations (5.2) and (5.5) over the length $l = 2\pi rn$ of the coil, being n the number of turns of the coil around the magnet, yields:

$$e_{em} = -\Delta\dot{w}_A B l \quad \text{and} \tag{5.6a}$$
$$f_{em} = -iBl. \tag{5.6b}$$

Defining the electro-mechanical transduction coefficient as

$$\psi = Bl, \tag{5.7}$$

the constitutive equations for the electro-magnetic transducer could be written as:

$$e_{em} = -\psi\Delta\dot{w}_A \quad \text{and} \tag{5.8a}$$
$$f_{em} = -\psi i. \tag{5.8b}$$

The mechanical behaviour of the electro-magnetic transducer, when it is connected to a shunt circuit as shown in plot (b) of figure 5.1, could be revised in terms of the base impedance introduced in section 4.2 of the previous chapter. In this case, in addition to the Newton's law for the base and seismic masses, also the Kirchhoff's voltage law should be inserted in the formulation:

$$m_b \ddot{w}_b = k \left(w_s - w_b \right) + c \left(\dot{w}_s - \dot{w}_b \right) + f_{em} + f_b, \tag{5.9a}$$

$$m_s \ddot{w}_s = -k \left(w_s - w_b \right) - c \left(\dot{w}_s - \dot{w}_b \right) - f_{em}, \tag{5.9b}$$

$$e_{em} + R_e i + L_e \frac{di}{dt} + Z_{sh} i = 0. \tag{5.9c}$$

Substituting equation (5.8b) into equations (5.9a) and (5.9b) and substituting equation (5.8a) into equation (5.9c) and considering the complex amplitudes of the time-harmonic functions gives:

$$\left(j\omega m_b + c + \frac{k}{j\omega} \right) \dot{w}_b(\omega) = \left(c + \frac{k}{j\omega} \right) \dot{w}_s(\omega) - \psi I(\omega) + f_b(\omega) \tag{5.10a}$$

$$\left(j\omega m_s + c + \frac{k}{j\omega} \right) \dot{w}_s(\omega) = \left(c + \frac{k}{j\omega} \right) \dot{w}_b(\omega) + \psi I(\omega) \tag{5.10b}$$

$$\psi \left(\dot{w}_s(\omega) - \dot{w}_b(\omega) \right) = - \left(R_e + j\omega L_e + Z_{sh} \right) I(\omega) \tag{5.10c}$$

Defining the electrical impedance of the series of the inherent resistance and inductor and the shunt circuit as:

$$Z_{el} = R_e + j\omega L_e + Z_{sh}, \tag{5.11}$$

from equation (5.10c) the complex amplitude of the current flowing in the coil result:

$$I(\omega) = -\frac{\psi}{Z_{el}} \left(\dot{w}_s(\omega) - \dot{w}_b(\omega) \right). \tag{5.12}$$

Substituting this expression in equations (5.10a) and (5.10b), gives

$$(Z_{mb} + Z_s) \, \dot{w}_b(\omega) = Z_s \dot{w}_s(\omega) + \psi \frac{\psi}{Z_{el}} \left(\dot{w}_s(\omega) - \dot{w}_b(\omega) \right) + f_b(\omega) \tag{5.13a}$$

$$(Z_{ms} + Z_s) \, \dot{w}_s(\omega) = Z_s \dot{w}_b(\omega) - \psi \frac{\psi}{Z_{el}} \left(\dot{w}_s(\omega) - \dot{w}_b(\omega) \right) \tag{5.13b}$$

where $Z_{mb} = j\omega m_b$ is the impedance of the base mass, $Z_{ms} = j\omega m_s$ is the impedance of the seismic mass and $Z_s = c + k/(j\omega)$ is the impedance of the

mechanical suspension. From equation (5.13b), the complex amplitude of the velocity of the seismic mass is derived as:

$$\dot{w}_s(\omega) = \frac{\left(Z_s + \dfrac{\psi^2}{Z_{el}}\right)}{\left(Z_{m_s} + Z_s + \dfrac{\psi^2}{Z_{el}}\right)}\dot{w}_b(\omega),$$ (5.14)

which, substituted in equation (5.13a), gives:

$$\left[Z_{m_b} + \frac{Z_{m_s}\left(Z_s + \dfrac{\psi^2}{Z_{el}}\right)}{\left(Z_{m_s} + Z_s + \dfrac{\psi^2}{Z_{el}}\right)}\right]\dot{w}_b(\omega) = f_b(\omega).$$ (5.15)

The base impedance of the shunted electro-magnetic transducer results thus given by [64, 65]:

$$Z_b(\omega) = \frac{f_b(\omega)}{\dot{w}_b(\omega)} = Z_{m_b} + \frac{Z_{m_s}\left(Z_s + \dfrac{\psi^2}{Z_{el}}\right)}{\left(Z_{m_s} + Z_s + \dfrac{\psi^2}{Z_{el}}\right)}.$$ (5.16)

This result shows that an electric shunt circuit could be used to modify the mechanical behaviour of the transducer. In figure 5.2 are shown the base impedance FRFs (magnitude top plot and phase bottom plot) of the open- (thin solid black lines) and short-circuited transducer (thick solid green lines). When the device operates in the open-circuit condition, the electrical impedance of shunt circuit results $Z_{sh} = \infty$, yielding $\psi^2/Z_{el} = 0$. The open-circuited transducer behaves thus like the purely mechanic TVA described in section 4.2 of the previous chapter.

When the transducer operates in the short-circuited mode, it presents the mass behaviour at frequencies below and well above the resonance frequency. However, as will be explained in the next section, the mechanical effect of the inherent coil resistance and inductance corresponds to a damping effect which smoothens the resonance peak of the transducer base impedance.

5.3 ELECTRO-MECHANICAL ANALOGIES

In this section the mechanical effect produced by elementary shunts connected to an idealised coil-magnet transducer are first analysed. The results
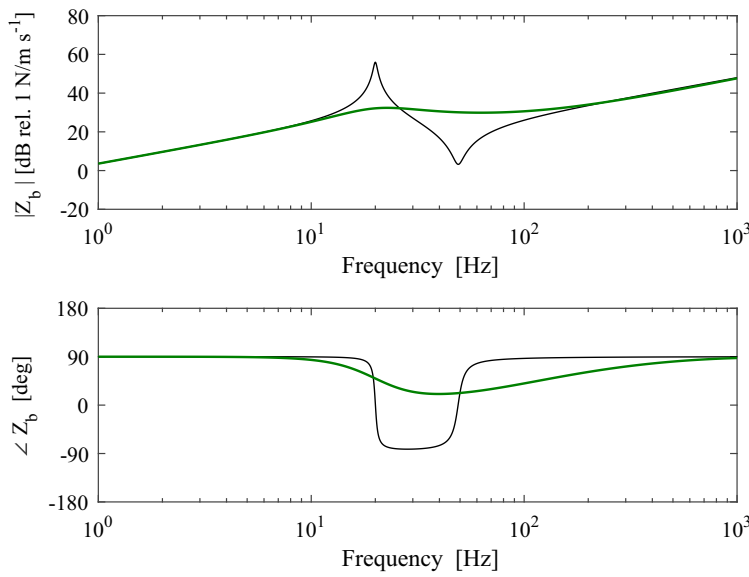
Figure 5.2: Base impedance FRFs (amplitude in the top plot and phase in the bottom plot) of the open- (thin solid black lines) and short-circuited (thick solid green lines) electro-magnetic transducer.

here reported represent an extension of the ones published by the author in [64, 65]. In figure 5.3 is shown the model used in the preliminary study. It consists of an electro-magnetic two poles element, which is composed by two massless elements connected via an idealised coil-magnet electro-mechanical transducer, whose passive mechanical and electrical effects are neglected. The idealised transducer is connected to an electrical shunt component.
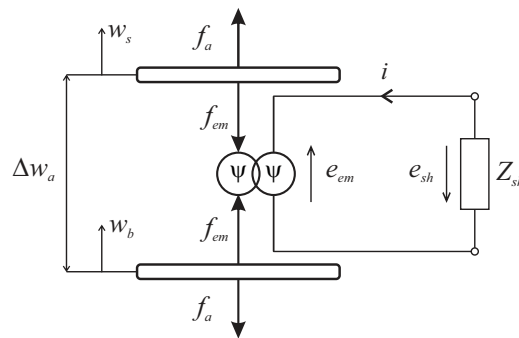
Figure 5.3: Model of the idealised coil-magnet transducer with an electrical shunt.

The equilibrium condition between the pair of external reactive forces f_a applied to the massless elements and the electro-magnetic forces f_{em} can be expressed as:

$$f_a(t) - f_{em}(t) = 0. \tag{5.17}$$

Kirchhoff's voltage law applied to the electric network gives:

$$e_{em}(t) + e_{sh}(t) = 0, \tag{5.18}$$

where e_{em} is the transducer back electromotive force and e_{sh} is the voltage drop across the shunt impedance. Substituting equation (5.8b) into equation (5.17) and considering the complex amplitudes of time-harmonic functions gives:

$$f_a(\omega) = -\psi I(\omega). \tag{5.19}$$

Also, substituting equation (5.8a) into equation (5.18) leads to the following equation:

$$Z_{sh}(\omega)I(\omega) = -\psi \Delta \dot{w}_A(\omega), \tag{5.20}$$
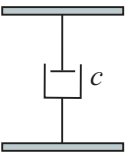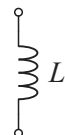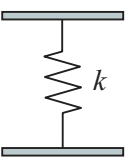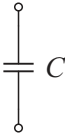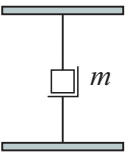
where the voltage drop produced by the shunt is expressed as $e_{sh}(\omega) = Z_{sh}(\omega)I(\omega)$, being $Z_{sh}(\omega)$ the electrical impedance of the shunt. Substitution of equation (5.20) into equation (5.19) leads to the equivalent mechanical impedance effect produced by the shunted idealised coil magnet [127, 158]:

$$Z_{mec}(\omega) = \frac{f_a(\omega)}{\Delta \dot{w}_A(\omega)} = \frac{\psi^2}{Z_{sh}(\omega)}. \tag{5.21}$$

When an electrical resistance is used as shunt element, characterised by an electrical impedance $Z_{sh} = R$, the equivalent mechanical impedance results $Z_{mec} = \psi^2/R$, which corresponds to the mechanical impedance of a damper [127]. If the idealised electro-mechanical device is shunted with an inductor, whose electrical impedance is given by $Z_{sh}(\omega) = j\omega L$, the equivalent mechanical impedance results given by $Z_{mec}(\omega) = \psi^2/(j\omega L)$, which corresponds to the mechanical behaviour of a spring. Finally, when a capacitor is connected to the idealised coil-magnet transducer, characterised by an electrical impedance given by $Z_{sh}(\omega) = 1/(j\omega C)$, the equivalent mechanical effect results $Z_{mec}(\omega) = j\omega \psi^2 C$, thus a mass-like behaviour. These results are summarised in table 5.2.

It is interesting to note that to obtain a large damping and stiffness effect, a small resistance and inductance is respectively required, while to obtain a large mass effect a large value of the capacitance is required.

Table 5.2: Mechanical equivalent effects produced by shunt of electric elements connected to the idealised coil-magnet electro-mechanical transducer. Adapted from [64, 65].

Element	Scheme	Electrical Impedance Z_{sh}	Equivalent Mechanical Impedance Z_{mec}	Equivalent Mechanical scheme
R		R	$\dfrac{\psi^2}{R}$	
L		$j\omega L$	$\dfrac{\psi^2}{j\omega L}$	
C		$\dfrac{1}{j\omega C}$	$j\psi^2\omega C$	

When several elementary electrical elements are connected in series, the resulting electrical impedance results given by:

$$Z_{sh}(\omega) = \sum_i Z_{sh,i}(\omega), \qquad (5.22)$$

where $Z_{sh,i}(\omega)$ is the electrical impedance of the i-th electrical element. The equivalent mechanical impedance could be obtained from equation (5.21) as:

$$Z_{mec}(\omega) = \frac{1}{\sum_i \dfrac{1}{Z_{mec,i}(\omega)}}, \qquad (5.23)$$

where $z_{mec,i}(\omega)$ is the equivalent mechanical effect of the i-th electrical element. Table 5.3 summarised the electro-mechanical analogies for the series of elementary elements.

When the electrical elements are connected in parallel, the resulting electrical impedance is given by:

$$\frac{1}{Z_{sh}(\omega)} = \sum_i \frac{1}{Z_{sh,i}(\omega)}, \qquad (5.24)$$

where $Z_{sh,i}(\omega)$ is the electrical impedance of the i-th electrical element. The mechanical equivalent impedance of electrical elements connected in parallel are given by:

$$Z_{mec}(\omega) = \sum_i Z_{mec,i}(\omega),$$ (5.25)

where $Z_{mec,i}(\omega)$ is the mechanical equivalent impedance of the i-th electrical element. Table 5.4 summarised the electro-mechanical analogies when the elementary elements are connected in parallel.

Comparing the two tables, it is interesting to note that there is a straightforward relationship between the electrical element and the equivalent mechanical elements only when the electrical elements are connected in parallel.

Considering for example the resistance and inductance elements represented in the first rows of table 5.3 and 5.4 for the series and parallel connection, respectively, the equivalent mechanical element is given by a stiffness and damper elements connected in series and parallel, respectively.

For the series case, the two equivalent mechanical elements result given by:

$$c_{eq} = \frac{\psi^2 R}{R^2 + \omega^2 L^2} \quad \text{and}$$ (5.26a)

$$k_{eq} = \frac{\omega^2 \psi^2 L}{R^2 + \omega^2 L^2}.$$ (5.26b)

The two equivalent mechanical elements assume values that depends on both the inductance and the resistance. Furthermore, their value is a frequency-dependent quantity.

For the parallel RL shunt, the equivalent damping and stiffness elements are given by:

$$c_{eq} = \frac{\psi^2}{R} \quad \text{and}$$ (5.27a)

$$k_{eq} = \frac{\psi^2}{L}.$$ (5.27b)

In this case there is a direct correspondence between one electrical element and one mechanical property, e.g. the damping effect is related to only the electrical resistance. Furthermore, the values of the equivalent mechanical elements are not frequency-dependent.

Table 5.3: Mechanical equivalent effects produced by shunt of electric elements in series connected to the idealised coil-magnet electro-mechanical transducer. Adapted from [64, 65].
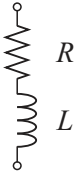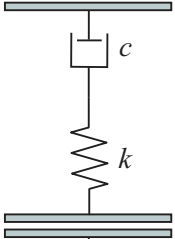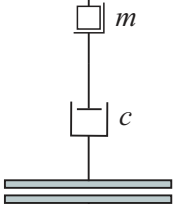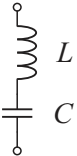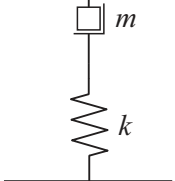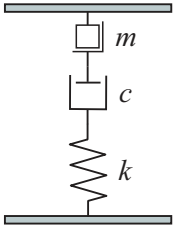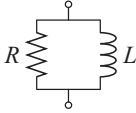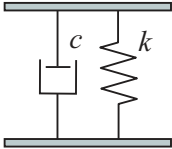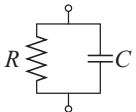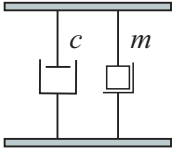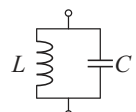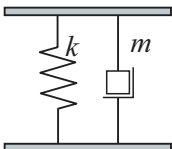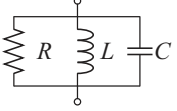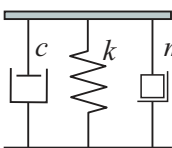
Circuit	Scheme	Electrical Impedance Z_{sh}	Equivalent Mechanical Impedance Z_{mec}	Equivalent Mechanical scheme
$R - L$		$R + j\omega L$	$\dfrac{\psi^2}{R + j\omega L}$	
$R - C$		$R + \dfrac{1}{j\omega C}$	$\dfrac{\psi^2}{R + \dfrac{1}{j\omega C}}$	
$L - C$		$j\omega L + \dfrac{1}{j\omega C}$	$\dfrac{\psi^2}{j\omega L + \dfrac{1}{j\omega C}}$	
$R - L - C$		$R + j\omega L + \dfrac{1}{j\omega C}$	$\dfrac{\psi^2}{R + j\omega L + \dfrac{1}{j\omega C}}$	

Table 5.4: Mechanical equivalent effects produced by shunt of electric elements in parallel connected to the idealised coil-magnet electro-mechanical transducer. Adapted from [64, 65].

Circuit	Scheme	Electrical Impedance Z_{sh}	Equivalent Mechanical Impedance Z_{mec}	Equivalent Mechanical scheme
$R - L$		$\dfrac{1}{\dfrac{1}{R} + \dfrac{1}{j\omega L}}$	$\dfrac{\psi^2}{R} + \dfrac{\psi^2}{j\omega L}$	
$R - C$		$\dfrac{1}{\dfrac{1}{R} + j\omega C}$	$\dfrac{\psi^2}{R} + \psi^2 j\omega C$	
$L - C$		$\dfrac{1}{\dfrac{1}{j\omega L} + j\omega C}$	$\dfrac{\psi^2}{j\omega L} + \psi^2 j\omega C$	
$R - L - C$		$\dfrac{1}{\dfrac{1}{R} + \dfrac{1}{j\omega L} + j\omega C}$	$\dfrac{\psi^2}{R} + \dfrac{\psi^2}{j\omega L} + \psi^2 j\omega C$	

The electro-mechanical analogy study could be furthermore consid-
ering the simplified model for the electro-magnetic transducer shown in figure
5.4, in which the mechanical properties of the transducer (masses, damping and
stiffness parameters) are considered but the inherent electrical properties of the
coil (resistance and inductance) are neglected.
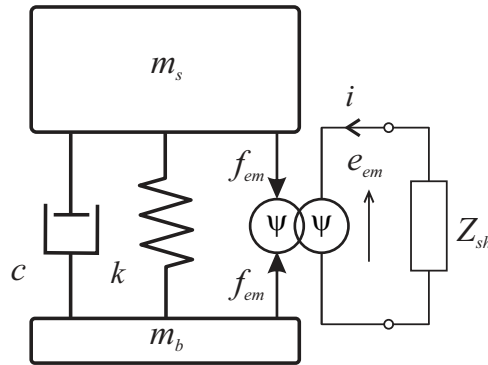
Figure 5.4: Simplified model of the electro-magnetic transducer with an electrical
shunt.

When the simplified model is shunted with a resistive element, the equivalent
mechanical element results in a damper element, as derived in the first row of
table 5.2. This results in parallel with the mechanical damper of the transducer,
as shown in the first row of table 5.5, thus the resulting damper element is given
by the sum of the two elements. As shown in the second row of table 5.5, if the
simplified transducer is shunted with an inductive element, the mechanical
equivalent results in a spring element, as derived from the second row of table
5.2. The mechanical and equivalent stiffness elements result in parallel, thus the
resulting stiffness element is given by the sum of the two elements.

When a capacitor is used to shunt the simplified electro-magnetic transducer,
the equivalent mechanical element is given by a mass element, as shown in
the third row of table 5.2. In this case the equivalent mass results in parallel
with the mechanical stiffness and damping element and in series with the base
and suspended masses. In this case it is not possible to define an equivalent
global element that takes into account the purely mechanical and the equivalent
parameter. This could also be observed considering equation (5.16), which for
a shunt circuit composed by a capacitor gives:
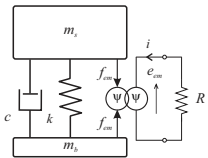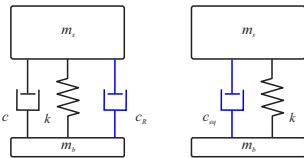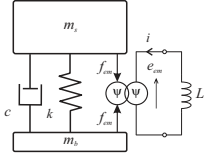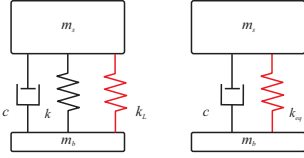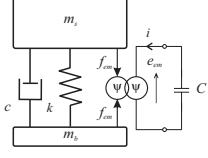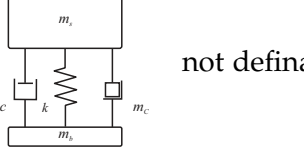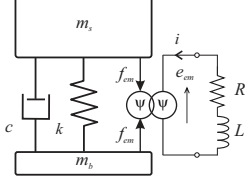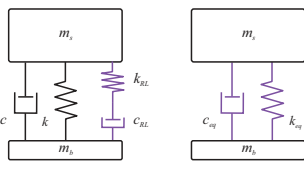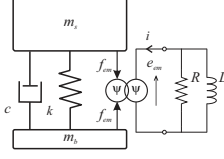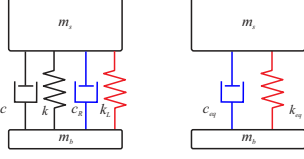
$$Z_b(\omega) = Z_{m_b} + \frac{Z_{m_s}\left(Z_s + Z_{m_{eq}}\right)}{Z_{m_s} + Z_s + Z_{m_{eq}}}, \tag{5.28}$$

where $Z_{m_{eq}} = j\omega\psi^2 C$ is the mechanical equivalent impedance of the electric capacitor.

In the fourth row of table 5.5 is considered the case in which the simplified electro-magnetic transducer is shunted with a resistance and an inductance in series. In this case, as shown in the first row of table 5.3, the equivalent mechanical system is given by a series of a damping and stiffness elements. In this case, both the stiffness and damping global elements result to be a function of the pertinent purely mechanical element and of the frequency ω and of both the resistance and the inductance of the shunt circuit.

Table 5.5: Mechanical equivalent effects produced by shunt of electric elements connected to the simplified coil-magnet electro-mechanical transducer.

Element \ Circuit	Simplified shunted transducer	Equivalent Mechanical transducer		Global equivalent Mechanical parameter
R				$c_{eq} = c + \dfrac{\psi^2}{R}$
L				$k_{eq} = k + \dfrac{\psi^2}{L}$
C			not definable	not definable
RL series				$c_{eq} = f(c, \omega, R, L)$ $k_{eq} = f(k, \omega, R, L)$
RL parallel				$c_{eq} = c + \dfrac{\psi^2}{R}$ $k_{eq} = k + \dfrac{\psi^2}{L}$

Finally, in the last row of table 5.5 is presented the simplified electro-magnetic transducer shunted with a parallel of a resistance and an inductance. As shown in the first row of table 5.4 this electrical shunt corresponds to a mechanical system composed by a parallel of a damping and stiffness elements. This two equivalent elements are in parallel with the inherent mechanical elements, thus the resulting global stiffness element is given by the sum of the inherent mechanical stiffness and of the equivalent stiffness element, which depends only on the electric inductance. Also, the resulting global damping element is given by the sum of the inherent mechanical and of the equivalent damping element, which depends only on the electric resistance.

5.4 TIME VARYING SHUNTED ELECTRO-MAGNETIC VIBRATION ABSORBERS

5.4.1 *Optimal shunt circuit*

Having established the mechanical effects produced by electric shunts connected to an idealised coil-magnet transducer, it is now possible to consider the mechanical response of the electro-magnetic transducer when connected to the specifically designed shunt circuit. The lumped parameter model of the electro-magnetic transducer connected to the specifically designed shunt is shown in figure 5.5 (a).
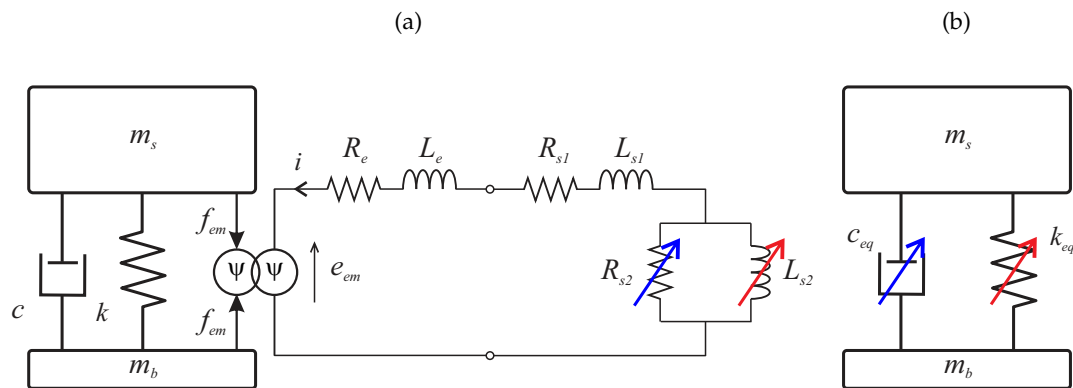
Figure 5.5: Lumped parameter model for the shunted electro-magnetic transducer (a) and equivalent purely mechanical system (b).

The shunt circuit is designed to both annihilate the effects produced by the inherent resistance and inductance of the coil and to tune the damping and stiffness parameters. It is thus composed by a negative resistance R_{s1} and a

negative inductance L_{s1} and in series with these elements is connected a parallel of a variable resistance R_{s2} and a variable inductance L_{s2}.

For simplicity, the electrical circuit shows idealised negative resistance R_{s1} and negative inductance L_{s1}, which in practice are produced by active circuits with operational amplifiers implementing negative impedance converters (NIC) [188]. These are tuned in such a way as to cancel the inherent resistance R_e and inductance L_e effects of the coil-magnet transducer.

The equivalent mechanical effects of the variable resistance R_{s2} and variable inductance L_{s2} are modelled as a variable damper ψ^2/R_{s2} and a variable stiffness ψ^2/L_{s2} in parallel with the mechanical damper and spring elements, c and k. The equivalent variable damping and variable stiffness parameters of the device are thus given by:

$$c_{eq} = c + \frac{\psi^2}{R_{s2}} \quad \text{and} \tag{5.29a}$$

$$k_{eq} = k + \frac{\psi^2}{L_{s2}}. \tag{5.29b}$$

The impedance of the suspension [127] results thus given by

$$Z_{s,eq}(\omega) = c_{eq} + \frac{k_{e}q}{j\omega} \tag{5.30}$$

and the base impedance of the electro-magnetic transducer shunted with the circuit shown in figure 5.5 (a) results given by:

$$Z_{b,eq}(\omega) = Z_{mb}(\omega) + \frac{Z_{ms}(\omega)Z_{s,eq}(\omega)}{Z_{ms}(\omega) + Z_{s,eq}(\omega)}. \tag{5.31}$$

The shunt elements could thus be used to modify the dynamic mechanic response of the electro-magnetic transducer. Plot (a) of figure 5.6 shows the base impedance of the transducer when the shunt inductance is varied in such a way as to tune the device to series of frequencies between 30 and 100 Hz. This graph enlightens a rather important aspect of the tuning mechanism, that is, the resonance peaks become progressively sharper as the tuning frequency rises. In plot (b) of figure 5.6 are shown the effects of increasingly lower values of the shunt resistance R_{s2} for three tuning frequencies. The shunted electro-magnetic transducer could thus be effectively used as a Tuned Vibration Absorber.
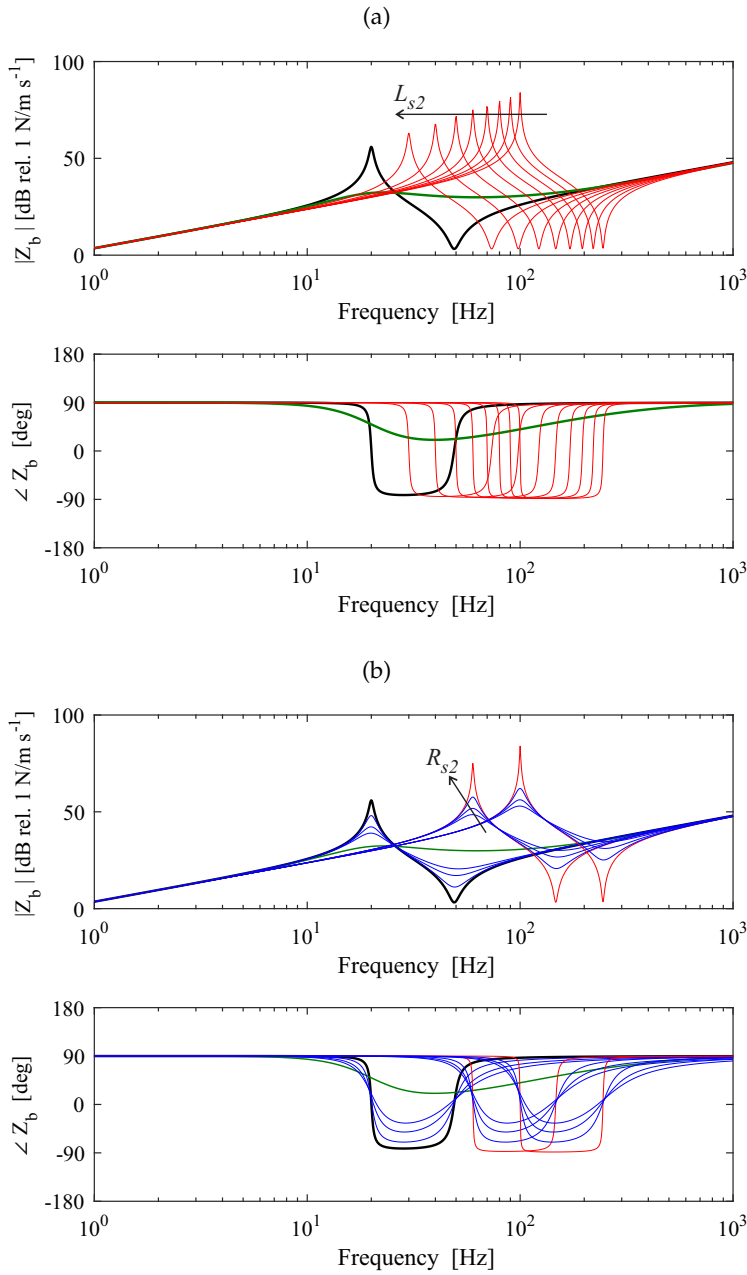
Figure 5.6: Base impedance FRFs (amplitude in the top plots and phase in the bottom plots) of the electro-magnetic transducer in open- (thin solid black lines), short-circuit (thick solid green lines) and when it is shunted with the proposed circuit for several values of the shunt inductance L_{s2}, faint solid red lines in plot (a), and of the shunt resistance R_{s2}, faint blue lines in plot (b).

Recalling that the fundamental natural frequency and the damping ratio of the two masses-damper-stiffness TVA are given by

$$\omega_A = \sqrt{\frac{k_{eq}}{m_s}} \quad \text{and} \tag{5.32a}$$

$$\zeta_A = \frac{c_{eq}}{2m_s\omega_A}, \tag{5.32b}$$

the values of the shunt inductance and resistance, for given values of the natural frequency and the damping ratio, are obtained from the following expressions:

$$L_{s2} = \frac{\psi^2}{k_{eq} - k} = \frac{\psi^2}{m_s \omega_A^2 - k} \quad \text{and} \tag{5.33a}$$

$$R_{s2} = \frac{\psi^2}{c_{eq} - c} = \frac{\psi^2}{2\zeta_A m_s \omega_A - c}. \tag{5.33b}$$

Figure 5.7 shows the variation of the shunt inductance L_{s2} (solid red line) and of the shunt resistance R_{s2} (dashed blue lines) against the natural frequency of the TVA in the 25-100 Hz frequency range when the TVA damping ratio is set at 5.8 %. This figure shows how the shunt inductance tends to a very high value when the tuning frequency approaches the inherent open circuit resonance frequency of the electro-magnetic transducer. The electro-magnetic TVA should thus be designed with a natural frequency much lower than the lower end of the target frequency range. It is furthermore important to note how in the higher frequency region the dynamic response of the system becomes very sensitive to the electrical parameters. Indeed, a very small variation of the shunt inductance L_{s2} will cause a variation of several Hertz of the natural frequency of the device.
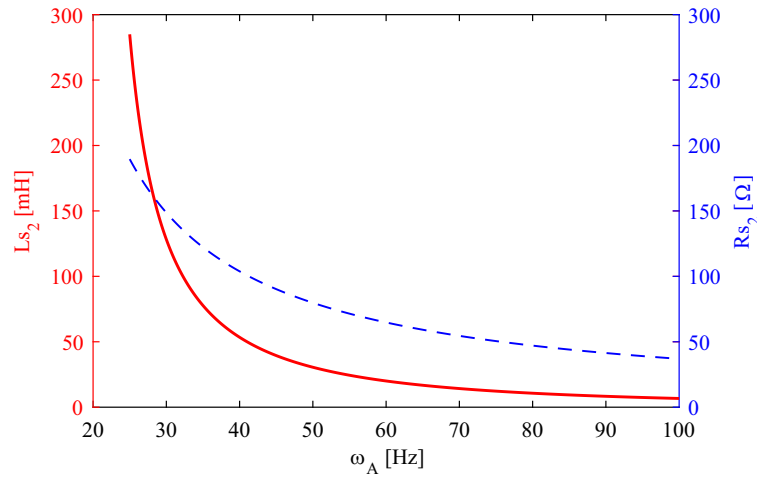
Figure 5.7: Shunt inductance (solid red line) and resistance (dashed blue line) versus the natural frequency of the TVA assuming a fixed value of the damping ratio $\zeta_A = 5.8\%$.

5.4.2   *Sweeping operation mode*

The shunted electro-magnetic TVA can be operated to periodically vary its stiffness and damping properties, so that the TVA fundamental natural frequency is continuously swept in a given frequency band and the TVA damping is set to maximise the vibration absorption at each frequency. This sweeping TVA [56, 58, 61, 62, 64, 65] can be applied on thin flexible structures to "blindly" control the flexural vibration in a broad frequency band. In this operation mode, there is no need to know in advance the dynamic response of the hosting structure.

For the simulation study presented in the following section, the shunt inductance was swept in such a way as the fundamental natural frequency of the TVA followed the periodic law:

$$\omega_A(t) = (\omega_{A,max} - \omega_{A,min}) \cos^2\left(\frac{2\pi}{T_h}t\right) + \omega_{A,min}, \tag{5.34}$$

where $\omega_{A,min}$ and $\omega_{A,max}$ are the lower and upper frequencies of the sweep respectively, assumed to be 25 and 100 Hz, and T_h is the period of the cosine harmonic function. It is worthwhile to note that since the sweep law is a second power of a cosine function, the period of the harmonic function results double of the period of the sweep, $T_{sw} = T_h/2$. The square cosine function was chosen to produce a greater frequency sweep rate at the higher frequency end of the sweep. As discussed in reference [56], the transient response of the TVA is controlled by its characteristic time constant, which decreases with the frequency. The chosen sweeping law allows a more uniform action of the TVA in the whole frequency of the sweep. Considering the mechanical properties of the cylindrical hosting structure listed in table 2.1 and the electro-mechanical properties of the electro-magnetic TVA listed in table 5.1, the period of the sweep was chosen after a trial and error simulation study which has shown that the control performances follow a smooth bell shape curve as the frequency of the sweep is increased from zero, with a maximum for $f_{sw} = 12$ Hz (thus $T_{sw} \cong 0.083$) s.

Also, the resistance was swept in such a way to ensure the damping ratio of the TVA was kept constant and equal to $\zeta_A = 5.8$ %, as for the case of the fixed TVA reported in table 4.3.

Using equations (5.33), the inductance L_{s2} and resistance R_{s2} of the shunt were swept according to the time law given in equation (5.34) in the ranges $L_{s2,min-max} = 7 - 285$ mH and $R_{s2,min-max} = 27 - 190$ Ω.
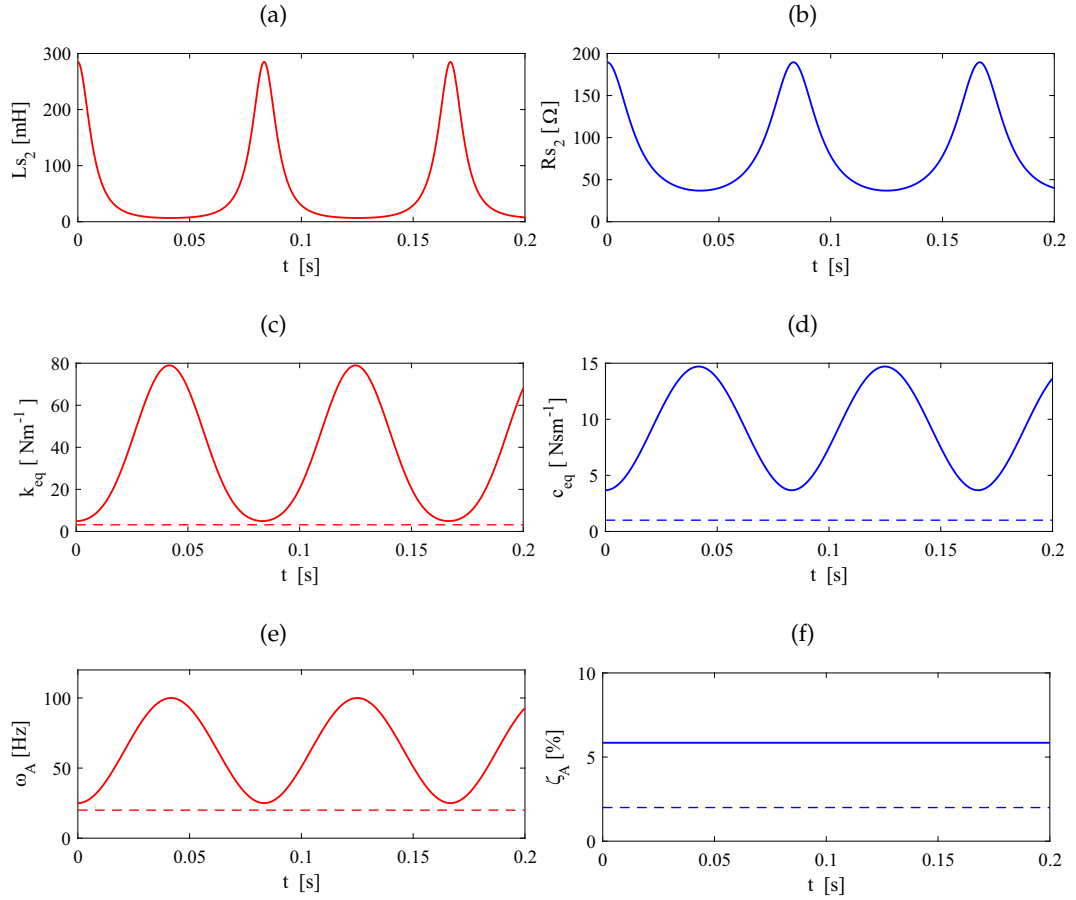
Figure 5.8: Shunt inductance (a) and resistance (b) and corresponding TVA equivalent stiffness (c) and equivalent TVA damping coefficient (d) necessary to produce the 25-100 Hz sweep of the TVA fundamental natural frequency (e) and constant damping ratio equal to 5.8 % (f). The dashed lines in plots (c), (d), (e) and (f) show the pertinent inherent parameters for the open-circuit TVA.

Figure 5.8 shows the periodic variation over time of the shunt inductance L_{s2} (plot (a)) and of the shunt resistance R_{s2} (plot (b)) as well as the resulting periodic variation of the TVA equivalent stiffness k_{eq} (plot (c)) and TVA equivalent damping factor c_{eq} (plot (d)), which lead to the desired periodic sweep of the TVA fundamental natural frequency ω_A between $\omega_{A,min} = 25$ Hz and $\omega_{A,max} = 100$ Hz (plot (e)) and the desired constant value of the TVA damping ratio $\zeta_A = 0.058$ (plot (f)). It is interesting to note that, as it can be deduced by the expressions in equations (5.29), the equivalent stiffness k_{eq} and the equivalent damping factor c_{eq} reach their maxima when the shunt inductance L_{s2} and resistance R_{s2} are at their minima and vice versa.

5.4.3 *Fully coupled structural-acoustic-sweeping TVA equation of motion*

The procedure to obtain the fully coupled structural-acoustic-TVA for the sweeping devices is the same as the one presented in section 4.6 of the previous chapter for the fixed TVAs.

When the sweeping TVAs are used to control the flexural vibration of the cylindrical shell and the acoustic response of the interior enclosure, the damping and stiffness properties of the TVAs are cyclically varied with time, thus the expression (4.29) for the force produced by the TVAs on the cylinder should be substituted with the following expression:

$$
\begin{aligned}
f_{A,j}(t) &= -m_{bj}\ddot{w}_{bj}(t) + c_{Aj}(t)\Delta \dot{w}_{Aj}(t) + k_{Aj}(t)\Delta w_{Aj}(t) \\
&= -m_{bj}\ddot{w}_{bj}(t) + \left(c_j + \frac{\psi^2}{R_{s2,j}(t)} \right) \Delta \dot{w}_{Aj}(t) + \left(k_j + \frac{\psi^2}{L_{s2,j}(t)} \right) \Delta w_{Aj}(t),
\end{aligned}
$$

$$(5.35)$$

where $c_{Aj}(t)$ is the equivalent damping coefficient given by equation (5.29a) of the j-th sweeping TVA, being c_j and $R_{s2,j}(t)$ the inherent mechanical damping coefficient and the time dependent shunt resistance for the j-th TVA. Also, $k_{Aj}(t)$ is the equivalent stiffness coefficient given by equation (5.29b) of the j-th sweeping TVA, with k_j and $L_{s2,j}(t)$ the inherent mechanical damping coefficient and the time dependent shunt inductance for the j-th TVA.

The time varying effects of the damping and stiffness properties of the TVA should also be taken into account in the equation of motion for the TVA given in equation (4.35), which, for the sweeping TVA, could be written as

$$
\begin{aligned}
m_{sj}\ddot{w}_{sj}(t) &= -c_{Aj}(t)\Delta \dot{w}_{Aj}(t) - k_{Aj}(t)\Delta w_{Aj}(t) \\
&= -\left(c_j + \frac{\psi^2}{R_{s2,j}(t)} \right) \Delta \dot{w}_{Aj}(t) - \left(k_j + \frac{\psi^2}{L_{s2,j}(t)} \right) \Delta w_{Aj}(t).
\end{aligned}
$$

$$(5.36)$$

Following the same procedure described in section 4.6, the fully coupled equation of motion for the structural-acoustic-sweeping TVA results given by:

$$
\begin{bmatrix} \overline{\mathbf{M}}_s & \mathbf{0} & \mathbf{0} \\ \mathbf{R} & \mathbf{Q} & \mathbf{0} \\ \mathbf{0} & \mathbf{0} & \mathbf{M}_A \end{bmatrix} \begin{Bmatrix} \ddot{\mathbf{b}}(t) \\ \ddot{\mathbf{a}}(t) \\ \ddot{\mathbf{w}}_A(t) \end{Bmatrix} + \begin{bmatrix} \overline{\mathbf{C}}_s(t) & \mathbf{0} & -\mathbf{c}_A(t) \\ \mathbf{0} & \mathbf{D} & \mathbf{0} \\ -\mathbf{c}_A^T(t) & \mathbf{0} & \mathbf{C}_A(t) \end{bmatrix} \begin{Bmatrix} \dot{\mathbf{b}}(t) \\ \dot{\mathbf{a}}(t) \\ \dot{\mathbf{w}}_A(t) \end{Bmatrix}
$$

$$
+ \begin{bmatrix} \overline{\mathbf{K}}_s(t) & -\mathbf{S} & -\mathbf{k}_A(t) \\ \mathbf{0} & \mathbf{H} & \mathbf{0} \\ -\mathbf{k}_A^T(t) & \mathbf{0} & \mathbf{K}_A(t) \end{bmatrix} \begin{Bmatrix} \mathbf{b}(t) \\ \mathbf{a}(t) \\ \mathbf{w}_A(t) \end{Bmatrix} = \begin{Bmatrix} \mathbf{\Phi}_s \\ \mathbf{0} \\ \mathbf{0} \end{Bmatrix} \mathbf{f}(t).
$$

$$(5.37)$$

where the expressions for all the matrices contained in equation (5.37) are given in section 4.6 of the previous chapter. Equation (5.37) could be written in a more compact form as:

$$
\mathbf{M}\ddot{\mathbf{q}}(t) + \mathbf{C}(t)\dot{\mathbf{q}}(t) + \mathbf{K}(t)\mathbf{q}(t) = \mathbf{\Phi}\mathbf{f}(t) \tag{5.38}
$$

The global damping and stiffness modal matrices of the fully coupled structural-acoustic-TVA system, $\mathbf{C}(t)$ and $\mathbf{K}(t)$, result time-dependent due to the time-dependent nature of the damping and stiffness properties of the sweeping TVAs.

5.4.4 *State space formulation*

The set of time-dependent differential equations given in matrix form by equation (5.38) can be cast in the following state space matrix formulation

$$
\dot{\mathbf{x}}(t) = \mathbf{A}(t)\mathbf{x}(t) + \mathbf{B}\mathbf{f}(t), \tag{5.39}
$$

where the state vector is given by

$$
\mathbf{x}(t) = \begin{Bmatrix} \dot{\mathbf{b}}(t) \\ \dot{\mathbf{a}}(t) \\ \dot{\mathbf{w}}_A(t) \\ \mathbf{b}(t) \\ \mathbf{a}(t) \\ \mathbf{w}_A(t) \end{Bmatrix} \tag{5.40}
$$

and the time-varying state matrix and the constant input matrix are given by:

$$\mathbf{A}(t) = \begin{bmatrix} \mathbf{0} & \mathbf{I} \\ -\mathbf{M}^{-1}\mathbf{K}(t) & -\mathbf{M}^{-1}\mathbf{C}(t) \end{bmatrix} \quad \text{and} \tag{5.41a}$$

$$\mathbf{B} = \begin{bmatrix} \mathbf{0} \\ -\mathbf{M}^{-1}\mathbf{\Phi} \end{bmatrix}. \tag{5.41b}$$

Here, the zero matrix $\mathbf{0}$ and the identity matrix $\mathbf{I}$ have dimensions $(2M + 2N + N_A) \times (2M + 2N + N_A)$.

For the time-varying system subject to stochastic disturbances considered in this chapter, the numerical integration of equation (5.39) requires a particular algorithm based on the Runge-Kutta integration methods, which is described in appendix C.

The time-dependent flexural modal velocities and the time-dependent acoustic modal pressures can be obtained from the state vector as:

$$\dot{\mathbf{b}}(t) = \mathbf{C}_b\mathbf{x}(t) \quad \text{and} \tag{5.42a}$$

$$\mathbf{a}(t) = \mathbf{C}_a\mathbf{x}(t), \tag{5.42b}$$

where the two output matrices are given by:

$$\mathbf{C}_b = \begin{bmatrix} \mathbf{I}_{2M\times2M} & \mathbf{0}_{2M\times2N} & \mathbf{0}_{2M\times N_A} & \mathbf{0}_{2M\times2M} & \mathbf{0}_{2M\times2N} & \mathbf{0}_{2M\times N_A} \end{bmatrix}, \tag{5.43a}$$

$$\mathbf{C}_a = \begin{bmatrix} \mathbf{0}_{2N\times2M} & \mathbf{0}_{2N\times2N} & \mathbf{0}_{2N\times N_A} & \mathbf{0}_{2N\times2M} & \mathbf{I}_{2N\times2N} & \mathbf{0}_{2N\times N_A} \end{bmatrix}. \tag{5.43b}$$

5.4.5 *Frequency formulation*

As in section 3.8.2 for the coupled structural-acoustic response and in section 4.6.1 for the coupled structural-acoustic-fixed TVA response, also for the coupled structural-acoustic-sweeping TVA the response of the system is studied in the frequency domain. In the previous chapters, the global flexural response and the global interior sound response were established by the flexural kinetic energy PSD and by the acoustic potential energy PSD.

When the time-varying shunted vibration absorbers are used, the time history of the total flexural kinetic energy and of the total acoustic potential energy are not stationary and therefore the two PSDs could not be defined [124, 125]. However, since the velocity of the sweep of the shunted electro-magnetic TVAs is such that a large number of cycles are completed over the time integration pe-

riod T, the process exhibits a second-order periodicity and can be classified as cyclostationary, allowing a Fourier transform analysis to estimate the flexural kinetic energy and acoustic potential energy PSDs [189].

The flexural kinetic energy PSD and the acoustic potential energy PSD are thus not derived with the procedure described in section 4.6.1 of the previous chapter, but a slightly different approach is used. Recalling that the two PSDs functions are defined as [28, 64, 72]:

$$S_K(\omega) = \frac{1}{2}\rho h \int_S \lim_{T\to\infty} E\left[\frac{1}{T}\dot{w}^*(\mathbf{x}_s,\omega)\dot{w}(\mathbf{x}_s,\omega)\right] dS, \tag{5.44a}$$

$$S_P(\omega) = \frac{1}{2\rho_0 c_0^2} \int_{V_c} \lim_{T\to\infty} E\left[\frac{1}{T}p^*(\mathbf{x},\omega)p(\mathbf{x},\omega)\right] dV \tag{5.44b}$$

and that the frequency dependent complex amplitudes of the flexural velocity $\dot{w}(\mathbf{x}_s,\omega)$ and of the acoustic pressure $p(\mathbf{x},\omega)$ could be expressed as

$$\dot{w}(\mathbf{x}_s,\omega) = \boldsymbol{\varphi}(\mathbf{x}_s)\dot{\mathbf{b}}(\omega) \quad \text{and} \tag{5.45a}$$

$$p(\mathbf{x},\omega) = \boldsymbol{\psi}(\mathbf{x})\mathbf{a}(\omega), \tag{5.45b}$$

the flexural kinetic energy PSD and the acoustic potential energy PSD could be expressed as:

$$S_K(\omega) = \frac{1}{2}m_c \text{Tr}\left[\boldsymbol{\Lambda}\mathbf{S}_{\mathbf{bb}}^n(\omega)\right] \quad \text{and} \tag{5.46a}$$

$$S_P(\omega) = \frac{V_c}{2\rho_0 c_0^2} \text{Tr}\left[\boldsymbol{\Gamma}\mathbf{S}_{\mathbf{aa}}^n(\omega)\right]. \tag{5.46b}$$

Here the superscript ^{n} indicates that the matrices with the PSDs of the modal structural velocities and of the modal pressure amplitudes are obtained with the numerical estimation algorithm presented in appendix C.

5.4.6 *Simulation results*

This section discusses the vibration and sound control effects produced by arrays of 12 and 18 sweeping shunted electro-magnetic TVAs. The TVAs are blindly operated to control the whole set of resonance peaks that characterise the 20 to 100 Hz spectra of the structural and acoustic response.

The position of the two arrays of sweeping TVAs are the same as those of the fixed TVAs, listed in table 4.3 and schematically represented in figure 4.13 of the previous Chapter. The shunt inductance L_{s2} and resistance R_{s2} of the TVAs

are synchronously varied in time such that the fundamental natural frequencies ω_A of the devices vary according to the sweeping law given in equation (5.34) between 25 and 100 Hz and the damping ratios of the TVAs ζ_A remain constant and equal to 5.8 %. The properties of the two arrays of TVAs are listed in table 5.6.

Table 5.6: TVA parameters for the sweeping operation mode.

TVA nr°	Frequency range f_A [Hz]	Damping ratio ζ_A [%]	Shunt inductance L_{s1} [mH]	L_{s2} [mH]	Shunt resistance R_{s1} [Ω]	R_{s2} [Ω]
1 ÷ 12	25 ÷ 100	5.8	−4.35	7 ÷ 285	−22	37 ÷ 190
1 ÷ 18	25 ÷ 100	5.8	−4.35	7 ÷ 285	−22	37 ÷ 190

The thick red line in plot (a) of figure 5.9 shows that, when the cylinder is equipped with 12 sweeping TVAs, the flexural response of the cylindrical structure is reduced in correspondence of the majority of the resonance frequencies, with attenuations of 7 to 10 dB below 60 Hz and much lower attenuations around 1 dB and 2 dB above 60 Hz.

The thick red line in plot (c) of figure 5.9 shows that the 12 sweeping TVAs effectively control the acoustic response at all the resonance frequencies of the structural modes that effectively couple to the interior acoustic field in the whole 20 - 100 Hz frequency band, with reductions comprised between 7 and 12 dB.

Considering the case in which the array of 18 sweeping TVAs is implemented, the thick green line of plot (b) in figure 5.9 the structural response is effectively reduced at the majority of the resonance peaks, with attenuations comprised between 3 dB and 12 dB. Also in this case, the higher reductions are obtained for frequencies below 60 Hz. Also, the thick green line of plot (d) in figure 5.9 shows that the array of 18 sweeping TVAs produce large reductions comprised between 10 and 15 dB at all the resonance frequencies of the structural modes that effectively couple to the interior acoustic field in the whole 20 - 100 Hz.

To better quantify and contrast the control effects produced by the two arrays of fixed tuned TVAs presented in the previous chapter and the arrays of sweeping TVAs presented in this one, figure 5.10 shows the third-octave band reductions of the flexural kinetic energy PSD (plot (a)) and acoustic potential energy PSD (plot (b)) produced by the 12 fixed tuned (orange first bars), 12 sweeping (red second bars), 18 fixed tuned (cyan third bars) and 18 sweeping TVAs (green fourth bars). From the two plots it can be gathered that the sweeping TVAs produce vibration and noise control effects comparable to those ob-
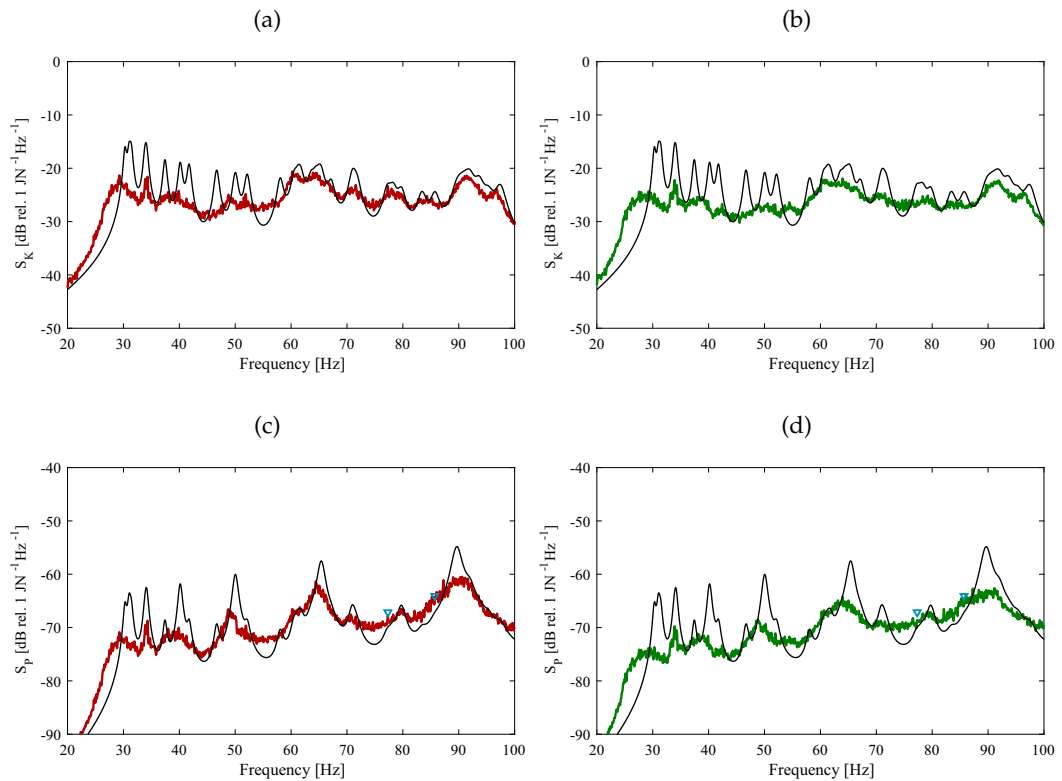
Figure 5.9: Spectra of the flexural kinetic energy PSD (top plots) and acoustic potential energy PSD (bottom plots) without TVAs (thin solid black lines), with 12 sweeping Tuneable Vibration Absorbers (thick red lines in plots (a) and (c)) and with 18 sweeping Tuneable Vibration Absorbers (thick green lines in plots (b) and (d)).

tained with the fixed tuned device. Furthermore it can be noted that the noise and control effects are higher in the low frequency band and tend to decrease as the frequency raises. It is worthwhile to note that the minimum reduction of the acoustic response occurs at the third-octave band centred at 80 Hz, which correspond to the third-octave band where the acoustic natural frequencies lay.

5.5 CHAPTER CONCLUDING REMARKS

The study presented in this chapter has shown the effects of using arrays of time-varying shunted electro-magnetic vibration absorbers attached to a thin cylindrical shell to control the flexural and internal sound responses in the low frequency range up to 100 Hz.

An electro-mechanical analogy study was presented, which led to the design of an optimal shunt circuit for the electro-magnetic transducers. The aim of the

(a)   (b)
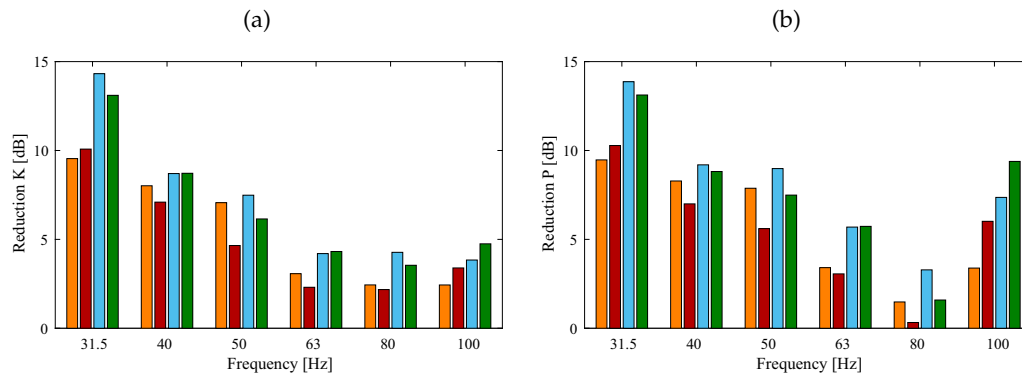
Figure 5.10: Third octave band reduction of the flexural kinetic energy PSD (plot (a)) and acoustic potential energy PSD (plot (b)) produced by 12 fixed tuned (orange 1st bars), 12 sweeping tuneable (red 2nd bars), 18 fixed tuned (cyan 3rd bars) and 18 sweeping tuneable vibration absorbers (green 4th bars).

shunt circuit is to both annihilate the inherent electrical properties of the transducer and to obtain independent damping and stiffness equivalent mechanical effects.

Continuous time variations of the electrical parameters of the shunt is proposed and analysed together with the control law. It was shown that these kind of sweeping absorbers are able to control both the flexural and the interior acoustic responses of the cylindrical shell. Better control performances were obtained for very low frequencies, where the cylinder flexural response is characterised by well separated resonance peaks, while at higher frequency the control performances are lower due to the overlap of the modal flexural response.

It was shown that the arrays of sweeping TVAs produce similar vibration and noise control effects than the arrays of fixed tuned TVAs. This is an important result, particularly when it is considered that the time-varying TVAs work without a precise tuning to targeted resonant frequencies, but only the damping ratio and initial and final values of the frequency range of the sweep are needed. Furthermore, they can be blindly operated in a given frequency band without the need of performing a system identification to obtain the hosting structural dynamic response.

<div style="text-align: right; font-size: 4em;">6</div>

EXPERIMENTAL RESULTS

This chapter reports the experimental implementation of a shunted electromagnetic TVA and the evaluation of its control performances of the flexural vibrations of a cylindrical shell.

First, the experimental characterisation of both the mechanical and electrical properties of an electromagnetic transducer is conducted.

Then the digital implementation of shunt circuit is presented. This was done using a dSPACE Auto Box DS1103 board system. A particular front-end circuit is required, whose design and features are described. The effects of several resistive and resistive-inductive shunt circuits, digitally implemented, on the Base Impedance response of the shunted EM transducer are assessed.

In the last part of the chapter, the response of a steel cylindrical shell is evaluated considering a shunted EM TVA operating in the fixed tuned and the sweeping operation mode.

Contents

6.1   DESCRIPTION OF THE TEST RIG

This chapter describes the initial experimental results regarding the vibration control performances of a shunted Electro-Magnetic Tuneable Vibration Absorber (EM TVA) connected to a cylindrical shell. Therefore it constitutes the experimental counterpart of the simulation results presented in the previous chapters 4 and 5, regarding the fixed tuned and sweeping operation mode of the TVA, respectively.

This section is devoted to the description of the test rig used in the experimental evaluations of the vibration control performances of the shunted EM TVA. Indeed, the results presented in this chapter are related to a simplified primary structure with respect to the analytical one presented in the previous chapters.

First, a different configuration of the cylindrical shell is adopted. The differences are related to the boundary conditions applied to the cylindrical shell and to its geometrical and physical properties. As shown in figure 6.1 (a), the cylindrical shell is suspended with four ropes and held to a specifically designed frame. In such a way the cylindrical shell is subject to *free-free* boundary conditions. This appears to be a discrepancy with the *simply-supported* boundary conditions considered in the previous chapters for the simulation results. As discussed in Chapter 3, the choice of the *simply-supported* boundary conditions for the cylindrical shell, in accordance with references [30, 66–68, 93–97], was led by possibility to obtain a simple closed-form analytic expression for the results. On the other hand, the *free-free* boundary conditions appears to be the easiest to achieve in practice [98]. Considering that the two boundary conditions are related to similar dynamic parameters (*i.e.* modal density and modal overlap factor) [190–192] and that the boundary conditions just slightly affect the dynamic response of the cylindrical shell [96], the discrepancy is therefore only apparent. As reported in table 6.1, the dimension of the cylinder was chosen such that it could more suitably be hosted into the "Laboratorio di Controllo e Regolazione Automatica" at the Università degli Studi di Udine. Finally, for manufacturing reasons, the cylinder was made in steel, despite the simulation results are related to an aluminium shell. As discussed in Section 3.3 for the *simply-supported* boundary conditions, the structural natural frequencies are a function of the ratio between the Young modulus and the density of the material, *i.e.* E/ρ. This ratio assumes comparable values considering the material as aluminium or steel [193]. Thus the choice of a different material, led by manufacturing reasons, would not affect considerably the results.

Second, only the vibration control effects of the TVA are assessed, neglecting the noise control ones. Precise noise measurements would require that the experiments are conducted in an anechoic chamber [194], with a dedicated configuration of the acquisition and analysis devices, to avoid that the operating noises of these devices alter the acoustic measurements. At the time of the experiments were conducted, the anechoic chamber of the Università degli Studi di Udine was not available, thus in order to avoid misleading results it was chosen to neglect the noise control performances of the TVA.

The electro-magnetic transducer used is a H2W TECHNOLOGIES NCM02-17-035-2F, shown in figure 6.1 (b). This voice coil transducer, as sketched in figure 5.1 (a) of the previous chapter, is composed of a cylindrical permanent magnet encircled by a ferromagnetic case which host the coil. The two elements are connected with a torsional spring. The physical parameters of the transducer are presented in table 6.1.

(a)   (b)
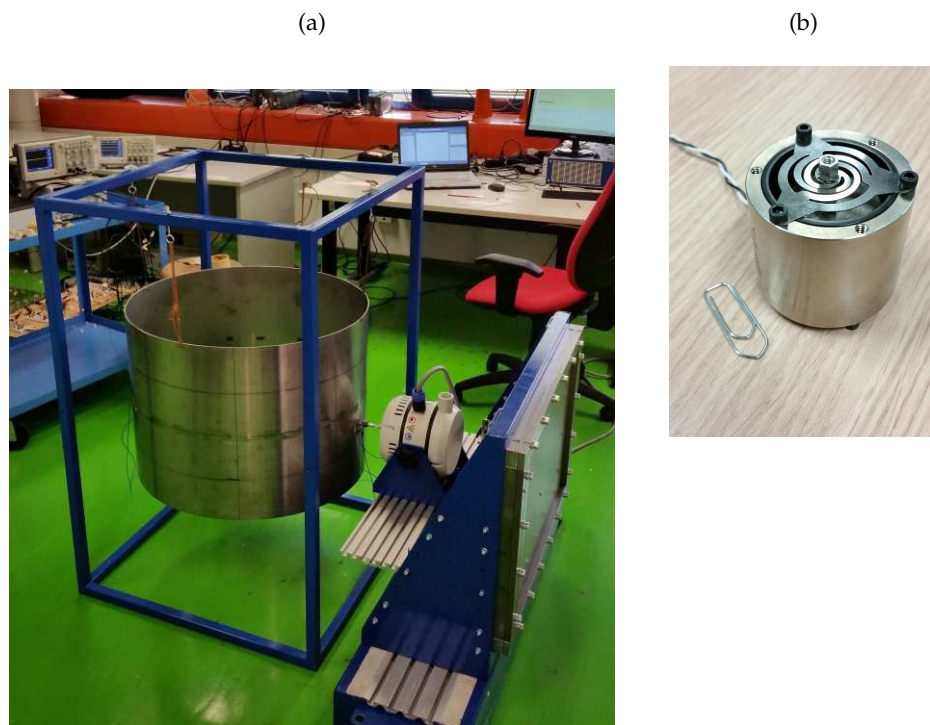
Figure 6.1: Images of the suspended cylindrical shell connected to the shaker (a) and of the electro-magnetic transducer (b).

Table 6.1: Geometrical and physical properties of the thin walled cylinder and of the electro-magnetic transducer.

	Parameter			Value
Cylindrical shell	Length	L	[mm]	500
	Radius	R	[mm]	350
	Thickness	h	[mm]	3
	Material			steel
	Mass	m_c	[kg]	26
Electro-magnetic transducer	Seismic mass	m_s	[g]	185
NCM02-17-035-2F	Base mass	m_b	[g]	115
	Natural frequency	f_t	[Hz]	18
	Damping ratio	ζ_t	[%]	22
	Coil resistance	R_e	[Ω]	22
	Coil inductance	L_e	[mH]	4.35
	Transduction coefficient	ψ	$[N/A]$	22.5

6.2 MECHANICAL AND ELECTRICAL CHARACTERISATION OF THE EM TRANSDUCER

In this section, the mechanical and electrical properties of the electro-magnetic transducer are presented. First, the Base Impedance of the transducer is considered, in both the open- and short-circuited conditions. The measured mechanical properties are then compared with the simulated Base Impedance obtained with the expression given in equation (5.16) of the previous chapter. The electrical impedance of the transducer is then analysed. The setup for the two experiments are presented in figure D.1 and D.2 of appendix D, respectively. Both measurements were conducted with the DataPhysics Abacus, which is shown in figure 6.2 (a). The main features of this dynamic signal analyser are:

- realtime rate of 49 kHz and 120 dB dynamic range, with a self-adjusting sampling rate depending on the higher frequency of the measurement;

- 16 BNC input channels and 1 BNC output channel with a voltage range of ±10V.

Both figures 6.4 and 6.5 show, together with the amplitude and phase of the FRF of the measured characteristic, the trend over frequency of the coherence function $\gamma(\omega)$. This quantity is defined as [124, 125, 195]

$$\gamma(\omega) = \frac{\left|S_{xy}(\omega)\right|^2}{S_{xx}(\omega)S_{yy}(\omega)},$$
(6.1)

where $S_{xx}(\omega)$, $S_{yy}(\omega)$ are the power spectral density functions of the input and output signals $x(t)$ and $y(t)$ and $S_{xy}(\omega)$ is the cross-spectral density. The coherence function, which results $0 \leq \gamma(\omega) \leq 1$, gives an insight of the quality of the measurement, since it assumes values less then one when the input and output signals are only partially linearly related. The reasons for the not perfect linear relationship between $x(t)$ and $y(t)$ could be the presence of noise in the measurement and the dependence of the output signal $y(t)$ to other input signals different from $x(t)$.

(a)   (b)
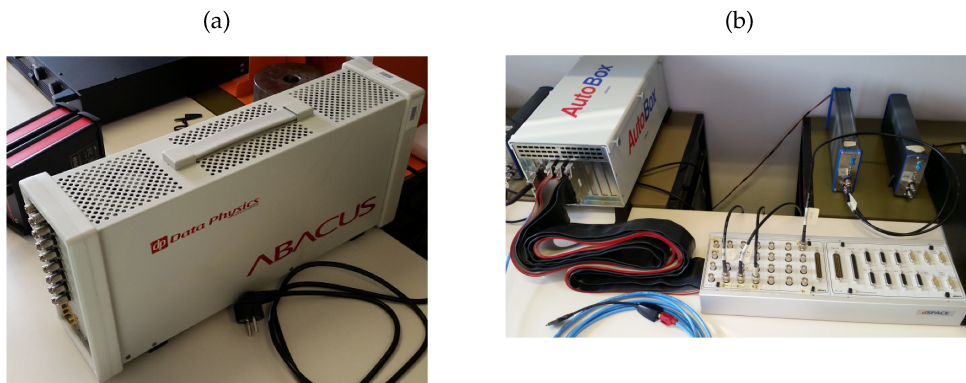
Figure 6.2: DataPhysics Abacus (a) and dSPACE AutoBox with board RT1103 and control panel (b).

6.2.1 *Mechanical characterisation*

As shown in figure 6.3 (a), for the experimental measurement of the open- and short-circuited Base Impedance of the electro-magnetic transducer, the device is mounted horizontally on the shaker. This configuration was chosen since the transducer will operate horizontally when applied to the cylinder. The shaker used in the measurement is a TIRA GmbH TV 51140. The electro-magnetic transducer and the shaker are connected by means of the PCB Piezotronics 288D01 Impedance Head, which is characterised by a natural frequency above 20kHz, a weight of 18 grams and a sensitivity of 9.94 mV/(m/s^2)

for the acceleration output and of 23.32 mV/N for the force output. The shaker was fed with a random signal and the upper frequency of the measured is set to 400 Hz with a sampling frequency of 1024 Hz.

(a)   (b)
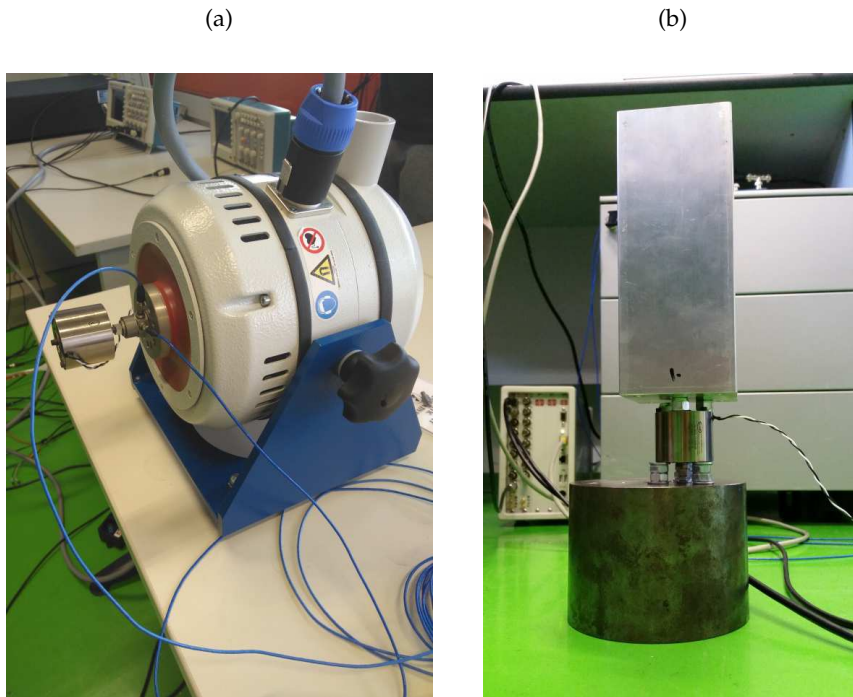
Figure 6.3: Pictures of the EM transducer mounted horizontally on the shaker (a) and blocked between two rigid and heavy masses (b).

In figure 6.4 is shown the 10-400 Hz FRF (amplitude in the top plot, phase in the central plot and coherence in the bottom plot) of the open- and short-circuited Base Impedance of the electro-magnetic transducer. The curves related to the measures (thin dashed black lines for the open-circuited and thin dashed blue lines for the short-circuited condition) show a good experimental agreement with the simulated curves (thick solid light grey lines for the open-circuited and thick solid cyan lines for the short-circuited condition). It is interesting to note that the coherence function for the open-circuited Base Impedance assumes values slightly lower than one for frequency below about 60 Hz. This is due to the fact that, as will be apparent in the following figures, the response of the transducer is characterised by secondary rocking modes which are not modelled and that affect the Base Impedance measurement which consider only the longitudinal vibration.
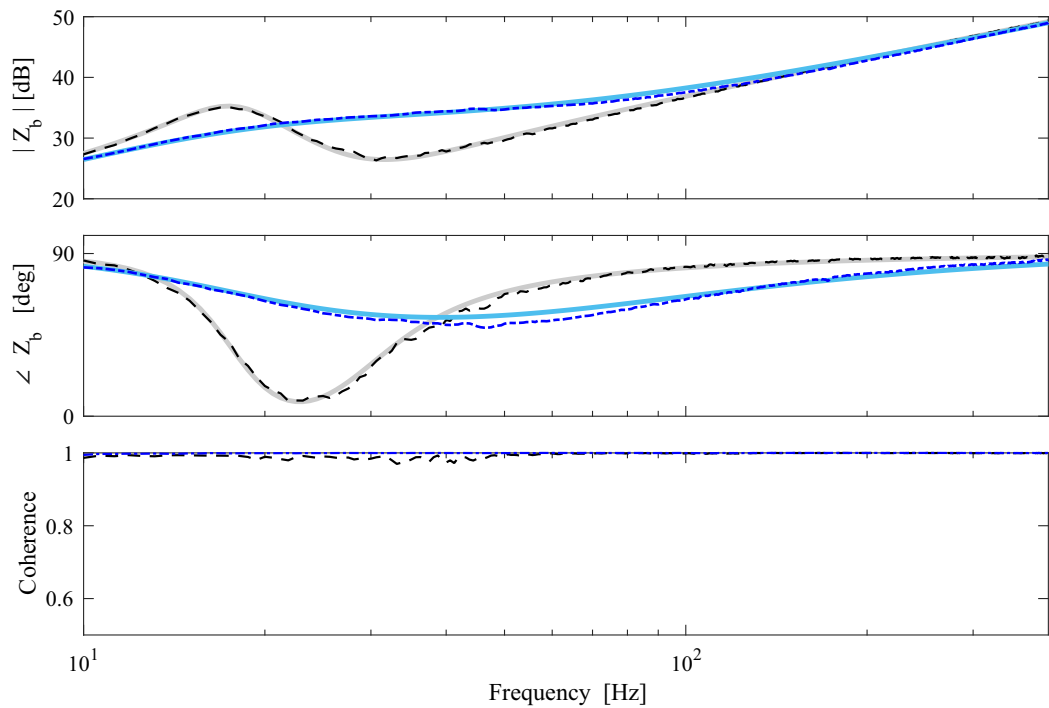
Figure 6.4: Base Impedance FRF (amplitude in the upper plot, phase in the central plot and coherence in the lower plot) of the electro-magnetic transducer in open- (thick solid grey lines simulated and thin dashed black lines measured) and short-circuit (thick solid cyan lines simulated and thin dot-dash blue lines measured).

6.2.2 *Electrical characterisation*

The electrical characterisation of the transducer is obtained connecting the wires of the device to the DataPhysics system through 2 BNC - Crocodile Clips test lead. In order to avoid the effect of the electromotive force e_{em}, related to the relative velocity of the magnet and the coil as expressed by equation (5.8a), the device was blocked between two heavy and very rigid masses, as shown in figure 6.3 (b). The transducer was fed with a random signal and the upper frequency range was fixed to 12 kHz, with a sampling frequency set to 32 kHz.

In figure 6.5 is shown the simulated (thick solid light grey lines) and measured (thin solid blue lines) FRFs (amplitude top plot, phase central plot and coherence bottom plot) of the electrical impedance of transducer. The two curve present a good agreement in the low frequency resistive region below about 100 Hz and above this value the two curve seem to describe different electrical behaviours. The amplitude of the simulated RL impedance, represented with the light grey lines, increase as the frequency increase following an inductive

behaviour. The amplitude of the measured electrical impedance raises with frequency with a different slope than the simulated one. This could be justified considering that in the real electro-magnetic transducer appear some capacitive effects that are not taken into account in the lumped parameter model. Figure 6.5 also reports with the red diamonds the values of the amplitude of the electrical impedance obtained with a BK PRECISION 878B RLC meter. These points are in good agreement with the values obtained with the DataPhysics, confirming the the good quality of the experimental measurements.
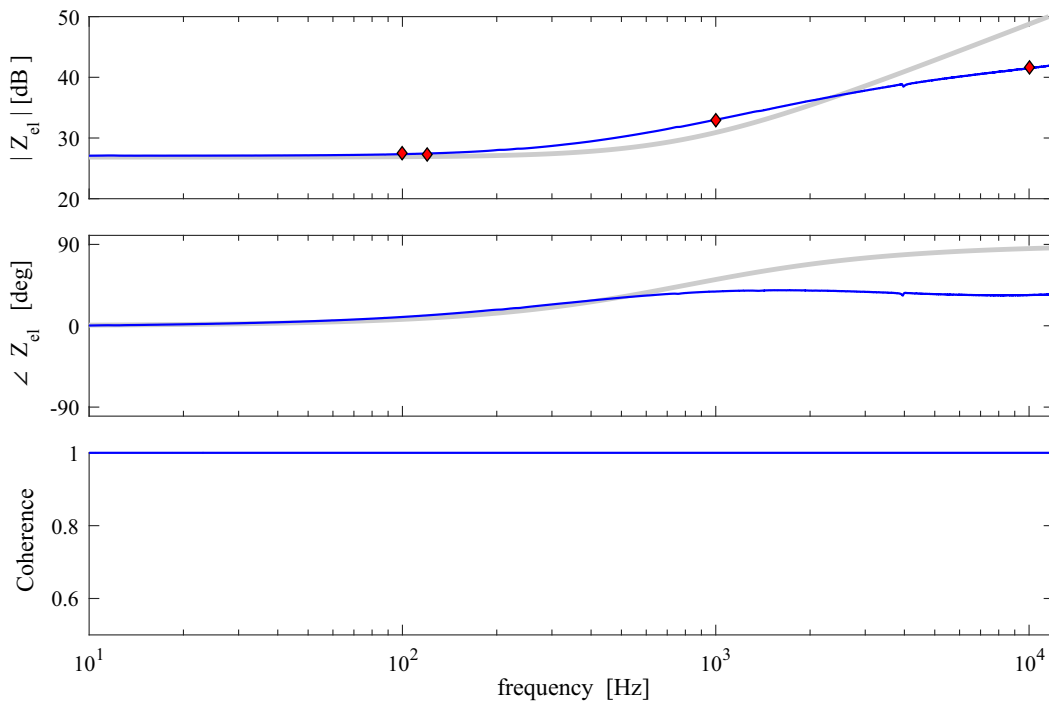
Figure 6.5: Simulated (thick solid grey lines) and measured (thin solid blue lines) electrical impedance FRFs (amplitude in the upper plot, phase in the central plot and coherence in the lower plot) of the blocked electro-magnetic transducer. The red diamonds in the amplitude plot are the measured points obtained with the RLC-meter.

6.3   DIGITAL IMPLEMENTATION OF THE SHUNT CIRCUIT

The shunt circuit used to tune the transducer described in the previous chapter 5, was digitally implemented with the dSPACE Auto Box DS1103 board shown in figure 6.2 (b). The main features of this controller board are

- a CPU with a 1 GHz clock, 32 MB of memory for the application and 96 MB for data storage;

- 4 sample and hold ADC converters connected to 16 multiplexed inputs with a voltage range of ± 10 V;

- 8 DAC converters with an output range of ± 10 V and ± 5 mA.

The sampling rate of the controller was set to 48 kHz. As schematically shown in figure 6.6, the electro-magnetic transducer is connected to the dSPACE board through a front-end circuit board, which is specifically designed to allow the interfacing between the transducer and the dSPACE board.
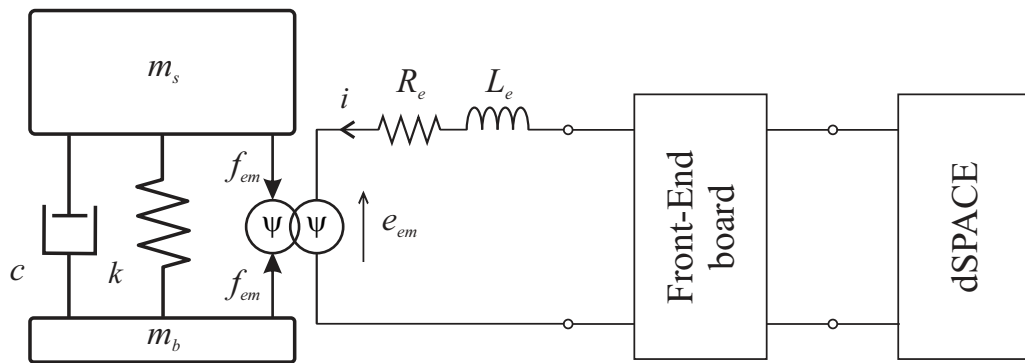
Figure 6.6: Scheme of electro-magnetic transducer connected the front-end circuit and the dSPACE board.

6.3.1 Front-end Circuit

The connection between the EM transducer and the dSPACE board is obtained by means of the front-end board shown in figure 6.7. The electrical circuit, whose schematic representation is shown in figure 6.8, was adapted from the one presented in references [196, 197].

The front-end circuit is basically composed by three stages. In the first stage the current i which flows through the coil of the transducer is measured with the resistance R1. This signal is then amplified with the amplifier U1A with a fixed gain set to 11 in order to obtain a high signal to noise ratio at the input of the digital controller. In the dSPACE unit the current is multiplied by the desired impedance and the voltage output of the controlled is added to the voltage measured with the resistance R1 to give the voltage across the

terminals of the transducer. The final stage of the front-end circuit is composed by an additional power amplifier which supplies the required values of current which are not obtainable connecting directly the transducer to the dSPACE board.
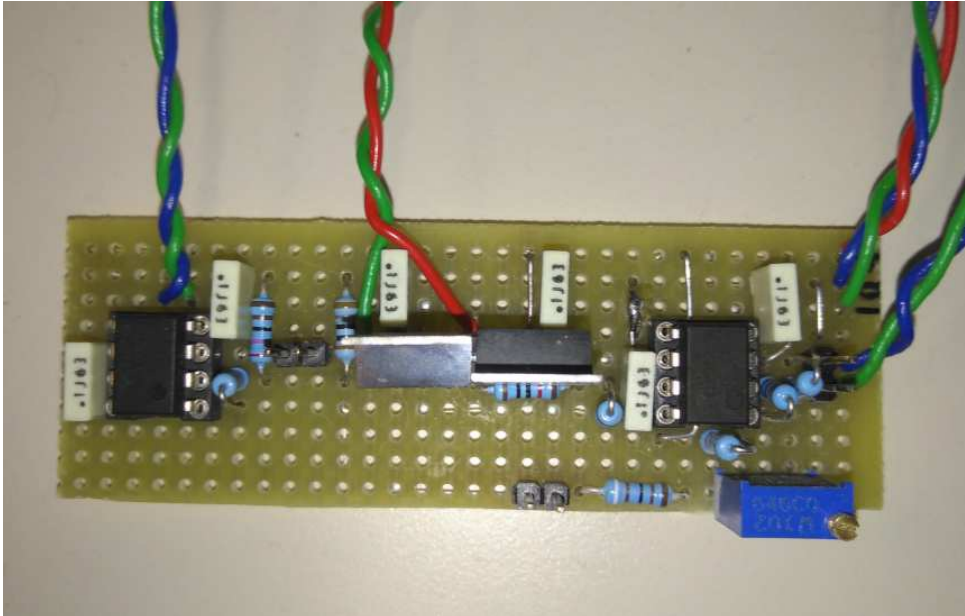
Figure 6.7: Picture of the front-end board.

In figures D.8 (b), D.9 (b) and D.10 (b) of appendix D are shown the experimental results of the three tests described in figures D.8 (a), D.9 (a) and D.10 (a). These tests were made to verify the correct construction and operation of the front-end board on the electrical impedance digitally implemented by the dSPACE unit. In such a way it was verified the absence of secondary effects due to the front-end circuit. The set of the three tests were conducted connecting directly the front-end board to the DataPhysics and providing a random excitation signal. The upper end of the frequency range was set to 2 kHz corresponding to a the sampling rate of about 5 kHz.
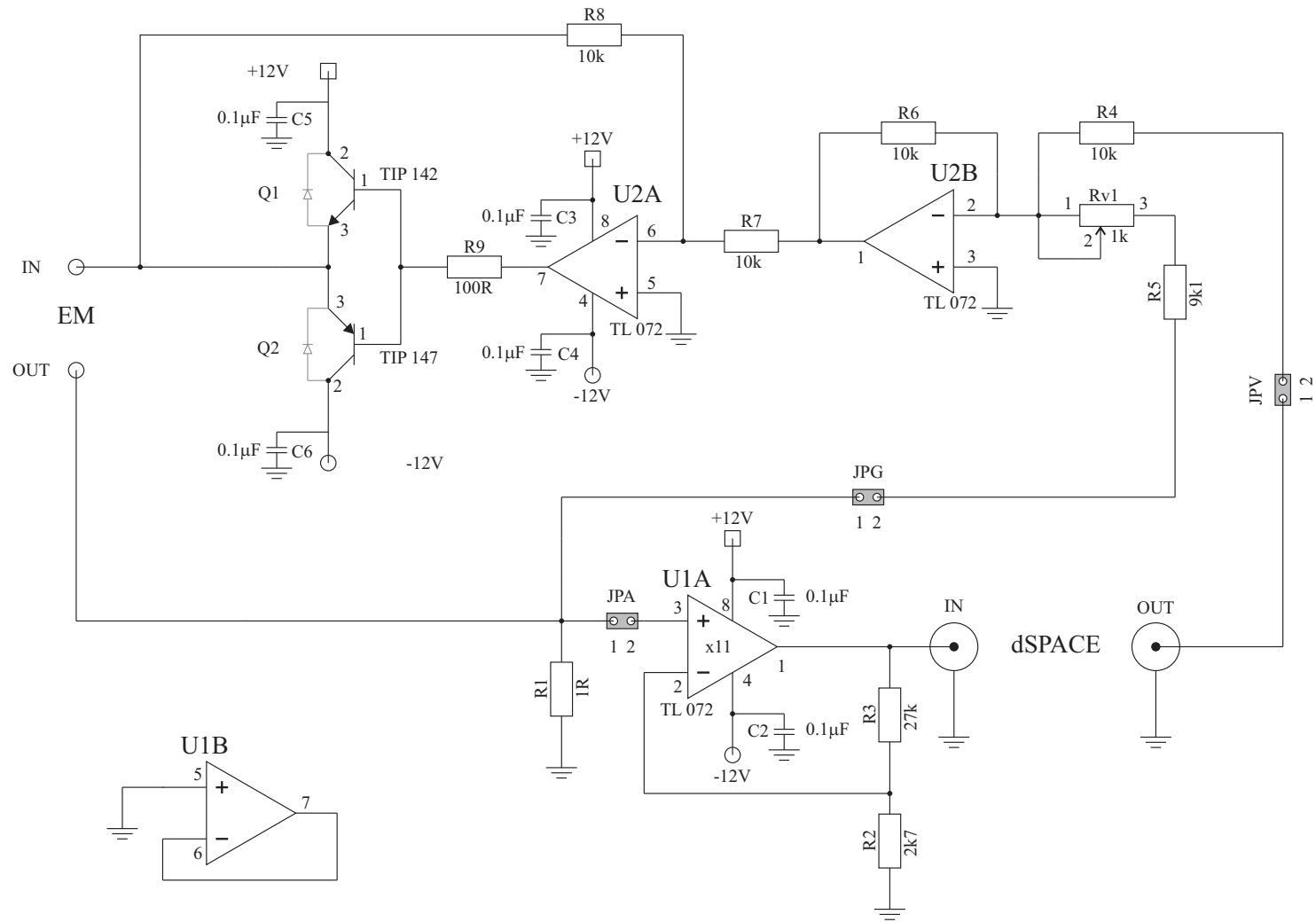
Figure 6.8: Schematic representation of the front-end circuit. Adapted from references [196, 197]

6.3.2 *Digital implementation of the shunt electrical impedance*

The digital implementation of the shunt electrical impedance is obtained with the dSPACE controller through the SIMULINK® scheme shown in figure 6.9. Several tests were made leading to the choice of a shunt circuit composed by a resistance and inductance connected in series, as will be explained in the following section 6.4. The practical digital implementation of the RL shunt inductance requires the addition of a low pass filter, such that the electrical impedance of the shunt is of the form:

$$Z_{sh}(\omega) = \frac{j\omega L_s + R_s}{j\omega \tau_f + 1},$$
(6.2)

where $\tau_f = 1/\omega_c$ is the time constant of filter, being ω_c the cut-off frequency. Several tests where conducted and it was observed that the system composed by the shunted transducer becomes unstable if the amplitude of the electrical impedance of the shunt is higher than 130 V/A. The cut-off frequency of the low-pass filter was therefore selected such that the amplitude of the electrical impedance of the RL circuit would not exceed 110 V/A. The cut-off frequency was thus tuned according to the following law:

$$\omega_c = \sqrt{\frac{g_{max}^2 - R_s^2}{L_s^2}},$$
(6.3)

where g_{max} is the maximum amplitude of the electrical impedance, set to 110 V/A.
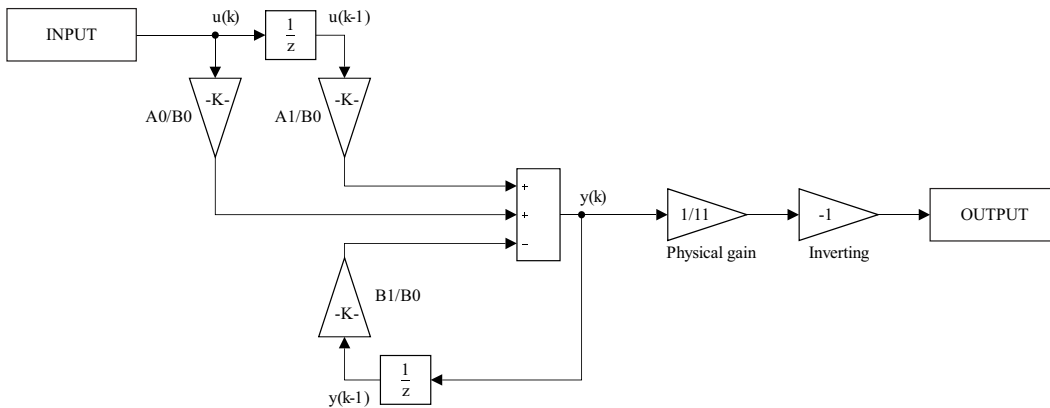
Figure 6.9: Scheme of the SIMULINK® model used for the digital implementation of the shunt impedance.

To obtain the best frequency-domain match between the continuous-time and discretized impedance of the shunt, the expression given in equation (6.2) is transformed in the discrete-time domain with the bilinear approximation (or Tustin) method [198]. This can be easily done with the double substitution $s = j\omega$ and

$$s = \frac{2}{T_s}\frac{z-1}{z+1}, \tag{6.4}$$

where s and z are the Laplace and discrete-time variables, respectively and T_s is the sampling period, set to $1/48000$ s. The discrete-time expression for the electrical impedance of the filtered shunt circuit could be expressed as:

$$Z_{sh}(z) = \frac{A_0 + A_1 z^{-1}}{B_0 + B_1 z^{-1}}, \tag{6.5}$$

where

$$A_0 = T_s R_s + 2L_S, \tag{6.6a}$$

$$A_1 = T_s R_s - 2L_S, \tag{6.6b}$$

$$B_0 = T_s + \frac{2}{\omega_c} \quad \text{and} \tag{6.6c}$$

$$B_1 = T_s - \frac{2}{\omega_c}. \tag{6.6d}$$

Recalling that the discrete-time expression for the electrical impedance of the filtered shunt is given by

$$Z_{sh}(z) = \frac{E(z)}{I(z)}, \tag{6.7}$$

the voltage across the terminals of the implemented shunt at the discrete-time step z could be expressed as

$$E(z) = \frac{A_0}{B_0}I(z) + \frac{A_1}{B_0}I(z-1) - \frac{B_1}{B_0}E(z-1). \tag{6.8}$$

The first part of the block diagram shown in figure 6.9 represents the expression given in equation 6.8. The subsequent two constant gain blocks are related to the constant gain by which the input signal of the dSPACE is amplified by the front-end board (Physical gain block) and the need to invert the sign of the output voltage of the dSPACE (Inverting block).

In figure 6.10 are shown the simulated (thick cyan lines) and the measured (thin purple lines) FRFs (amplitude top plot, phase central plot and coherence bottom plot) of the discrete-time electrical impedance of the filtered shunt circuit assuming a shunt resistance of -22.5Ω and a shunt inductance of 40 mH.

The cut-off frequency of the filter, derived by equation (6.3), results to be of about 430 Hz. The two curves present a very good agreement especially at frequency below 1 kHz. Above this frequency value the delay due to the AD and DA conversions causes a phase lag which was estimated to be of about 4 deg/kHz. In figure 6.10 it is also shown with the ochre lines the FRFs of the ideal RL shunt (without the low pass filter). It is interesting to note how the presence of the low pass filter affects both the amplitude and the phase of the electrical impedance of the RL shunt circuit.
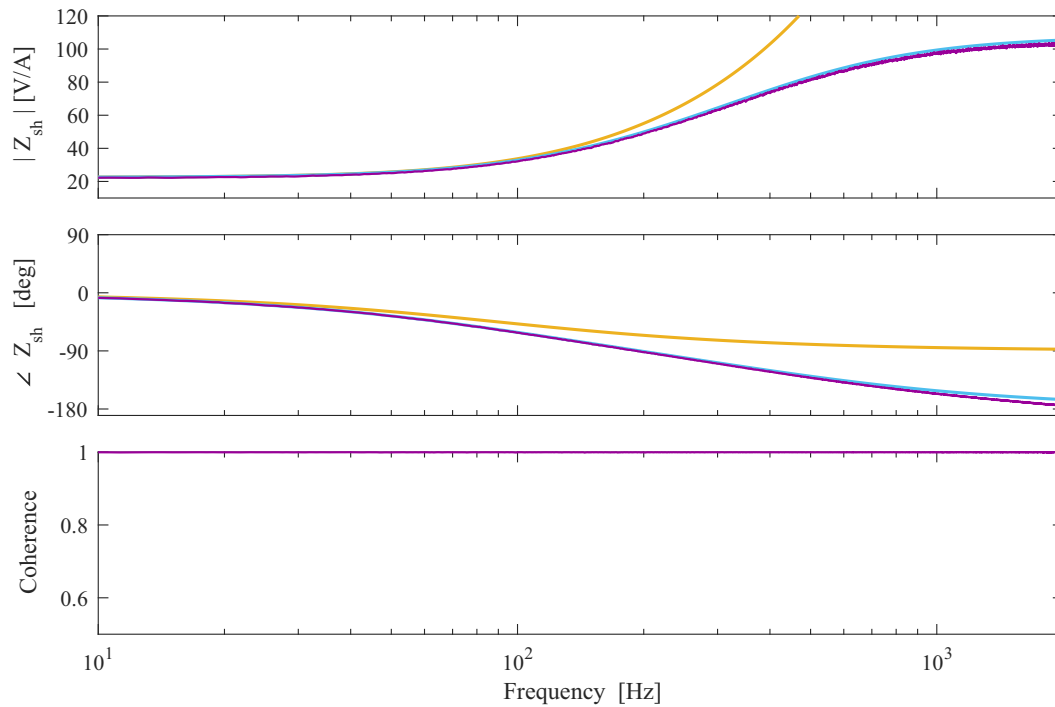
Figure 6.10: Simulated (thick cyan lines) and measured (thin purple lines) FRFs (magnitude top plot, phase central plot and coherence bottom plot) of the electrical impedance of the RL shunt assuming R_s = -22.5Ω and L_s = 40 mH. The thick ochre lines represent the simulated electrical impedance of the shunt circuit without the low-pass filter.

6.4   BASE IMPEDANCE OF THE SHUNTED EM TRANSDUCER

In this section the experimental results of the implementation of the digital shunt circuit and its effects on the Base Impedance of the electro-magnetic transducer are presented.

Several attempts where made to implement the optimally designed shunt circuit depicted in figure 5.5 of the previous chapter, but two main hurdles was encountered. Firstly, as shown in figure 6.5, the actual electrical behaviour of the electro-magnetic transducer does not coincide with the one modelled with the inherent resistance R_e and inductance L_e of the coil. This results particularly true in the high-frequency inductive region. Furthermore the electrical parameters appear to be extremely depending on the working conditions. Indeed, the inherent resistance R_e resulted to be strongly dependent on the room temperature and on the temperature reached in the coil due to Joule heating effect.

Secondly, when the shunt parameters are chosen to annihilate the effects produced by the inherent coil parameters, the system composed by the shunted transducer becomes unstable, leading to the saturation of the dSPACE output.

In order to overcome these difficulties, the choice has fallen upon the implementation of a shunt circuit composed by a resistance R_s and a inductance L_s connected in series, as shown in figure 6.11 (a). These elements simply sums with the inherent electrical elements of the coil and, as shown by the fourth row of table 5.5 of the previous chapter, they produce an equivalent mechanical effect which could be modelled with a series of a dashpot and a spring, as shown in figure 6.11 (b).
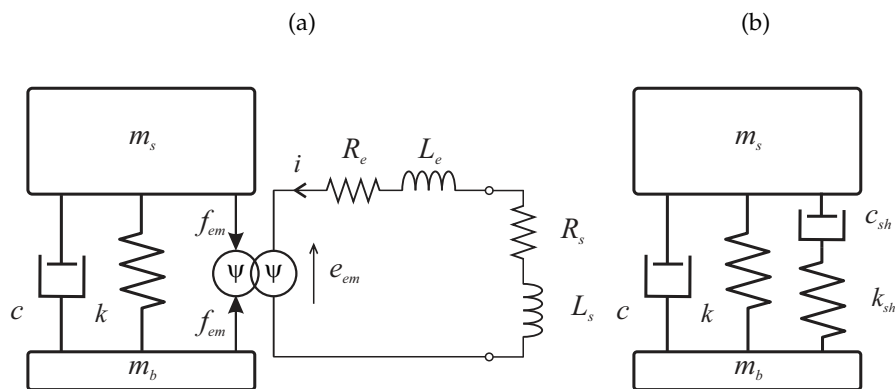
Figure 6.11: Lumped parameter model for the shunted electro-magnetic transducer (a) and equivalent lumped parameter model (b).

In section 5.3 of Chapter 5 was discussed the electro-mechanical analogies. In particular, in the first row of table 5.3 is reported the equivalent mechanical impedance of a shunt circuit composed by a resistance and a inductance connected in series. As discussed in the previous section of this Chapter, two other effects have to be taken in account. First, the application of the low-pass filter, whose cut-off frequency is selected according to the electrical elements of the

shunt circuit. Furthermore, the AD and DA conversions causes a delay in the actuation of the output od the dSPACE controller. The total electrical impedance seen by the electro-magnetic transducer could therefore be expressed as:

$$Z_{sh}(\omega) = \frac{j\omega L_s + R_s}{(j\omega \tau_d + 1)\left(j\omega\sqrt{\frac{L_s^2}{g_{max}^2 - R_s^2}} + 1\right)},$$

(6.9)

where τ_d is the time-delay due to the AD and DA conversion.

In this case it was not possible to obtain a simple expression for the dashpot c_{sh} and the stiffness k_{sh} due to the electrical shunt as a function of the shunt resistance R_s and the shunt inductance L_s. From the experimental results it was found that expressions similar to the ones given in equations (5.29) could be used as a rule of thumb:

$$c_{sh} \propto \frac{1}{R_e + R_s} \quad \text{and}$$

(6.10a)

$$k_{sh} \propto \frac{1}{L_e + L_s}.$$

(6.10b)

A preliminary consideration could be made considering the short-circuited transducer. The mechanical response, expressed in term of the Base Impedance, of the short-circuited transducer is characterised by a more smoother curve than the one corresponding to the open-circuited configuration, as shown in figure 6.4. This is due to the higher value of damping introduced by the presence of the coil resistance.

Considering the equivalent mechanical parameters of the inherent electrical elements, the equivalent damping element is softer than the equivalent stiffness element. The equivalent damping element could therefore considered as rigidly connected to the suspended mass and the base mass. The effect of the inherent inductance of the coil could thus be neglected as far as the equivalent stiffness element is more rigid than the equivalent damping element. In the next section the effects of different configurations of the digitally implement shunt is assessed considering the base impedance of the transducer.

6.4.1   *Positive resistive shunt*

The first case considered is related to a shunt circuit composed by a purely resistive positive element. In this case, the definition of the cut-off frequency of

the low-pass filter, given by equation (6.3), is no longer applicable. The cut-off frequency was therefore set to 10 kHz.

The positive shunt resistance R_s sums with the inherent resistance of the coil R_e, yielding to a resulting resistance which is higher than the inherent one. The equivalent mechanical element (*i.e.* the damping element) results therefore softer as the shunt resistance Rs increases, as express by equation (6.10a). The resulting global damping of the transducer, given by the sum of the purely mechanical damping (open-circuited configuration) and the one due to the shunt circuit, assumes values which gradually approaches the purely mechanical one as the shunt resistance increases. This behaviour could be clearly seen in figure 6.12. Here the FRF (amplitude in top plot, phase in central plot and coherence in bottom plot) of measured Base Impedance of the shunted transducer, considering a digitally implemented positive resistance of $R_s = 160\Omega$ (thin solid blue lines) is compared with the measured Base Impedance obtained considering the open- (thick dashed black lines) and short-circuited (thick dotted black lines) configurations. The positive resistive shunted response is characterised by a lighter damping compared to the short-circuit configuration and by a higher damping compared to the open-circuited configuration. Figure 6.12 also reports the Base Impedance measured shunting the transducer with a physical resistance, drawn in the thick solid yellow lines. The responses obtained shunting the transducer with a digitally implemented and a physical positive resistance are in very good agreement, confirming the good quality of the measurements and of the digital implementation of the shunt circuit.

Figure 6.13 shows the effect on the Base Impedance of the shunted transducer of increasing positive values of the shunt resistance R_s. As the value of R_s assumes higher values, the measured Base Impedance of the shunted transducer, drawn in the solid thin blue lines, tend towards the measured Base Impedance of the open-circuited transducer. Again, this is due to the fact that for increasing positive values of the shunt resistance, the equivalent damping effect assumes gradually smaller values. The global damping effect therefore tends to the purely mechanical damping, which corresponds to the damping characteristic of the open-circuited configuration.
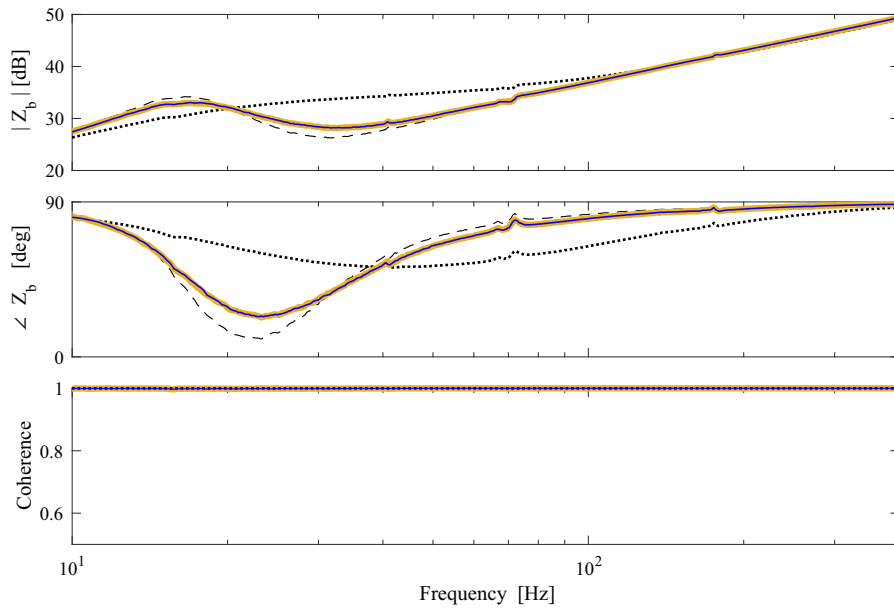
Figure 6.12: Measured Base Impedance FRF (amplitude in the upper plot, phase in the central plot and coherence in the lower plot) of the electro-magnetic transducer in open- (thick dashed black lines), short-circuit (thick dotted black lines) and with a physical (thick solid yellow lines) and digitally implemented shunt circuit (thin solid blue lines) composed by a $R_s = 160\ \Omega$ resistance.
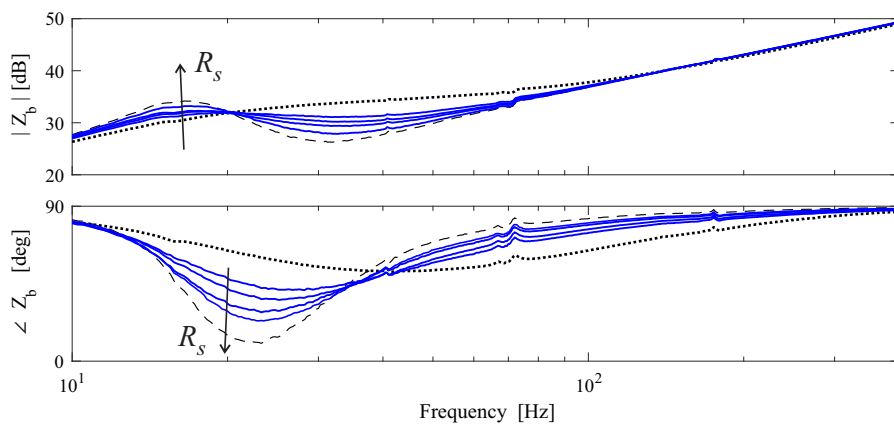
Figure 6.13: Measured Base Impedance FRF (amplitude in the upper plot and phase in the lower plot) of the electro-magnetic transducer in open- (thick dashed black lines), short-circuit (thick dotted black lines) and shunted with increasing values of digitally implemented positive resistance (thin solid blue lines).

6.4.2 *Negative resistive shunt*

The second case considered is related to a shunt circuit composed by a negative resistance. In this case, the global resistance of the transducer assumes values which are smaller than the inherent one. Consequently, as expressed by equation (6.10a), the equivalent damping parameter assumes higher values than the one obtained considering the short-circuited configuration. The equivalent damping parameter assumes therefore values characterised by an impedance comparable to the impedance of the equivalent spring element, related to the inherent coil inductance L_e. The equivalent spring elements could no more be neglected if a shunt circuit composed by a negative resistance is considered. The equivalent spring element combines with the mechanical spring element, given a global stiffness which is higher than the purely mechanical one, obtainable considering the open-circuited transducer. The effect of the global stiffness is shown in figure 6.14, where in the purple lines is drawn the measured Base Impedance of the transducer shunted with a digitally implemented negative resistance of $R_s = -21\Omega$.
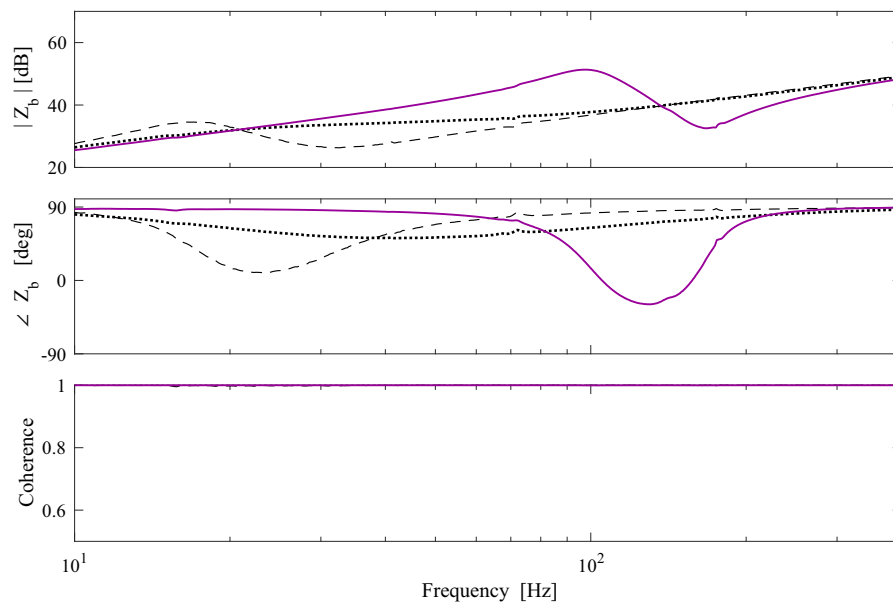
Figure 6.14: Measured Base Impedance FRF (amplitude in the upper plot and phase in the lower plot) of the electro-magnetic transducer in open- (thick dashed black lines), short-circuit (thick dotted black lines) and with a digitally implemented shunt circuit (thin solid purple lines) composed by a $R_s = -21\ \Omega$ resistance.

The Base Impedance of the shunted transducer is characterised by a higher resonance frequency compared to the one obtained with the open-circuited transducer, drawn in the thick dashed black lines. The value of the resonance frequency is closely related to the value of the inherent coil inductance L_e.

Figure 6.15 shows the effects on the measured Base Impedance of increasing values of the shunt resistance. The response of the shunted response, drawn in the thin solid purple lines, is compared with the open- (thick dashed black lines) and short-circuited (thick dotted black lines) configurations. It is interesting to note that, in contrast to the previous case, as the shunt resistance R_s increases the response of the shunted transducer is characterised by a higher value of the damping. This is due to the fact that as the global resistive characteristic assumes lower values (i.e. for a higher absolute value of negative shunt resistance R_s), the equivalent mechanical damping tends toward a rigid connection. The equivalent mechanical stiffness, related to the inherent coil inductance L_e, assumes gradually more importance contributing to the global stiffness of the shunted transducer.
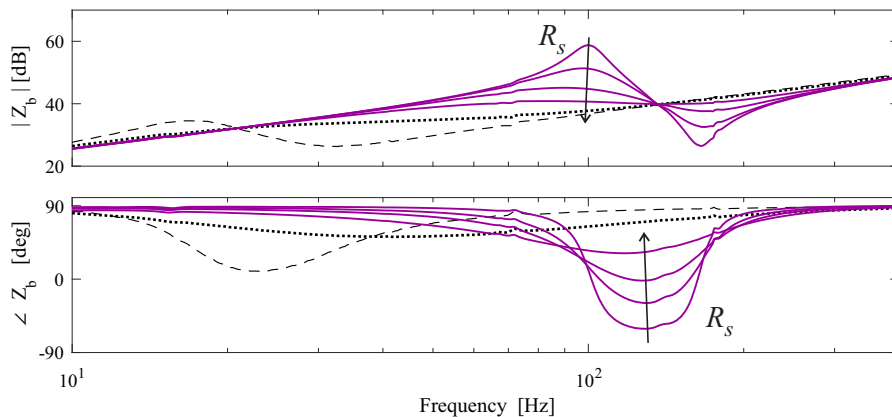
Figure 6.15: Measured Base Impedance FRF (amplitude in the upper plot and phase in the lower plot) of the electro-magnetic transducer in open- (thick dashed black lines), short-circuit (thick dotted black lines) and shunted with increasing values of digitally implemented negative resistance (thin solid purple lines).

6.4.3 *Negative resistive-inductive shunt*

The last analysis of the effects of the digitally implemented shunt circuit on the Base Impedance of the transducer is related to the possibility of shifting the resonance frequency of the shunted transducer. This could be obtained varying the value of the global inductance of the electrical circuit of the transducer. In-

deed, considering the expression given in equation (6.10b), the equivalent stiffness parameter is, to a first approximation, inversely proportional to the global inductance, which results given by the sum of the inherent coil inductance L_e and the shunt inductance L_s. A change in the value of the shunt inductance L_s corresponds to a variation of the equivalent mechanical stiffness elements and therefore a shift of the resonance frequency.

Figure 6.16 shows a comparison of the measured Base Impedance FRFs obtained considering the open- (thick dashed black lines), short-circuited (thick dotted black lines) and shunted (thin solid red lines) transducer. The shunt considered here is composed by a series of a negative resistance fixed to $R_s = -22\Omega$ and an inductance fixed to $L_s = 5$ mH. In this case the measured resonance frequency is about 80 Hz, which results smaller compared to the value of about 100 Hz obtained for the configuration presented in figure 6.14.
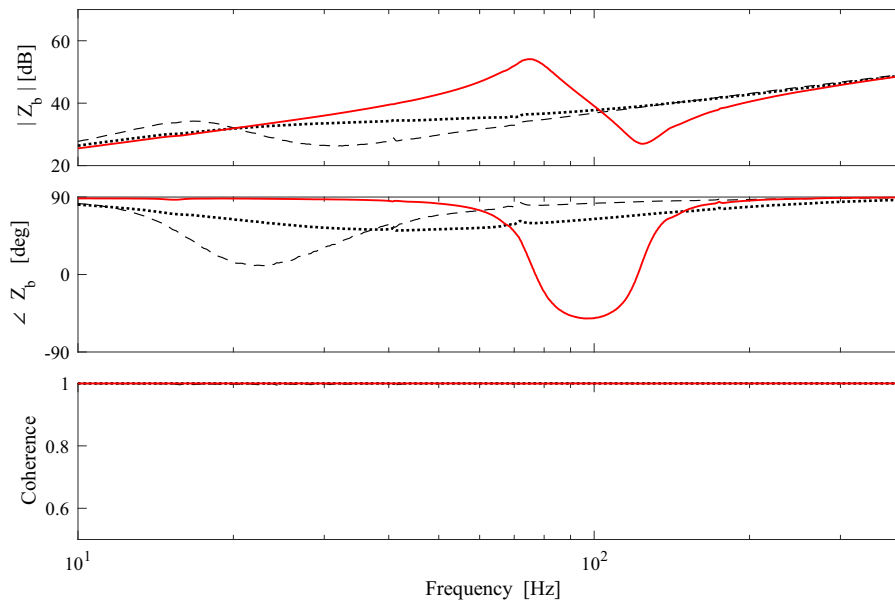
Figure 6.16: Measured Base Impedance FRF (amplitude in the upper plot, phase in the central plot and coherence in the lower plot) of the electro-magnetic transducer in open- (thick dashed black lines), short-circuit (thick dotted black lines) and with a digitally implemented shunt circuit (thin solid red lines) composed by a $R_s = -22\ \Omega$ resistance and a $L_s = 5$ mH inductance.

For increasing values of the shunt resistance, the Base Impedance response appears smoother, corresponding to increasing values of the damping. This behaviour is shown in figure 6.17, where the Base Impedance responses obtained in the open- and short-circuited configurations are compared to the responses of the shunted transducer obtained considering a shunt circuit composed of an

inductance fixed to $L_s = 5$ mH and a negative resistance R_s assuming increasing values.
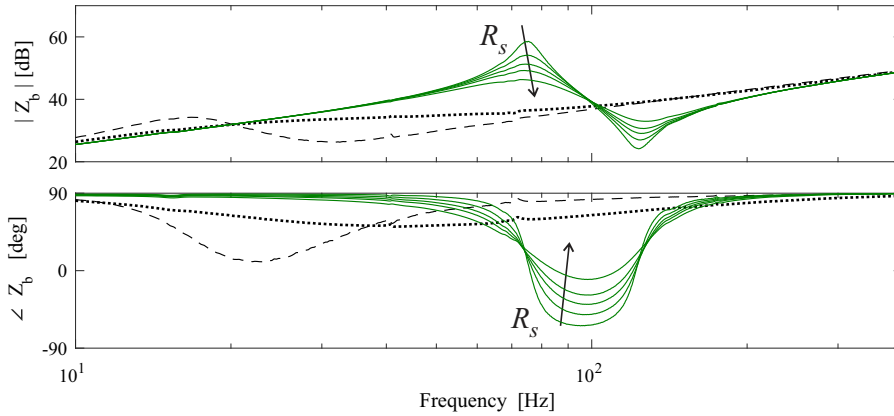
Figure 6.17: Measured Base Impedance FRF (amplitude in the upper plot and phase in the lower plot) of the electro-magnetic transducer in open- (thick dashed black lines), short-circuit (thick dotted black lines) and shunted with a digitally implemented circuit composed by a series of a negative resistance R_s assuming increasing values and an inductance fixed to $L_s = 5$ mH (thin solid green lines).

An interesting behaviour of the shunted transducer could be noted considering figure 6.18. Here the Base Impedance response of the transducer operating in the open- (thick dashed black lines) and in the short-circuited (thick dotted black lines) configurations are compared to the responses of the shunted transducer (thin solid red lines). In this case the shunt circuit is composed by a negative resistance fixed to $R_s = -22\Omega$ and an inductance L_s, whose values are gradually increased. As the shunt inductance L_s increases, the resonance frequency decreases, as suggested by equation (6.10b). Moreover, as the shunt inductance L_s increases, the resonance peak gradually smooths over. This effect is related to the inherent mechanical damping element, whose effect on the resonance peak is related to the frequency at which the peak assumes the maximum value. Recalling that the damping ratio is defined as:

$$\zeta = \frac{c}{2m_s\omega_n},\tag{6.11}$$

it appears clear that for a fixed value of the damping coefficient c, the damping ratio ζ assumes lower values as the natural frequency ω_n increases. The analysis of figure 6.18 lead to the conclusion that at low frequency the damping ratio could not assumes values particularly smaller than the one related to the open-circuited configuration of the transducer. As reported in table 6.1, the damping ratio related to the purely mechanical damping mechanism assumes

a particularly high value, $\zeta_t = 22\%$, compared to the optimal values derived in Section 4.6.2 for the fixed TVA.

It is interesting to compare figures 5.6 (a) and (b) presented in Chapter 5 to figures 6.17 and 6.18, which represent their experimental counterpart.
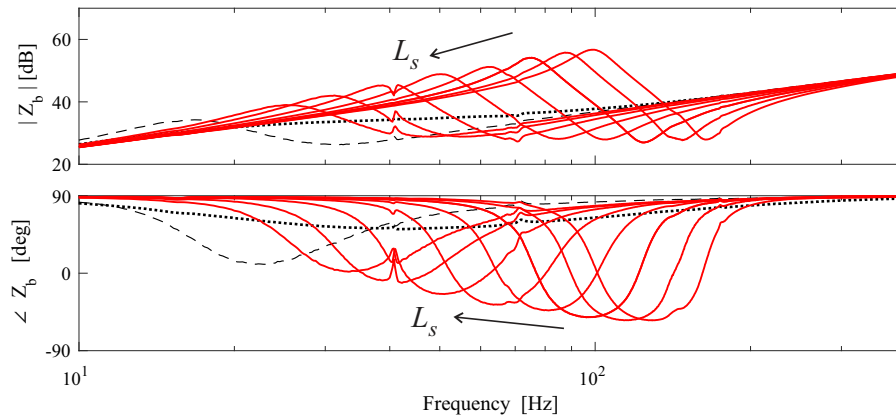
Figure 6.18: Measured Base Impedance FRF (amplitude in the upper plot and phase in the lower plot) of the electro-magnetic transducer in open- (thick dashed black lines), short-circuit (thick dotted black lines) and shunted with a digitally implemented circuit composed by a series of a negative resistance fixed to $R_s = -22\Omega$ and an inductance L_s characterised by increasing values (thin solid red lines).

It is furthermore worth mentioning that all the measured responses of the Base Impedance presented in this Section are characterised, by different amounts, by discontinuities at about 40 and 70 Hz. These are due to the presence of secondary *rocking* vibration modes of the electro-magnetic transducer.

To conclude the analysis of the effects of the digitally implemented shunt circuit on the Base Impedance response, figure 6.19 shows some of the measured Base Impedance responses. Here are compared the FRFs (amplitude top plot and phase bottom plot) of the open- (thick dashed black lines), short-circuited (thick dotted black lines) and shunted transducer. The responses related to a shunt resistance fixed to $R_s = -21.5\Omega$ are here drawn in cyan, the curves related to a shunt resistance fixed to $R_s = -22\Omega$ are drawn in purple and finally the curves related to a shunt resistance fixed to $R_s = -225\Omega$ are drawn in green. The several curves are obtained implementing a shunt inductance L_s fixed respectively to $-6, -4, -2, 0, 2, 5, 10, 20, 40, 80$ and 150 mH (from right to left).
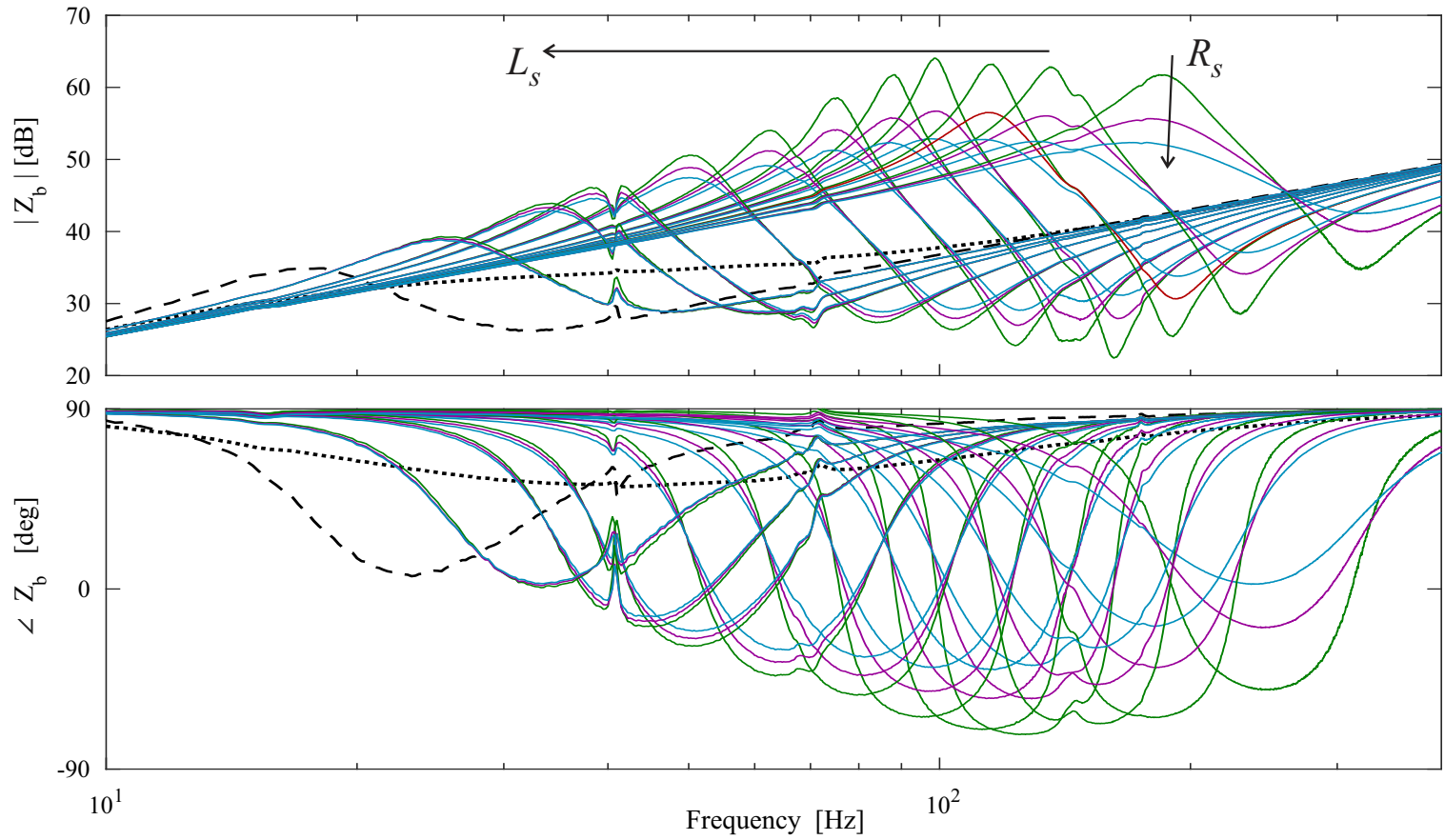
Figure 6.19: Measured Base Impedance FRF (magnitude top plot and phase bottom plot) of the open- (dashed black lines), short-circuited (dotted black lines) and shunted electro-magnetic transducer. The coloured curves are obtained implementing a negative shunt resistance R_s of $-22.5\ \Omega$ (green lines), $-22\ \Omega$ (purple lines) and $-21.5\ \Omega$ (cyan lines) and with a shunt inductance L_s of -6, -4, -2, 0, 2, 5, 10, 20, 40, 80 and 150 mH, from right to left respectively.

6.5   STRUCTURAL RESPONSE OF THE CYLINDER EQUIPPED WITH THE SHUNTED TVA

In this section, the experimental evaluation of the vibration control of the fixed and the sweeping electro-magnetic TVA are assessed considering the TVA mounted on the cylindrical shell.

The first part of the section is devoted to the dynamic characterisation of the cylindrical shell. The flexural velocity of the cylindrical shell is first measured in two points by means of two PCB Piezotronics 288D01 Impedance Heads. The two sensors are characterised by a natural frequency above 20kHz, a weight of 18 grams and a sensitivity of 9.94 mV/(m/s^2) for the acceleration output and of 23.32 mV/N for the force output. The two sensors, whose positions are reported in table 6.2, are connected to the TIRA GmbH TV 51140 shaker and to the EM transducer. A vibrometric analysis of the plain cylindrical shell is then presented, which leads to the identification of the deflection shapes of the cylinder. This analysis allows for the definition of best position of the EM TVA.

In the second part of the section the control performances of the TVA, both in the fixed and the sweeping operation modes, are presented. Based on the experimental results presented in the previous Section, the EM transducer is connected to a digitally implemented shunt circuit in order to modify its mechanical response. Finely selecting the electrical parameters, the dynamic characteristic of the transducer could be accurately tuned. Consequently, as presented in Chapter 4, the EM transducer would behave like a fixed TVA when mounted on the cylindrical shell. By means of a dedicated algorithm, the electrical parameters of the shunt circuit could be periodically varied over time, yielding to a cyclically variation over time of the mechanical behaviour of the transducer. Therefore, as presented in Chapter 5, the EM transducer would behave as a sweeping TVA when mounted on the cylindrical shell.

Figure 6.20 shows a picture of the test rig used for the measurements of the velocity in the two points. The right side of the picture shows the shaker mounted on a very rigid and heavy frame. The shaker is connected to the cylinder through a stinger connected to the Impedance Head. The left side of the picture shows the connection between the cylindrical shell and the electro-magnetic transducer, whose wires are connected to the dSPACE board. The schematic representation of the experimental setup is shown in figure D.7 of Appendix D.

Table 6.2: Positions of the excitation point and of the TVA application point.

	Axial [mm]	Circumferential [deg]
Shaker	135	0
TVA	185	170
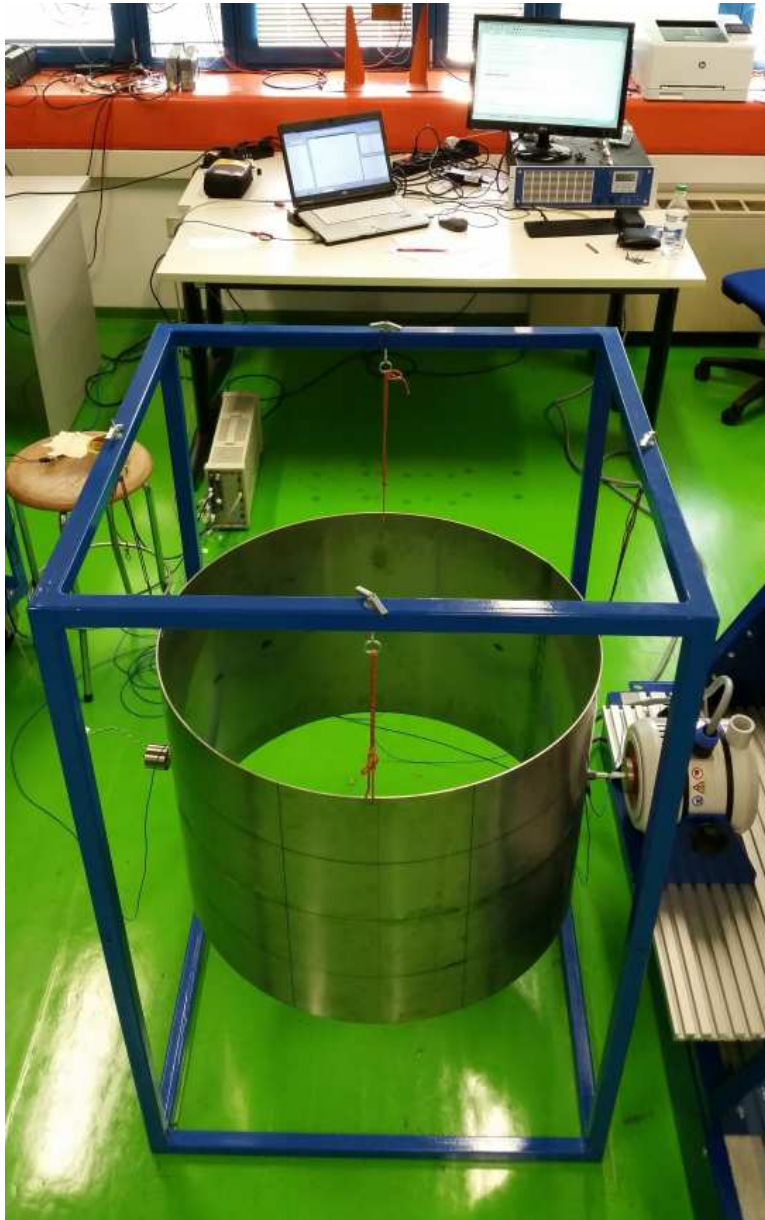
Figure 6.20: Picture of the cylinder connected to the shaker and to the EM transducer.

6.5.1 *Response of the plain cylinder*

The setup for the experimental measurement of the velocity of the plain cylinder is presented in figure D.5 of Appendix D. The shaker is fed with a random signal in order to excite the cylinder with a stochastic white-noise point force. The acceleration signals of the two Impedance Heads are integrated in post-processing to obtain the velocities at the two points. The force signal produced by the Impedance Head connected to the shaker is used as reference signal to obtain the velocity response per unit primary force excitation.

Figure 6.21 shows the 10-150 Hz spectra of the amplitude of the velocity per unit primary excitation force measured at the excitation point, plot (a), and at the control point, plot (b). The two responses are characterised by several well separated resonance peaks, whose amplitudes are fairly even. In correspondence of about 45, 85 and 103 Hz a two resonance peaks are clustered in a small band of few Hz. The peculiar characteristic of the response at these frequencies will be explained and justified by means of the vibrometric analysis. It is furthermore interesting to note how the resonance peaks are fairly separated by anti-resonance for the response measured at the forcing position, plot (a), while for the response measured at the control position the recurrence of resonance and anti-resonance peaks is less even.
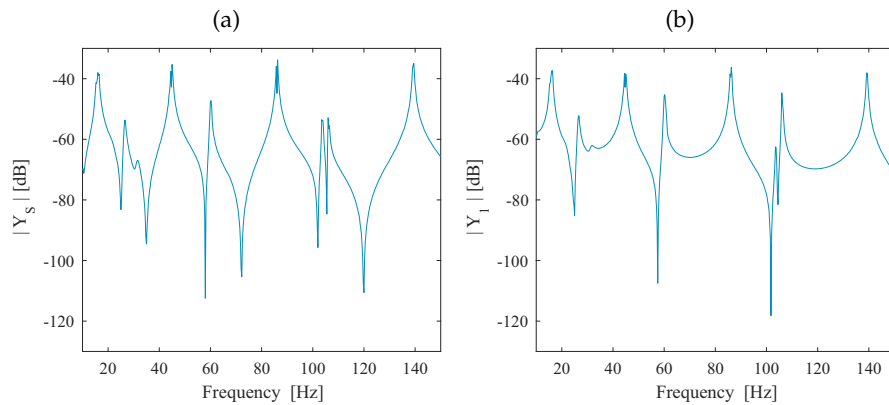
Figure 6.21: Spectra of the velocity per unit primary force excitation of the plain cylinder measured at the positions where the force acts (plot (a)) and at the control position (plot (b))

6.5.2 *Vibrometric analysis of the plain cylinder*

The dynamic response of the cylindrical shell is furthermore investigated by means of the vibrometric analysis. The setup of the test is presented in figure D.6 of Appendix D. A panoramic picture of setup is shown in figure 6.22. Here are shown the Polytec PSV-500 Scanning Vibrometer used, in the centre of figure, the Front End and the laptop in the left side and the cylinder connected to the shaker in the right side.
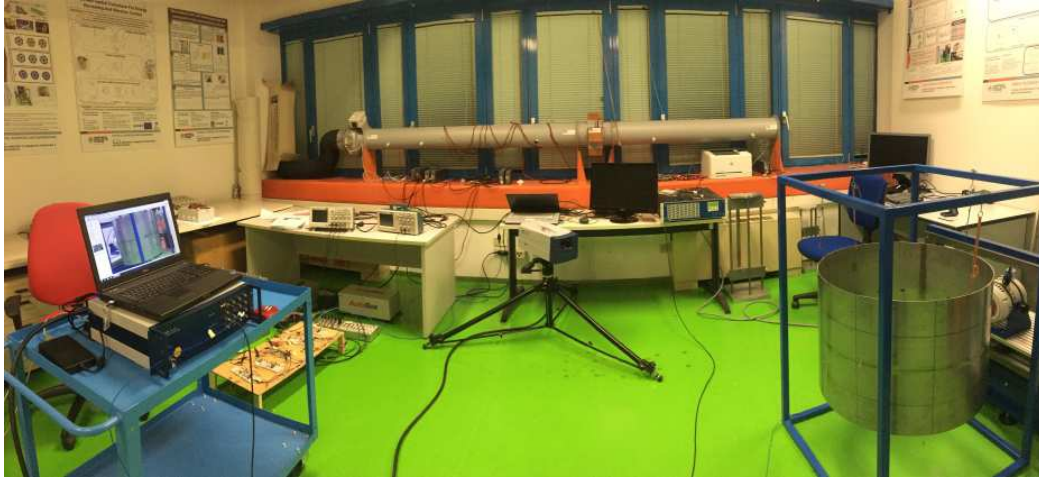
Figure 6.22: Panoramic view of the vibrometic measurements on the plain cylindrical shell.

The Vibrometer used is a 1D acquisition system, suitable for measurements of flat surfaces. In order to obtain a measurements of the deflection shapes of the cylindrical shell, the cylindrical surface was divided into sector of angular dimension of $\pi/4$. Due to the symmetry of the domain, four scan was sufficient to obtain the deflection modes. The position of the scanning head in the four scans sections are shown in figure 6.23 (a). For each scan, the vibration level is acquired in 45 point, arrange in a grid of 5 vertical positions and 9 horizontal (circumferential) positions, as shown in figure 6.23 (b). The data obtained with the four acquisitions are subsequently merged together in post-processing.

For the *free-free* cylindrical shell here considered, the analytical mode shapes could be expressed as [199]:

$$\varphi_m^s(\mathbf{x}_s) = \cos\left(\frac{m_1\pi}{L}x\right)\cos\left(m_2\vartheta\right) \quad \text{and} \tag{6.12a}$$

$$\varphi_m^a(\mathbf{x}_s) = \cos\left(\frac{m_1\pi}{L}x\right)\sin\left(m_2\vartheta\right), \tag{6.12b}$$

(a)

(b)
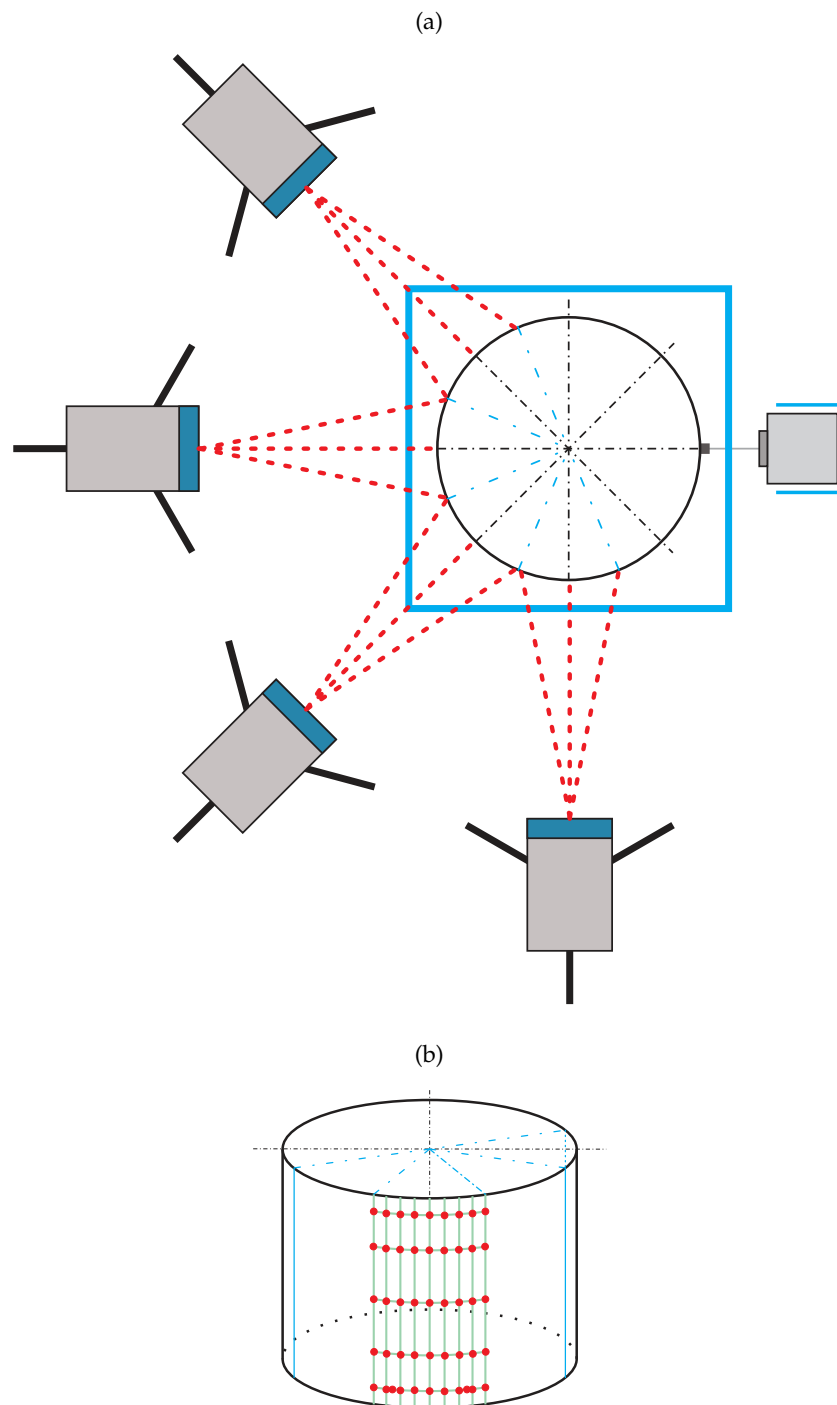
Figure 6.23: Positions of the scanning head in 4 different sectors, plot (a), and acquisition grid, plot (b)

where the subscript m indicates the couple of modal indices (m_1, m_2) and two components for each mode shape should be taken into account due to the cylindrical symmetry.

Figure 6.24 shows a comparison between the analytical mode shapes expressed by equations (6.12) and the measured deflection shapes. Here the analytical mode shapes are shown in the left image of each plot while the deflection shapes are shown in the right image of each plot.

As highlighted in Section 3.4.4 of Chapter 3, if a single point force excites the cylindrical shell, independently to the boundary conditions, the modes shapes orientates in order to present the maximum deflection in correspondence to the angular position of the force. This suggest that for the case at hand, a single component is sufficient to describe the deflection of the cylindrical shell. Considering for example plots (c) and (d) of figure 6.24, which correspond to the deflection shapes of the resonance peaks of 44 and 45 Hz, it is clear that them are characterised by the same spatial distribution, and thus by the same combination of modal indices m_1 and m_2, but a different circumferential geometry. The same could be noted considering plots (f) and (g) corresponding to the responses at 85 and 86 Hz and also plots (h) and (i) corresponding to the responses measured at 103 and 106 Hz, respectively.

The presence of two resonance peaks characterised by two very close resonance frequencies, which present the same spatial distribution is mainly due to the weld joint. This section represents indeed a discontinuity on the cylindrical surface and therefore the flexural wave propagating in the cylindrical shell are, in some amount, obstructed by the presence of the weld joint.

Figure 6.25 shows the overlay of the average velocity response per unit primary excitation force obtained with the vibrometric analysis and the identification of the deflection shape for each resonance frequency. The average spectra is obtained by summing together the responses measured in correspondence of the 180 points (4×45) and therefore does not present any anti-resonance.

(a) $f_r = 16$ Hz

(b) $f_r = 26$ Hz

(c) $f_r = 44$ Hz

(d) $f_r = 45$ Hz

(e) $f_r = 60$ Hz

(f) $f_r = 85$ Hz

(g) $f_r = 86$ Hz

(h) $f_r = 103$ Hz

(i) $f_r = 106$ Hz

(j) $f_r = 139$ Hz
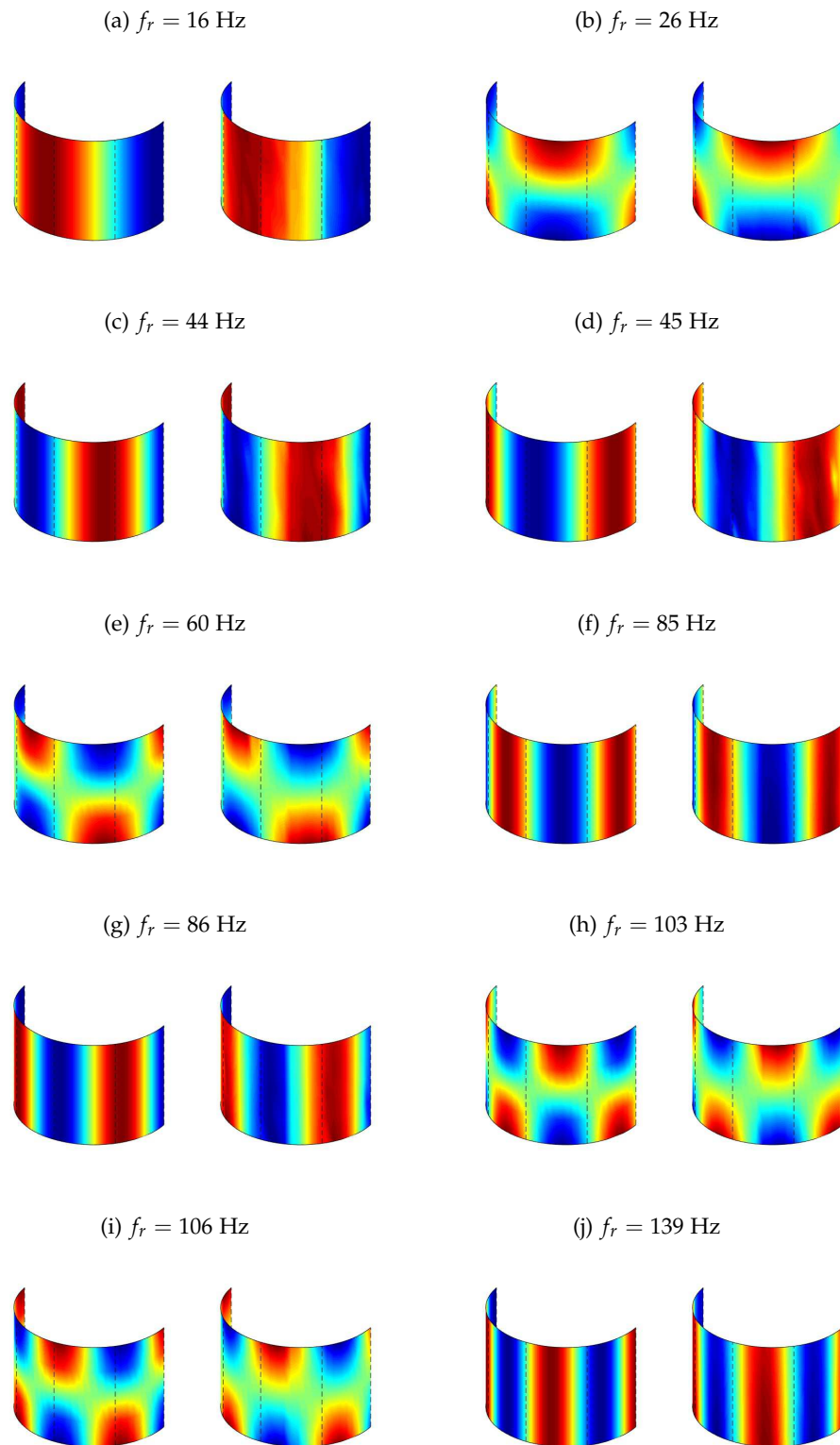
Figure 6.24: Comparison of the simulated mode shapes and of the measured deflection shapes of the *free-free* cylindrical shell for the $(0,2)$ (a), $(1,2)$ (b), $(0,3)$ (c) and (d), $(1,3)$ (e), $(0,4)$ (f) and (g), $(1,4)$ (h) and (i) and for the $(0,5)$ (j) mode and deflection shapes.
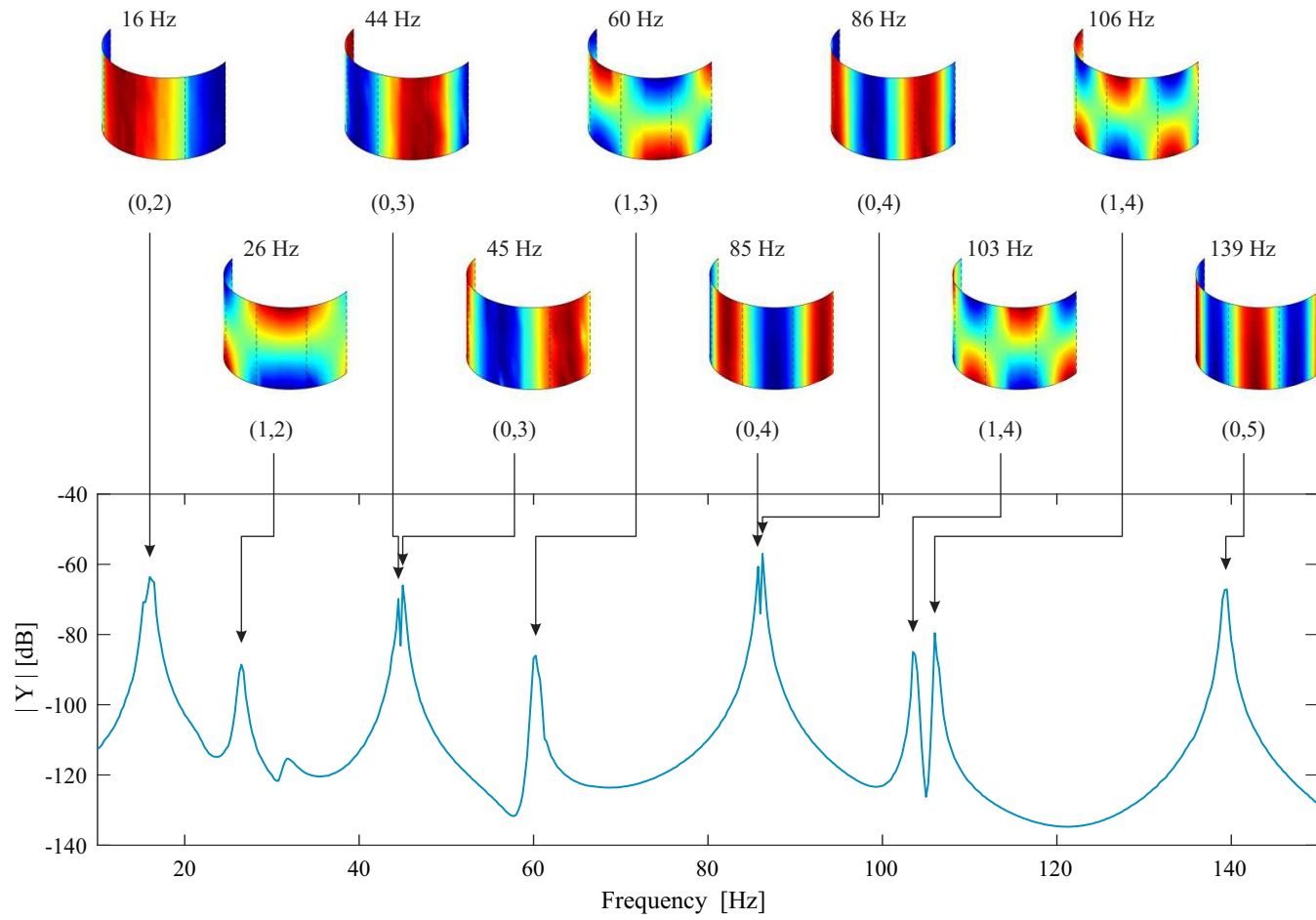
Figure 6.25: Overlay of the average velocity response of the cylindrical shell and of the deflection shapes.

6.5.3 *Response of the cylinder equipped with the fixed shunted EM TVA*

Based on the vibrometric analysis presented in the previous section, the control position where the EM TVA is connected is selected in order to be the most suitable for the flexural control, as discussed in section 4.5 of Chapter 4. The selected control position is reported in table 6.2.

First, the effects on the open-circuited transducer mounted on the cylindrical shell are considered. Figure 6.26 shows the 10-150 Hz spectra of the velocity per unit primary force measured at the excitation point, plot (a), and at the control point, plot (b). The responses of the plain cylinder are drawn in thick solid cyan lines and the responses of the cylinder equipped with the open-circuit EM TVA are drawn in the thin solid black lines. The open-circuited EM TVA presents, as reported in table 6.1, a resonance frequency of about 16 Hz which is slightly lower than the first resonance frequency of about 18 Hz. The device is therefore mistuned and, in addition to its high value of the damping, it does not provide significant control performances. The two responses of the cylinder equipped with the open-circuit EM TVA are furthermore only slightly affected at higher frequency by the mass-like impedance of the TVA.
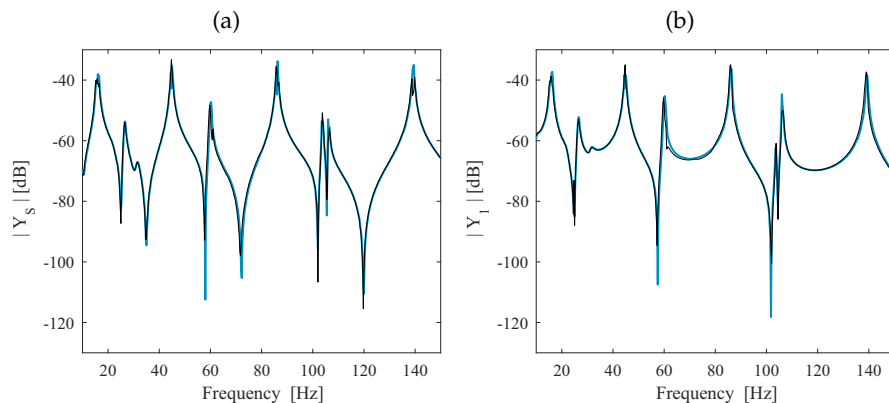
Figure 6.26: Measured spectra of the velocity per unit primary force excitation at the positions where the force acts (plot (a)) and at the control position (plot (b)) without the TVA (thick solid cyan lines) and when the open-circuited TVA is mounted on the cylinder (thin solid black lines).

Based on the results obtained in Section 6.4 of this Chapter, the EM TVA is then shunted with a digitally implemented circuit composed by a negative resistance R_s and an inductance L_s. The electrical parameters are selected in order to tuned the shunted EM TVA to the fourth, sixth and ninth resonance modes, whose frequencies are 45, 85 and 106 Hz respectively. The selected electrical parameters are reported in table 6.3.

Table 6.3: TVA parameters for fixed and sweeping operation modes.

Operation mode	Frequency range f_A [Hz]	Damping ratio ζ_A [%]	Shunt inductance L_1 [mH]	Shunt resistance R_1 [Ω]
Fixed (6.27 (a), (b))	45	10.5	40	-22.5
Fixed (6.27 (c), (d))	85	4	2.5	-22.5
Fixed (6.27 (e), (f))	106	4	-1	-22.5
Sweeping	$40 \div 150$	$4 \div 11$	$-5 \div 45$	-22.5

Figure 6.27 shows the 10-150 Hz spectra of the velocity per unit primary force measured at the excitation position, left plots, and at the control position, right plots. Here the responses obtained considering the open-circuited EM TVA are drawn in solid thin black lines ones obtained considering the fixed shunted EM TVA are drawn in solid thin red lines. Plots (a) and (b) are related to the fixed TVA tuned to the fourth resonance frequency, plots (c) and (d) are related to the fixed TVA tuned to the sixth resonance frequency and finally plots (e) and (f) are related to the fixed TVA tuned to the ninth resonance frequency. The frequencies at which the fixed TVA is tuned are highlighted by the red arrows.

The fixed tuned shunted TVA effectively control the resonance peaks corresponding at the target resonance frequencies at which they are tuned, presenting reductions of 9 to 15 dB at the excitation position and of 11 to 20 dB at the control position.

It is worth mentioning that higher reductions are obtained in correspondence to the resonance peaks characterised by the higher resonance frequency. This is justified considering the results obtained in Section 6.4 of this Chapter. Indeed, as shown in figures 6.18 and 6.19, the damping ratio of the transducer decreases as the resonance frequency raises. Tuning the resonance frequency of the transducer to 45 Hz implies that the damping ratio assumes a higher value than the optimal one, which results to be about 4 %.

It is furthermore important to highlight how these results are obtained by accurately tuning the TVA to the resonance frequencies of the cylindrical shell.
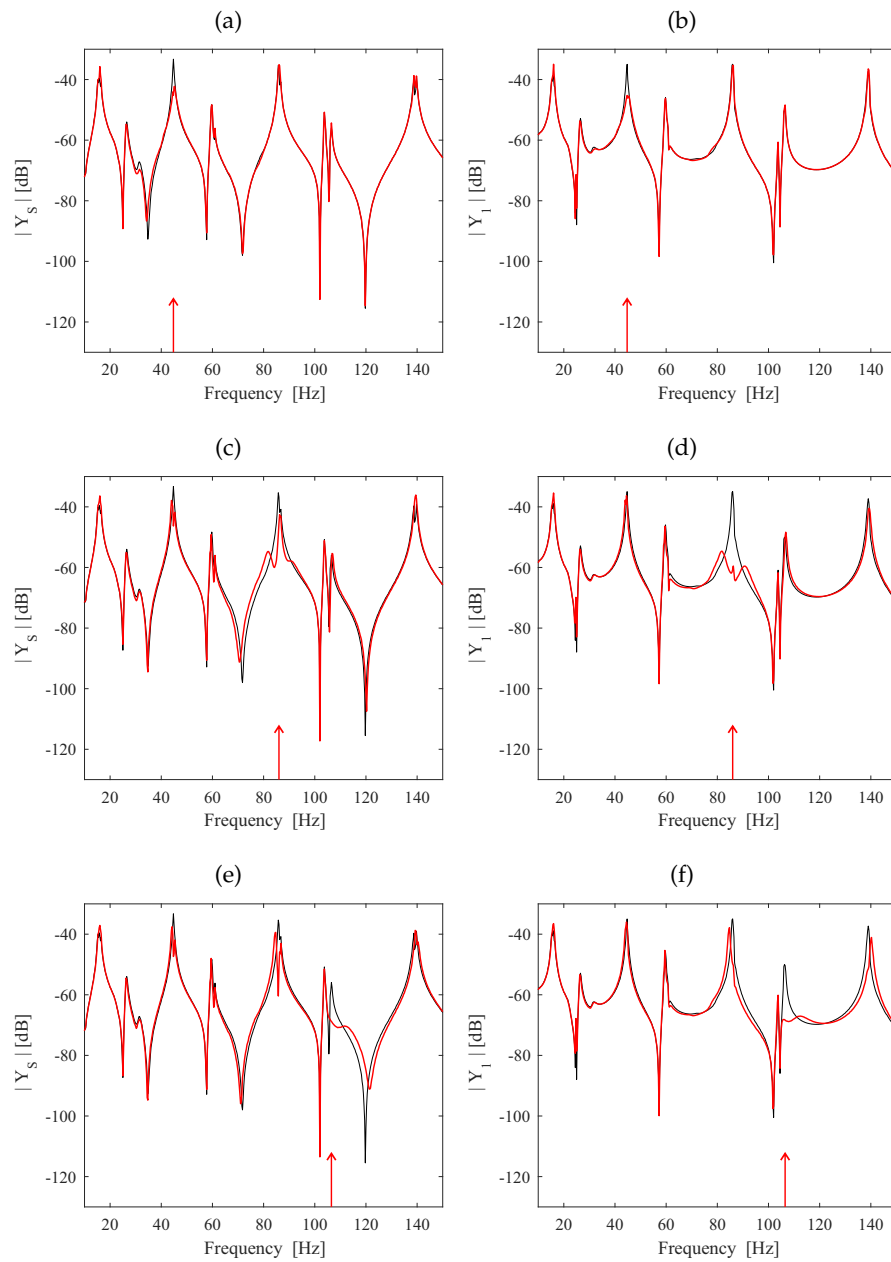
Figure 6.27: Measured spectra of the velocity per unit primary force excitation at the positions where the force acts (left plots) and at the control position (right plots) of the cylinder with the open-circuited TVA (solid thin black lines) and with the TVA tuned to control the resonant response of the fourth (plots (a) and (b)), sixth (plots (c) and (d)) and ninth (plots (e) and (f)) structural modes (solid thin black lines).

6.5.4   *Response of the cylinder equipped with the sweeping shunted EM TVA*

In this section the flexural vibration control performances of a sweeping shunted EM TVA are assessed. As introduced in Section 5.4 of Chapter 5, when the shunted EM TVA are operated in the sweeping mode, it cyclically varies its resonance frequency while the damping ratio is constant over time and fixed to the optimal value. This could be achieved periodically varying the electrical parameters of the shunt circuit.

As highlighted by the results discussed in Section 6.4 of this Chapter, it is not possible to obtain a simple and straightforward relation between the electrical parameters of the shunt circuit and the mechanical parameters of the shunted transducer. This is due to series circuit selected to shunt the transducer. In addition to this, the effects of the low-pass filter and of the delay introduced by the AD and DA conversions have to take into account.

A different approach to obtain the sweeping operation mode has been adopted. By means of the experimental findings presented in Section 6.4, it is possible to select the value of the shunt inductance L_s in order to obtain a given resonance frequency. Subsequently, instead of considering the analytic sweeping law presented in Section 5.4 of the previous Chapter, the following periodic law was chosen for the time-variation of the shunt inductance:

$$L_s(t) = L_{s,max} - (L_{s,max} - L_{s,min}) \cos^2 (2\pi f_{sw} t) , \qquad (6.13)$$

where $L_{s,max}$, $L_{s,min}$ are the upper and lower values of the shunt inductance, set to 45 and -5 mH respectively and f_{sw} is the frequency of the sweep, which was set at 10 Hz after several experimental test. The shunt resistance was set to $R_s = -22.5 \ \Omega$ and kept constant over time in order to obtain the minimum value of the damping of the shunted sweeping TVA for each value of the shunt inductance.

The frequency range of the sweep and the electrical parameters are reported in the last row of table 6.3.

Figure 6.28 shows the 10-150 Hz spectra of the velocity per unit primary force measured at the excitation position, plot (a), and at the control position, plot (b). Here the velocity responses of the cylinder equipped with the open-circuited EM are drawn in solid thin black lines and the velocity response considering the sweeping shunted EM TVA are drawn in solid thick green lines. Figure 6.28 shows that, when the cylinder is equipped with the shunted sweeping TVA, the structural response is effectively reduced at the majority of the resonance peaks, with reductions comprised between 3 dB and 10 dB for the point where

the force is applied and between 6 dB and 10 dB for the response measured where the sweeping TVA is applied.
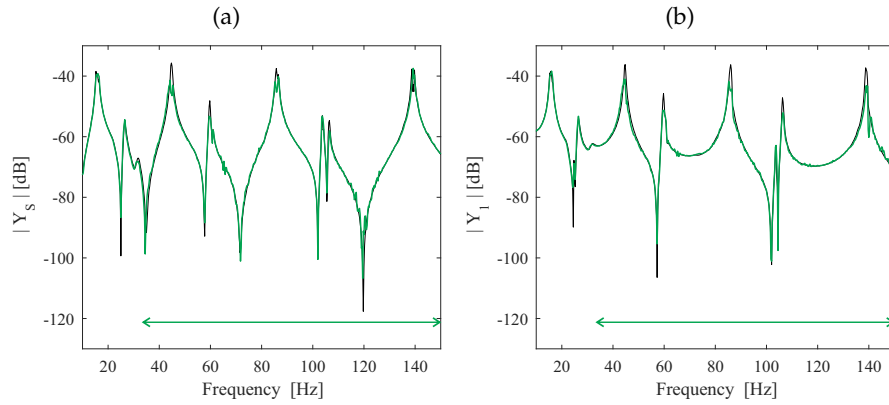
Figure 6.28: Measured spectra of the velocity per unit primary force excitation at the positions where the force acts (plot (a)) and at the control position (plot (b)) of the cylinder with the open-circuited TVA (solid thin black lines) and when the shunted TVA operating in the sweeping mode (solid thick green lines) in the frequency range pointed by the green arrows.

6.6 CHAPTER CONCLUDING REMARKS

This chapter presented experimental results of the semi-active control effects of fixed tuned and sweeping vibration tuneable absorbers on a thin cylindrical shell using a digitally implemented shunted electro-magnetic transducer.

First, the test rig used for the experimental validation of the sweeping electro-magnetic TVA is presented. Unlike the simulated results presented in the previous Chapters, the cylindrical shell here considered is subject to *free-free* boundary condition. This anyway does not constitute a limitation of the experimental work since, as stated in Chapter 2, the developed analytical model has the purpose of only provide an estimation of the performances of the control device. Indeed, a *free-free* cylinder presents the same dynamic properties (*i.e* modal density and modal overlap factor) of a *simply-supported* cylindrical shell with the same geometrical dimensions. Also the choice of a different material (*i.e.* steel instead of aluminium) does not constitute a significant difference with the results presented in the previous Chapters. This is due to the fact that the two materials present comparable values of the Young's modulus to density ratios (E/ρ). Therefore the choice has fallen upon a material which is easier to weld, yielding to economic benefits. The choice of different geometrical dimensions for the cylindrical shell was driven by the necessity for it to be suitably by

hosted into the "Laboratorio di Controllo e Regolazione Automatica" at the Università degli Studi di Udine. The geometrical dimensions was anyway selected in order to present a length to radius ratio (L/R) comparable to the one considered in the simulation study. The control performances of the shunted EM TVA are assessed only by means of the vibration control effects, neglecting the noise control ones. This is due to the fact that the anechoic chamber of the Università degli Studi di Udine was not available at the time when the experiments were made.

The mechanical and electrical characteristics of the actual electro-magnetic transducer were evaluated, showing how the two mass-daspot-spring model presented in chapter 5 could be effectively used to predict the mechanical response of the transducer. On the other hand, the electrical behaviour of the actual transducer appears to be different to the one modelled with the inherent electrical resistance and inductance. This aspect would require a further investigation and an improvement of the analytical model of the electro-magnetic transducer. This set of analyses was not included in the present investigation. This choice was made after pondering all the variables and selecting the most representative for this study considering the limited amount of time available for the present work.

A specific front-end circuit was designed and tested for the connection of the electro-magnetic transducer and the controller platform. The digital implementation of shunt circuit was obtained with a discrete-time algorithm implemented on the dSPACE platform.

The effects of the digitally implemented shunt circuit on the Base Impedance of the transducer was measured. Several types of resistive, both with positive and negative values, and resistive-inductive shunt circuits were tested. This survey led to the development of general guidelines for the design of the shunt circuit. The shunt considered in the experimental study is composed by a series of a resistance and an inductance. This aspect represents a substantial difference with the ideal shunt circuit presented in Chapter 5. Indeed, the ideal shunt circuit is composed by a series of a negative resistance and a negative inductance connected to a parallel of a resistance and an inductance. The first to negative electrical elements are tuned to cancel the inherent resistance and inductive effects of the coil. Considering the non ideal electrical behaviour of the actual transducer, the cancellation of the inherent electrical effects are extremely difficult. Furthermore the inherent electrical effects appears to be strongly dependent on the operation conditions, due to the Joule heating effect. The choice of RL series shunt circuit led to the experimental demonstration of how the

electrical shunt could modify the mechanical behaviour of the shunted electromagnetic transducer.

The last part of the Chapter is devoted to the evaluation of the vibration control performances of a shunted EM TVA, in both the fixed and the sweeping operation mode. The dynamic response of the cylindrical structure is first evaluated. In particular, the cylinder was identified in terms of its resonance frequency and the deflection shapes associated to these frequencies. A vibrametric analysis was conducted in order to identify the deflection shapes associated to each resonance frequency. The scanning vibrometer used for the measurement is an instrument suitable for the analysis of flat surface. Four measurements to adjacent sections of the cylindrical surface were conducted. The data obtained with the four measurements are subsequently merged together in postprocessing in order to show the deflection of half the cylindrical surface. The deflection shapes are then compared to the analytical mode shapes for the *free-free* cylinder. One interesting finding that emerge from this analysis is that the response of the cylindrical shell is characterised, in the low frequency region, by well separated resonance peaks. At some frequencies two resonance peaks are clustered in small bands of few Hz. The two resonant modes whose resonance frequencies are clustered are associated with the same spatial distribution of flexural waves. This effect is ascribable to the weld joint, which, by different amounts, obstructs the circumferential propagation of the flexural waves.

The vibration control performances are assessed considering the velocity of two points on the cylindrical surface, namely the position where the force due to the shaker is exerted and the point where the EM transducer is connected to the cylindrical shell. Firstly, the control performances of the fixed tuned shunted TVA are evaluated. The results obtained considering the fixed TVA finely tuned to three resonance frequency are presented. The experimental results showed very good reduction performances both at the control and excitation points, with reduction of the order of $10 \div 20$ dB. Secondly, the effects of the sweeping shunted TVA on the vibration of the cylindrical shell are assessed. Due to the different shunt circuit adopted, the ideal time-variation law described in Chapter 5 could not be implemented. Thus, a different sweeping law is used, which led to a time-variation of the shunt inductance and therefore of the resonance frequency of the shunted EM TVA. The shunt resistance was set to the minimum possible value and kept constant over time. The sweeping EM TVA would therefore be characterised by the minimum value of damping for each value of the shunt inductance. The reduction obtained with this operation mode were quantified to be of the order of $5 \div 10$ dB. This is a rather

promising result, considering that the sweeping TVA does not require a precise tuning to targeted resonant frequency. Indeed, it can blindly operated in a given frequency band.

7

SUMMARY, CONCLUSIONS AND FUTURE WORK

This final Chapter recapitulates the principal findings of this thesis and suggests advancements for future research work. A more detailed discussion of the results is provided at the end of each Chapter.

7.1 SUMMARY

In chapter 3 the fully coupled structural-acoustic system is described. The *in vacuo* response of the cylindrical shell is first derived according to the Donnell-Mushtari shell theory [98, 101], which is particularly suitable for the description of the flexural vibration of cylindrical structures. The twofold degeneracy due to the cylindrical symmetry of the structure leads to the representation of each structural natural mode shape with two components, referred as symmetric and anti-symmetric components. A graphical representation of the two structural mode shape components is given, concerning in particular the positions of the nodal and anti-nodal positions. The response of the cylindrical shell subject to an array of 24 white noise uncorrelated rain on the roof point forces is assessed in terms of the flexural kinetic energy PSD [60, 64, 65, 72]. A simplified model consisting of a single structural mode and either single or couples of point forces is used to obtain a criteria for the orientation of the resulting flexural deflection. Then, the acoustic response of the *rigidly walled* cylindrical enclosure is considered. The acoustic modal shapes need a representation *via* two components due to the cylindrical symmetry of the acoustic enclosure. An array of distributed white noise uncorrelated point monopole sources are considered to excite the acoustic domain. The acoustic response is assessed in terms of the total acoustic potential energy PSD [28, 60, 64, 65]. The chapter concludes with the analysis of the coupled structural-acoustic response. The approach to obtain the coupled response is based on the Modal Interaction Model [30, 99], which describe the coupled flexural displacement in terms of the *in vacuo* flex-

ural modes and the acoustic pressure in terms of the *rigidly walled* acoustic modes. The coupling phenomenon is expressed in terms of structural-acoustic and acoustic-structural coupling terms [28, 30, 64, 120, 136].

Chapter 4 presented the simulation studies on the noise and vibration control effects produced by arrays of fixed Tuned Vibration Absorbers. First, the dynamic behaviour of the TVA is analysed in terms of the device Base Impedance [154]. Several tuning criteria presented in literature [159] are reported . The principal operating issues of the TVA are also presented, in particular the effect of the mistuning of the TVA is assessed considering a simplified model composed by a single degree of freedom primary system. The effects of a single TVA on a multi degrees of freedom system is also considered. A simplified model composed by a single structural mode is used to obtain general guidelines for the positioning of the TVAs both when the excitation field permits a precise knowledge of the resulting orientation of the flexural displacement and when the distribution of forces or the stochastic nature of these do not allow the prediction of the resulting anti-nodal positions. A fully coupled structural-acoustic-TVA [64, 65] model is presented, and the noise and vibration control performances are assessed in terms of the PSDs energies. The study showed that the fixed tuned TVAs could effectively be used to control the resonance response of both the flexural and acoustic domains. Large attenuations are obtained for frequencies below 60 Hz while smaller reductions are obtained for frequencies comprised between 60 and 100 Hz. This could be explained considering the high modal overlap factor which characterise the cylindrical shell structures.

In chapter 5 the time-varying tuneable vibration absorbers are presented [58, 61, 65]. These device are obtained using electro-magnetic transducers, thus the chapters starts with a description of this kind of transducers, focusing in particular on the physical laws that govern the electro-magnetic-mechanical interaction [184–186]. The mechanical response of the shunted device is studied in terms of the Base Impedance, which turns out to be dependent on the electrical elements of the shunt circuit. An idealised coil-magnet transducer is used to conduct a survey on the equivalent mechanical effects produced by shunt circuits composed by elementary passive electrical elements and series and parallel connection of these [64, 65]. The results of the survey reveal that the parallel connection between electrical elements is the most suitable for the shunting of electro-magnetic, since this configuration allows an independent tuning of the equivalent mechanical parameters. Based on these results, a shunted circuit is presented, which is composed by a series of a negative resistance and nega-

tive inductance connected with a parallel of a variable resistance and variable inductance [64, 65]. The first part of the shunt is used to annihilate the inherent electrical characteristic of the coil while the latter part is used to obtain a precise tuning of the device. If the electric elements of the tuning section are varied over time with a specific time-harmonic law, the shunted electro-magnetic transducer could be used as a sweeping TVA. The noise and vibration control performances are assessed with reference of the coupled structural-acoustic system and result to be comparable to those obtained with the fixed tuned devices. Considering that with the sweeping TVAs there is no need to perform a system identification of the hosting structure to determine its physical properties, as the sweeping operation mode only requires the initial and final values of the targeted frequency band and the damping ratio value, they can offer significant practical advantages for the development of effective, robust and easy to use modular devices.

In chapter 6 the experimental evaluation of the vibration control performances of a shunted electro-magnetic TVA mounted on a cylindrical shell were presented. Several experimental test were presented in order to characterise the mechanical and electrical behaviour of an actual electro-magnetic transducer. These results showed how the two-degrees-of-freedom system presented in chapter 5 could effectively be used to model the mechanical behaviour of the transducer. On the other hand, the electrical behaviour of the transducer coil presents an high-frequency discrepancy with the simulated resistive-inductive model. Furthermore, the electrical characteristics of the transducer result to be extremely dependent on the room and operating temperature. These aspects led to the implementation of a shunt circuit constituted by a series of a resistance and an inductance, which needs a low-pass filter for its actual use. The effects on the Base Impedance of the transducer of several resistive and resistive-inductive digitally implemented shunts are experimentally assessed. These results provided general guidelines for the tuning of the electrical elements of the shunt circuit. The final part of the Chapter was focused on the vibration control performances on a cylindrical shell of the electro-magnetic TVA operating in both the fixed and the sweeping mode. The experimental results showed that the fixed tuned operation modes guarantees the best control performances but requires a detailed tuning. On the other hand, also if the attenuations obtained with the shunted electro-magnetic TVA result smaller than the ones obtained with the fixed TVA, these are achieved without the precise tuning of the absorber. Indeed with the sweeping operation mode there is no need to perform a

system identification of the primary structure in order to determine its dynamic properties and therefore it blindly operates in a given frequency range.

7.2   CONCLUSIONS

The research presented in this thesis is focused on the broadband noise and vibration control of thin cylindrical structures using fixed Tuned Vibration Absorbers and sweeping Tuneable Vibration Absorbers. The sweeping TVAs are realised with electro-magnetic transducers connected to a specifically designed RL shunt circuit, which allows an independent tuning of the damping and stiffness properties of the TVAs.

The results presented in this study show that single-unit or arrays of sweeping TVA effectively control the flexural vibrations of a cylindrical shell. The performances of proposed sweeping absorber are assessed both with simulation and experimental results.

In Chapter 3 the Modal Interaction Model have been adopted. The advantages in simplicity and easiness of this method are exploited, obtaining a full analytical description of the dynamics involved. Due to the extremely selectivity of the structural-acoustic coupling, a dedicated convergence study has been performed. This technique has led to a comparable, or even better, description of the global vibration and acoustic fields compared to similar studies [28, 94, 138], achieved with a much lower computational cost.

In Chapter 4, some original contribution have been proposed, related to the positioning criteria of the fixed TVA on cylindrical shells. This aspect appears to be quite a novelty, since very little research work is present in the literature [169].

Chapter 5 has described the the model of an electro-magnetic TVA. A simple model for the study of the electro-mechanical analogies has been presented. This analogy study has been furthermore improved yielding to a deep understanding of how the electrical parameters could affect the mechanical response of an electro-magnetic transducer. The analogy study was based on the classical analytical model of an electro-magnetic transducer [29, 162, 181, 200]. The choice of consider an analytic model for the electromagnetic transducer was made due to the lack of experimental data on the mechanical and electrical properties of actual transducer when the analogy study was performed. Based on the analogy study, a novel shunt circuit has been proposed, which allows for an independent tuning of the TVA damping and stiffness parameter. The control performances of a sweeping electromagnetic TVA, obtained by period-

ically varying its stiffness and damping parameters, are numerically assessed. The simulation study has shown that the proposed sweeping shunted electromagnetic TVA produce similar performances than those produced by fixed tuned TVA [64, 65].

In Chapter 6 the flexural vibration control performance of a fixed tuned and a sweeping shunted electromagnetic TVA are experimentally proved. The unavailability of the anechoic chamber of the Università degli Studi di Udine during the experimental work prevented the possibility of evaluate the noise control performances of the device. These are anyway strictly connected with the vibration control performances, as highlighted in the simulation results [60, 64, 65]. The prototype on which the control performances of the EM TVA are assessed is a suspended steel cylinder. The choice of this configuration, which resembles the *free-free* boundary condition does not limit the validity of the results, since the dynamic characteristics (*i.e.* modal density and modal overlap factor) of the simulated and tested structures are comparable. Furthermore, the selection of a different material, driven by manufacturing reasons, does not constitute a discrepancy with the analytical model, since the two materials are characterised by comparable values of the Young's modulus to density ratio (E/ρ). The dimensions of the actual cylindrical shell where designed in order to it to be suitably be hosted into the "Laboratorio di Controllo e Regolazione Automatica" at the Università degli Studi di Udine. These has been selected in order to present a length to radius ratio (L/R) comparable to the one considered in the simulation study. The electrical characterisation of the actual electromagnetic transducer has shown some discrepancy with the one obtainable with the analytical model of the devise. A further investigation of this aspect was not included due to the limited period of time of the present work. The electrical behaviour of the transducer, together with its dependence on the operating conditions, has led to a different implementation of the shunt circuit. This aspect does not constitute a limitation of the objective of the present research study, which is primarily focused on the implementation of a shunt circuit for the mechanical tuning of the electromagnetic transducer usable as a vibration absorber. A comprehensive experimental survey has shown the capability of resistive and resistive-inductive shunt circuits to modify the mechanical dynamic response of the shunted transducer. This survey furthermore has led to hints necessary for the development of general guidelines for the tuning of the shunted electromagnetic transducer. Finally, the experimental results have shown that the sweeping shunted TVA, blindly operating in a given frequency band, has produces similar reduction of the flexural vibration of the cylindrical shell than the

ones produced by the fixed tuned TVA which, on the contrary, has required a detailed tuning to targeted resonance frequencies, which have been identified by means of the analysis the dynamic response of the cylindrical shell.

7.3   FUTURE WORK

The following works could be carried out concerning the Modal Interaction Model presented in chapter 3 for the fully coupled structural acoustic system:

- Study the coupled system with a numerical method (*e.g.* using structural-acoustic finite element analysis) and compare the results obtained with the analytical formulation derived with the Modal Interaction Model.

- Investigate the effects of localised structural elements such as rings, stringers and longerons to obtain a more accurate model for the aircraft fuselage.

For the fixed tuned vibration absorbers presented in chapter chapter 4, further work could progress regarding the following points:

- Study of the effective footprint contact surface of the TVA and in what amount the non idealised point TVA force affect the positioning criteria.

- Investigate the effects of distributed TVA, which could be smeared along some particular direction of the cylindrical shell.

In addition, regarding the shunted electro-magnetic absorbers presented in chapter 5, the following ideas emerged as a natural continuation of the current research:

- Study the effect of the implementation of a capacitive shunt. As shown in the electro-mechanical analogy study, this passive electrical element produces a mass-like mechanical equivalent effect, which could enhance the control performances of the shunted TVA.

- Study the effects of an asynchronously time variation of the elements of the arrays, in which the sweeping law of each device presents a given phase shift each other.

- Consider the possibility of replacing the resistor in the shunt with an energy scavenging circuit and study the amount of energy that could be harvested in order to obtain self-powered shunted electro-magnetic vibration absorbers.

Finally, with respect to the experimental implementation of the shunted electromagnetic TVA presented in chapter 6, the following features could be further investigated:

- Measure the noise control performances of the fixed and sweeping TVA.

- Study the electrical characteristic of the actual transducer in order to realise a model which is able to trace the actual electrical behaviour.

- Implement a tracking algorithm which measure the inherent resistance of the transducer coil. In this way the variation of the electrical parameters due to the working conditions would not affect the desired mechanical behaviour.

- Study the effects of the time delay induced by the digital conversion and of the low-pass filter on the relations between the electrical elements of the shunt and the mechanical equivalent elements in order to obtain an univocal expression between the elements.

- Evaluate the effects of the positions of the shunted TVA on its vibration control performances and conduct a study aimed at the identification of the best position for the sweeping TVA.

- Investigate the vibration control effects of arrays of sweeping TVA.

LIST OF PUBLICATIONS

INTERNATIONAL PEER REVIEWED JOURNAL PUBLICATIONS

1. E. Turco and P. Gardonio, Sweeping shunted electro-magnetic tuneable vibration absorber: Design and implementation, *Journal of Sound and Vibration*, vol 407, pp. 82-105, 2017.

2. P. Gardonio and E. Turco, Tuning and positioning of Tuned Vibration Absorbers and Helmholtz Resonators for broad-band control, (in preparation), 2017.

3. E. Turco, P. Gardonio and R. Petrella, Experimental implementation of sweeping shunted electro-magnetic tuneable vibration absorber for broad-band vibration control, (in preparation), 2017.

FULL PAPERS IN PROCEEDINGS OF INTERNATIONAL CONFERENCES

1. E. Turco and P. Gardonio, *On the use of tuneable mass dampers for broad-band noise control in a cylindrical enclosure*, Proceedings of the 22nd International Congress on Sound and Vibration (ICSV), 2015, Florence, Italy.

2. E. Turco, P. Gardonio and L. Dal Bo, *Time-varying shunted electro-magnetic tuneable vibration absorber*, Proceedings of the International Conference on Motion and Vibration Control (13th MoViC) and of the International Conference on Recent Advances in Structural Dynamics (12th RASD), 2016, Southampton, UK.

A

NORMALIZATION COEFFICIENTS FOR THE CYLINDRICAL SHELL AND ENCLOSURE

In this appendix the normalization matrices for the structural and the acoustical domain, $\mathbf{\Lambda}$ and $\mathbf{\Gamma}$, are derived. From these matrices the modal structural inertia matrix $\mathbf{M}_s$ and the modal acoustic inertia matrix $\mathbf{Q}$ can be obtained from equations (3.61a) and (3.138a), respectively.

A.1 STRUCTURAL NORMALIZATION COEFFICIENTS

From equation (3.61a), the modal structural inertia matrix can be expressed as:

$$
\begin{aligned}
\mathbf{M}_s &= \rho h \int_S \boldsymbol{\varphi}^T(\mathbf{x}_s) \boldsymbol{\varphi}(\mathbf{x}_s) \mathrm{d}S \\
&= \rho h \int_S \left[\boldsymbol{\varphi}^s(\mathbf{x}_s) \quad \boldsymbol{\varphi}^a(\mathbf{x}_s) \right]^T \left[\boldsymbol{\varphi}^s(\mathbf{x}_s) \quad \boldsymbol{\varphi}^a(\mathbf{x}_s) \right] \mathrm{d}S \\
&= \rho h \int_S \begin{bmatrix} \boldsymbol{\varphi}^{sT}(\mathbf{x}_s)\boldsymbol{\varphi}^s(\mathbf{x}_s) & \boldsymbol{\varphi}^{sT}(\mathbf{x}_s)\boldsymbol{\varphi}^a(\mathbf{x}_s) \\ \boldsymbol{\varphi}^{aT}(\mathbf{x}_s)\boldsymbol{\varphi}^s(\mathbf{x}_s) & \boldsymbol{\varphi}^{aT}(\mathbf{x}_s)\boldsymbol{\varphi}^a(\mathbf{x}_s) \end{bmatrix} \mathrm{d}S \\
&= m_c \begin{bmatrix} \mathbf{\Lambda}^{ss} & \mathbf{\Lambda}^{sa} \\ \mathbf{\Lambda}^{as} & \mathbf{\Lambda}^{aa} \end{bmatrix} \\
&= m_c \mathbf{\Lambda},
\end{aligned}
\tag{A.1}
$$

where m_c is the mass of the cylindrical shell and the $2M \times 2M$ matrix of the structural normalization coefficients can be considered as a block matrix.

The generic element of each of the four sub-matrices is of the form:

$$
\Lambda_{m,p}^{\alpha,\beta} = \frac{m_c}{\rho h} \int_S \varphi_m^\alpha(\mathbf{x}_s) \varphi_p^\beta(\mathbf{x}_s) \mathrm{d}S,
\tag{A.2}
$$

where $\alpha, \beta = s, a$ and $m, p = 1, 2, \ldots, M$.

A.1.1 *Orthogonality of the structural modes*

The structural mode shapes are said to be orthogonal if:

$$\int_S \varphi_m^\alpha(\mathbf{x}_s)\varphi_p^\alpha(\mathbf{x}_s)\mathrm{d}S = 0 \qquad \forall p \neq m. \tag{A.3}$$

In order to prove the orthogonality property, it is sufficient to prove that

$$\int_0^L \sin\left(\frac{m_1\pi}{L}x\right)\sin\left(\frac{p_1\pi}{L}x\right)\mathrm{d}x = 0 \qquad \text{if } p_1 \neq m_1. \tag{A.4}$$

Recalling Werner's formula

$$\sin(a)\sin(b) = \frac{1}{2}\left[\cos\left(a - b\right) - \cos\left(a + b\right)\right], \tag{A.5}$$

equation (A.4) can be expressed as:

$$
\begin{aligned}
\int_0^L \sin\left(\frac{m_1\pi}{L}x\right)\sin\left(\frac{p_1\pi}{L}x\right)\mathrm{d}x &= \frac{1}{2}\int_0^L \left\{\cos\left[\frac{(m_1 - p_1)\pi}{L}x\right] - \cos\left[\frac{(m_1 + p_1)\pi}{L}x\right]\right\}\mathrm{d}x \\
&= \frac{1}{2}\int_0^L \cos\left[\frac{(m_1 - p_1)\pi}{L}x\right]\mathrm{d}x \\
&\quad - \frac{1}{2}\int_0^L \cos\left[\frac{(m_1 + p_1)\pi}{L}x\right]\mathrm{d}x \\
&= \frac{L}{2(m_1 - p_1)}\sin\left[\frac{(m_1 - p_1)\pi}{L}x\right]\Bigg|_0^L \\
&\quad - \frac{L}{2(m_1 + p_1)}\sin\left[\frac{(m_1 + p_1)\pi}{L}x\right]\Bigg|_0^L.
\end{aligned}
\tag{A.6}
$$

Since $m_1, p_1 \in \mathbb{N}$, it follows that $(m_1 - p_1), (m_1 + p_1) \in \mathbb{Z}$. Both sine function in the result will thus be of the form $\sin(k\pi)$ which, for $k \in \mathbb{Z}$ is equal to zero. This proves the orthogonality property defined in equation (A.4), thus:

$$\rho h \int_S \varphi_m^s(\mathbf{x}_s)\varphi_p^s(\mathbf{x}_s)\mathrm{d}S = \rho h \int_S \varphi_m^a(\mathbf{x}_s)\varphi_p^a(\mathbf{x}_s)\mathrm{d}S = 0 \quad \text{if } p \neq m. \tag{A.7}$$

A.1.2 *Orthogonality of the symmetrical and anti-symmetrical components of the structural modes*

In this section it is proved that the symmetrical and anti-symmetrical component of the structural modes shapes are orthogonal:

$$\int_S \varphi_m^s(\mathbf{x}_s)\varphi_m^a(\mathbf{x}_s)\mathrm{d}S = \int_S \varphi_m^a(\mathbf{x}_s)\varphi_m^s(\mathbf{x}_s)\mathrm{d}S = 0 \qquad \forall m. \tag{A.8}$$

To prove this it is sufficient to prove that:

$$\int_0^{2\pi} \cos(m_2\vartheta)\sin(m_2\vartheta)\mathrm{d}\vartheta = 0. \tag{A.9}$$

Recalling Werner's formula,

$$\sin(a)\cos(b) = \frac{1}{2}\left[\sin(a+b) + \sin(a-b)\right], \tag{A.10}$$

the integral in equation (A.8) results:

$$\begin{aligned}
\int_0^{2\pi} \cos(m_2\vartheta)\sin(m_2\vartheta)\mathrm{d}\vartheta &= \frac{1}{2}\int_0^{2\pi} \sin(2m_2\vartheta)\,\mathrm{d}\vartheta \\
&= -\frac{1}{4m_2}\cos(m_2\vartheta)\Big|_0^{2\pi} \\
&= 0.
\end{aligned} \tag{A.11}$$

Thus the orthogonality of the symmetrical and anti-symmetrical component of the structural modes is proved.

A.1.3 *Derivation of the structural normalization coefficients*

The result obtained in equation (A.11) yields to the fact that the off-diagonal sub-matrices are matrices of zeros:

$$\mathbf{\Lambda}^{sa} = \mathbf{\Lambda}^{as} = \mathbf{0}. \tag{A.12}$$

The result obtained in equation (A.7) yields to the fact that the main-diagonal sub-matrices are diagonal matrices.

These two results reduce the problem of determining the normalization factors to the evaluation of the integrals

$$
\rho h \int_S [\varphi_m^s(\mathbf{x}_s)]^2 \, dS = \rho h \int_0^L \int_0^{2\pi} \sin^2\left(\frac{m_1 \pi}{L} x\right) \cos^2(m_2 \vartheta) R \, d\vartheta \, dx
$$
$$
= \rho h \int_0^L \sin^2\left(\frac{m_1 \pi}{L} x\right) dx \int_0^{2\pi} \cos^2(m_2 \vartheta) R \, d\vartheta
$$

(A.13)

and

$$
\rho h \int_S [\varphi_m^a(\mathbf{x}_s)]^2 \, dS = \rho h \int_0^L \int_0^{2\pi} \sin^2\left(\frac{m_1 \pi}{L} x\right) \sin^2(m_2 \vartheta) R \, d\vartheta \, dx
$$
$$
= \rho h \int_0^L \sin^2\left(\frac{m_1 \pi}{L} x\right) dx \int_0^{2\pi} \sin^2(m_2 \vartheta) R \, d\vartheta.
$$

(A.14)

The integrals to be solved are thus:

$$
\int_0^L \sin^2\left(\frac{m_1 \pi}{L} x\right) dx,
$$

(A.15a)

$$
\int_0^{2\pi} \cos^2(m_2 \vartheta) R \, d\vartheta \quad \text{and}
$$

(A.15b)

$$
\int_0^{2\pi} \sin^2(m_2 \vartheta) R \, d\vartheta.
$$

(A.15c)

The integral presented in (A.15a), common to both components, can be solved considering the trigonometric identity

$$
\sin^2(a) = \frac{1 - \cos(2a)}{2},
$$

(A.16)

which, substituted into equation (A.15a), gives:

$$
\begin{aligned}
\int_0^L \sin^2\left(\frac{m_1 \pi x}{L}\right) dx &= \int_0^L \frac{1}{2}\left[1 - \cos\left(\frac{2m_1 \pi}{L} x\right)\right] dx \\
&= \frac{1}{2}\int_0^L dx - \frac{1}{2}\int_0^L \cos\left(\frac{2m_1 \pi}{L} x\right) dx \\
&= \frac{1}{2} x\Big|_0^L - \frac{L}{4m_1 \pi} \sin\left(\frac{2m_1 \pi x}{L}\right)\Big|_0^L \\
&= \frac{L}{2} - \frac{L}{4m_1 \pi}\left[\sin\left(2m_1 \pi\right) - \sin(0)\right] \\
&= \frac{L}{2}.
\end{aligned}
$$

(A.17)

The solution to the integral along the circumferential direction for the symmetrical component, equation (A.15b), depends on the value of the circumfer-

ential index m_2. Two cases must be considered; the first case, in which $m_2 = 0$, the integral (A.15a) results in:

$$\int_0^{2\pi} \cos^2(0\vartheta) R d\vartheta = \int_0^{2\pi} R d\vartheta = 2\pi R. \tag{A.18}$$

In the case in which $m_2 \neq 0$, the solution is obtained recalling the trigonometric identity:

$$\cos^2(a) = \frac{1 + \cos(2a)}{2}, \tag{A.19}$$

which substituted into (A.15b), gives

$$
\begin{aligned}
\int_0^{2\pi} \cos^2(m_2\vartheta) R d\vartheta &= \int_0^{2\pi} \frac{1 + \cos(2m_2\vartheta)}{2} R d\vartheta \\
&= \frac{1}{2} \int_0^{2\pi} R d\vartheta + \frac{1}{2} \int_0^{2\pi} \cos(2m_2\vartheta) R d\vartheta \\
&= \frac{1}{2} \left. R\vartheta \right|_0^{2\pi} + \frac{R}{4m_2} \left. \sin(2m_2\vartheta) \right|_0^{2\pi} \\
&= \pi R.
\end{aligned}
\tag{A.20}
$$

The results obtained in equations (A.18) and (A.20) can be summarized as:

$$\int_0^{2\pi} \cos^2(m_2\vartheta) R d\vartheta = \begin{cases} 2\pi R & \text{if} \quad m_2 = 0 \\ \pi R & \text{if} \quad m_2 \neq 0 \end{cases}. \tag{A.21}$$

Also the integral concerning the anti-symmetric component along the circumferential direction, equation (A.15c), depends upon the circumferential index. For $m_2 = 0$, it results

$$\int_0^{2\pi} \sin^2(0\vartheta) R d\vartheta = \int_0^{2\pi} 0 R d\vartheta = 0. \tag{A.22}$$

When the circumferential index is such that $m_2 \neq 0$, with equation (A.16), equation (A.15c) gives:

$$
\begin{aligned}
\int_0^{2\pi} \sin^2(m_2\vartheta) R d\vartheta &= \int_0^{2\pi} \frac{1 - \cos(2m_2\vartheta)}{2} R d\vartheta \\
&= \frac{1}{2} \int_0^{2\pi} R d\vartheta - \frac{1}{2} \int_0^{2\pi} \cos(2m_2\vartheta) R d\vartheta \\
&= \frac{1}{2} \left. R\vartheta \right|_0^{2\pi} - \frac{R}{4m_2} \left. \sin(2m_2\vartheta) \right|_0^{2\pi} \\
&= \pi R.
\end{aligned}
\tag{A.23}
$$

The results obtained in equations (A.22) and (A.23) can be summarized as:

$$\int_0^{2\pi} \sin^2(m_2 \vartheta) R \mathrm{d}\vartheta = \begin{cases} 0 & \text{if} \quad m_2 = 0 \\ \pi R & \text{if} \quad m_2 \neq 0 \end{cases}. \tag{A.24}$$

Combining now the results of equations (A.17) and (A.21), the integral in equation (A.13) gives:

$$\rho h \int_S [\varphi_m^s(\mathbf{x}_s)]^2 \, \mathrm{d}S = \rho h \frac{L}{2} \begin{cases} 2\pi R \\ \pi R \end{cases} = \begin{cases} \rho h \pi R L & \text{if} \quad m_2 = 0 \\ \dfrac{\rho h \pi R L}{2} & \text{if} \quad m_2 \neq 0 \end{cases}. \tag{A.25}$$

Since the mass of the cylinder is obtained as

$$m_c = \rho 2\pi R L h, \tag{A.26}$$

equation (A.25) can be rewritten as:

$$\rho h \int_S [\varphi_m^s(\mathbf{x}_s)]^2 \, \mathrm{d}S = \begin{cases} \dfrac{1}{2} m_c & \text{if} \quad m_2 = 0 \\ \dfrac{1}{4} m_c & \text{if} \quad m_2 \neq 0 \end{cases}. \tag{A.27}$$

Similarly, considering the results of equations (A.22) and (A.24), and the definition of the mass of the cylinder given in equation (A.26), the integral in equation (A.14) gives:

$$\rho h \int_S [\varphi_m^a(\mathbf{x}_s)]^2 \, \mathrm{d}S = \begin{cases} 0 & \text{if} \quad m_2 = 0 \\ \dfrac{1}{4} m_c & \text{if} \quad m_2 \neq 0 \end{cases}. \tag{A.28}$$

The modal structural normalization matrix $\mathbf{\Lambda}$ is thus a $2M \times 2M$ diagonal matrix whose first $1, 2, \ldots, M$ diagonal elements and second $M+1, M+2, \ldots, 2M$ diagonal elements, respectively for the symmetric and anti-symmetric flexural modes, are given by:

$$\Lambda_{m,m} = \begin{cases} \dfrac{1}{2} & \text{if} \quad m_2 = 0 \\ \dfrac{1}{4} & \text{if} \quad m_2 \neq 0 \end{cases} \tag{A.29}$$

and

$$\Lambda_{m+M,m+M} = \begin{cases} 0 & \text{if} \quad m_2 = 0 \\[2mm] \dfrac{1}{4} & \text{if} \quad m_2 \neq 0 \end{cases}, \tag{A.30}$$

where $m = 1, \ldots, M$.

A.2   ACOUSTICAL NORMALIZATION COEFFICIENTS

From equation (3.138a), the modal acoustic inertia matrix may be defined as

$$\begin{aligned} \mathbf{Q} &= \int_{V_c} \boldsymbol{\psi}^T(\mathbf{x}) \boldsymbol{\psi}(\mathbf{x}) \, \mathrm{d}V \\ &= \int_{V_c} \begin{bmatrix} \boldsymbol{\psi}^s(\mathbf{x}) & \boldsymbol{\psi}^a(\mathbf{x}) \end{bmatrix}^T \begin{bmatrix} \boldsymbol{\psi}^s(\mathbf{x}) & \boldsymbol{\psi}^a(\mathbf{x}) \end{bmatrix} \, \mathrm{d}V \\ &= \int_{V_c} \begin{bmatrix} \boldsymbol{\psi}^{sT}(\mathbf{x})\boldsymbol{\psi}^s(\mathbf{x}) & \boldsymbol{\psi}^{sT}(\mathbf{x})\boldsymbol{\psi}^a(\mathbf{x}) \\ \boldsymbol{\psi}^{aT}(\mathbf{x})\boldsymbol{\psi}^s(\mathbf{x}) & \boldsymbol{\psi}^{aT}(\mathbf{x})\boldsymbol{\psi}^a(\mathbf{x}) \end{bmatrix} \, \mathrm{d}V \\ &= V_c \begin{bmatrix} \boldsymbol{\Gamma}^{ss} & \boldsymbol{\Gamma}^{sa} \\ \boldsymbol{\Gamma}^{as} & \boldsymbol{\Gamma}^{aa} \end{bmatrix} \\ &= V_c \boldsymbol{\Gamma}, \end{aligned} \tag{A.31}$$

where V_c is the volume of the cylindrical enclosure and $\boldsymbol{\Gamma}$ is the $2N \times 2N$ matrix of the acoustic normalization coefficients, which can be considered as a block matrix.

The generic element of each of the four sub-matrices is of the form:

$$\Gamma_{n,q}^{\alpha,\beta} = \frac{1}{V_c} \int_{V_c} \psi_n^\alpha(\mathbf{x}) \varphi_q^\beta(\mathbf{x}) \mathrm{d}V, \tag{A.32}$$

where $\alpha, \beta = s, a$ and $n, q = 1, 2, \ldots, N$.

A.2.1   *Orthogonality of the acoustical modes*

The acoustical mode shapes are said to be orthogonal if they satisfy the relation

$$\int_{V_c} \psi_n^\alpha(\mathbf{x}) \psi_q^\alpha(\mathbf{x}) \mathrm{d}V = 0 \qquad \forall q \neq n. \tag{A.33}$$

In order to prove the orthogonality property, it is sufficient to prove that

$$\int_0^L \cos\left(\frac{n_1\pi}{L}x\right)\cos\left(\frac{q_1\pi}{L}x\right)\mathrm{d}x = 0 \qquad \text{if } n_1 \neq q_1. \tag{A.34}$$

Recalling Werner's formula

$$\cos(a)\cos(b) = \frac{1}{2}\left[\cos\left(a+b\right)+\cos\left(a-b\right)\right], \tag{A.35}$$

equation (A.34) can be expressed as:

$$
\begin{aligned}
\int_0^L \cos\left(\frac{n_1\pi}{L}x\right)\cos\left(\frac{q_1\pi}{L}x\right)\mathrm{d}x &= \frac{1}{2}\int_0^L\left\{\cos\left[\frac{(n_1+q_1)\,\pi}{L}x\right]+\cos\left[\frac{(n_1-q_1)\,\pi}{L}x\right]\right\}\mathrm{d}x \\
&= \frac{1}{2}\int_0^L\cos\left[\frac{(n_1+q_1)\,\pi}{L}x\right]\mathrm{d}x \\
&\quad + \frac{1}{2}\int_0^L\cos\left[\frac{(n_1-q_1)\,\pi}{L}x\right]\mathrm{d}x \\
&= \frac{L}{2(n_1+q_1)}\sin\left[\frac{(n_1+q_1)\,\pi}{L}x\right]\Bigg|_0^L \\
&\quad + \frac{L}{2(n_1-q_1)}\sin\left[\frac{(n_1-q_1)\,\pi}{L}x\right]\Bigg|_0^L.
\end{aligned}
\tag{A.36}
$$

The result obtained in equation (A.36) is analogous to that obtained in equation (A.6), thus it yields to the same conclusion.

This proves the orthogonality of the acoustical mode shapes:

$$\int_{V_c} \psi_n^s(\mathbf{x})\psi_q^s(\mathbf{x})\mathrm{d}V = \int_{V_c} \psi_n^a(\mathbf{x})\psi_q^a(\mathbf{x})\mathrm{d}V = 0 \quad \text{if } q \neq n. \tag{A.37}$$

A.2.2   *Orthogonality of the symmetrical and anti-symmetrical components of the structural modes*

Another characteristic of the acoustic mode shapes is that the symmetrical and the anti-symmetrical component of each mode are orthogonal:

$$\int_{V_c} \psi_n^s(\mathbf{x})\psi_n^a(\mathbf{x})\mathrm{d}V = \int_{V_c} \psi_n^a(\mathbf{x})\psi_n^s(\mathbf{x})\mathrm{d}V = 0 \qquad \forall n. \tag{A.38}$$

To prove this it is to prove that:

$$\int_0^{2\pi} \cos(n_2\vartheta)\sin(n_2\vartheta)\mathrm{d}\vartheta = 0, \tag{A.39}$$

which corresponds to the condition for the structural modes and was already proved in section A.1.2. Following the same procedure, the orthogonality of the symmetrical and anti-symmetrical component of the acoustical mode shapes could be proved.

A.2.3 *Derivation of the acoustical normalization coefficients*

The orthogonality of the two components of the acoustical mode shapes, equation (A.38), yields to the fact that the off-diagonal sub-matrices are matrices of zeros:

$$\mathbf{\Gamma}^{sa} = \mathbf{\Gamma}^{as} = \mathbf{0} \tag{A.40}$$

and the orthogonality of the modes, equation (A.37), yields to the fact that the main-diagonal sub-matrices are diagonal matrices.

These two results reduce the problem of determining the normalization factors to the evaluation of the integrals

$$\int_{V_c} [\psi_n^s(\mathbf{x})]^2 \, dV = \int_0^L \int_0^{2\pi} \int_0^R \cos^2\left(\frac{n_1\pi}{L}x\right) \cos^2(n_2\vartheta) J_{n_2}^2\left(\frac{\lambda_{n_2 n_3}}{R}r\right) dr r d\vartheta dx$$
$$= \int_0^L \cos^2\left(\frac{n_1\pi}{L}x\right) dx \int_0^{2\pi} \cos^2(n_2\vartheta) d\vartheta \int_0^R J_{n_2}^2\left(\frac{\lambda_{n_2 n_3}}{R}r\right) r dr \tag{A.41}$$

and

$$\int_{V_c} [\psi_n^a(\mathbf{x})]^2 \, dV = \int_0^L \int_0^{2\pi} \int_0^R \cos^2\left(\frac{n_1\pi}{L}x\right) \sin^2(n_2\vartheta) J_{n_2}^2\left(\frac{\lambda_{n_2 n_3}}{R}r\right) dr r d\vartheta dx$$
$$= \int_0^L \cos^2\left(\frac{n_1\pi}{L}x\right) dx \int_0^{2\pi} \sin^2(n_2\vartheta) d\vartheta \int_0^R J_{n_2}^2\left(\frac{\lambda_{n_2 n_3}}{R}r\right) r dr. \tag{A.42}$$

Thus, the integrals to be solved are:

$$\int_0^L \cos^2\left(\frac{n_1\pi}{L}x\right) dx, \tag{A.43a}$$

$$\int_0^{2\pi} \cos^2(n_2\vartheta) d\vartheta, \tag{A.43b}$$

$$\int_0^{2\pi} \sin^2(n_2\vartheta) d\vartheta \quad \text{and} \tag{A.43c}$$

$$\int_0^R J_{n_2}^2\left(\frac{\lambda_{n_2 n_3}}{R}r\right) r dr. \tag{A.43d}$$

The integrals in equations (A.43b) and (A.43c) are analogous to the ones of the structural case, equations (A.15b) and (A.15c), whose solutions are:

$$\int_0^{2\pi} \cos^2(n_2\vartheta)\mathrm{d}\vartheta = 2\pi\,\epsilon_{n_2}^s \tag{A.44}$$

and

$$\int_0^{2\pi} \sin^2(n_2\vartheta)\mathrm{d}\vartheta = 2\pi\,\epsilon_{n_2}^a, \tag{A.45}$$

where

$$\epsilon_{n_2}^s = \begin{cases} 1 & \text{if} \quad n_2 = 0 \\ \dfrac{1}{2} & \text{if} \quad n_2 \neq 0 \end{cases} \tag{A.46}$$

and

$$\epsilon_{n_2}^a = \begin{cases} 0 & \text{if} \quad n_2 = 0 \\ \dfrac{1}{2} & \text{if} \quad n_2 \neq 0 \end{cases}. \tag{A.47}$$

For the acoustical mode shapes, since the axial acoustic modal index may also assume the value zero, the integral along the axial direction, equation (A.43a), depends on the value of the axial index n_1. For $n_1 = 0$, equation (A.43a) results:

$$\int_0^L \cos^2(0x)\mathrm{d}x = \int_0^L \mathrm{d}x = L. \tag{A.48}$$

Otherwise, for $n_1 \neq 0$, the solution is obtained recalling the trigonometric identity given in equation (A.19), which substituted into (A.43a), results in

$$\begin{aligned} \int_0^L \cos^2\left(\frac{n_1\pi}{L}x\right)\mathrm{d}x &= \int_0^L \frac{1}{2}\left[1 + \cos\left(\frac{2n_1\pi}{L}x\right)\right]\mathrm{d}x \\ &= \frac{1}{2}\int_0^L \mathrm{d}x + \frac{1}{2}\int_0^L \cos\left(\frac{2n_1\pi}{L}x\right)\mathrm{d}x \\ &= \frac{1}{2}\left.x\right|_0^L + \frac{L}{4n_1\pi}\left.\sin\left(\frac{2n_1\pi}{L}x\right)\right|_0^{2\pi} \\ &= \frac{L}{2}. \end{aligned} \tag{A.49}$$

The results obtained in equations (A.48) and (A.49) can be summarized as:

$$\int_0^L \cos^2\left(\frac{n_1\pi}{L}x\right)\mathrm{d}x = L\,\epsilon_{n_1}, \tag{A.50}$$

where

$$\epsilon_{n_1} = \begin{cases} L & \text{if} \quad n_1 = 0 \\ \dfrac{L}{2} & \text{if} \quad n_1 \neq 0 \end{cases}. \tag{A.51}$$

The integral along the radial direction, equation (A.43d), can solved considering the following property of the Bessel functions [129, 133, 134, 201]:

$$\int J_m^2(z) z \, dz = \frac{z^2}{2} \left[J_m^2(z) - J_{m-1}(z) J_{m+1}(z) \right],$$

(A.52)

which, applied to equation (A.43d), gives:

$$\int_0^R J_{n_2}^2 \left(\frac{\lambda_{n_2 n_3}}{R} r \right) r \, dr = \frac{R^2}{2} \left[J_{n_2}^2(\lambda_{n_2 n_3}) - J_{n_2-1}(\lambda_{n_2 n_3}) J_{n_2+1}(\lambda_{n_2 n_3}) \right].$$

(A.53)

In order to obtain a result which depends only on the Bessel function of order n_2, the following properties of the Bessel function may be considered:

$$J_m'(z) = J_{m-1}(z) - \frac{m}{z} J_m(z) \quad \text{and}$$

(A.54a)

$$J_m'(z) = -J_{m+1}(z) + \frac{m}{z} J_m(z).$$

(A.54b)

where the superscript $'$ indicates the derivative. Since $J_{n_2}'(\lambda_{n_2 n_3}) = 0$, the relations (A.54) result in

$$J_{n_2-1}(\lambda_{n_2 n_3}) = \frac{n_2}{\lambda_{n_2 n_3}} J_{n_2}(\lambda_{n_2 n_3}) \quad \text{and}$$

(A.55a)

$$J_{n_2+1}(\lambda_{n_2 n_3}) = \frac{n_2}{\lambda_{n_2 n_3}} J_{n_2}(\lambda_{n_2 n_3}),$$

(A.55b)

which, substituted in equation (A.53) gives

$$\int_0^R J_{n_2}^2 \left(\frac{\lambda_{n_2 n_3}}{R} r \right) r \, dr = \frac{R^2}{2} \left[J_{n_2}^2(\lambda_{n_2 n_3}) - \left(\frac{n_2}{\lambda_{n_2 n_3}} \right)^2 J_{n_2}^2(\lambda_{n_2 n_3}) \right]$$

$$= \frac{R^2}{2} J_{n_2}^2(\lambda_{n_2 n_3}) \left[1 - \left(\frac{n_2}{\lambda_{n_2 n_3}} \right)^2 \right].$$

(A.56)

Combining the results of equations (A.44), (A.50) and (A.56), equation (A.41) results:

$$\int_{V_c} [\psi_n^s(\mathbf{x})]^2 \, dV = L \, \epsilon_{n_1} 2\pi \, \epsilon_{n_2}^s \frac{R^2}{2} J_{n_2}^2(\lambda_{n_2 n_3}) \left[1 - \left(\frac{n_2}{\lambda_{n_2 n_3}} \right)^2 \right],$$

(A.57)

which, recognising the volume of the cylindrical enclosure as

$$V_c = \pi R^2 L,$$

(A.58)

could be written as:

$$\int_{V_c} [\psi_n^s(\mathbf{x})]^2 \, dV = V_c \, \epsilon_{n_1} \, \epsilon_{n_2}^s J_{n_2}^2(\lambda_{n_2 n_3}) \left[1 - \left(\frac{n_2}{\lambda_{n_2 n_3}} \right)^2 \right]. \tag{A.59}$$

Similarly, considering the results obtained in equations (A.50), (A.45) and (A.56), equation (A.42) results in

$$\int_{V_c} [\psi_n^a(\mathbf{x})]^2 \, dV = V_c \, \epsilon_{n_1} \, \epsilon_{n_2}^a J_{n_2}^2(\lambda_{n_2 n_3}) \left[1 - \left(\frac{n_2}{\lambda_{n_2 n_3}} \right)^2 \right]. \tag{A.60}$$

The modal acoustical normalization matrix Γ is thus a $2N \times 2N$ diagonal matrix whose first $1, 2, \dots, N$ diagonal elements and second $N + 1, N + 2, \dots, 2N$ diagonal elements, respectively for the symmetric and anti-symmetric acoustical modes, are given by:

$$\Gamma_{n,n} = \epsilon_{n_1} \, \epsilon_{n_2}^s J_{n_2}^2(\lambda_{n_2 n_3}) \left[1 - \left(\frac{n_2}{\lambda_{n_2 n_3}} \right)^2 \right] \tag{A.61}$$

and

$$\Gamma_{n+N, n+N} = \epsilon_{n_1} \, \epsilon_{n_2}^a J_{n_2}^2(\lambda_{n_2 n_3}) \left[1 - \left(\frac{n_2}{\lambda_{n_2 n_3}} \right)^2 \right], \tag{A.62}$$

where $n = 1, \dots, N$ and the definitions of the coefficients ϵ_{n_1}, $\epsilon_{n_2}^s$ and $\epsilon_{n_2}^a$ are given in equations (A.51), (A.46) and (A.47), respectively.

A.3   BESSEL FUNCTIONS

In table A.1 are listed the values of the extrema of the Bessel function of the first kind, $\lambda_{n_2 n_3}$, such that

$$\left. \frac{dJ_{n_2}(x)}{dx} \right|_{x = \lambda_{n_2 n_3}} = 0, \tag{A.63}$$

and in table A.2 are listed the zeros of the Bessel functions of the first kind, $\gamma_{n_2 n_3}$, such that

$$J_{n_2}(\gamma_{n_2 n_3}) = 0. \tag{A.64}$$

In figure A.1 are shown the graphs of the Bessel functions of the first kind of order 0 (upper row), of order 1 (central row) and of order 2 (bottom plots) of the type:

$$J_{n_2}(\lambda_{n_2 n_3} x), \tag{A.65}$$

where the variable x is in the range $0 - 1$.

Table A.1: Extrema of the Bessel functions of the first kind $\lambda_{n_2 n_3}$.

n_2	n_3				
	0	1	2	3	4
0	0	3.83	7.02	10.17	13.32
1	1.84	5.33	8.54	11.71	14.86
2	3.05	6.71	9.97	13.17	16.35
3	4.20	8.02	11.35	14.59	17.79
4	5.32	9.28	12.68	15.96	19.20
5	6.41	10.52	13.99	17.31	20.58

Table A.2: Zeros of the Bessel functions of the first kind $\gamma_{n_2 n_3}$.

n_2	n_3				
	0	1	2	3	4
0	-	2.40	5.52	8.65	11.79
1	0	3.83	7.02	10.17	13.32
2	0	5.14	8.42	11.62	14.80
3	0	6.38	9.76	13.02	16.22
4	0	7.59	11.06	14.37	17.62
5	0	8.77	12.34	15.70	18.98
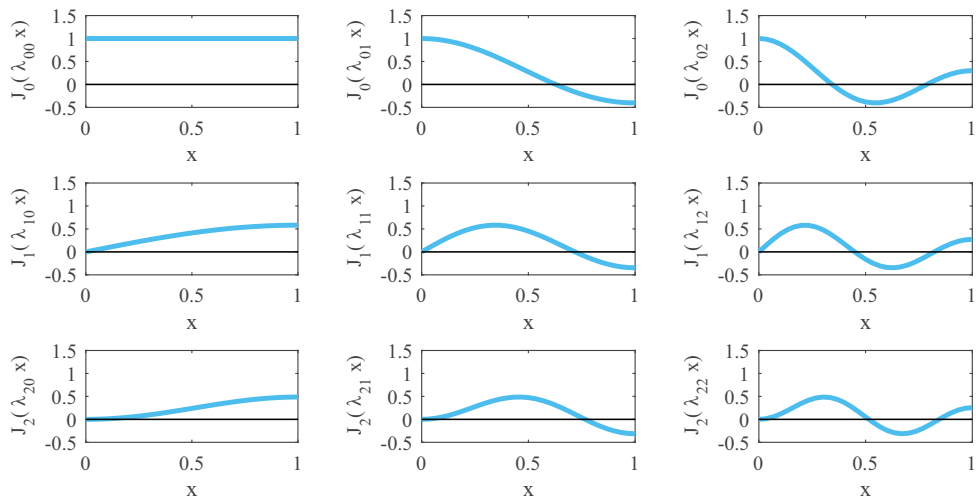
Figure A.1: Graphs of the Bessel functions of the first kind of order 0, 1 and 2 in the range 0-1.

B

COUPLING COEFFICIENT AND COUPLING ALGORITHM

In section 3.8 the fully coupled structural-acoustic response of the cylindrical shell and acoustic cylindrical enclosure is derived using the Modal-Interaction-Model. Since with this technique the flexural vibration and interior acoustic fields are modelled with *in-vacuo* simply supported flexural modes and *rigid-walled* acoustic modes, the coupled equation of motion for the coupled system, equation (3.171), contains off-diagonal matrices that couple the two sets of modal equations and thus represent the coupling between the two domains. In this appendix the derivation of the acoustic-structural matrix $\mathbf{R}$ and of the structural-acoustic matrix $\mathbf{S}$ is first provided with a description of the coupling mechanism. The convergence analysis aimed at finding the number of structural and acoustic natural modes that should be included in the modal expansions is also presented.

B.1   DERIVATION OF THE COUPLING COEFFICIENT

The coupling matrices present in equation (3.171) derived by the mathematical procedure implemented to obtain the coupled equation of motion. In particular, the structural-acoustic coupling matrix is defined as

$$\mathbf{S} = \int_S \boldsymbol{\varphi}^T(\mathbf{x}_s) \boldsymbol{\psi}(\mathbf{x}_s) \, \mathrm{d}S, \tag{B.1}$$

where $\boldsymbol{\varphi}(\mathbf{x}_s) = \begin{bmatrix} \boldsymbol{\varphi}^s(\mathbf{x}_s) & \boldsymbol{\varphi}^a(\mathbf{x}_s) \end{bmatrix}$ is the $1 \times 2M$ row vector with the flexural mode shapes and $\boldsymbol{\psi}(\mathbf{x}_s) = \begin{bmatrix} \boldsymbol{\psi}^s(\mathbf{x}_s) & \boldsymbol{\psi}^a(\mathbf{x}_s) \end{bmatrix}$ is the $1 \times 2N$ column vector with the acoustic mode shapes evaluated on the cylindrical surface of the enclosure. The acoustic-structural coupling matrix is defined as:

$$\mathbf{R} = 2\rho_0 c_0^2 \int_{V_c} \boldsymbol{\psi}^T(\mathbf{x}) \boldsymbol{\varphi}(\mathbf{x}_s) \delta(r - R) \, \mathrm{d}V = 2\rho_0 c_0^2 \int_S \boldsymbol{\psi}^T(\mathbf{x}_s) \boldsymbol{\varphi}(\mathbf{x}_s) \, \mathrm{d}S, \tag{B.2}$$

where the integral property of the Dirac delta function is used to obtain the surface integral. Comparing equations (B.1) and (B.2), the following relation can be established:

$$\mathbf{R} = 2\rho_0 c_0^2 \mathbf{S}^T, \tag{B.3}$$

which relates the acoustic-structural and the structural-acoustic coupling matrices. In the following only the structural-acoustic coupling matrix $\mathbf{S}$ is considered for the derivation of the coupling coefficients. Expanding the expression for the modes shapes, equation (B.1) can be rewritten as:

$$
\begin{aligned}
\mathbf{S} &= \int_S \boldsymbol{\varphi}^T(\mathbf{x}_s) \boldsymbol{\psi}(\mathbf{x}_s) \, \mathrm{d}S \\
&= \int_S \begin{bmatrix} \boldsymbol{\varphi}^s(\mathbf{x}_s) & \boldsymbol{\varphi}^a(\mathbf{x}_s) \end{bmatrix}^T \begin{bmatrix} \boldsymbol{\psi}^s(\mathbf{x}_s) & \boldsymbol{\psi}^a(\mathbf{x}_s) \end{bmatrix} \, \mathrm{d}S \\
&= \int_S \begin{bmatrix} \boldsymbol{\varphi}^{sT}(\mathbf{x}_s)\boldsymbol{\psi}^s(\mathbf{x}_s) & \boldsymbol{\varphi}^{sT}(\mathbf{x}_s)\boldsymbol{\psi}^a(\mathbf{x}_s) \\ \boldsymbol{\varphi}^{aT}(\mathbf{x}_s)\boldsymbol{\psi}^s(\mathbf{x}_s) & \boldsymbol{\varphi}^{aT}(\mathbf{x}_s)\boldsymbol{\psi}^a(\mathbf{x}_s) \end{bmatrix} \, \mathrm{d}S \\
&= \begin{bmatrix} \mathbf{S}^{ss} & \mathbf{S}^{sa} \\ \mathbf{S}^{as} & \mathbf{S}^{aa} \end{bmatrix},
\end{aligned}
\tag{B.4}
$$

thus the structural-acoustic coupling matrix could be considered as a block matrix, in which each block couples the components of the mode shapes of one domain to the components of the mode shapes of the other domain.

Considering the expressions for the structural and acoustic mode shapes given in equations (3.51) and (3.128) respectively, the generic elements of the sub-matrices are of the form:

$$
\begin{aligned}
S_{mn}^{ss} &= \int_S \varphi_m^s(\mathbf{x}_s)\, \psi_n^s(\mathbf{x}_s) \, \mathrm{d}S \\
&= \int_0^L \int_0^{2\pi} \sin\left(\frac{m_1\pi}{L}x\right)\cos(m_2\vartheta)\cdot\cos\left(\frac{n_1\pi}{L}x\right)\cos(n_2\vartheta)J_{n_2}\left(\frac{\lambda_{n_2 n_3}}{R}R\right)\mathrm{d}x R\mathrm{d}\vartheta \\
&= R J_{n_2}(\lambda_{n_2 n_3}) \int_0^L \sin\left(\frac{m_1\pi}{L}x\right)\cos\left(\frac{n_1\pi}{L}x\right)\mathrm{d}x \int_0^{2\pi} \cos(m_2\vartheta)\cos(n_2\vartheta)\mathrm{d}\vartheta,
\end{aligned}
\tag{B.5}
$$

$$
\begin{aligned}
S_{mn}^{sa} &= \int_S \varphi_m^s(\mathbf{x}_s)\, \psi_n^a(\mathbf{x}_s) \, \mathrm{d}S \\
&= \int_0^L \int_0^{2\pi} \sin\left(\frac{m_1\pi}{L}x\right)\cos(m_2\vartheta)\cdot\cos\left(\frac{n_1\pi}{L}x\right)\sin(n_2\vartheta)J_{n_2}\left(\frac{\lambda_{n_2 n_3}}{R}R\right)\mathrm{d}x R\mathrm{d}\vartheta \\
&= R J_{n_2}(\lambda_{n_2 n_3}) \int_0^L \sin\left(\frac{m_1\pi}{L}x\right)\cos\left(\frac{n_1\pi}{L}x\right)\mathrm{d}x \int_0^{2\pi} \cos(m_2\vartheta)\sin(n_2\vartheta)\mathrm{d}\vartheta,
\end{aligned}
\tag{B.6}
$$

$$
\begin{aligned}
S_{mn}^{as} &= \int_S \varphi_m^a\left(\mathbf{x}_s\right)\psi_n^s\left(\mathbf{x}_s\right)\mathrm{d}S \\
&= \int_0^L \int_0^{2\pi} \sin\left(\frac{m_1\pi}{L}x\right)\sin(m_2\vartheta)\cdot\cos\left(\frac{n_1\pi}{L}x\right)\cos(n_2\vartheta)J_{n_2}\left(\frac{\lambda_{n_2n_3}}{R}R\right)\mathrm{d}xR\mathrm{d}\vartheta \\
&= RJ_{n_2}\left(\lambda_{n_2n_3}\right)\int_0^L \sin\left(\frac{m_1\pi}{L}x\right)\cos\left(\frac{n_1\pi}{L}x\right)\mathrm{d}x\int_0^{2\pi}\sin(m_2\vartheta)\cos(n_2\vartheta)\mathrm{d}\vartheta
\end{aligned}
$$

$$\text{(B.7)}$$

and

$$
\begin{aligned}
S_{mn}^{aa} &= \int_S \phi_m^a\left(\mathbf{x}_s\right)\psi_n^a\left(\mathbf{x}_s\right)\mathrm{d}S \\
&= \int_0^L \int_0^{2\pi} \sin\left(\frac{m_1\pi}{L}x\right)\sin(m_2\vartheta)\cdot\cos\left(\frac{n_1\pi}{L}x\right)\sin(n_2\vartheta)J_{n_2}\left(\frac{\lambda_{n_2n_3}}{R}R\right)\mathrm{d}xR\mathrm{d}\vartheta \\
&= RJ_{n_2}\left(\lambda_{n_2n_3}\right)\int_0^L \sin\left(\frac{m_1\pi}{L}x\right)\cos\left(\frac{n_1\pi}{L}x\right)\mathrm{d}x\int_0^{2\pi}\sin(m_2\vartheta)\sin(n_2\vartheta)\mathrm{d}\vartheta.
\end{aligned}
$$

$$\text{(B.8)}$$

First, it is now shown that the mode shape components of different domains are orthogonal:

$$
\int_S \varphi_m^s\left(\mathbf{x}_s\right)\psi_n^a\left(\mathbf{x}_s\right)\mathrm{d}S = \int_S \varphi_m^a\left(\mathbf{x}_s\right)\psi_n^s\left(\mathbf{x}_s\right)\mathrm{d}S = 0. \tag{B.9}
$$

To prove this it is sufficient to prove that

$$
\int_0^{2\pi}\cos(m_2\vartheta)\sin(n_2\vartheta)\mathrm{d}\vartheta = \int_0^{2\pi}\sin(m_2\vartheta)\cos(n_2\vartheta)\mathrm{d}\vartheta = 0 \quad \forall\, m_2, n_2. \tag{B.10}
$$

The case in which $m_2 = n_2$ was already proved in equation (A.11). For $m_2 \neq n_2$, using the Werner's formula given in equation (A.10), equation (B.10) could be written as:

$$
\begin{aligned}
\int_0^{2\pi}\sin(m_2\vartheta)\cos(n_2\vartheta)\mathrm{d}\vartheta &= \frac{1}{2}\int_0^{2\pi}\sin\left[(m_2+n_2)\,\vartheta\right]\mathrm{d}\vartheta \\
&\quad + \frac{1}{2}\int_0^{2\pi}\sin\left[(m_2-n_2)\,\vartheta\right]\mathrm{d}\vartheta \\
&= -\frac{1}{2\left(m_2+n_2\right)}\cos\left[(m_2+n_2)\,\vartheta\right]\big|_0^{2\pi} \\
&\quad - \frac{1}{2\left(m_2-n_2\right)}\cos\left[(m_2-n_2)\,\vartheta\right]\big|_0^{2\pi} = 0.
\end{aligned}
$$

$$\text{(B.11)}$$

Thus, the cross-terms between the components of the mode shapes in the two domains are zero; this leads to the fact that the off-diagonal blocks of the couplig matrix are matrices of zeros:

$$\mathbf{S}^{sa} = \mathbf{S}^{as} = \mathbf{0}, \tag{B.12}$$

this means that the coupling between the structural and the acoustic domain is possible only through mode shapes with the same circumferential symmetry.

This also reduces the number of integrals to be solved, which result:

$$\int_0^L \sin\left(\frac{m_1 \pi}{L} x\right) \cos\left(\frac{n_1 \pi}{L} x\right) \mathrm{d}x = I_x, \tag{B.13a}$$

$$\int_0^{2\pi} \cos(m_2 \vartheta) \cos(n_2 \vartheta) \mathrm{d}\vartheta \quad \text{and} \tag{B.13b}$$

$$\int_0^{2\pi} \sin(m_2 \vartheta) \sin(n_2 \vartheta) \mathrm{d}\vartheta. \tag{B.13c}$$

The results of the integrals presented in equations (B.13b) and (B.13c) are derived in equations (A.44) and (A.45) and can be rewritten in this case as:

$$\int_0^{2\pi} \cos(m_2 \vartheta) \cos(n_2 \vartheta) \mathrm{d}\vartheta = 2\pi \, \gamma_{n_2}^s \tag{B.14}$$

and

$$\int_0^{2\pi} \sin(m_2 \vartheta) \sin(n_2 \vartheta) \mathrm{d}\vartheta = 2\pi \, \gamma_{n_2}^a, \tag{B.15}$$

where

$$\gamma_{n_2}^s = \begin{cases} 0 & \text{if} \quad m_2 \neq n_2 \\ 1 & \text{if} \quad m_2 = n_2 = 0 \\ \frac{1}{2} & \text{if} \quad m_2 = n_2 \neq 0 \end{cases} \tag{B.16}$$

and

$$\gamma_{n_2}^a = \begin{cases} 0 & \text{if} \quad m_2 \neq n_2 \\ 0 & \text{if} \quad m_2 = n_2 = 0 \\ \frac{1}{2} & \text{if} \quad m_2 = n_2 \neq 0 \end{cases}. \tag{B.17}$$

From these results one can see that the structural and acoustical mode shapes couple only between pair of modes with the same circumferential index.

The integral (B.13a) can be solved considering again the Werner's formula (A.10), which substituted yields:

$$
\begin{aligned}
I_x &= \int_0^L \frac{1}{2} \left\{ \sin\left[\frac{(m_1 + n_1)\,\pi}{L}x\right] + \sin\left[\frac{(m_1 - n_1)\,\pi}{L}x\right] \right\} dx \\
&= \frac{1}{2} \int_0^L \sin\left[\frac{(m_1 + n_1)\,\pi}{L}x\right] dx + \frac{1}{2} \int_0^L \sin\left[\frac{(m_1 - n_1)\,\pi}{L}x\right] dx \\
&= -\frac{L}{2\pi\,(m_1 + n_1)} \cos\left[\frac{(m_1 + n_1)\,\pi}{L}x\right]\Big|_0^L - \frac{L}{2\pi\,(m_1 - n_1)} \cos\left[\frac{(m_1 - n_1)\,\pi}{L}x\right]\Big|_0^L \\
&= \frac{L}{2\pi\,(m_1 + n_1)} \left[1 - \cos\left[\pi\,(m_1 + n_1)\right]\right] + \frac{L}{2\pi\,(m_1 - n_1)} \left[1 - \cos\left[\pi\,(m_1 - n_1)\right]\right].
\end{aligned}
\tag{B.18}
$$

Since $m_1, n_1 \in \mathbb{N}$, it follows that $(m_1 + n_1), (m_1 - n_1) \in \mathbb{Z}$, thus substituting the trigonometric identity

$$
\cos(n\pi) = (-1)^n \qquad n \in \mathbb{Z}
\tag{B.19}
$$

into the previous expression leads

$$
\begin{aligned}
I_x &= \frac{L}{2\pi\,(m_1 + n_1)} \left[1 - (-1)^{(m_1 + n_1)}\right] + \frac{L}{2\pi\,(m_1 - n_1)} \left[1 - (-1)^{(m_1 - n_1)}\right] \\
&= \frac{L}{2\pi\,(m_1^2 - n_1^2)} \left[m_1 - n_1 - (m_1 - n_1)(-1)^{m_1 + n_1} + m_1 + n_1 - (m_1 + n_1)(-1)^{m_1 - n_1}\right] \\
&= \frac{L}{2\pi\,(m_1^2 - n_1^2)} \left[2m_1 - (m_1 - n_1)(-1)^{m_1 + n_1} - (m_1 + n_1)(-1)^{m_1 - n_1}\right].
\end{aligned}
\tag{B.20}
$$

The results depends on the values of the axial modal indices. If both indices are even, they can be written as :

$$
\begin{cases}
m_1 = 2a \\
n_1 = 2b
\end{cases}
\longrightarrow
\begin{cases}
2a + 2b = 2(a + b) \\
2a - 2b = 2(a - b)
\end{cases}
\tag{B.21}
$$

and, independently of the actual values of the two indices, both the sum and the difference are even numbers, thus:

$$
(-1)^{m_1 + n_1} = (-1)^{m_1 - n_1} = 1 \longrightarrow I_x = 0.
\tag{B.22}
$$

When the indices m_1 e n_1 are both odd numbers, they can be written as:

$$
\begin{cases}
m_1 = 2a + 1 \\
n_1 = 2b + 1
\end{cases}
\longrightarrow
\begin{cases}
2a + 2b + 2 = 2(a + b + 1) \\
2a - 2b + 1 - 1 = 2(a - b)
\end{cases}
\tag{B.23}
$$

and both their sum and difference result in even numbers, thus it results:

$$
(-1)^{m_1 + n_1} = (-1)^{m_1 - n_1} = 1 \longrightarrow I_x = 0.
\tag{B.24}
$$

When one index is even and the other is odd, as for example

$$
\begin{cases}
m_1 = 2a \\
n_1 = 2b + 1
\end{cases}
\longrightarrow
\begin{cases}
2a + 2b + 1 = 2(a + b) + 1 \\
2a - 2b - 1 = 2(a - b) - 1
\end{cases}
,
\tag{B.25}
$$

both the sum and the difference are odd numbers, thus:

$$
(-1)^{m_1 + n_1} = (-1)^{m_1 - n_1} = -1.
\tag{B.26}
$$

In this last case, the integral in equation (B.20) may be written as:

$$
\begin{aligned}
I_x &= \frac{L}{2\pi \left(m_1^2 - n_1^2 \right)} \left[2m_1 - \left(-m_1 + n_1 - m_1 - n_1 \right) (-1)^{m_1 + n_1} \right] \\
&= \frac{L}{2\pi \left(m_1^2 - n_1^2 \right)} \left[2m_1 + 2m_1 \right] \\
&= \frac{4m_1 L}{2\pi \left(m_1^2 - n_1^2 \right)} \\
&= \frac{2m_1 L}{\pi \left(m_1^2 - n_1^2 \right)}.
\end{aligned}
\tag{B.27}
$$

According to the results obtained in equations (B.22),(B.24) and (B.26), the integral in equation (B.13a) results:

$$
\int_0^L \sin \left(\frac{m_1 \pi}{L} x \right) \cos \left(\frac{n_1 \pi}{L} x \right) \mathrm{d}x = L \delta_{m_1, n_1},
\tag{B.28}
$$

where

$$
\delta_{m_1, n_1} =
\begin{cases}
0 & \text{if} \quad (m_1 + n_1) \text{ even} \\
\dfrac{2m_1}{\pi \left(m_1^2 - n_1^2 \right)} & \text{if} \quad (m_1 + n_1) \text{ odd}
\end{cases}.
\tag{B.29}
$$

Considering the results obtained in equations (B.14), (B.16) and (B.28), the coupling term in equation (B.5) results:

$$S_{mn}^{ss} = \int_S \varphi_m^s (\mathbf{x}_s) \, \psi_n^s (\mathbf{x}_s) \, \mathrm{d}S = R J_{n_2} (\lambda_{n_2 n_3}) \, 2\pi \, \gamma_{n_2}^s L \delta_{m_1,n_1}, \tag{B.30}$$

where it is possible to recognise the lateral surface of the cylindrical shell,

$$S = 2\pi R L. \tag{B.31}$$

Then, equation (B.30) could be written as:

$$S_{mn}^{ss} = \int_S \varphi_m^s (\mathbf{x}_s) \, \psi_n^s (\mathbf{x}_s) \, \mathrm{d}S = S J_{n_2} (\lambda_{n_2 n_3}) \, \gamma_{n_2}^s \delta_{m_1,n_1}. \tag{B.32}$$

Similarly, considering the results obtained in equations (B.15), (B.17) and (B.28), the coupling term in equation (B.8) results:

$$S_{mn}^{aa} = \int_S \varphi_m^a (\mathbf{x}_s) \, \psi_n^a (\mathbf{x}_s) \, \mathrm{d}S = S J_{n_2} (\lambda_{n_2 n_3}) \, \gamma_{n_2}^a \delta_{m_1,n_1}. \tag{B.33}$$

The elements of the structural-acoustic coupling matrix **S** thus result:

$$S_{m,n} = S J_{n_2} (\lambda_{n_2 n_3}) \, \gamma_{n_2}^s \delta_{m_1,n_1} \tag{B.34}$$

and

$$S_{m+M,n+N} = S J_{n_2} (\lambda_{n_2 n_3}) \, \gamma_{n_2}^a \delta_{m_1,n_1}, \tag{B.35}$$

with the coefficients $\gamma_{n_2}^s, \gamma_{n_2}^a$ and δ_{m_1,n_1} defined in equations (B.16), (B.17) and (B.29) respectively, $m = 1, 2, \ldots, M$ and $n = 1, 2, \ldots, N$.

The elements of the acoustic-structural coupling matrix **R**, from equation (B.3), can be defined as:

$$R_{n,m} = 2\rho_0 c_0^2 S J_{n_2} (\lambda_{n_2 n_3}) \, \gamma_{n_2}^s \delta_{m_1,n_1} \tag{B.36}$$

and

$$R_{n+N,m+M} = 2\rho_0 c_0^2 S J_{n_2} (\lambda_{n_2 n_3}) \, \gamma_{n_2}^a \delta_{m_1,n_1}. \tag{B.37}$$

The former analysis led to three conditions that have to be satisfied for an acoustic mode and a structural mode to be coupled [30, 120, 136]:

  i correspondence of the circumferential symmetry, thus symmetric components of the structural modes couple only with symmetrical components of the acoustic modes and the same for the anti-symmetric components;

ii equality of the circumferential wavelength, which corresponds to the equality of the circumferential modal index;

iii a relationship of the axial wavelength such that the sum of the axial indices is an odd number.

Figure B.1 presents the four possible coupling configurations of the $(1,2)$ structural mode and the $(0,2,0)$ acoustic mode shape. For the sake of improving the clarity and readability, the mode shapes are represented in just half of the circumferential domain and apart from each other. Furthermore, to highlight the differences between the two domains, both the flexural displacement and the acoustic pressure are shown in absolute value. This anyway does not constitute a difficulty, keeping in mind the cyclic nature of the positions of nodes and anti-nodes presented in tables 3.1 and 3.2. Plot (a) shows the sym-
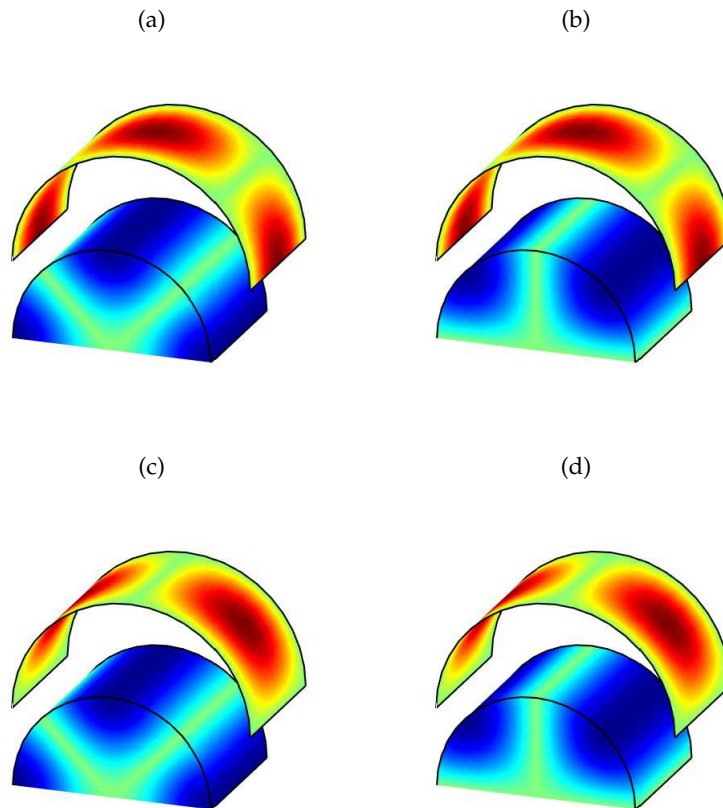

(a) (b)

(c) (d)

Figure B.1: Coupling configurations between the $(1,2)$ structural mode and the $(0,2,0)$ acoustic mode, S-S (a), S-A (b), A-S (c) and A-A (d).

metric component of the structural mode and the symmetric component of the acoustical mode (S-S configuration), plot (b) shows the S-A configuration, in

which the symmetric component of the structural mode and the anti-symmetric component of the acoustic mode are considered, plot (c) presents the A-S configuration and finally plot (d) presents the A-A configuration. As expressed by equation (B.12), different components of the two domains are orthogonal, thus the combination of the components shown in plots (b) and (c) does not provide any coupling. This appears quite evident since at a nodal position for one domain corresponds an anti-nodal position for the other domain. For example, the effect of the flexural displacement on the acoustical pressure gives a global effect that balances out, resulting thus in no net effect. On the other side, for the S-S and A-A configurations of plot (a) and (d), each section of the domain delimited by two adjacent nodal lines sums with the others, giving a net effect different than zero. Thus these two configurations effectively couple the structural and acoustic domains.

Figure B.2 shows the S-S (left plots) and the A-A coupling configurations for the $(1,2)$ structural mode and $(1,2,0)$ acoustic mode, plot (a), and for the $(1,2)$ structural mode and the $(0,1,0)$ acoustic mode, plot (b).

In the first case shown in plot (a) the two modes have axial indices such that their sum is an even number, thus according to equation (B.29), they do not couple. Considering the axial anti-nodal region of the structural mode, the acoustic mode presents here a nodal line which divide two axial regions with opposite amplitude. The source effect of the structural vibration on the acoustic domain in one zone is therefore compensated on the other zone, giving as a result a net effect which correspond to no source effect of the structural vibration.

Considering now the two modes shown in figure B.2 (b), they present a different number of circumferential wavelengths, thus different circumferential modal indices. According to equations (B.14) and (B.15), these two modes do not couple, also for the S-S and A-A configurations. Indeed, the two domains could be imagined as composed by circumferential subsections which present amplitudes with opposite sign. The coupling effect in one subregion is compensated by the contribution obtained in other region, thus the net result is zero.

The analysis of figures B.1 and B.2 gives thus a graphical interpretation of the coupling conditions given in equations (B.16), (B.16) and (B.29). This is made considering low values for the modal indices in order to provide a clear and readable observation of the coupling phenomenon, but can easily be extended to higher values of the modal indices.

(a)

(b)
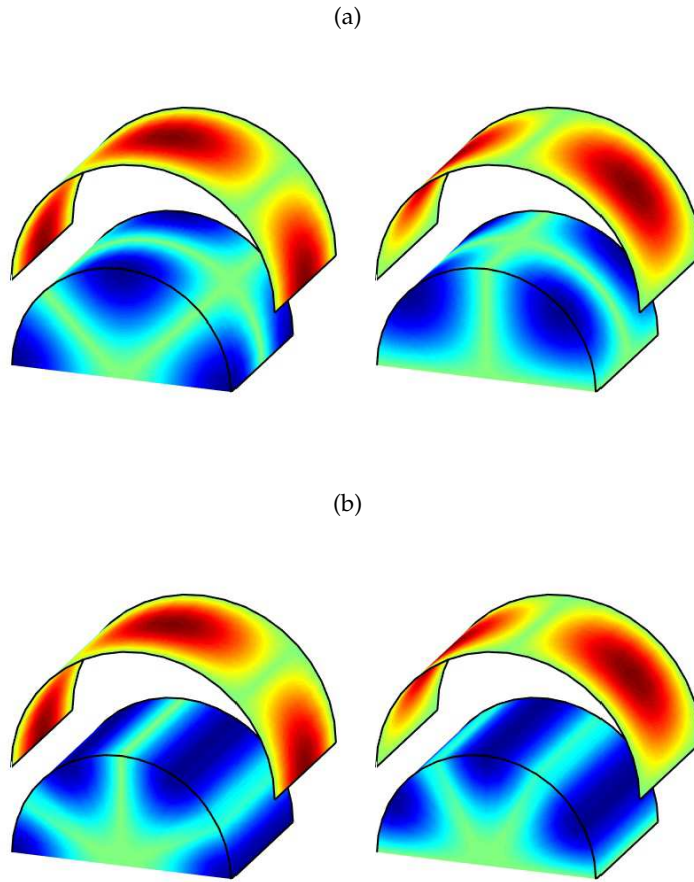
Figure B.2: S-S (left plots) and A-A (right plots) coupling configurations for the $(1,2)$ structural mode and the $(1,2,0)$ acoustic mode, plot (a) and for the $(1,2)$ structural mode and the $(0,1,0)$ acoustic mode, plot (b).

B.2 COUPLING ALGORITHM FOR THE COUPLED STRUCTURAL-ACOUSTIC RESPONSE

For the low frequency analysis of cylindrical structural-acoustic coupled system, the most severe coupling condition results to be the equality of the circumferential wavelength, expressed mathematically in equations (B.16) and (B.17). This is due to the different dependence of the structural and acoustic natural frequencies on the circumferential indices. Indeed, as highlighted in sections 3.3 and 3.6, lower acoustic natural frequencies $f_{a,n}$ are associated with lower values of the circumferential index n_2 while lower structural natural frequencies $f_{s,m}$ are associated with values of the circumferential indices m_2 that depend on the geometrical dimensions of the shell and are generally given by values comprised between 10 and 20 [98].

With the geometrical dimensions assumed in this study, reported in table 2.1 and considering the 20-100 Hz frequency range adopted for the simulation study, there is no structural mode with natural frequency comprised between 0-100 Hz that couples with an acoustic mode characterised by a natural frequency in the same range.

Figure B.3 (a) shows the variation of the structural natural frequency $f_{s,m}$ with the circumferential index m_2 for several values of the axial index m_1 (thin solid black lines) plotted on top of the variation of the acoustic natural frequency $f_{a,n}$ with the circumferential index n_2 for several values of the axial index n_1 and for radial index $n_3 = 0$ (thin solid blue lines), $n_3 = 1$ (thin dashed blue lines) and $n_3 = 2$ (thin dotted blue lines).
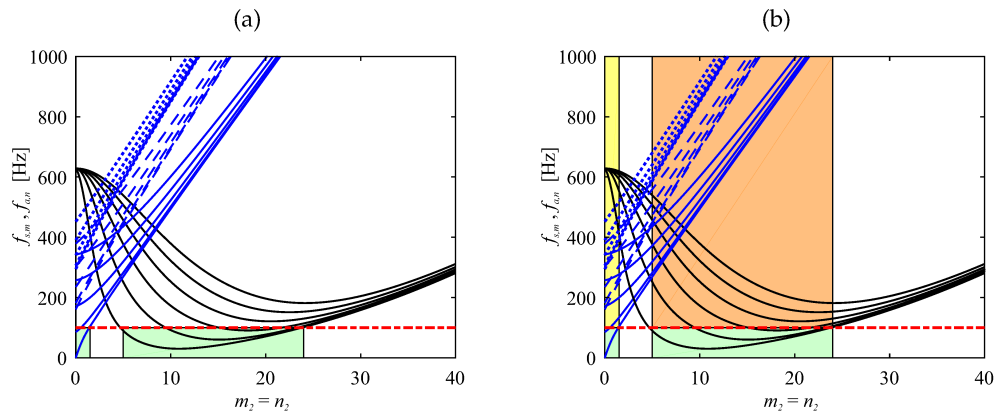
Figure B.3: Variation of the structural natural frequency $f_{s,m}$ with the circumferential index m_2 for different values of the axial index m_1 (thin solid black lines) and variation of the acoustic natural frequency $f_{a,n}$ with the circumferential index n_2 for different values of the axial index n_1 for $n_3 = 0$ (thin solid blue lines), $n_3 = 1$ (thin dashed blue lines) and $n_3 = 2$ (thin dotted blue lines). The horizontal dashed red lines, set at 100 Hz, represents the upper value of the frequency range considered for the simulation study. The light green regions in plot (a) represent the regions in which structural and acoustic modes with natural frequency less then 100 Hz lay. In plot (b) the light yellow region represents the zone in which the structural modes effectually couple with the considered acoustic modes and the light orange region corresponds to the zone in which the acoustic modes effectually couple with the structural modes considered.

The upper value of the frequency, assumed equal to 100 Hz and represented with the thick dashed red lines in figure B.3, separates the zone in which lay the acoustic and structural modes whose natural frequency is comprised in frequency range considered from those characterised by a higher natural frequency. These two regions are indicated with the light green rectangles, the

left one related to the acoustic modes and the right one associated with the structural modes.

Since these two regions does not have any point in common, there is no coupling between the structural and acoustic modes characterised by natural frequencies in the 0-100 Hz range. Thus, considering just the $\hat{M}$ structural modes with natural frequency in the 0-100 Hz ($\hat{M} = 39$) in the truncated modal summation for the flexural displacement and just the $\hat{N}$ acoustic modes with natural frequency in the 0-100 Hz ($\hat{N} = 3$) in the truncated modal summation for the acoustic pressure , the coupling matrices **S** and **R** result matrices of zeros, leading to no coupling between the two domains.

A first attempt to solve this problem and obtain a fully coupled system is to increase the upper frequency which correspond to the threshold of the natural frequency for the modes to be included in the truncated modal summations, keeping the same frequency range for the study. However, following this approach, a huge number of structural and acoustic modes have to be included before the modes which actually couple with the mode of interest are included. This will exponentially and uselessly increment the dimension of the system and thus the computational cost of the analysis. Figure B.4 (a) shows the total number of elements (thin black line) and the number of non-zero elements (thin red line) of the structural-acoustic matrix **S** considering an increasing value of the frequency under which modes are included in the truncated modal summations. Figure B.4 (b) shows the ratio of the non-zero elements to the total number of elements of the structural-acoustic coupling matrix. This ratio is zero up
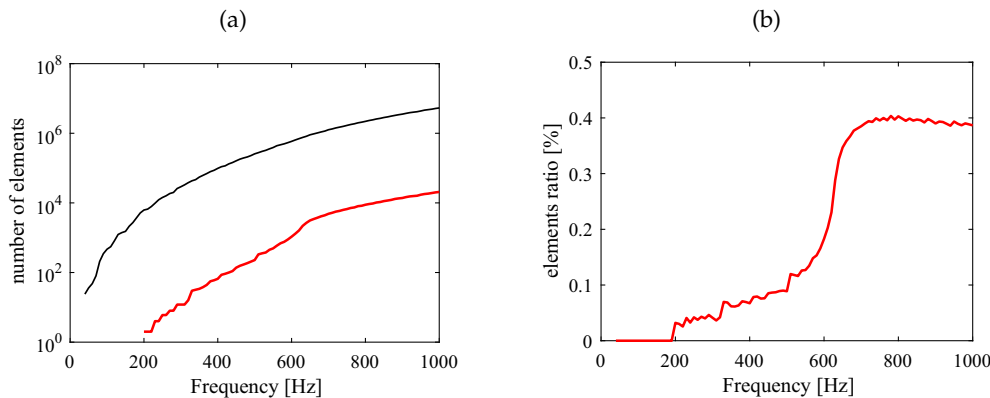
Figure B.4: Variation of the total number of elements (thin black line) and of the number of non-zero elements (thin red line) of the structural-acoustic matrix **S** with the frequency under which the structural and acoustic modes are included in the modal summations, plot (a) and ratio of the nonzero elements to the total number of elements of the structural-acoustic coupling matrix, plot (b).

to about 200 Hz, where the first combination of structural and acoustic modes couple. But at this frequency the total number of elements is already about 10^4, and it is not guaranteed that the coupling phenomenon occurs between modes characterised by a natural frequency comprised in the 0-100 frequency band. Increasing the frequency under which structural and acoustic modes are included in the modal summations, the elements ratio raises between 600 and 700 Hz and then slightly decreases. The maximum value of the ratio is 0.4%, thus the number of structural and acoustic modes that effectively couple are very small compared to the total number of structural and acoustic modes considered in the truncated modal summation for the flexural displacement and the acoustic pressure.
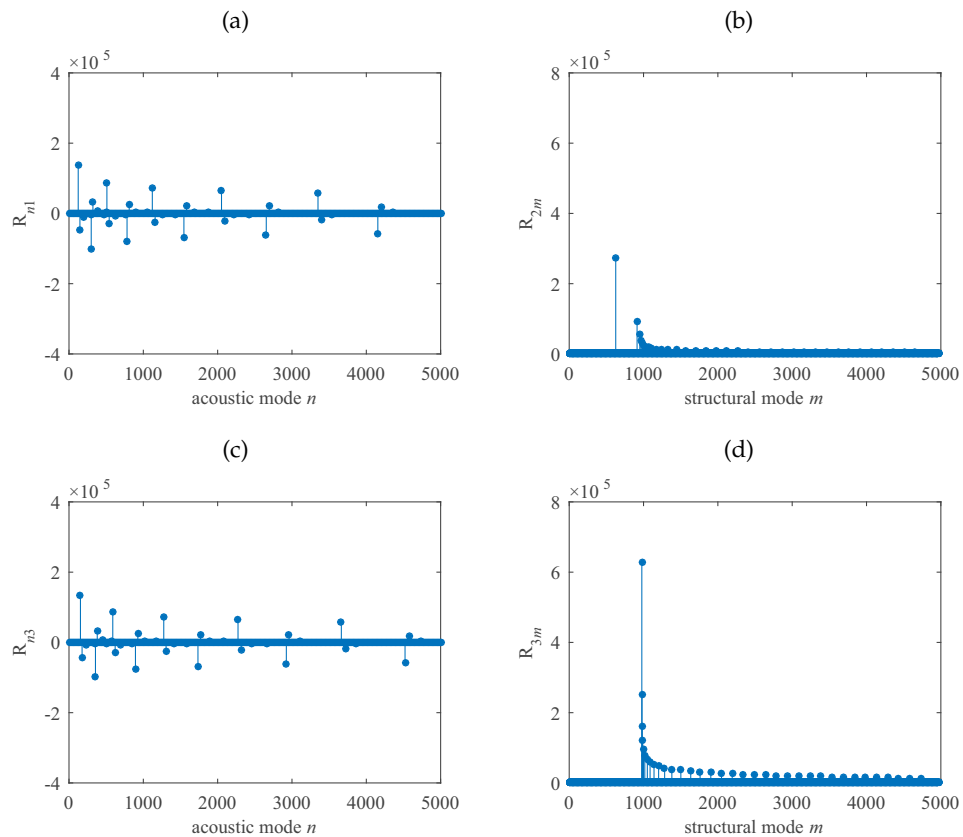
Figure B.5: First (plot (a)) and third (plot (c)) columns and second (plot (b)) and third (plot (d)) rows of the acoustic-structural coupling matrix **R** obtained considering 5000 structural modes and 5000 acoustic modes.

Figure B.5 shows some of the terms of the acoustic-structural coupling matrix **R**, obtained considering 5000 structural modes and 5000 acoustic modes. In particular, plots (a) and (c) represent the first and the third columns of the matrix **R**, which correspond to the coupling terms between the first and the third

structural modes with the 5000 acoustic modes and plots (b) and (d) show the second and the third rows of the matrix **R**, which correspond to the coupling terms between the second and the third acoustic modes with the 5000 structural modes. For all four considered cases, the first non-zero elements correspond to a higher-order mode; in particular the first acoustic mode which couples with the first structural mode ($m = 1$) is the 124th ($n = 124$) and for the third structural mode ($m = 3$) it is the 154th acoustic mode ($n = 154$). The first mode which couples with the second acoustic mode ($n = 2$) is the 626th structural mode ($m = 626$) and for the third acoustic mode ($n = 3$) the structural mode is the 977th, ($m = 977$). It is interesting to note that the highest coupling coefficient correspond to the couple of mode with the lowest order and the value of the coupling coefficient decreases as the modal order increases.
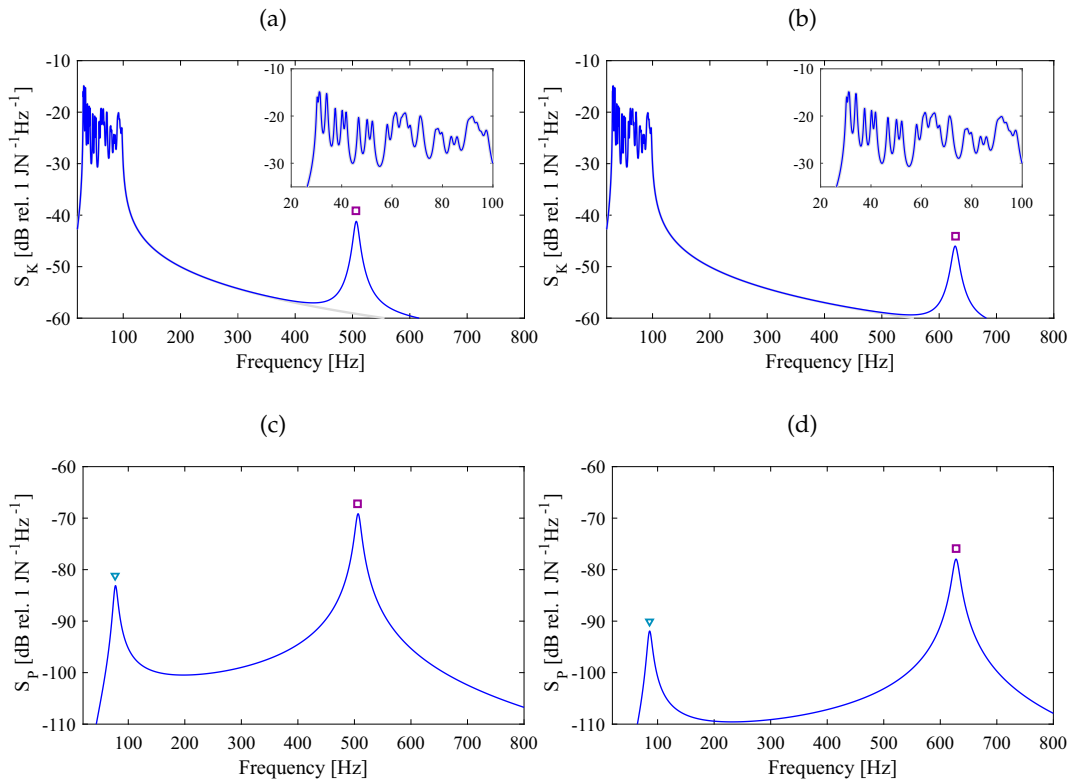
Figure B.6: Spectra of the flexural kinetic energy PSD (top plots) and acoustic potential energy PSD (bottom plots) of the *in vacuo* cylinder (thick solid light grey lines), and of the coupled system (thin blue lines) adding to the truncated modal summation of the flexural displacement the structural mode which couples with the second acoustic mode (plots (a) and (c)) and with the third acoustic mode (plots (b) and (d)).

In figure B.6 are shown the spectra of the flexural kinetic energy PSD (top plots) and of the acoustic potential energy PSD (bottom plots) when in the

truncated modal summation for the flexural displacement are considered only the $\hat{M}$ *in vacuo* structural modes (thick grey lines in plots (a) and (b)) and when in the addition to the $\hat{M}$ structural modes are considered also the structural mode which couples with the second acoustic mode (blue lines in plots (a) and (c)) and with the third acoustic mode (blue lines in plots (b) and (d)). The addition of an higher-order structural mode does not modify the 20-100 Hz structural response but it allows the presence of the resonance peak of the resonant acoustic mode which effectively couples with the added structural mode.
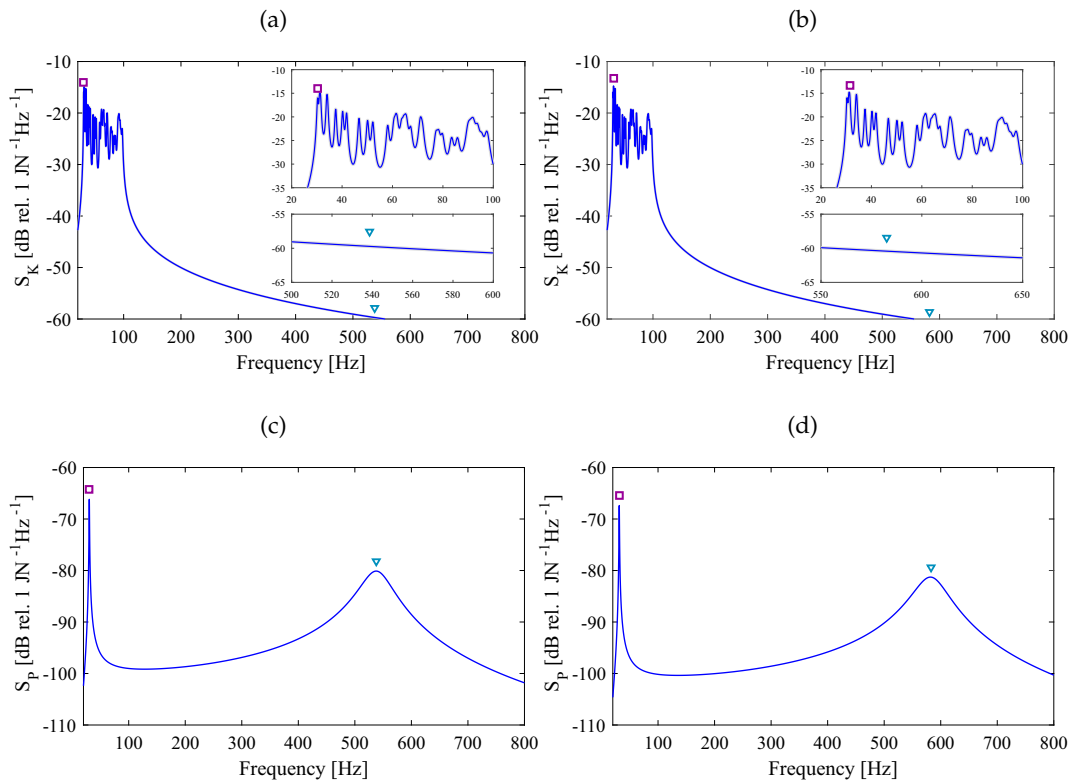
Figure B.7: Spectra of the flexural kinetic energy PSD (top plots) and acoustic potential energy PSD (bottom plots) of the *in vacuo* cylinder (thick solid light grey lines), and of the coupled system (thin blue lines) adding to the truncated modal summation of the acoustic pressure the acoustic mode which couples with the first structural mode (plots (a) and (c)) and with the third structural mode (plots (b) and (d)).

In figure B.7 are shown the spectra of the flexural kinetic energy PSD (top plots) and of the acoustic potential energy PSD (bottom plots) when in the truncated modal summation for the flexural displacement are considered only the $\hat{M}$ *in vacuo* structural modes (thick grey lines in plots (a) and (b)) and in the truncated modal summation for the acoustic pressure are considered the

acoustic mode which couples with the first structural mode (plots (a) and (c)) and with the third strictural mode (plots (b) and (d)). The addition of an higher-order acoustic mode does not modify the 20-100 Hz structural response but it allows the presence of a resonance peak at a frequency which corresponds to the one of the structural mode at which it is coupled.

A different approach is thus followed, which consists of adding in the structural modal summations just the modes which actually couple with the $\hat{N}$ acoustic modes with natural frequency comprised between 0 and 100 Hz and adding in the truncated modal summation for the acoustic pressure just the acoustic modes which actually couple with the $\hat{M}$ structural characterised by a natural frequency comprised between 0 and 100 Hz. This approach is graphically shown in figure B.3 (b), in which the light yellow region identifies the structural modes which, satisfying the circumferential coupling condition, could effectively couple with the $\hat{N}$ acoustic modes. Also, the light orange region identifies the region for the acoustic modes that satisfy the circumferential coupling condition with the $\hat{M}$ structural mode. Nevertheless, the structural modes in the yellow region and the acoustic modes in the orange region have also to satisfy the axial coupling condition.

The effects of the addition in the truncated modal summations of structural and acoustic modes which actually couple with the $\hat{M}$ structural and $\hat{N}$ acoustic modes with resonance frequency in the range 0-100 Hz is considered in terms of the time-averaged total flexural kinetic energy K and the time-averaged total acoustic potential energy P, which can be obtained by the flexural kinetic energy and acoustic potential energy PSDs given in equations (3.182) as [28, 124, 125]:

$$K = \frac{1}{2\pi} \int_0^{628} S_K(\omega) d\omega \quad \text{and} \tag{B.38a}$$

$$P = \frac{1}{2\pi} \int_0^{628} S_P(\omega) d\omega, \tag{B.38b}$$

where the range of integration corresponds to the frequency considered in the convergence study, 0-100 Hz.

The following algorithm is used for obtaining the number M of structural modes to be considered in the truncated modal summation for the flexural displacement:

- for each of the $\hat{N}$ acoustic modes, Δm structural modes which present the maximum coupling term are added in the truncated modal summation for the flexural displacement, with $\Delta m = 1, 2, \ldots, 40$;

- the time-averaged total flexural kinetic energy and total acoustic potential energy are then evaluated, once the PSDs functions are obtained using the formulation presented in section 3.8.

The result of this procedure is shown in figure B.8 (a) where the variations of the time-averaged total flexural kinetic energy (left graph) and the variation of the time-averaged total acoustic potential energy (right graph) are plotted against the number of structural modes Δm added in the structural modal summation for each of the $\hat{N}$ acoustic modes. With this procedure, high-order structural modes are added in the truncated modal summation for the flexural displacement, characterised by a natural frequency well above the frequency of considered in this study. The structural response in the 0-100 Hz is not affected by the increased number of structural mode considered. The inclusion of higher-order structural modes, leads to the presence of the $\hat{N}$ resonance peaks in the acoustic response. These peaks are relatively smooth, due to the value of the acoustical modal damping ζ_0 assumed, and thus in this case P assumes low values.

Also, an analogous algorithm is used to obtain the number N of acoustic modes to be added in the truncated modal summation for the acoustic pressure:

- for each of the $\hat{M}$ structural modes, Δn acoustic modes which present the maximum coupling term are added in the truncated modal summation for the acoustic pressure, with $\Delta n = 1, 2, \ldots, 40$;

- the time-averaged total flexural kinetic energy and total acoustic potential energy is then evaluated, once the PSDs functions are obtained using the formulation presented in section 3.8.

The results of this procedure are presented in figure B.8 (b) where the time-averaged total flexural kinetic and acoustic potential energies are plotted against the number of acoustic modes Δn added for each of the $\hat{M}$ structural modes. The acoustic modes that effectively couple with the structural modes represent a damping term on the structural response [99], but this effect just slightly affect the structural response since the considered fluid is air. The acoustic response in the 20-100 Hz frequency range is instead very affected by the addition of acoustic modes, also if these are characterised by a natural frequency much higher than the upper frequency limit considered in the simulation study. This

(a)

(b)
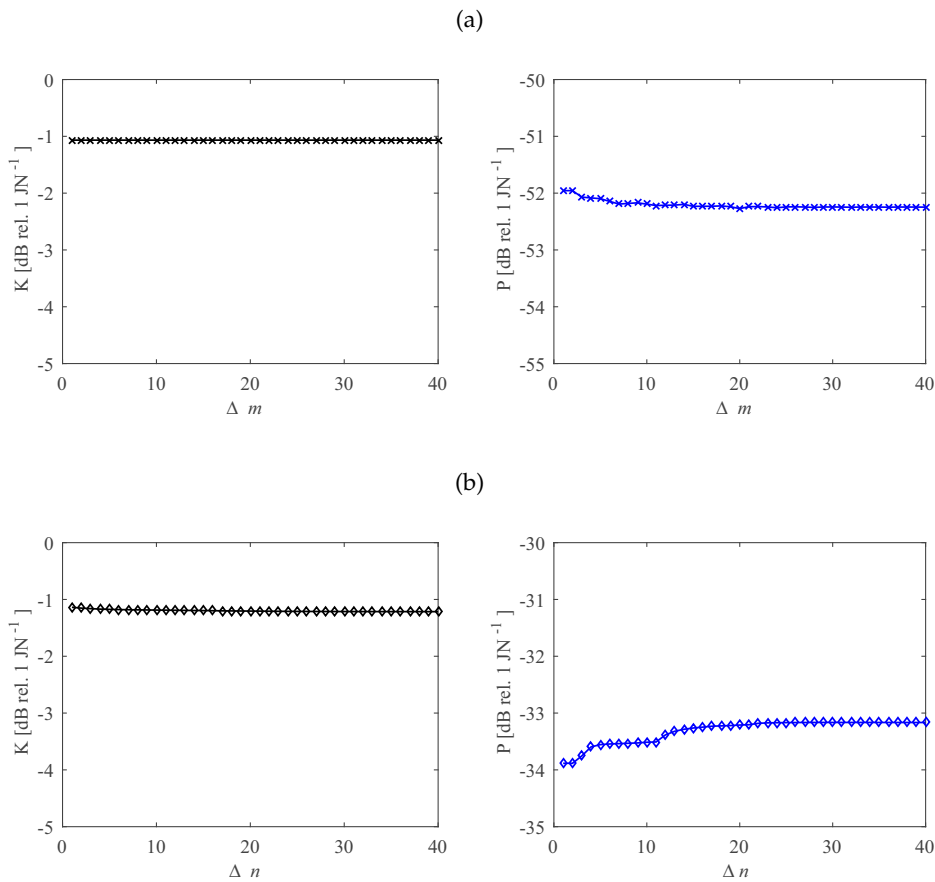
Figure B.8: Variation of time-averaged total flexural kinetic energy K (left graphs) and of the time-averaged total acoustic potential energy P (right graphs) for an increasing number of structural modes (plot (a)) and for an increasing number of acoustic modes (plot (b)) considered in the truncated modal summations.

is due to the fact that, since these acoustic modes effectively couple with the $\hat{M}$ structural modes, resonance peaks in correspondence to the $\hat{M}$ structural frequency appears in the acoustic response, as shown in figure B.7.

The presented convergence analysis highlights that, for the 20-100 Hz frequency band considered in this study, it is necessary to include the 39 flexural natural modes with natural frequencies comprised between 0 and 100 Hz plus three higher order flexural natural modes with natural frequencies beyond 100 Hz for a total of 42 flexural natural modes.

Also, it is necessary to include the 3 acoustic natural modes with natural frequencies comprised between 0 and 100 Hz plus other 39 acoustic modes which are selected in such a way as to have for each of the 39 structural modes

with natural frequency comprised between 0 and 100 Hz the acoustic mode that give raise to the highest structural-acoustic coupling.

Table B.1 summarises the modal indices and natural frequencies of the flexural modes and the acoustic modes considered in the simulation study. The table highlights that, to achieve a correct convergence of both the flexural kinetic energy PSD and acoustic potential energy PSD it would be necessary to include acoustic modes with natural frequency much higher than the 100 Hz limit considered in the simulation.

Table B.1: Structural and acoustic natural modes considered in the simulations.

flexural modes of the cylindrical wall			acoustic modes of the cylindrical cavity			coupling coefficient
m	(m_1, m_2)	$f_{s,m}[Hz]$	n	(n_1, n_2, n_3)	$f_{a,n}[Hz]$	$R_{nm}\ (\times 10^5)$
1	1,11	30.3	124	0,11,0	538.6	1.38
2	1,10	31.0	101	0,10,0	494.2	1.32
3	1,12	31.4	154	0,12,0	582.8	1.34
4	1,13	33.9	190	0,13,0	626.8	1.31
5	1,9	34.1	80	0,9,0	449.8	1.47
6	1,14	37.4	227	0,14,0	670.8	1.28
7	1,8	40.2	60	0,8,0	405.1	1.52
8	1,15	41.7	273	0,15,0	714.7	1.25
9	1,16	46.7	318	0,16,0	758.5	1.23
10	1,7	50.1	46	0,7,0	360.2	1.59
11	1,17	52.1	368	0,17,0	802.2	1.20
12	1,18	58.1	432	0,18,0	845.9	1.18
13	2,15	60.6	278	1,15,0	719.8	0.83
14	2,16	61.3	324	1,16,0	763.3	0.82
15	2,14	61.7	231	1,14,0	676.3	0.86
16	2,17	63.6	377	1,17,0	806.8	0.80
17	1,19	64.4	494	0,19,0	889.4	1.16
18	2,13	65.1	194	1,13,0	632.7	0.87
19	1,6	65.5	33	0,6,0	314.9	1.67
20	2,18	67.1	435	1,18,0	850.2	0.79
21	2,12	71.0	159	1,12,0	589.0	0.89
22	1,20	71.1	559	0,20,0	933.0	1.14
23	2,19	71.8	502	1,19,0	893.6	0.77
24	2,20	77.2	565	1,20,0	936.9	0.76
25	1,21	78.2	640	0,21,0	976.5	1.12
26	2,11	79.8	132	1,11,0	545.4	0.92
27	2,21	83.4	644	1,21,0	980.2	0.75
28	1,22	85.7	719	0,22,0	1020.1	1.11
29	1,5	89.9	22	0,5,0	269.4	1.76
30	2,22	90.2	727	1,22,0	1023.6	0.74
31	3,18	90.9	454	2,18,0	863.1	0.71
32	3,19	91.5	519	2,19,0	905.8	0.69
33	2,10	92.0	107	1,10,0	501.6	0.95
34	3,17	92.1	395	2,17,0	820.3	0.72
35	1,23	93.6	805	0,23,0	1063.4	1.09
36	3,20	93.7	585	2,20,0	948.6	0.68
37	3,16	95.3	345	2,16,0	777.6	0.73
38	3,21	97.3	669	2,21,0	991.4	0.67
39	2,23	97.6	817	1,23,0	1066.8	0.73
626	1,1	506.3	2	0,1,0	77.2	2.74
976	1,0	627.8	1	0,0,0	0	9.42
977	2,0	627,8	3	1,0,0	85.7	6.28

NUMERICAL ALGORITHMS FOR THE TIME VARYING SYSTEM

This appendix is devoted to the description of the numeric algorithms used in the derivation of the response of the fully coupled structural-acoustical-sweeping TVA. As described in chapter 5, the global damping and stiffness matrices of the fully coupled structural-acoustic-sweeping TVA equation of motion, equation (5.38), result time-dependent due to the time-dependence of the damping and stiffness properties of the sweeping TVAs. Thus a specific algorithm is required to obtain the structural and acoustic coupled responses.

In the first part of this chapter is described the numerical integration of stochastic differential equations. Indeed, the coupled system is considered to be subject to a stochastic white noise rain on the roof excitation, thus a dedicated integration algorithm is used, which is based on the Runge-Kutta integration methods.

The numerical estimation of PSD the structural velocities and pressure amplitudes matrices is then presented. This is obtained considering the MATLAB® *pwelch* function, focusing on the description of the several parameters used in the simulation study.

C.1 NUMERICAL INTEGRATION OF STOCHASTIC DIFFERENTIAL EQUATIONS

The time integration of *time-invariant* equations of motion is usually derived by casting the equation in the following state-space form:

$$\dot{\mathbf{x}}(t) = \mathbf{A}\mathbf{x}(t) + \mathbf{B}\mathbf{f}(t), \tag{C.1}$$

where $\mathbf{x}(t)$ is the state vector, $\mathbf{A}$ and $\mathbf{B}$ are the state (or system) and input matrices, respectively and t is the time. The several algorithms found in commercial software to solve differential equations of the type given in equation (C.1) are usually based on the Runge-Kutta integration methods. When deterministic

processes are considered, the deterministic *time-invariant* ordinary differential equation (C.1) is expressed with the Runge-Kutta method as [202]:

$$\dot{\mathbf{x}}(t) = f(\mathbf{x}, t), \tag{C.2}$$

where $f(\mathbf{x}, t)$ is a deterministic function of the state vector and time. The Runge-Kutta method approximates the Taylor series of $f(\mathbf{x}, t)$ with a linear combination of values of $f(\mathbf{x}, t)$, which does not require a explicit evaluation of the time-derivatives of $f(\mathbf{x}, t)$. The solution at the instant t_{k+1} is thus approximated as [202]:

$$\mathbf{x}_{k+1} = \mathbf{x}_k + \alpha_1 \mathbf{k}_1 + \alpha_2 \mathbf{k}_2 + \cdots + \alpha_n \mathbf{k}_n, \tag{C.3}$$

where

$$\mathbf{k}_1 = \Delta t f(\mathbf{x}_k, t_k), \tag{C.4a}$$

$$\mathbf{k}_j = \Delta t f \left(\mathbf{x}_k + \sum_{i=1}^{j-1} \beta_{ij} \mathbf{k}_i(t_k) + \Delta t \gamma_j \right), \tag{C.4b}$$

Δt is the time step if the integration and n is the order of approximation of the algorithm. The coefficients α_i, β_{ij} and γ_j are calculated by matching the coefficients of the Taylor expansion of $\mathbf{x}(t)$ and the coefficients of the Taylor expansion of $\mathbf{x}_k$ to ensure that the Runge-Kutta solution $\mathbf{x}_k$ approximates the exact solution $\mathbf{x}(t)$ with an error of order $(\Delta t)^{n+1}$ [202]. Usually commercial software use variable step integration algorithms to reduce the simulation time. The integration time is varied comparing the value of the derivative of the approximated solution calculated at every time step of integration with a tolerance value.

When stochastic stochastic disturbances are considered, as the white noise rain on the roof stochastic forces considered in this thesis, the differential equation is expressed with the Runge-Kutta method as [202, 203]:

$$\dot{\mathbf{x}}(t) = f_1(\mathbf{x}, t) + \mathbf{B} \mathbf{f}, \tag{C.5}$$

where the first term accounts for deterministic dependence of $\mathbf{x}$ and t and the second one is related to the stochastic dependence of the disturbance. The approximated solution at time t_{k+1} can be written as [202, 203]:

$$\mathbf{x}_{k+1} = \mathbf{x}_k + \sigma_1 \mathbf{g}_1 + \sigma_2 \mathbf{g}_2 + \cdots + \sigma_n \mathbf{g}_n, \tag{C.6}$$

where

$$\mathbf{g}_1 = \Delta t f_1(\mathbf{x}_k, t_k) + \Delta t \mathbf{B} \mathbf{f}_1, \tag{C.7a}$$

$$\mathbf{g}_j = \Delta t f_1 \left(\mathbf{x}_k + \sum_{i=1}^{j-1} \tau_{ij} \mathbf{k}_i(t_k) + \Delta t \eta_j \right) + \Delta t \mathbf{B} \mathbf{f}_j \tag{C.7b}$$

and $\mathbf{f}_j$ is a vector of random forces generated at each step. In order for the numerical solution $\mathbf{x}_k$ to have the same statistical properties of the exact solution $\mathbf{x}(t)$, the coefficients σ_i, τ_{ij} and η_j are determined by matching the coefficients of the Taylor expansion of the covariance matrix of the exact solution and the approximated one. The values of the coefficients σ_i, τ_{ij} and η_j of the fourth order Runge-Kutta algorithm used to obtain the results presented in section 5.4 can be found in [202]. Since in the case of stochastic disturbance also the error is estimated on the covariance of the solution, for this class of problems fix time step integration algorithms must be used.

C.2 NUMERICAL ESTIMATION OF PSD THE STRUCTURAL VELOCITIES AND PRESSURE AMPLITUDES MATRICES

The estimated matrices with the PSD of the modal structural velocities and of the modal pressure amplitudes in equations (5.46), $\mathbf{S}_{\mathbf{bb}}^n(\omega)$ and $\mathbf{S}_{\mathbf{aa}}^n(\omega)$, are numerically obtained from the time-dependent pertinent values given in equations (5.42). This could be obtained using MATLAB® *pwelch* function, whose output is the PSD estimate of the input signal, and whose parameters with the values used in this study are:

window: divides the input signal vector in sub-vectors, this study considered windows of 100000 samples which means windows with a length of 3.3 seconds;

noverlap: specifies the overlap in samples, set to 50%;

nfft: sets the number of DFT points, also 500000 samples were considered which gives a resolution of 0.02 Hz for the output vector;

fs: indicates the sampling frequency of the input time vector, set to 10 kHz.

The validity of this approach is proved considering the spectra of the flexural kinetic energy PSD and of the acoustic potential energy PSD of the plain coupled structural-acoustic system (without TVAs). Figure C.1 shows the two responses calculated with equations (3.182) (thin solid black lines) and obtained

substituting in equations (3.178) the matrices $\mathbf{S}^n_{\mathbf{bb}}(\omega)$ and $\mathbf{S}^n_{\mathbf{aa}}(\omega)$ obtained using the numerical integration algorithm and the numeric estimation technique (thick solid green lines).

The curves match quite well, there are only some differences at the first structural natural frequency at around 30 Hz, where the response calculated via the finite Fourier transform is somewhat overestimated. Nevertheless, this was found to be the best trade-off between the random error present in the signal and the correct estimation of the peaks [124, 198, 204].
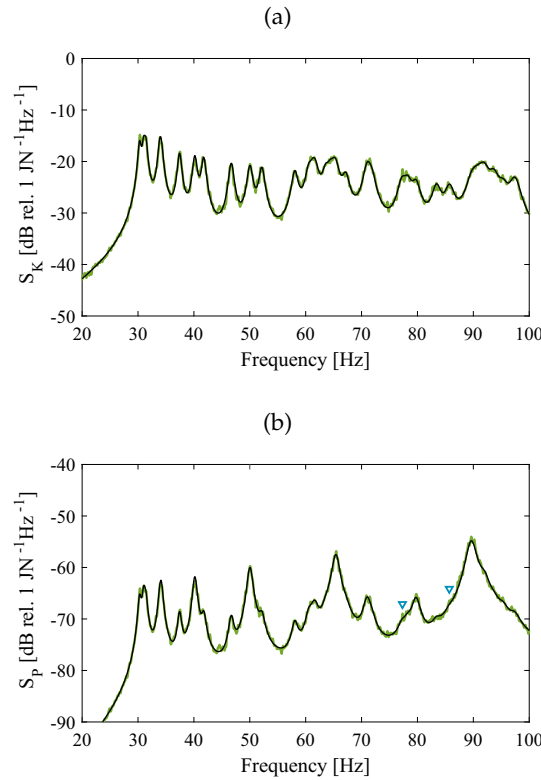

Figure C.1: Spectra of the flexural kinetic energy PSD (plot (a)) and acoustic potential energy PSD (plot (b)) obtained using equations (3.182) (thin black lines) and using the numerical approach (thick green lines).

C.3   NUMERIC INTEGRATION OF THE TIME VARYING EQUATION OF MOTION

The numerical integration of the stochastic ordinary differential equation for the coupled structural-acoustic system equipped with the sweeping TVA is characterised by time-varying stiffness and damping parameters of the TVA. In this case, the matrix $\mathbf{A}$ in equation (5.39) is updated with the new stiffness and

damping parameters at every time step of the integration algorithm described above.

D

SETUPS OF THE MEASUREMENTS AND TESTS ON THE FRONT END BOARD

In this appendix are briefly presented the schematic representation of the setups of the measurements presented in chapter 6 and the tests made on the front-end board.

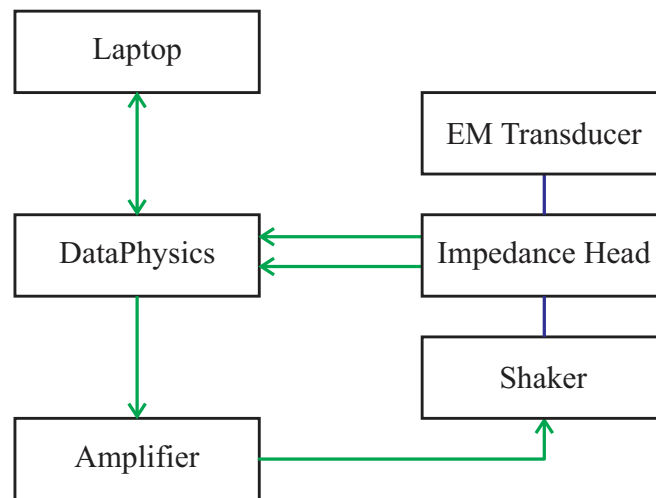### D.1 SETUPS FOR THE EXPERIMENTS

Figure D.1: Schematic representation of the setup for the measurement of the electromagnetic transducer Base Impedance.
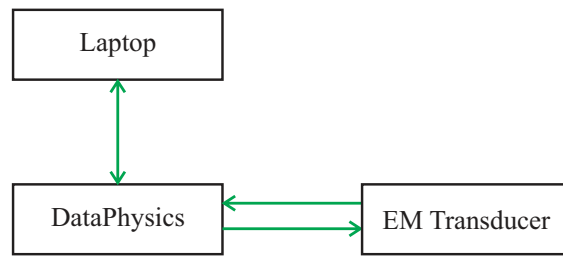
Figure D.2: Schematic representation of the setup for the measurement of the electro-magnetic transducer electrical impedance.
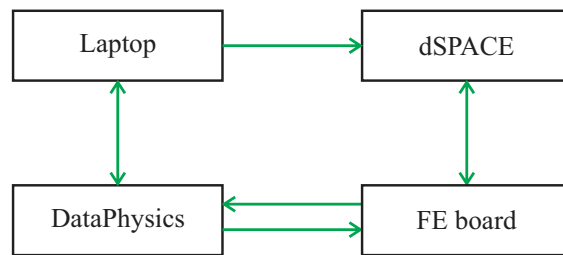

Figure D.3: Schematic representation of the setup for the measurement of the digitally implemented shunt electrical impedance.
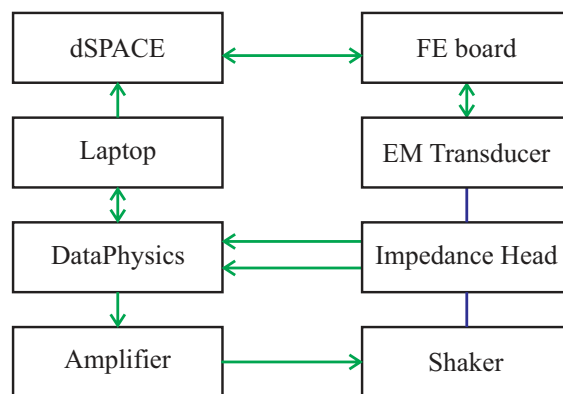
Figure D.4: Schematic representation of the setup for the measurement of the base impedance of the shunted electro-magnetic transducer.
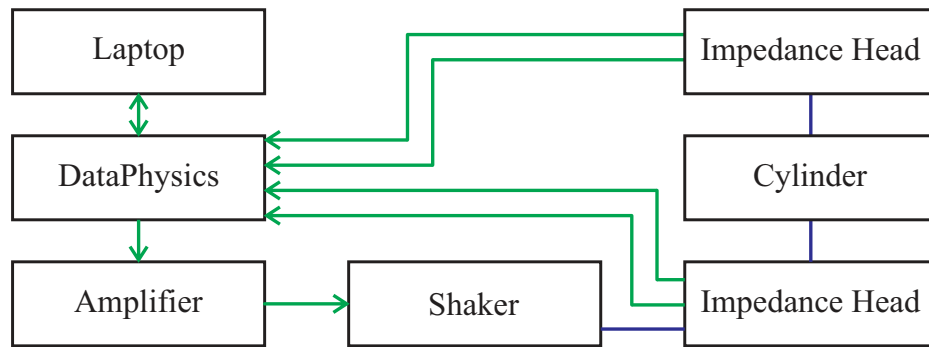
Figure D.5: Schematic representation of the setup for the measurement of the response of the plain cylinder.
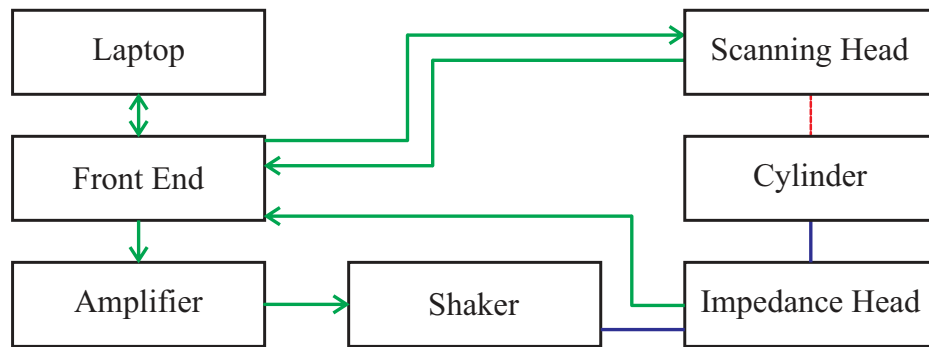
Figure D.6: Schematic representation of the setup for the vibrometric analysis of the plain cylindrical shell.
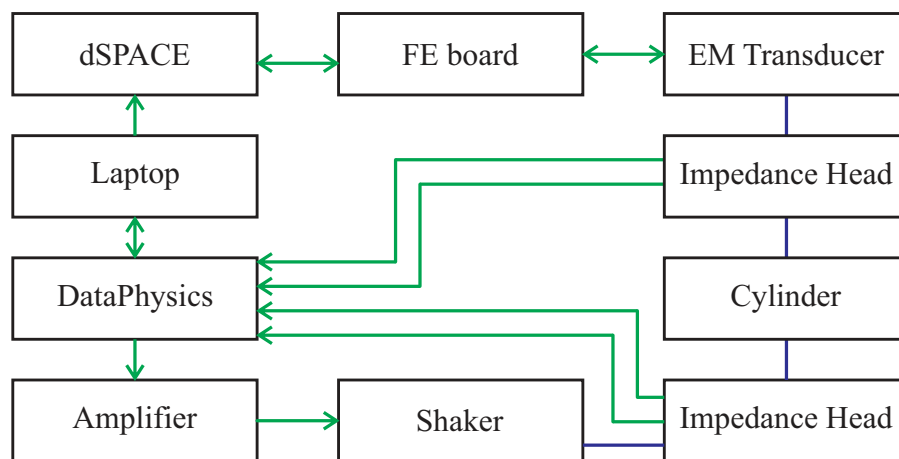
Figure D.7: Schematic representation of the setup for the measurement of the response of the cylinder equipped with the electro-magnetic TVA.

D.2 TESTS OF THE FRONT END BOARD
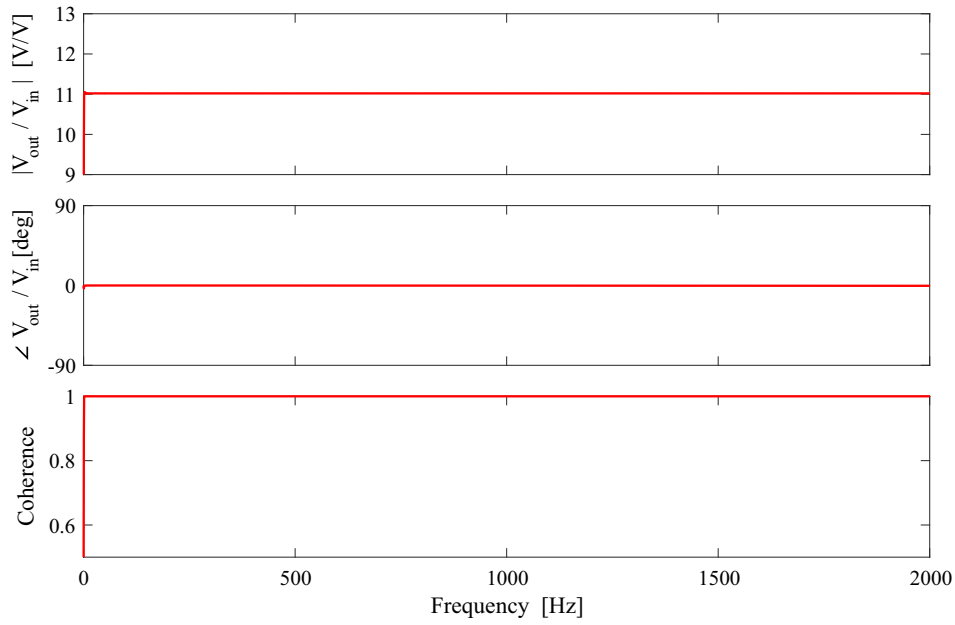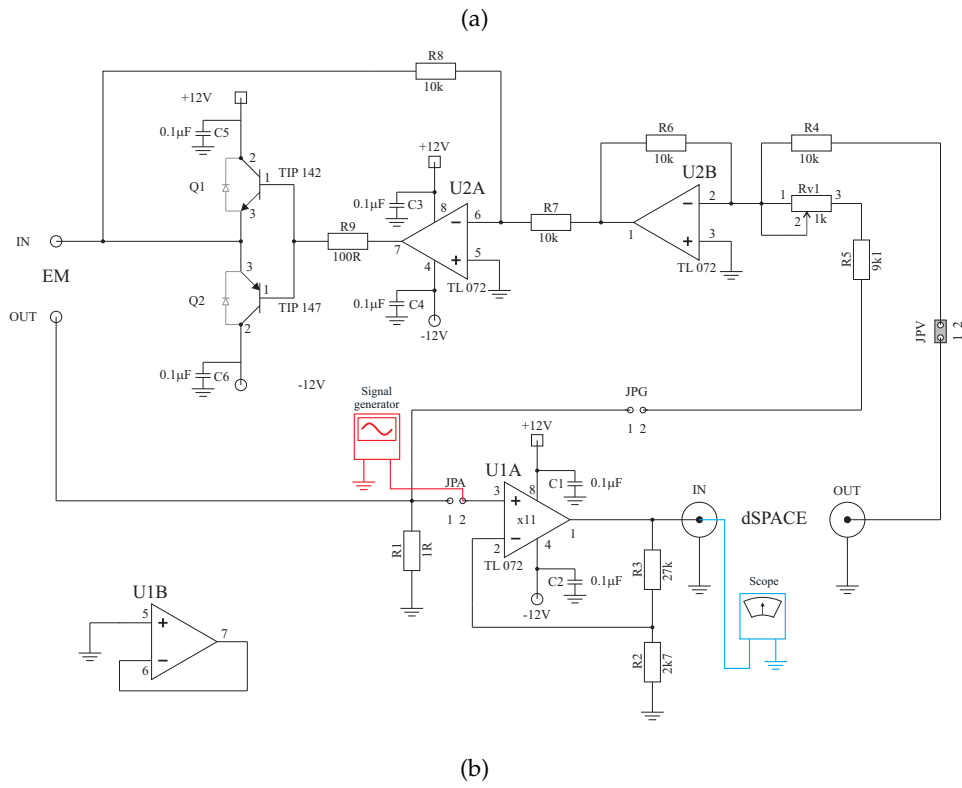
Figure D.8: Scheme (plot (a)) and measurement results (plot (b)) of the first test made on the front-end board.

(a)

(b)
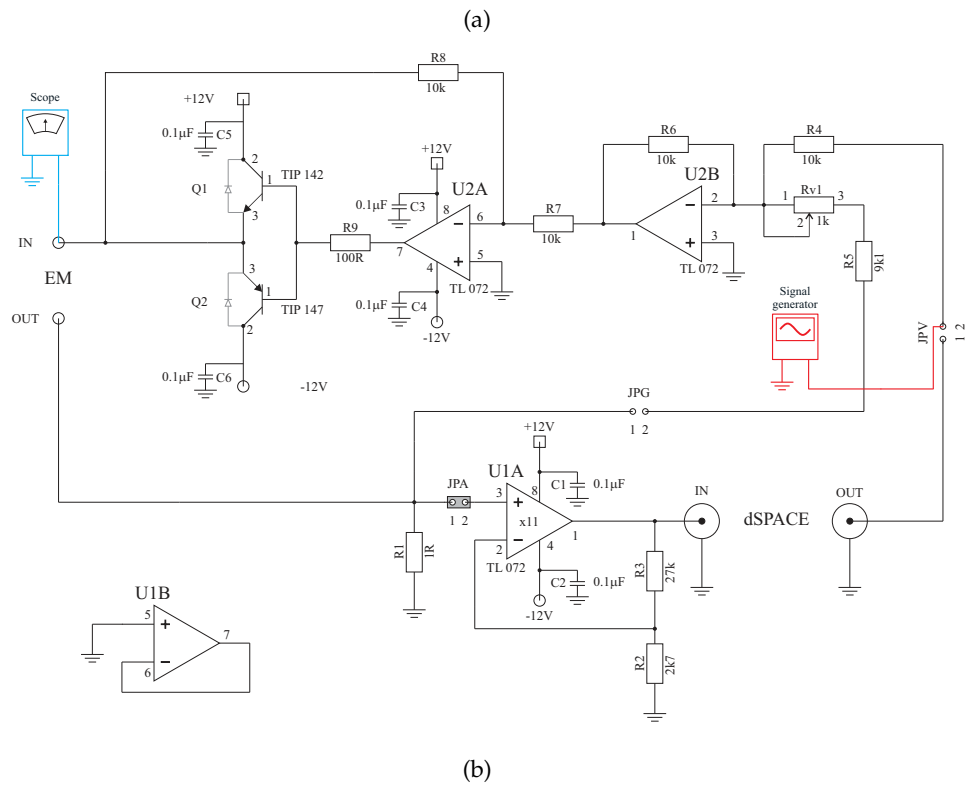
Figure D.9: Scheme (plot (a)) and measurement results (plot (b)) of the second test made on the front-end board.

(a)

(b)
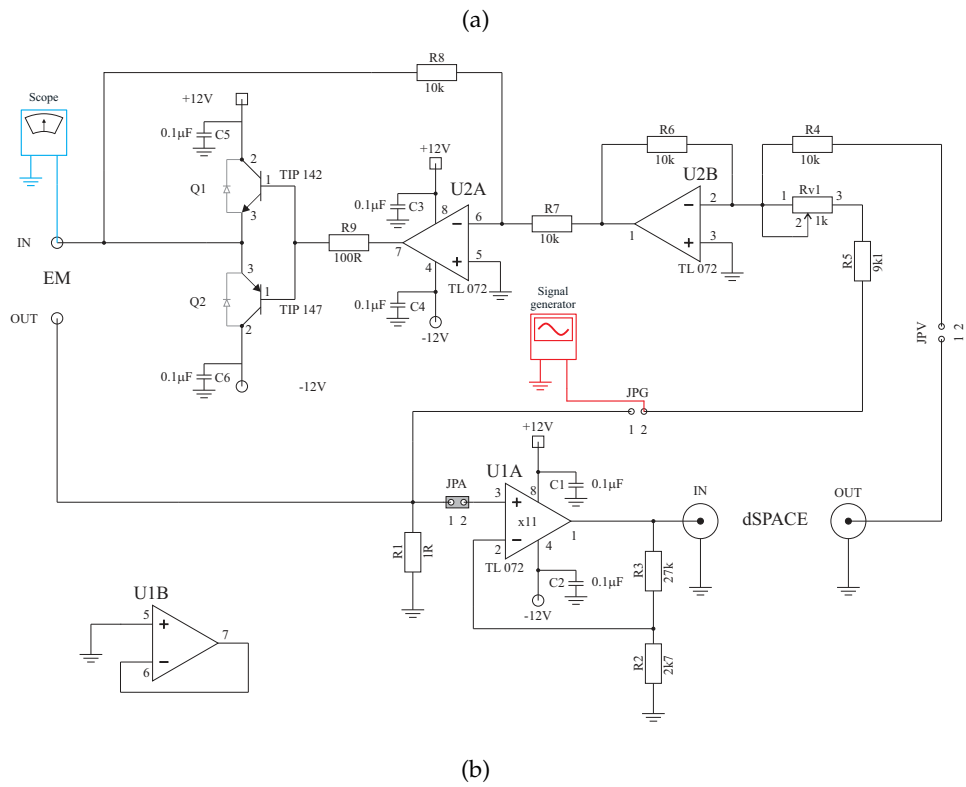
Figure D.10: Scheme (plot (a)) and measurement results (plot (b)) of the third test made on the front-end board.

[1] D. J. Thompson and J. Dixon, Vehicle Noise, in *Advanced Applications in Acoustics, Noise & Vibration* (F. J. Fahy and J. Walker, eds.), ch. 6, London, UK: Spon Press, 2004.

[2] D. J. Thompson, *Railway Noise and Vibration: Mechanisms, Modelling and Means of Control.* Amsterdam, NL: Elsevier, 2009.

[3] J. S. Mixson and J. S. Wilby, Interior Noise, in *Aeroacustics of Flight Vehicles, Theory and Practice* (H. Hubbard, ed.), ch. 16, Hampton, VA: NASA, 1995.

[4] M. Griffith, *Handbook of human vibration.* London, UK: Academic Press, 1990.

[5] I. Flindell, Human response to sound, in *Fundamentals of Sound and Vibration* (F. J. Fahy and D. J. Thompson, eds.), ch. 6, Boca Raton, FL: CRC Press, 2nd ed., 2015.

[6] M. Griffith, Human responses to vibration, in *Fundamentals of Sound and Vibration* (F. Fahy and D. J. Thompson, eds.), ch. 7, Boca Raton, FL: CRC Press, 2nd ed., 2015.

[7] M. J. Brennan and N. Ferguson, Vibration control, in *Advanced Applications in Acoustics, Noise & Vibration* (F. J. Fahy and J. Walker, eds.), ch. 12, London, UK: Spon Press, 2004.

[8] B. Mace, Fundamentals of vibration, in *Fundamentals of Sound and Vibration* (F. Fahy and D. J. Thompson, eds.), ch. 3, Boca Raton, FL: CRC Press, 2nd ed., 2015.

[9] Directive 2003/10/EC of the European Parliament and of the Council of 6 February 2003 on the minimum health and safety requirements regarding the exposure of workers to the risks arising from physical agents (noise) (Seventeenth individual Directive withi, *Official Journal of the European Union*, vol. 42, pp. 38–44, 2003.

[10] Directive 2006/42/EC of the European Parliament and of the Council of 17 May 2006 on machinery, and amending Directive 95/16/EC (recast) (Text with EEA relevance), *Official Journal of the European Union*, vol. 157, pp. 24–86, 2006.

[11] Directive 2002/44/EC of the European Parliament and of the Council of 25 June 2002 on the minimum health and safety requirements regarding the exposure of workers to the risks arising from physical agents (vibration) (sixteenth individual Directive within, *Official Journal of the European Union*, vol. 177, pp. 13–20, 2002.

[12] Directive 2000/14/EC of the European Parliament and of the Council of 8 May 2000 on the approximation of the laws of the Member States relating to the noise emission in the environment by equipment for use outdoors, *Official Journal of the European Union*, vol. 162, pp. 1–78, 2000.

[13] W. X., *Vehicle Noise and Vibration Refinement*. New York, NY: CRC Press, 2010.

[14] D. Thomas, Noise control, in *Fundamentals of Sound and Vibration* (F. J. Fahy and D. Thompson, eds.), ch. 5, Boca Raton, FL: CRC Press, 2nd ed., 2015.

[15] L. E. Goodman, Material and slip damping, in *Harris' Shock and Vibration Handbook* (A. G. Piersol and T. L. Paez, eds.), ch. 35, New York, NY: McGraw-Hill, 6th ed., 2010.

[16] D. A. Bies and C. H. Hansen, *Engineering Noise Control, Theory and Practice*. New York, NY: CRC Press, 2009.

[17] D. J. Mead, *Passive Vibration Control*. Chichester, UK: John Wiley & Sons, Ltd, 1999.

[18] A. D. Nashif, D. I. G. Jones, and J. P. Henderson, *Vibration Damping*. Chichester, UK: John Wiley & Sons, Ltd, 1985.

[19] D. J. Inman, *Vibration with Control*. Chichester, UK: John Wiley & Sons, Ltd, 2006.

[20] K. T. Kedward, Engineering Properties of Composites, in *Harris' Shock and Vibration Handbook* (A. G. Piersol and T. Paez, eds.), ch. 34, New York, NY: McGraw-Hill, 6th ed., 2010.

[21] A. Akay and A. Carcaterra, Damping Mechanisms, in *Active and Passive Vibration Control of Structurs* (P. Hagedorn and G. Spelsberg-Korspeter, eds.), ch. 6, Udine, IT: Springer, 2014.

[22] C. Fuller, S. J. Elliott, and P. A. Nelson, *Active Control of Vibration*. San Diego, CA: Academic Press, 1996.

[23] P. A. Nelson and S. J. Elliott, *Active Control of Sound*. London, UK: Academic Press, 1992.

[24] P. Gardonio, Composite smart panels for active control of sound radiation, in *Encyclopedia of composites* (L. Nicolais and A. Borzachiello, eds.), ch. 45, Chichester, UK: John Wiley & Sons, Ltd, 2012.

[25] P. Gardonio, Active Noise Control, in *Encyclopedia of Aerospace Engineering* (R. Blockley and W. Shyy, eds.), ch. 36, Chichester, UK: John Wiley & Sons, Ltd, 2010.

[26] S. J. Elliott, Active noise and vibration control in vehicles, in *Vehicle Noise and Vibration Refinement* (X. Wang, ed.), ch. 11, New York, NY: CRC Press, 2010.

[27] C. Hansen, S. Snyder, and X. Qiu, *Active Control of Noise and Vibration*. New York, NY: CRC Press, 2012.

[28] P. Gardonio, Boundary Layer Noise - Part 2: Interior Noise Radiation and Control, in *Noise Sources in Tubulent Shear Flows: Fundamentals and Applications* (R. Camussi, ed.), ch. 7, Udine, IT: Springer, 2013.

[29] A. Preumont, *Twelve lectures on structural dynamics*, vol. 198. Dordrec, NL: Springer, 2013.

[30] P. Gardonio, N. Ferguson, and F. Fahy, A Modal Expansion Analysis of Noise Transmission Through Circular Cylindrical Shell Structures With Blocking Masses, *Journal of Sound and Vibration*, vol. 244, no. 2, pp. 259–297, 2001.

[31] J. Den Hartog, *Mechanical Vibrations*. New York, NY: McGraw-Hill, 4th ed., 1956.

[32] B. Korenev and L. Reznikov, *Dynamic Vibration Absorbers: Theory and Technical Applications*. New York, NY: John Wiley & Sons, Ltd, 1993.

[33] M. J. Brennan and J. Dayou, Global control of vibration using a tuneable vibration neutralizer, *Journal of Sound and Vibration*, vol. 232, no. 3, pp. 585–600, 2000.

[34] S. Krenk, Frequency Analysis of the Tuned Mass Damper, *Journal of Applied Mechanics*, vol. 72, no. 6, pp. 936–942, 2005.

[35] J. Rohlfing and P. Gardonio, Ventilation duct with concurrent acoustic feed-forward and decentralised structural feedback active control, *Journal of Sound and Vibration*, vol. 333, pp. 630–645, feb 2014.

[36] S. J. Elliott, *Signal Processing for Active Control*. London, UK: Academic Press, 2001.

[37] M. J. Brennan, Vibration control using a tunable vibration neutralizer, *Proceedings of the Institution of Mechanical Engineers, Part C: Journal of Mechanical Engineering Science*, vol. 211, pp. 91–108, feb 1997.

[38] E. Rustighi, M. J. Brennan, and B. R. Mace, A shape memory alloy adaptive tuned vibration absorber: design and implementation, *Smart Materials and Structures*, vol. 14, no. 19, 2005.

[39] P. Bonello, M. J. Brennan, S. J. Elliott, J. F. V. Vincent, and G. Jeronimidis, Designs for an adaptive tuned vibration absorber with variable shape stiffness element, *Proceeding of the Royal Society A: Mathematical, Physical and Engineering Science*, vol. 461, no. 2064, pp. 3955–3976, 2005.

[40] S. Guenneau and V. Craster, Fundamentals of Acoustic Metamaterials, in *Acoustic Metamaterials* (V. Craster and S. Guenneau, eds.), ch. 1, Dordrecht, NL: Springer, 2013.

[41] L. Airoldi, M. Senesi, and M. Ruzzene, Piezoelectric Superlattices and Shunted Periodic Arrays as Tuneable Periodic Structures and Metamaterials, in *Wave Propagation in Linear and Nonlinear Periodic Media, Analysis and Applications* (F. Romeo and M. Ruzzene, eds.), ch. 2, Udine, IT: Springer, 2012.

[42] M. Zientek, P. Gardonio, and D. Casagrande, Smart metamaterials for noise and vibration control, in *Proceedings of ISMA 2016 - International Conference on Noise and Vibration Engineering and USD2016 - International Conference on Uncertainty in Structural Dynamics 2016*, (Leuven, BE), pp. 1291–1305, 2016.

[43] M. Zientek and P. Gardonio, Metamaterial panel with arrays of piezoelectric patches connected to multi-resonant electrical shunts, in *Proceedings of the 24nd International Congress on Sound and Vibration (ICSV)*, (London, UK), 2017.

[44] N. W. Hagood and A. von Flotow, Damping of structural vibrations with piezoelectric materials and passive electrical networks, *Journal of Sound and Vibration*, vol. 146, no. 2, pp. 243–268, 1991.

[45] S. O. R. Moheimani and A. J. Fleming, *Piezoelectric Transducers for Vibration Control and Damping*. Berlin, DE: Springer, 2006.

[46] M. Zilletti, *Self-tuning vibration absorbers*. Phd thesis, University of Southampton, 2011.

[47] D. E. Casagrande, *Piezoelectric transducers for broadband vibration control*. Phd thesis, Università degli Studi di Udine, 2016.

[48] J. Rohlfing, *Decentralised velocity feedback control for thin homogeneous and lightweight sandwich panels*. Phd thesis, University of Southampton, 2009.

[49] H. Ji, J. Qiu, P. Xia, and D. Guyomar, The influence of switching phase and frequency of voltage on the vibration damping effect in a piezoelectric actuator, *Smart Materials and Structures2*, vol. 20, no. 1, pp. 1–16, 2010.

[50] M. Lallart, S. Harari, L. Petit, D. Guyomar, T. Richard, C. Richard, and L. Gaudiller, Blind switch damping (BSD): A self-adaptive semi-active damping technique, *Journal of Sound and Vibration*, vol. 328, no. 1-2, pp. 29–41, 2009.

[51] D. Guyomar, C. Richard, and S. Mohammadi, Semi-passive random vibration control based on statistics, *Journal of Sound and Vibration*, vol. 307, no. 3-5, pp. 818–833, 2007.

[52] K. A. Cunefare, S. de Rosa, N. Sadegh, and G. Larson, State-Switched Absorber for Semi-Active Structural Control, *Journal of Intelligent Material Systems and Structures*, vol. 11, no. 4, pp. 300–310, 2000.

[53] M. H. Holdhusen and K. A. Cunefare, A State-Switched Absorber Used for Vibration Control of Continuous Systems, *Journal of Vibration and Acoustics*, vol. 129, no. 5, p. 577, 2007.

[54] W. W. Clark, Vibration Control with State-Switched Piezoelectric Materials, *Journal of Intelligent Material Systems and Structures*, vol. 11, pp. 263–271, apr 2000.

[55] P. Gardonio and M. Zilletti, Semi-active multimodal vibration absorber, in *Proceedings of the International Conference on Noise and Vibration Engineering ISMA 2012*, (Leuven, BE), pp. 17–19, 2012.

[56] P. Gardonio and M. Zilletti, Integrated tuned vibration absorbers: A theoretical study, *The Journal of the Acoustical Society of America*, vol. 134, no. 5, p. 3631, 2013.

[57] M. Zilletti and P. Gardonio, Experimental implementation of switching and sweeping tuneable vibration absorbers for broadband vibration control, *Journal of Sound and Vibration*, vol. 334, pp. 164–177, 2015.

[58] P. Gardonio and M. Zilletti, Sweeping tuneable vibration absorbers for low-mid frequencies vibration control, *Journal of Sound and Vibration*, vol. 354, pp. 1–12, 2015.

[59] D. E. Casagrande, P. Gardonio, and M. Zilletti, Time-varying shunted piezoelectric patch absorbers for broadband vibration control, in *Proceedings of the 22nd International Congress on Sound and Vibration (ICSV)*, vol. 400, (Florence, IT), pp. 288–304, Elsevier Ltd, 2015.

[60] E. Turco and P. Gardonio, On the use of tuneale mass dampers for broadband noise control in a cylindrical enclosure, in *Proceedings of the 22nd International Congress on Sound and Vibration (ICSV)*, (Florence, IT), 2015.

[61] D. Casagrande, P. Gardonio, and M. Zilletti, Smart panel with time-varying shunted piezoelectric patch absorbers for broadband vibration control, *Journal of Sound and Vibration*, vol. 400, pp. 288–304, jul 2017.

[62] D. E. Casagrande, P. Gardonio, and M. Zilletti, Sweeping piezoelectric patch vibration absorbers, in *Proceedings of the International Conference on Motion and Vibration Control (13th MoViC) and of the International Conference on Recent Advances in Structural Dynamics (12th RASD)*, (Southampton, UK), 2016.

[63] P. Gardonio and D. Casagrande, Shunted piezoelectric patch vibration absorber on two-dimensional thin structures: Tuning considerations, *Journal of Sound and Vibration*, vol. 395, pp. 26–47, 2017.

[64] E. Turco and P. Gardonio, Sweeping shunted electro-magnetic tuneable vibration absorber: Design and implementation, *Journal of Sound and Vibration*, vol. 407, pp. 82–105, 2017.

[65] E. Turco, P. Gardonio, and L. Dal Bo, Time-varying shunted electromagnetic tuneable vibration absorber, in *Proceedings of the International Conference on Motion and Vibration Control (13th MoViC) and of the International Conference on Recent Advances in Structural Dynamics (12th RASD)*, (Southampton, UK), 2016.

[66] A. Bullmore, *The active minimisation of harmonic enclosed sound fields with particular application to propeller induced cabin noise.* Phd thesis, University of Southampton, 1987.

[67] D. Thomas, P. Nelson, and S. Elliott, Active Control Of The Transmission Of Sound Through A Thin Cylindrical Shell, Part II: The Minimization Of Acoustic Potential Energy, *Journal of Sound and Vibration*, vol. 167, pp. 113–128, oct 1993.

[68] D. R. Thomas, P. A. Nelson, and S. J. Elliott, Active control of the transmission of sound through a thin cylindrical sheel, Part I: the minimization of Vibration energy, *Journal of Sound and Vibration*, vol. 167, no. 1, pp. 113–128, 1993.

[69] Y. M. Huang and C. R. Fuller, The effects of dynamic absorbers on the forced vibration of a cylindrical shell and its coupled interior sound field, *Journal of Sound and Vibration*, vol. 200, no. 4, pp. 401–418, 1997.

[70] "https://www.skybrary.aero/index.php/File:A748_3D.jpg."

[71] "https://commons.wikimedia.org/wiki/File:Avro_748_A10-604_RAAF_East_Sale_Lavtn_18.04.71_edited-3.jpg."

[72] P. Gardonio, S. Miani, F. Blanchini, D. Casagrande, and S. J. Elliott, Plate with decentralised velocity feedback loops: Power absorption and kinetic energy considerations, *Journal of Sound and Vibration*, vol. 331, no. 8, pp. 1722–1741, 2012.

[73] A. Nilsson and B. Liu, *Vibro-Acoustics, Volume 2*. Berlin, Heidelberg: Springer Berlin Heidelberg, 2nd ed., 2015.

[74] H. Frahm, Device for damping vibrations of bodies, *US PATENT 989958*, 1911.

[75] J. Ormondroyd and J. Den Hartog, The theory of dynamic vibration absorber, *Journal of Applied Mechanics*, vol. 50, no. 7, pp. 9–22, 1928.

[76] S. J. Estève, *Control of sound transmission into payload fairings using distributed vibration absorbers and Helmholtz resonators*. Phd thesis, Virginia Polytecnic Institute, 2004.

[77] A. B. Nagy, Aeroacoustics reserch in Europe: The CEAS-ASC report on 2010 highlights, *Journal of Sound and Vibration*, vol. 330, pp. 4955–4980, 2011.

[78] O. Jiříček, Aeroacoustics research in Europe: The CEAS-ASC report on 2015 highlights, *Journal of Sound and Vibration*, vol. 381, pp. 101–120, 2016.

[79] K. Lee, J. Lee, D. Kim, K. Kim, and W. Seong, Propeller sheet cavitation noise source modeling and inversion, *Journal of Sound and Vibration*, vol. 333, no. 5, pp. 1356–1368, 2014.

[80] A. C. Nilsson, Noise Reduction of Bow Thrusters, in *Shipboard Acoustics* (J. Buiten, ed.), pp. 417–432, Dordrecht, NL: Springer Netherlands, 1986.

[81] R. Fisher, Bow Thruster Induced Noise and Vibration, in *Proceedings of Dynamic Positioning Conference*, (Houston, TX), 2000.

[82] Y. Gao, J. M. Muggleton, Y. Liu, and E. Rustighi, An analytical model of ground surface vibration due to axisymmetric wave motion in buried fluid-filled pipes, *Journal of Sound and Vibration*, vol. 395, pp. 142–159, 2017.

[83] J. M. Muggleton and E. Rustighi, 'Mapping the Underworld': recent developments in vibro-acoustic techniques to locate buried infrastructure, *Géotechnique Letters*, vol. 3, no. 3, pp. 137–141, 2013.

[84] M. C. Junger and D. Feit, *Sound, Structures, and Their Interaction*. Cambridge, MA: MIT Press, 2nd ed., 2003.

[85] E. H. Dowell, *Aeroelasticity of Plates and Shells*. New York, NY: Springer, 1974.

[86] E. Dowell, G. Gorman, and D. Smith, Acoustoelasticity: General theory, acoustic natural modes and forced response to sinusoidal excitation, including comparisons with experiment, *Journal of Sound and Vibration*, vol. 52, no. 4, pp. 519–542, 1977.

[87] S. D. Algazin and I. Kijko, *Aeroelastic Vibrations and Stability of Plates and Shells*. Berlin, DE: Walter de Gruyter GmbH, 2015.

[88] C. R. Fuller, Structural influence of the cabin floor on sound transmission into aircraft - Analytical investigations, *Journal of Aircraft*, vol. 24, no. 10, pp. 731–736, 1987.

[89] L. Pope, E. Wilby, C. Willis, and W. Mayes, Aircraft interior noise models: Sidewall trim, stiffened structures, and cabin acoustics with floor partition, *Journal of Sound and Vibration*, vol. 89, no. 3, pp. 371–417, 1983.

[90] L. Pope, D. Rennison, C. Willis, and W. Mayes, Development and validation of preliminary analytical models for aircraft interior noise prediction, *Journal of Sound and Vibration*, vol. 82, no. 4, pp. 541–575, 1982.

[91] L. Pope, E. Wilby, and J. Wilby, Propeller aircraft interior noise model, part I: Analytical model, *Journal of Sound and Vibration*, vol. 118, no. 3, pp. 449–467, 1987.

[92] L. Pope, C. Willis, and W. Mayes, Propeller aircraft interior noise model, part II: Scale-model and flight-test comparisons, *Journal of Sound and Vibration*, vol. 118, no. 3, pp. 469–493, 1987.

[93] A. Bullmore, P. Nelson, and S. Elliott, Theoretical studies of the active control of propeller-induced cabin noise, *Journal of Sound and Vibration*, vol. 140, no. 2, pp. 191–217, 1990.

[94] S. J. Esteve and M. E. Johnson, Adaptive Helmholtz resonators and passive vibration absorbers for cylinder interior noise control, *Journal of Sound and Vibration*, vol. 288, no. 4-5, pp. 1105–1130, 2005.

[95] V. Bokil and U. Shirahatti, A Technique for the Modal Analysis of Sound-Structure Interaction Problems, *Journal of Sound and Vibration*, vol. 173, no. 1, pp. 23–41, 1994.

[96] L. Cheng and J. Nicolas, Free vibration analysis of a cylindrical shell—circular plate system with general coupling and various boundary conditions, *Journal of Sound and Vibration*, vol. 155, no. 2, pp. 231–247, 1992.

[97] L. Cheng, Fluid-Structural Coupling Of A Plate-Ended Cylindrical Shell: Vibration And Internal Sound Field, *Journal of Sound and Vibration*, vol. 174, no. 5, pp. 641–654, 1994.

[98] A. W. Leissa, *Vibration of Shells*. Washington: NASA, 1973.

[99] F. Fahy and P. Gardonio, *Sound and Structural Vibrations*. Oxford: Academic Press, 2nd ed., 2007.

[100] J. N. Pinder and F. J. Fahy, A method for assessing noise reduction provided by cylinders, *Proceedings of the Institute of Acoustics*, vol. 15, no. 3, pp. 195–205, 1993.

[101] W. Soedel, *Vibration of Shells and Plates*. New York: CNR Press, 3rd ed., 2004.

[102] S. Timoshenko and S. Woinowski-Krieger, *Theory of Plates and Shells*. New York, NY: McGraw-Hill, 2nd ed., 1987.

[103] D. S. Houghton and D. J. Johns, A Comparison of the Characteristic Equations in the Theory of Circular Cylindrical Shells, *Aeronautical Quarterly*, vol. 12, no. 03, pp. 228–236, 1961.

[104] A. Gol'denveizer, Methods for justifying and refining the theory of shells (Survey of recent results), *Journal of Applied Mathematics and Mechanics*, vol. 32, no. 4, pp. 704–718, 1968.

[105] J. M. Klosner and H. S. Levine, Further comparison of elasticity and shell theory solutions., *AIAA Journal*, vol. 4, no. 3, pp. 467–480, 1966.

[106] S. Markus, *The Mechanics of Vibrations of Cylindrical Shells*. Oxford: Elsevier Science & Technology, 1988.

[107] C. R. Calladine, *Theory of shell structure*. Cambridge: Cambridge University Press, 1983.

[108] A. Gol'denveizer, *Theory of elastic thin shells*. London, UK: Pergamon Press LTD, 1961.

[109] H. Kraus, *Thin Elastic Shells*. New York, NY: John Wiley & Sons, Ltd, 1967.

[110] A. C. Ugural, *Stresses in Beams, Plates and Shells*. Boca Raton: CRC Press, 3rd ed., 2010.

[111] A. E. H. Love, The Small Free Vibrations and Deformation of a Thin Elastic Shell, *Philosophical Transactions of the Royal Society A: Mathematical, Physical and Engineering Sciences*, vol. 179, pp. 491–546, 1888.

[112] A. E. H. Love, *A Treatise on the Mathematical Theory of Elasticity*. New York, NY: Dover Publications, Inc., 4th ed., 1944.

[113] A. Nilsson and B. Liu, *Vibro-Acoustics, Volume 1*. Berlin, DE: Springer Berlin Heidelberg, 2nd ed., 2015.

[114] L. Meirovitch, *Principles and Techniques of Vibration*. Upper Saddle River, NJ: Prentice Hall, 1997.

[115] E. Ventsel and T. Krauthammer, *Thin Plates and Shells: Theory, Analysis and Applications*. New York: CRC Press, 2001.

[116] A. W. Leissa and M. S. Qatu, *Vibrations of Continuous Systems*. McGraw-Hill, 2011.

[117] A. W. Leissa, *Vibration of Plates*. Washington: NASA, 1969.

[118] D. K. Miller and F. D. Hart, Modal density of thin circular cylinders, NASA CR - 897, tech. rep., Washington, 1967.

[119] F. D. Hart and K. Shah, Compendium of modal densities for structures, NASA CR - 1773, tech. rep., NASA, Washington, 1971.

[120] F. J. Fahy, Response of a cylindrer to random sound in the contained fluid, *Journal of Sound and Vibration1*, vol. 13, no. 2, pp. 171–194, 1970.

[121] M. P. Norton and D. G. Karczub, *Fundamentals of Noise and Vibration Analysis for Engineers*. Cambridge: Cambridge University Press, 2nd ed., 2003.

[122] R. S. Langley, Wave motion and energy flow in cylindrical shells, *Journal of Sound and Vibration*, vol. 169, no. 1, pp. 29–42, 1994.

[123] R. S. Langley, The modal density and mode count of thin cylinders and curved panels, *Journal of Sound and Vibration*, vol. 169, no. 1, pp. 43–53, 1994.

[124] K. Shin and J. Hammond, *Fundamentals of signal processing for sound and vibration*. Chichester, UK: John Wiley & Sons, Ltd, 2008.

[125] J. Bendat and A. G. Piersol, *Random Data Analysis and Measurement Procedures*. New York, NY: John Wiley & Sons, Ltd, 3dr ed., 1990.

[126] L. Cremer, M. Heckl, and B. A. T. Petersson, *Structure - Borne Sound*. Berlin, DE: Springer, 3rd ed., 2005.

[127] P. Gardonio and M. J. Brennan, Mobility and impedance methods in structural dynamics, in *Advanced Applications in Acoustics, Noise & Vibration* (F. J. Fahy and J. Walker, eds.), ch. 9, London: Spon Press, 2004.

[128] L. E. Kinsler, A. R. Frey, A. B. Coppens, and J. V. Sanders, *Fundamentals of Acoustics*. Hoboken, NJ: John Wiley & Sons, Ltd, 4th ed., 2000.

[129] P. M. Morse and K. U. Ingard, *Theretical Acosutics*. Priceton, NJ: Princeton University Press, 1987.

[130] A. D. Pierce, *Acoustics, An Introduction to its Physical Principles and Applications*. Melville: Acoustic Society of America, 1989.

[131] P. M. Morse, *Vibration and Sound*. New York: McGraw-Hill, 2nd ed., 1948.

[132] S. L. Garrett, *Understanding Acoustics*. Cham, CH: Springer, 2017.

[133] M. Abramowitz and I. A. Stegun, *Handbook of Mathematical Functions*. Toronto, ON: Dover Publications, Inc., 1965.

[134] M. R. Spiegel, *Mathematical Handbook of Formulas and Tables*. New York: McGraw-Hill, scaum's ou ed., 1968.

[135] H. Kuttruff, *Room Acoustics*. London, UK: Spon Press, 5th ed., 2009.

[136] F. J. Fahy, Vibration of containeng structures by sound in the contained fluid, *Journal of Sound and Vibration1*, vol. 10, no. 3, pp. 490–512, 1969.

[137] E. H. Dowell, Interior noise studies for single- and double-walled cylindrical shells, *Journal of Aircraft*, vol. 17, no. 9, pp. 690–699, 1980.

[138] S. J. Estève and M. E. Johnson, Reduction of sound transmission into a circular cylindrical shell using distributed vibration absorbers and Helmholtz resonators., *The Journal of the Acoustical Society of America*, vol. 112, no. 6, pp. 2840–2848, 2002.

[139] R. Wright and M. Kidner, Vibration absorbers: A review of applications in interior noise control of propeller aircraft, *Journal of Vibration and Control*, vol. 10, no. 8, pp. 1221–1237, 2004.

[140] J. D. Jones and C. Fuller, Reduction of interior sound field in flexible cylinders by active vibration control, in *Proceeding of the 6th IMAC Conference*, (Kissimmee, FL), 1983.

[141] B. J. Brévart and C. R. Fuller, Active control of coupled wave propagation in fluid-filled elastic cylindrical shells, *The Journal of the Acoustical Society of America*, vol. 94, no. 3, pp. 1467–1475, 1993.

[142] D. S. Mandic and J. D. Jones, Adaptive active control of sound fields in elastic cylinders via vibrational inputs, *AIAA Journal*, vol. 29, no. 10, pp. 1552–1561, 1991.

[143] C. R. Fuller and J. D. Jones, Experiments on reduction of propeller induced interior noise by active control of cylinder vibration, *Journal of Sound and Vibration*, vol. 112, pp. 389–395, 1987.

[144] C. R. Fuller, Mechanisms of Transmission and Control of Low-Frequency Sound in Aircraft Interiors, in *AIAA paper 85-0879*, 1985.

[145] E. H. Waterman, D. Kaptein, and S. L. Sarin, Fokker's Activities in Cabin Noise Control for Propeller Aircraft, in *SAE Paper 830736*, 1983.

[146] W. G. Halvorsen and U. Emborg, Interior Noise Control of the Saab 340 Aircraft, in *SAE Paper 891080*, 1989.

[147] H. J. Hackstein, I. U. Borchers, K. Renger, and K. Vogt, The Dornier 32 B Acoustic Test Cell (ATC) for interior noise tests and selected test results, in *Proceedings of the DGLR/AIAA 14th Aeroacoustics Conference*, (Aachen, DE), 1991.

[148] J. Q. Sun, M. R. Jolly, and M. A. Norris, Passive, Adaptive and Active Tuned Vibration Absorbers—A Survey, *Journal of Mechanical Design*, vol. 117, no. B, pp. 234–242, 1995.

[149] J. C. Snowdon, *Vibration and Shock in Damped Mechanical Systems*. New York, NY: John Wiley & Sons, Ltd, 1968.

[150] D. J. Inman, *Engineering Vibration*. Upper Saddle River, NJ: Prentice Hall, 2007.

[151] J. B. Hunt, *Dynamic Vibration Absorbers*. London, UK: Mechanical Engineering Publications, 1979.

[152] J. E. Brock, A note on the Damped vibration Absorber, *Journal of Applied Mechanics*, vol. 68, pp. A–268, 1946.

[153] J. E. Brock, Theory of the Damped Dynamic Vibration Absorber for Inertial Disturbances, *Journal of Applied Mechanics*, vol. 16, pp. 86–92, 1949.

[154] J. Rohlfing, P. Gardonio, and S. J. Elliott, Base impedance of velocity feedback control units with proof-mass electrodynamic actuators, *Journal of Sound and Vibration*, vol. 330, no. 20, pp. 4661–4675, 2011.

[155] J. Rohlfing, S. J. Elliott, and P. Gardonio, Feedback compensator for control units with proof-mass electrodynamic actuators, *Journal of Sound and Vibration*, vol. 331, no. 15, pp. 3437–3450, 2012.

[156] A. Kras and P. Gardonio, Velocity feedback control with a flywheel proof mass actuator, *Journal of Sound and Vibration*, vol. 402, pp. 31–50, 2017.

[157] S. Rubin, Dynamic Vibration Absorbers and Auxiliary Mass Dampers, in *Harris' Shock and Vibration Handbook* (A. G. Piersol and T. Paez, eds.), ch. 6, New York, NY: McGraw-Hill, 6th ed., 2010.

[158] P. Gardonio and M. Brennan, On the Origins and Development of Mobility and Impedance Methods in Structural Dynamics, *Journal of Sound and Vibration*, vol. 249, no. 3, pp. 557–573, 2002.

[159] M. Zilletti, S. J. Elliott, and E. Rustighi, Optimisation of dynamic vibration absorbers to minimise kinetic energy and maximise internal power dissipation, *Journal of Sound and Vibration*, vol. 331, no. 18, pp. 4093–4100, 2012.

[160] T. Asami, O. Nishihara, and A. M. Baz, Analytical Solutions to H_infinity and H_2 Optimization of Dynamic Vibration Absorbers Attached to Damped Linear Systems, *Journal of Vibration and Acoustics*, vol. 124, no. 2, p. 284, 2002.

[161] O. Nishihara and T. Asami, Closed-Form Solutions to the Exact Optimizations of Dynamic Vibration Absorbers (Minimizations of the Maximum Amplitude Magnification Factors), *Journal of Vibration and Acoustics*, vol. 124, no. 4, p. 576, 2002.

[162] S. H. Crandall and W. D. Mark, *Random Vibration in Mechanical Systems*. London, UK: Academic Press, 1963.

[163] G. B. Warburton, Optimum absorber parameters for various combinations of response and excitation parameters, *Earthquake Engineering & Structural Dynamics*, vol. 10, no. 3, pp. 381–401, 1982.

[164] Y. Iwata, On the construction of the dynamic vibration absorber, *Japanese Society of Mechanical Engineering*, vol. 820, pp. 150–152, 1982.

[165] R. L. Clark, W. R. Saunders, and G. P. Gibbs, *Adaptive structures: dynamics and control*. New York, NY: Wiley, 1998.

[166] D. W. Miller, E. F. Crawley, and B. A. Ward, Inertial actuator design for maximum passive and active energy dissipation in flexible space structures, in *Proceedings of the 26th Conference of the AIAA/ASME/ASCE/AHS, Structures, Structural Dynamics and Materials*, (Orlando, FL), pp. 536–544, 1985.

[167] H. Yamaguchi, Damping of transient vibration by a dynamic absorber., *Transactions of the Japan Society of Mechanical Engineers Series C*, vol. 54, no. 499, pp. 561–568, 1988.

[168] F. Fahy and C. Schofield, A note on the interaction between a Helmholtz resonator and an acoustic mode of an enclosure, *Journal of Sound and Vibration*, vol. 72, no. 3, pp. 365–378, 1980.

[169] S. O. R. Moheimani, D. Halim, and A. J. Fleming, *Spatial Control of Vibration, Theory and Experiments*. River Edge, NJ: World Scientific Publishing Co. Pte. Ltd., 2003.

[170] M. Zilletti, Feedback control unit with an inerter proof-mass electrodynamic actuator, *Journal of Sound and Vibration*, vol. 369, pp. 16–28, 2015.

[171] S. J. Elliott and M. Zilletti, Scaling of electromagnetic transducers for shunt damping and energy harvesting, *Journal of Sound and Vibration*, vol. 333, no. 8, pp. 2185–2195, 2014.

[172] S. Camperi, M. Zilletti, and S. J. Elliott, Active vibration control of an inertial actuator subject to broadband excitation, *Journal of Physics: Conference Series*, vol. 744, no. 1, p. 012028, 2016.

[173] S. Perfetto, J. Rohlfing, F. Infante, D. Mayer, and S. Herold, Test rig with active damping control for the simultaneous evaluation of vibration control and energy harvesting via piezoelectric transducers, *Journal of Physics: Conference Series*, vol. 744, no. 1, p. 012010, 2016.

[174] C. González Díaz, C. Paulitsch, and P. Gardonio, Active damping control unit using a small scale proof mass electrodynamic actuator, *Journal of the Acoustical Society of America*, vol. 124, no. 2, pp. 886–897, 2008.

[175] C. Paulitsch, P. Gardonio, and S. J. Elliott, Active vibration control using an inertial actuator with internal damping, *The Journal of the Acoustical Society of America*, vol. 119, no. 4, pp. 2131–2140, 2006.

[176] A. Fleming and S. Moheimani, Inertial vibration control using a shunted electromagnetic transducer, *IEEE/ASME Transactions on Mechatronics*, vol. 11, no. 1, pp. 84–92, 2006.

[177] S. Behrens, A. J. Fleming, and S. O. R. Moheimani, Vibration Isolation using a Shunted Electromagnetic Transducer, vol. 5386, pp. 506–515, 2004.

[178] S. Behrens, A. Fleming, and S. Reza Moheimani, Electromagnetic shunt damping, in *Proceedings 2003 IEEE/ASME International Conference on Advanced Intelligent Mechatronics (AIM 2003)*, vol. 2, (Kobe, JP), pp. 1145–1150, IEEE.

[179] S. Behrens, A. Fleming, and S. Moheimani, Passive Vibration Control via Electromagnetic Shunt Damping, *IEEE/ASME Transactions on Mechatronics*, vol. 10, no. 1, pp. 118–122, 2005.

[180] D. Niederberger, S. Behrens, A. Fleming, S. Moheimani, and M. Morari, Adaptive electromagnetic shunt damping, *IEEE/ASME Transactions on Mechatronics*, vol. 11, no. 1, pp. 103–108, 2006.

[181] A. Preumont, *Mechatronics: Dynamics of Electromechanical and Piezoelectric Systems*. Dordrecht, NL: Springer, 2006.

[182] D. B. Hiemstra, G. Parmar, and S. Awtar, Performance Tradeoffs Posed by Moving Magnet Actuators in Flexure-Based Nanopositioning, *IEEE/ASME Transactions on Mechatronics*, vol. 19, no. 1, pp. 201–212, 2014.

[183] L. Dal Bo and P. Gardonio, Comparison between alectromagnetic and piezoelectric seismic vibration energy harvesters, in *Proceedings of ISMA 2016 - International Conference on Noise and Vibration Engineering and USD2016 - International Conference on Uncertainty in Structural Dynamics 2016*, (Leuven, BE), 2016.

[184] J. R. Brauer, *Magnetic Actuators and Sensors*. Piscataway, NJ: Wiley-IEEE Press, 2nd ed., 2014.

[185] P. Krause, O. Wasynczuk, and S. Pekarek, *Electromechanical Motion Devices*. Piscataway, NJ: Wiley-IEEE Press, 2nd ed., 2012.

[186] S. H. Crandall, *Dynamics of Mechanical and Electromechanical Systems*. Malabar, FL: Krieger Publishing Co., Inc., reprint 19 ed., 1982.

[187] F. V. Hunt, *Electroacoustics: The Analysis of Transduction, and Its Historical Background*. Cambridge, MA: Harvard University Press, 2nd ed., 1982.

[188] P. Horowitz and W. Hill, *The Art of Electronics*. Cambridge, UK: Cambridge University Press, 2nd ed., 1989.

[189] W. A. Gardner, *Statistical Spectral Analysis: a Nonprobabilistic Theory*. Englewood Cliff, NJ: Prentice Hall, 1987.

[190] F. D. Hart and K. Shah, Compendium of modal densities for structures, tech. rep., NASA, Washington D.C., 1971.

[191] B. Mace, Statistical energy analysis, energy distribution models and system modes, *Journal of Sound and Vibration*, vol. 264, no. 2, pp. 391–409, 2003.

[192] G. Xie, D. J. Thompson, and C. J. C. Jones, Mode count and modal density of structural systems: Relationships with boundary conditions, *Journal of Sound and Vibration*, vol. 274, no. 3-5, pp. 621–651, 2004.

[193] M. F. Ashby, *Materials Selection in Mechanical Design*. Oxford, UK: Elsevier, 3rd ed., 2005.

[194] F. J. Fahy, Measurement of audio-frequency sound in air, in *Fundamentals of Sound and Vibration* (F. J. Fahy and D. J. Thompson, eds.), ch. 8, Boca Raton, FL: CRC Press, 2nd ed., 2015.

[195] T. Waters, Vibration testing, in *Fundamentals of Sound and Vibration* (F. J. Fahy and D. J. Thompson, eds.), ch. 9, Boca Raton, FL: CRC Press, 2nd ed., 2015.

[196] M. Zilletti, S. J. Elliott, and M. G. Tehrani, Electromechanical pendulum for vibration control and energy harvesting, in *Proceeding of the 6th EACS*, (Sheffield, UK), 2016.

[197] M. Zilletti, S. J. Elliott, and M. G. Tehrani, Tuneable electromechanical pendulum for vibration control, in *Proceeding of the XXXV IMAC*, (Los Angeles, CA), 2017.

[198] A. V. Oppenheim and R. Schafer, *Digital Signal Processing*. Englewood Cliff, NJ: Prentice Hall, 1975.

[199] R. D. Blevins, *Formulas for Dynamics, Acoustics and Vibration*. Chichester, UK: John Wiley & Sons, Ltd, 2015.

[200] S. Behrens, A. J. Fleming, and S. O. R. Moheimani, Passive vibration control via electromagnetic shunt damping, *IEEE/ASME Transactions on Mechatronics*, vol. 10, no. 1, pp. 118–122, 2005.

[201] B. Korenev, *Bessel Functions and their Applications*. New York, NY: Taylor & Francis, 2002.

[202] N. J. Kasdin, Runge-Kutta Algorithm for the Numerical Integration of Stochastic Differential Equations, *Journal of Guidance, Control, and Dynamics*, vol. 18, no. 1, pp. 114–120, 1995.

[203] N. J. Kasdin and L. J. Stankievech, On Simulating Randomly Driven Dynamic Systems, *The Journal of the Astronautical Sciences*, vol. 57, no. 1-2, pp. 289–311, 2009.

[204] D. Newland, *An Introduction to Random Vibrations, Spectral & Wavelet Analysis*. London, UK: Longman, 3rd ed., 1993.